JOTCS A

Journal of the Turkish Chemical Society
Section: A
Chemistry

Volume: 1, No: 1 June 2015

An Open-Access-Based Scholarly Chemical Journal

www.dergipark.ulakbim.gov.tr/Jotcsa

Published, in English, Biannually
(every June and December)
Turkish Translations of Titles and Abstracts are Available.

TURKISH
CHEMICAL SOCIETY

jotcsa@turchemsoc.org

Correspondance to:
Dr. Barbaros AKKURT, PHD, Managing Editor

Turkish Chemical Society
Halaskargazi Str. Uzay. Apt. No:25 D:8, Harbiye-Sisli-Istanbul/Turkey

Journal of the Turkish Chemical Society, Section A: Chemistry (JOTCSA)

e-ISSN: 2149-0120

A biannual, open-access chemical journal, hosted by Dergipark
(Published, in English, in every February and August)

Address: Halaskargazi Str. Uzay Apt. No: 15/8, 34373 Harbiye, Istanbul/Turkey.
Fax: +90 212 231 70 37
E-mail: jotcsa@turchemsoc.org
Website: http://dergipark.ulakbim.gov.tr/jotcsa

ETHICAL GUIDELINES

Guidelines for the Editors

An editor (editors, associate editors, etc.) should provide impartial consideration to all manuscripts offered for publication, judging each on its particular feature without regard to race, religion, nationality, sex, seniority, or institutional affiliation of the author(s). An editor should review and treat a manuscript submitted for publication with all reasonable speed. An editor takes the sole responsibility for accepting or rejecting a manuscript for publication. An editor may seek assistance on a manuscript from specialists chosen for their expertise and fair judgment. An editor should not reveal any information about the manuscript under consideration to anyone other than the author and designated reviewers until after the evaluation process is complete. An editor should respect the intellectual independence of authors.

Authors

Our journal considers a person as an author who is responsible at least for a part of the work. Authors should be able to explain the problem in study in a deep manner. For our journal, all authors are responsible for the content they submitted. The corresponding author is responsible for the agreement of all the authors and to keep them informed about the submission process since first submission of their manuscript. He/she is responsible for providing the license to publish, in case of acceptance, on behalf of all the authors. Our journal assumes that submitting the paper implies in total agreement from all the authors. For manuscripts with more than 8 authors, all the authors should provide a declaration specifying what was their contribution to the manuscript. It is not acceptable for JOTCSA to consider for publication anything that was previously published, neither entirely nor partly in other journals. Anything sent to our journal must not be under analysis by anywhere else. Simultaneous submissions to JOTCSA and any other journal, is considered a major conduct flaw, and all the authors will be definitely banned, and all their previous publications in JOTCSA will be publicly retracted. Plagiarism and self-plagiarism will be treated in the same way. Multiple manuscripts, dealing with closely related subjects and/or variables are discouraged as long as they could figure in a single paper.

Reviewers

JOTCSA invites peers to review its submissions, relying on their expertise, curricula, and their will to review them as volunteers. By accepting to review a manuscript, the reviewer commits himself to do so in due time. Delays are extremely negative to the review process and makes it last much longer than it should. When a reviewer is requested, he/she is gently asked to answer the invitation e-mail, informing if he/she is willing or not willing to review the manuscript. It is a gesture of politeness, and it avoids delays too. By accepting to review a manuscript, the reviewer declares that no conflicts of interests do exist, and he/she is doing his/her revision for the wealth and progress of Science. Those reviewers who answer our requests, agreeing or not, and those who respect the deadlines, are scored positively, and eventual submissions they could send to JOTCSA will be treated with priority.

The online version of this declaration can be viewed on http://dergipark.ulakbim.gov.tr/public/journals/5106/ethical_guidelines.pdf.

Journal of the Turkish Chemical Society, Section A: Chemistry (JOTCSA)

e-ISSN: 2149-0120

A biannual, open-access chemical journal, hosted by Dergipark
(Published, in English, in every February and August)

Contents (February 2016-August 2016)

JOTCSA, Volume 3, issue 1, (2016), pp. 75-88. **Research article**

Journal homepage: http://dergipark.ulakbim.gov.tr/jotcsa

e-ISSN: 2149-0120

CHEMICAL REACTIVITY OF ETHYL 4-(1-ETHYL-1,2-DIHYDRO-4-HYDROXY-2-OXOQUINOLIN-3-YL)-2,4-DIOXOBUTANOATE TOWARDS SOME NUCLEOPHILIC REAGENTS

Magdy A. Ibrahim[1], Hany M. Hassanin[1]*, and Shimaa Badran[1]

[1]*Department of Chemistry, Faculty of Education, Ain Shams University, Roxy, Heliopolis 11757, Cairo, Egypt.*

Abstract: A novel series of heterocyclic systems linked with quinolin-2-one was efficiently synthesized from reaction of ethyl 4-(1-ethyl-1,2-dihydro-4-hydroxy-2-oxoquinolin-3-yl)-2,4-dioxobutanoate (**1**) with a variety of nitrogen and/or carbon nucleophiles. A variety of heterocyclic systems such as pyrazoles, pyrimidines, pyrazines, oxazines and triazines containing quinoline moiety were synthesized. Structures of the new synthesized products were deduced on basis of their analytical and spectral data.

Keywords: Quinolin-2-one, diketoester, active methylene, nucleophilic reaction, heterocyclization.
Submitted: December 12, 2015. **Revised:** January 11, 2016. **Accepted:** February 7, 2016.

Cite this: Ibrahim M, Hassanin H, Badran S. CHEMICAL REACTIVITY OF ETHYL 4-(1-ETHYL-1,2-DIHYDRO-4-HYDROXY-2-OXOQUINOLIN-3-YL)-2,4-DIOXOBUTANOATE TOWARDS SOME NUCLEOPHILIC REAGENTS. Journal of the Turkish Chemical Society, Section A: Chemistry. 2016;3(2):75–88.
DOI: 10.18596/jotcsa.11975.
Correspondence to: Hany M. Hassanin. E-mail: hanyhassnin@yahoo.com.

INTRODUCTION

4-Hydroxyquinolin-2(1H)-ones represent one of the most important classes of heterocycles possessing a wide spectrum of biological activities [1-4]. Quinoline derivatives have been used as bactericidal [5], anti-inflammatory [6], antimalarial [7], antitumor [8], antioxidant [9], antileishmanial [10] and antiplatelet activities [11] such as DNA binding capabilities and DNA-intercalating carrier [12]. Also, a broad number of important pharmacological activities have been associated with 3-substituted 4-hydroxyquinolin-2(1H)-ones [13, 14]. The present work aimed to synthesize ethyl 4-(1-ethyl-4-hydroxy-2-oxo-1,2-dihydroquinolin-3-yl)-2,4-dioxobutyrate (**1**) [15] as a starting material and study its chemical reactivity towards a variety of nucleophilic reagents, in a hope to obtain a novel series 4-hydroxyquinolin-2(1H)-ones bearing variable heterocyclic systems of expected biological activity.

EXPERIMENTAL SECTION

General. Melting points were determined on a digital Stuart SMP3 apparatus. Fourier-transform infrared spectra were taken on FT-IR Nicolet IS10 spectrophotometer (cm^{-1}), using KBr disks. ^1H NMR (300 MHz) spectra were measured on Mercury-300BB, using DMSO-d_6 as a solvent and tetramethylsilane as an internal standard. Mass spectra were measured using GC-2010 Shimadzu Gas chromatography instrument mass spectrometer (70 eV) GC-MS qp 1000 ex Shimadzu instrument (70 eV). Elemental microanalyses were performed on a Perkin-Elmer CHN-2400 analyzer at the Chemical War Department, Ministry of Defense, Egypt. Ethyl 4-(1-ethyl-4-hydroxy-2-oxo-1,2-dihydroquinolin-3-yl)-2,4-dioxobutyrate (**3**) [15] was prepared according to the literature method.

Ethyl 1-(2-cyanoacetyl)-5-(1-ethyl-1,2-dihydro-4-hydroxy-2-oxoquinolin-3-yl)-1H-pyrazole-3-carboxylate (3).

A mixture of diketoester **1** (0.50 g, 1.51 mmol) and cyanoacetohydrazide (0.15 g, 1.51 mmol), in absolute ethanol (20 mL), containing few drops of acetic acid, was stirred at room temperature for 2 h. The beige precipitate so formed was filtered and crystallized from EtOH to give compound **3** as beige crystals, yield (0.30 g, 54%), m.p. > 300 ^oC. FT-IR (KBr, cm^{-1}): 3446 (OH), 2987, 2934 ($CH_{aliph.}$), 2263 (C≡N), 1756 ($C=O_{ester}$), 1695 ($C=O_{ketone}$), 1638 ($C=O_{quinolone}$), 1572 (C=N) and 1504 (C=C). ^1H NMR (δ, 300 MHz, DMSO-d_6): 1.16-1.32 (m, 6H, $2CH_2CH_3$), 3.90 (s, 2H, CH_2), 4.19 (q, 2H, NCH_2CH_3), 4.48 (q, 2H, OCH_2CH_3), 7.20 (s, 1H, H-$4_{pyrazole}$), 7.32 (t, 1H, H-$6_{quinolone}$), 7.59 (d, 1H, H-$8_{quinolone}$), 7.72 (t, 1H, H-$7_{quinolone}$), 8.06 (d, 1H, H-$5_{quinolone}$), 11.90 (bs, 1H, OH exchangeable with D_2O). Mass spectrum, m/z (I_r %): 394 ($M^{+\cdot}$, 14), 393 (60), 363 (24), 368 (11), 327 (17), 268 (47), 230 (10), 212 (18), 197 (16), 188 (8), 172 (8), 161 (8), 146 (19), 132 (29), 119 (21), 102 (66), 91 (25), 77 (79), 64 (96) and 55 (100). Anal. Calcd. for $C_{19}H_{19}N_3O_5$ (394.38); C, 60.91; H, 4.60; N, 14.21%. Found: C, 60.80; H, 4.55; N, 14.08%.

Ethyl 5-(1-ethyl-1,2-dihydro-4-hydroxy-2-oxoquinolin-3-yl)-1-[(pyridine-3-yl) carbonyl]-1H-pyrazole-3-carboxylate (4).

A mixture of diketoester **1** (0.50 g, 1.51 mmol) and nicotinic acid hydrazide (0.21 g, 1.51 mmol), in absolute ethanol (20 mL), containing few drops of acetic acid, was heated under reflux for 2 h. The brown crystals deposited after cooling were filtered and recrystallized from ethanol to give compound **4** as pale brown crystals, yield (0.24 g, 37%), m.p. > 300 ^{o}C; FT-IR (KBr) ν_{max} 3446 (OH), 2981, 2931 ($CH_{aliph.}$), 1706 ($C=O_{ester}$), 1683 ($C=O_{ketone}$), 1632 ($C=O_{quinolone}$), 1617 (C=N) and 1550 cm^{-1} (C=C); ^{1}H NMR (DMSO-d_6, 300 MHz) δ 1.18-1.30 (m, 6H, 2CH2C*H*$_3$), 4.10-4.25 (m, 4H, 2C*H*$_2$CH$_3$), 7.10 (s, 1H, H-4$_{pyrazole}$), 7.40-7.60 (m, 3H, H-6$_{quinolone}$, H-8$_{quinolone}$ and H-7$_{quinolone}$), 8.10 (d, 1H, H-5$_{quinolone}$), 8.30 (t, 1H, H-5$_{pyridine}$), 8.60-8.80 (m, 2H, H-4$_{pyridine}$ and H-6$_{pyridine}$), 8.90 (s, 1H, H-2$_{pyridine}$), 10.00 (bs, 1H, OH exchangeable with D_2O); Mass spectrum, m/z (rel. int. %): 432 [M$^{+\cdot}$] (6), 347 (3), 327 (6), 281 (5), 269 (4), 224 (4), 182 (9), 132 (6), 120 (5), 106 (37) and 64 (100). Anal. Calcd for $C_{23}H_{20}N_4O_5$ (432.44), C, 63.90%; H, 4.50%; N, 12.88%; Found, C, 63.88%, H, 4.66%, N, 12.96%.

Ethyl 1-(7-chloroquinolin-4-yl)-5-(1-ethyl-1,2-dihydro-4-hydroxy-2-oxoquinolin-3-yl)-1H-pyrazole-3-carboxylate (5).

A mixture of diketoester **1** (0.50 g, 1.51 mmol) and 7-chloro-4-hydrazinoquinoline (**2**) (0.29 g, 1.51 mmol), in absolute ethanol (20 mL), containing few drops of acetic acid, was heated under reflux for 4 h. The reaction mixture was left to cool at room temperature. The solid so formed was filtered and crystallized from DMF to give compound **5** as red-brown crystals, yield (0.35 g, 47%), m.p. > 300 ^{o}C; FT-IR (KBr) ν_{max} 3406 (OH), 3076 ($CH_{arom.}$), 2931 ($CH_{aliph.}$), 1707 ($C=O_{ester}$), 1628 ($C=O_{quinolone}$), 1608 (C=N) and 1586 cm^{-1} (C=C); ^{1}H NMR (DMSO-d_6, 300MHz) δ 1.19-1.22 (m, 6H, 2CH$_2$C*H*$_3$), 4.10-4.30 (m, 4H, 2C*H*$_2$CH$_3$), 6.40 (s, 1H, H-4$_{pyrazole}$), 7.12 (t, 1H, H-6$_{quinolone}$), 7.32-7.46 (m, 2H, H-8$_{quinolone}$ and H-6$_{quinoline}$), 7.46 (s, 1H, H-8$_{quinoline}$), 7.6 (t, 1H, H-7$_{quinolone}$), 7.60-8.00 (m, 2H, H-5$_{quinolone}$ and H-5$_{quinoline}$), 8.15 (d, 1H, H-2$_{quinoline}$), 8.32 (d, 1H, H-3$_{quinoline}$); Mass spectrum, m/z (rel. int. %): 489 [M$^{+\cdot}$] (67), 464 (91), 432 (77), 417 (97), 352 (80), 319 (83), 272 (65), 229 (95), 206 (97), 178 (100) and 77 (76). Anal. Calcd for $C_{26}H_{21}ClN_4O_4$ (488.93), C 63.70%; H 4.40%; N 11.36%; found, C 63.87%; H 4.33%; N 11.46%.

Ethyl 5-(1-ethyl-1,2-dihydro-4-hydroxy-2-oxoquinolin-3-yl)[1,2,4]triazolo[4,3-*a*] pyrimidine-7-carboxylate (7).

A mixture of diketoester **1** (0.50 g, 1.51 mmol) and 3-amino[1,2,4]triazole (**6**) (0.13 g, 1.51 mmol), in absolute ethanol (20 mL) containing few drops of acetic acid, was heated under reflux for 4 h. The yellow crystals deposited after cooling were filtered and crystallized from EtOH to give compound **7** as golden yellow crystals, yield (0.38 g, 67%), m.p. 200-201 ^{o}C; FT-IR (KBr) ν_{max} 3447 (OH), 3103 ($CH_{arom.}$), 2970, 2925, 2854 ($CH_{aliph.}$), 1751 ($C=O_{ester}$), 1635 ($C=O_{quinolone}$), 1609 (C=N) and 1570 cm^{-1} (C=C). ^{1}H NMR (DMSO-d_6, 300 MHz) δ 1.21 (t, 3H, *J*=6.9 Hz, N-CH$_2$C*H*$_3$), 1.38 (t, 3H, *J*=6.7 Hz, O-CH$_2$C*H*$_3$), 4.24 (q, 2H, *J*=6.9 Hz, N-C*H*$_2$CH$_3$), 4.50 (q, 2H, *J*=6.7 Hz, O-C*H*$_2$CH$_3$), 7.20 (t, 1H, H-6$_{quinolone}$), 7.51 (d, 1H, H-8$_{quinolone}$), 7.60 (t, 1H, H-7$_{quinolone}$), 8.03 (d, 1H, J=6.7 Hz, H-5$_{quinolone}$), 8.73 (s, 1H, H-5$_{pyrimidine}$), 9.40 (s, 1H, H-3$_{triazole}$), 17 (bs, 1H, OH exchangeable with D_2O). Mass spectrum, m/z (rel. int. %): 379 [M$^{+\cdot}$] (95), 360 (61), 331 (71), 279 (67), 267 (67), 223 (84), 203 (61), 162 (69), 132 (100), 89 (47) and 77 (84). Anal. Calcd for $C_{19}H_{17}N_5O_4$ (379.38), C, 60.20%; H, 4.65%; N, 18.52%; found, C 60.15%; H 4.52%; N 18.46%.

Ethyl 4-(1-ethyl-1,2-dihydro-4-hydroxy-2-oxoquinolin-3-yl)pyrimido[1,2-*a*] benzimidazole-2-carboxylate (9).

A mixture of diketoester **1** (0.50 g, 1.51 mmol) and 2-aminobenzimidazole (**8**) (0.20 g, 1.51 mmol), in absolute ethanol (20 mL), containing few drops of acetic acid, was heated under reflux for 2 h. The orange-red crystals obtained during heating was filtered and crystallized from DMF to give compound **9** as orange-red, yield (0.50 g, 77%), m.p. > 300 °C; FT-IR (KBr) ν_{max} 3359 (OH), 3093 ($CH_{arom.}$), 2970, 2925 ($CH_{aliph.}$), 1707 ($C=O_{ester}$), 1645 ($C=O_{quinolone}$), 1612 (C=N) and 1588 cm^{-1} (C=C); ^{1}H NMR (DMSO-d_6, 300 MHz) δ 1.19-1.24 (m, 6H, $2CH_2CH_3$), 4.20-4.30 (m, 4H, $2CH_2CH_3$), 6.90 (s, 1H, H-$3_{pyrimidine}$), 7.02-7.04 (m, 2H, Ar-H), 7.22-7.24 (m, 2H, Ar-H), 7.41 (t, 1H, *J*=7.5 Hz, H-$6_{quinolone}$), 7.64 (d, 1H, *J*=8.7 Hz, H-$8_{quinolone}$), 7.79 (t, 1H, *J*=7.5 Hz, H-$7_{quinolone}$), 8.26 (d, 1H, *J*=7.8 Hz, H-$5_{quinolone}$); Mass spectrum, m/z (rel. int. %): 428 [$M^{+\cdot}$] (83), 386 (100), 346 (65), 296 (77), 233 (90), 177 (87), 134 (90), 109 (48), 92 (76) and 70 (75). Anal. Calcd for $C_{24}H_{20}N_4O_4$ (428.45), C, 67.17%; H, 4.82%; N, 13.10%; found, C, 67.28%; H, 4.71%; N, 13.08%.

1-Ethyl-3-[2-(3,4,5,6-tetrahydro-3-oxopyrazin-3-yl)acetyl]-4-hydroxyquinolin-2(1H)-one (10).

A mixture of diketoester **1** (0.50 g, 1.51 mmol) and ethylene diamine (0.09 mL), in absolute ethanol (20 mL) containing few drops of acetic acid, was heated under reflux for 2 h. The solid obtained after cooling was filtered and crystallized from EtOH to give compound **10** as brown crystals, yield (0.21 g, 41%), m.p. > 300 °C; FT-IR (KBr) ν_{max} 3425 (OH), 3340 (NH), 3067 ($CH_{arom.}$), 2975, 2936 ($CH_{aliph.}$), 1675 ($C=O_{amide}$), 1632 ($C=O_{ketone}$ and $C=O_{quinolone}$) and 1559 cm^{-1} (C=N and C=C); ^{1}H NMR (DMSO-d_6, 300 MHz) δ 1.16 (t, 3H, CH_2CH_3), 2.70 (s, 2H, CH_2), 3.21-3.30 (m, 4H, N-CH_2-CH_2-N), 4.35 (q, 2H, CH_2CH_3), 7.16 (t, 1H, *J*=6.0 Hz, H-$6_{quinolone}$), 7.36 (d, 1H, *J*=7.2 Hz, H-$8_{quinolone}$), 7.60 (t, 1H, H-$7_{quinolone}$), 8.07 (d, 1H, *J*=7.8 Hz, H-$5_{quinolone}$), 8.70 (bs, 1H, NH exchangeable with D_2O). Mass spectrum, m/z (I_r %): 327 ($M^{+\cdot}$, 1), 246 (63), 233 (24), 216 (100), 189 (45), 172 (4), 146 (14), 132 (28), 119 (13), 91 (9), 77 (66) and 64 (50). Anal. Calcd for $C_{17}H_{17}N_3O_4$ (327.34), C, 62.31%; H, 5.31%; N, 12.89%; found, C, 62.38; H, 5.23; N, 12.84%.

1-Ethyl-3-[2-(1,2-dihydro-2-oxoquinoxalin-3-yl)acetyl]-4-hydroxyquinolin-2(1H)-one (11).

A mixture of diketoester **1** (0.50 g, 1.51 mmol) and o-phenylene diamine (0.16 g, 1.51 mmol) in absolute ethanol (20 mL), containing few drops of acetic acid, was heated under reflux for 2 h. The orange crystals obtained during heating were filtered and crystallized from DMF to give compound **11** as pale orange crystals, yield (0.33 g, 62%), m.p. > 300 °C; FT-IR (KBr) ν_{max} 3447 (OH), 3121 (NH), 3050 ($CH_{arom.}$), 2931 ($CH_{aliph.}$), 1685 ($C=O_{amide}$), 1647 ($C=O_{ketone}$ and $C=O_{quinolone}$), 1601 (C=N) and 1559 cm^{-1} (C=C). ^{1}H NMR (DMSO-d_6, 300 MHz) δ 1.18 (t, 3H, CH_2CH_3), 2.60 (s, 2H, CH_2), 4.24 (q, 2H, CH_2CH_3), 7.01-8.10 (m, 8H, Ar-H), 12.10 (bs, 1H, NH exchangeable with D_2O), 12.80 (bs, 1H, OH exchangeable with D_2O); Mass spectrum, m/z (rel. int. %): 375 [$M^{+\cdot}$] (10), 347 (4), 329 (3), 261 (3), 216 (6), 189 (9), 160 (15), 132 (22), 119 (6), 103 (6) and 64 (100). Anal. Calcd for $C_{21}H_{17}N_3O_4$ (375.39), C, 67.28%; H, 4.45%; N, 11.32%; found, C, 67.19%; H, 4.56%; N, 11.19%.

1-Ethyl-3-[2-(2-oxo-2H-benzo[b][1,4]-oxazin-3-yl)acetyl]-4-hydroxyquinolin-2(1H)-one (12).

A mixture of diketoester **1** (0.50 g, 1.51 mmol) and 2-aminophenol (0.16 g, 1.51 mmol), in absolute ethanol (20 mL), containing few drops of acetic acid, was heated under reflux for 2 h. The solid obtained during heating was filtered and crystallized from DMF to give compound **12** as orange crystals, yield (0.2 g, 37%), m.p. 260-261 ^{o}C; FT-IR (KBr) ν_{max} 3140 (OH), 3050 ($CH_{arom.}$), 2928 ($CH_{aliph.}$), 1752 ($C=O_{\alpha\text{-pyrone}}$), 1641 ($C=O_{ketone}$ and $C=O_{quinolone}$), 1604 (C=N) and 1560 cm^{-1} (C=C); ^{1}H NMR (DMSO-d_6, 300 MHz) δ 1.22 (t, 3H, *J*=6.6 Hz, CH_2CH_3), 2.60 (s, 2H, CH_2), 4.26 (q, 2H, *J*=6.6 Hz, CH_2CH_3), 7.15-7.26 (m, 3H, Ar-H), 7.50 (d, 1H, *J*=8.1 Hz, Ar-H), 7.69 (d, 1H, *J*=6.9 Hz, Ar-H), 7.76 (t, 1H, *J*=7.8 Hz, Ar-H), 8.12-8.20 (m, 2H, Ar-H), 12.14 (bs, 1H, OH exchangeable with D_2O); Mass spectrum, m/z (rel. int. %): 376 [$M^{+\cdot}$] (17), 348 (21), 313 (21), 298 (23), 223 (18), 188 (21), 154 (22), 133 (100), 120 (64), 104 (89) and 77 (33). Anal. Calcd for $C_{21}H_{16}N_2O_5$ (376.37), C, 67.10%; H, 4.38%; N, 7.54%; found, C, 67.02%; H, 4.28%; N, 7.44%.

5-Ethyl-3[(1,2-dihydro-2-oxoquinoxalin-3-yl)methyl]-1H-pyrazolo[4,3-c] quinolin-4(5H)-one (13).

A mixture of compound **11** (0.50 g, 1.30 mmol) and hydrazine hydrate (0.06 mL), in absolute ethanol (20 mL), containing one drop of sulfuric acid, was heated under reflux for 10 h. The solid obtained during heating was filtered and crystallized from DMF to give compound **13** as dark orange crystals, yield (0.30 g, 61%), m.p. > 300 ^{o}C; FT-IR (KBr) ν_{max} 3196, 3129 (NH), 3040 ($CH_{arom.}$), 2975 ($CH_{aliph.}$), 1685 ($C=O_{amide}$), 1647 ($C=O_{quinolone}$), 1596 (C=N) and 1559 cm^{-1} (C=C); ^{1}H NMR (DMSO-d_6, 300 MHz) δ 1.26 (t, 3H, *J*=6.9 Hz, CH_2CH_3), 2.60 (s, 2H, CH_2), 4.28 (q, 2H, *J*=6.9 Hz, CH_2CH_3), 7.01-8.20 (m, 8H, Ar-H), 12.09 (bs, 1H, NH exchangeable with D_2O), 13.68 (bs, 1H, NH exchangeable with D_2O); Mass spectrum, m/z (rel. int. %): 370 [$M^{+\cdot}$-1] (0.4), 347 (6), 319 (2), 291 (2), 216 (24), 189 (9), 188 (14), 160 (42), 132 (100), 120 (30), 104 (15) and 64 (16). Anal. Calcd for $C_{21}H_{17}N_5O_2$ (371.40), C, 67.80%; H, 4.69%; N, 18.98%; found, C, 67.91%; H, 4.61%; N, 18.86%.

1-Ethyl-3-[2-chloro-2-(1,2-dihydro-2-oxoquinoxalin-3-yl)acetyl]-4-hydroxyquinolin-2(1H)-one (14).

To a suspension of compound **11** (0.50 g, 1.30 mmol) in 1,4-dioxane (30 mL), sulfuryl chloride (3 mL) was added, then the reaction mixture was stirred at room temperature for 1 h and poured onto crushed ice (*ca*. 100 g). The formed precipitate was collected by filtration and crystallized from EtOH to give compound **14** as pale yellow crystals, yield (0.38 g, 91%). m.p. 240-241 ^{o}C; FT-IR (KBr) ν_{max} 3446 (OH), 3223 (NH), 3040 ($CH_{arom.}$), 2961, 2925 ($CH_{aliph.}$), 1670 ($C=O_{amide}$ and $C=O_{ketone}$), 1636 ($C=O_{quinolone}$) and 1559 cm^{-1} (C=N and C=C); ^{1}H NMR (DMSO-d_6, 300 MHz) δ 1.26 (t, 3H, *J*=6.9 Hz, CH_2CH_3), 4.31 (q, 2H, *J*=6.9 Hz, CH_2CH_3), 7.03 (s, H, CHCl), 7.20-7.25 (m, 2H, Ar-H), 7.31-7.37 (m, 2H, Ar-H), 7.48 (d, 1H, J=8.7 Hz, Ar-H), 7.63 (t, 1H, *J*=6.9 Hz, Ar-H), 7.79 (d, 1H, *J*=6.9 Hz, Ar-H), 8.23 (d, 1H, *J*=6.9 Hz, Ar-H), 13.69 (bs, 1H, NH exchangeable with D_2O). Mass spectrum, m/z (I_r %): 410 ($M^{+\cdot}$, 4), 375 (3), 347 (6), 305 (49), 290 (20), 277 (42), 248 (17), 213 (3), 189 (6), 172 (5), 160 (6), 144 (10), 132 (42), 118 (21), 91 (24), 77 (75) and 64 (100). Anal. Calcd for $C_{21}H_{16}ClN_3O_4$ (409.83), C, 61.50%; H, 4.00%; N, 10.44%; found, C, 61.55%; H, 3.94%; N, 10.25%.

1-Ethyl-3-[2-dibromo-2-(1,2-dihydro-2-oxoquinoxalin-3-yl)acetyl]-4-hydroxyquinolin-2(1H)-one (15).

A solution of bromine (0.07 mL) in acetic acid (10 mL) was added dropwise to a solution of compound **11** (0.50 g, 1.30 mmol) in acetic acid (10 mL). The reaction mixture was stirring at room temperature for 30 min. The orange crystals obtained during stirring were filtered and recrystallized from ethanol to give **15** as orange-red crystals, yield (0.30 g, 49%), mp > 300 ◦ C; FT-IR (KBr, cm^{-1}): 3445 (OH), 3201 (NH), 3090 ($CH_{arom.}$), 2923, 2853 ($CH_{aliph.}$), 1700 ($C=O_{ketone}$), 1652 ($C=O_{amide}$), 1640 ($C=O_{quinolone}$), 1615 (C=N) and 1575 (C=C); ^{1}H NMR (DMSO-d_6, 300 MHz) δ 1.29 (t, 3H, *J*=6.9 Hz, CH_2CH_3), 4.31 (q, 2H, *J*=6.9 Hz, CH_2CH_3), 7.05 (s, H, CHBr), 7.29-7.99 (m, 7H, Ar-H), 8.29 (t, 1H, *J*=8.7 Hz, Ar-H), 12.9 (bs, 1H, NH exchangeable with D_2O); Mass spectrum, m/z (rel. int. %): 454 ($M^{+\cdot}$] (5), 413 (4), 411 (4), 360 (4), 358 (5), 288 (4), 286 (4), 227 (3), 225 (4), 216 (4), 187 (10), 155 (4), 153 (4), 136 (4), 134 (4), 121 (5), 104 (7), 80 (100) and 77 (8). Anal. Calcd for $C_{21}H_{16}BrN_3O_4$ (454.28), C, 55.78%; H, 3.67%; N, 9.34%; found, C, 55.52%; H, 3.55%; N, 9.25%.

1-Ethyl-3-[2-nitro-2-(1,2-dihydro-2-oxoquinoxalin-3-yl)acetyl]-4-hydroxyquinolin-2(1H)-one (16).

To solution of compound **11** (1.00 g, 2.60 mmol) in glacial acetic acid (10 mL), a mixture of concentrated nitric acid (2 mL) and concentrated sulfuric acid (2 mL) was carefully added portion wise with continuous stirring at room temperature for 30 min then poured onto crushed ice (*ca*. 50 gm). The solid obtained was filtered, washed with water, air-dried and crystallized from EtOH to give compound **16** as yellow crystals, yield (0.50 g, 45%), m.p. 270 ^oC. FT-IR (KBr, cm^{-1}): 3435 (OH), 3223 (NH), 2923, 2854 ($CH_{aliph.}$), 1751 ($C=O_{ketone}$), 1676 ($C=O_{amide}$), 1639 ($C=O_{quinolone}$) and 1579 (C=N and C=C). ^{1}H NMR (DMSO-d_6, δ, 300MHz): 1.22 (t, 3H, CH_2CH_3), 4.48 (q, 2H, CH_2CH_3), 7.07 (s, 1H, $CHNO_2$), 7.42-8.22 (m, 8H, Ar-H), 13.2 (bs, 1H, NH exchangeable with D_2O). Mass spectrum, m/z (I_r %): 420 ($M^{+\cdot}$, 1), 305 (1), 267 (1), 215 (2), 188 (2), 155 (3), 149 (4), 139 (5), 132 (3), 125 (11), 121 (11), 85 (36), 77 (6), 64 (30) and 57 (100). Anal. Calcd. for $C_{21}H_{16}N_4O_6$ (420.38), C, 60.00%; H, 3.84%; N, 13.33%; found, C, 60.50%; H, 4.09%; N, 13.58%.

1-Ethyl-3-[2-(2,3,4,5-tetrahydro-3-thioxo-4-amino-5-oxo-1,2,4-triazin-6-yl)acetyl]-4-hydroxyquinolin-2(1H)-one (17).

A mixture of diketoester **1** (0.50 g, 1.51 mmol) and thiocarbohydrazide (0.106 g, 1.51 mmol), in absolute ethanol (20 mL), containing few drops of acetic acid, was heated under reflux for 2 h. The orange crystals obtained during heating was filtered and crystallized from DMF to give compound **17** as pale orange crytals, yield (0.56 g, 57%), m.p. > 300 ^oC; FT-IR (KBr) v_{max} 3464 (OH), 3333 (NH), 3238 (NH_2), 2981 ($CH_{aliph.}$), 1669 ($C=O_{triazine}$), 1646 ($C=O_{ketone}$), 1621 ($C=O_{quinolone}$), 1595 (C=N) and 1563 cm^{-1} (C=C); ^{1}H NMR (DMSO-d_6, 300 MHz) δ 1.20 (t, 3H, *J*=6.9 Hz, CH_2CH_3), 4.25 (q, 2H, *J*=6.9 Hz, CH_2CH_3), 4.48 (s, 2H, CH_2), 6.54 (bs, 2H, NH_2 exchangeable with D_2O), 7.34 (t, 1H, *J*=7.2 Hz, H-$6_{quinolone}$), 7.61 (d, 1H, J=8.7 Hz, H-$8_{quinolone}$), 7.80 (t, 1H, *J*=7.5 Hz, H-$7_{quinolone}$), 8.14 (d, 1H, *J*=8.1 Hz, H-$5_{quinolone}$), 12.70 (bs, 1H, NH exchangeable with D_2O), 14.00 (bs, 1H, OH exchangeable with D_2O); mass spectrum, m/z (rel. int. %): 373 [$M^{+\cdot}$] (17), 357 (11), 327 (1), 267 (2), 255 (6), 229 (7), 216 (100), 189 (8), 161 (3), 132 (14), 119 (6), 103 (5) and 64 (10). Anal. Calcd for $C_{16}H_{15}N_5O_4S$ (373.39), C, 51.50%; H, 4.19%; N, 18.68%; S, 8.65%; found, C, 51.47%; H, 4.05%; N, 18.76%; S, 8.59%.

N-{6-[2-(1-ethyl-4-hydroxy-2-oxo-1,2-dihydroquinolin-3-yl)-2-oxoethyl]-5-oxo-3-thioxo-2,5-dihydro-1,2,4-triazin-4(3H)-yl}acetamide (18).

A solution of compound **17** (0.5 g, 1.20 mmol) in acetic acid (10 mL) was heated under reflux for 4 h. The solid obtained during heating was filtered and crystallized from DMF to give compound **18** as orange crystals, yield (0.25 g, 45 %), m.p. > 300 ^{o}C; FT-IR (KBr) ν_{max} 3433 (OH), 3201 (NH), 3238 (NH_2), 2924 and 2856 ($CH_{aliph.}$), 1739 ($C=O_{acetamide}$), 1675 ($C=O_{triazine}$), 1626 ($C=O_{quinolone}$ and $C=O_{ketone}$), 1595 (C=N) and 1500 cm^{-1} (C=C); ^{1}H NMR (DMSO-d_6, 300 MHz) δ 1.30 (t, 3H, CH_2CH_3), 3.09 (s, 3H, CH_3), 4.59 (q, 2H, CH_2CH_3), 4.29 (s, 2H, CH2), 7.53 (t, 1H, H-$6_{quinolone}$), 7.81-7.86 (m, 2H, H-$8_{quinolone}$ and H-$7_{quinolone}$), 8.22 (d, 1H, H-$5_{quinolone}$), 8.97 (bs, 1H, NH exchangeable with D_2O), 12.7 (bs, 1H, NH exchangeable with D_2O). Mass spectrum, m/z (I_r %): 415 ($M^{+\cdot}$, 2), 389 (4), 376 (26), 332 (3), 305 (26), 277 (53), 215 (2), 189 (3), 169 (4), 132 (5), 119 (4), 101 (7) 91 (5), 77 (9) and 64 (100). Anal. Calcd for $C_{18}H_{17}N_5O_5S$ (415.42), C, 52.12%; H, 4.22%; N, 16.78%; S, 7.68%; found, C, 52.04%; H, 4.12%; N, 16.86%; S, 7.72%.

Ethyl 3-cyano-6-(1-ethyl-1,2-dihydro-4-hydroxy-2-oxoquinolin-3-yl)-2-oxo-2H-pyran-4-carboxylate (19).

A mixture of diketoester **3** (0.50 g, 1.51 mmol) and malononitrile (0.26 g, 1.51 mmol) in ethanol (20 mL) containing few drops of TEA or acetic acid was heated under reflux for 30 min. The solid that formed during heating was filtered and crystallized from DMF to give compound **19** as pale brown crystal, yield (0.30 g, 41 %), m.p. 233-234 ^{o}C; FT-IR (KBr) ν_{max} 3445 (OH), 3265 (NH), 2985, 2922, 2843 ($CH_{aliph.}$), 2228 (C≡N), 1726 ($C=O_{ester}$), 1634 ($C=O_{quinolone}$), 1595 (C=N) and 1571 cm^{-1} (C=C). ^{1}H NMR (DMSO-d_6, 300 MHz) δ 1.24 (t, 3H, *J*=6.9 Hz, N-CH_2CH_3), 1.49 (t, 3H, *J*=6.9 Hz, O-CH_2CH_3), 4.32 (q, 2H, *J*=6.9 Hz, N-CH_2CH_3), 4.49 (q, 2H, *J*=6.9 Hz, O-CH_2CH_3), 7.29 (t, 1H, *J*=7.2 Hz, H-6), 7.56 (d, 1H, *J*=8.4 Hz, H-8), 7.73 (t, 1H, *J*=8.4 Hz, H-7), 8.08 (d, 1H, *J*=8.1 Hz, H-5), 8.20 (s, 1H, H-5_{pyrane}), 9.29 (bs, 1H, NH exchangeable with D_2O), 14 (bs, 1H, OH exchangeable with D_2O).Mass spectrum, m/z (rel. int. %): 379 [$M^{+\cdot}$] (14), 365 (15), 351 (29.54), 323 (12.8), 278 (6.9), 160 (22), 146 (66.86), 132 (100), 120 (27.5), 104 (9.3) and 77 (5.35). Anal. Calcd for $C_{20}H_{17}N_3O_5$ (379.38), C, 63.20%; H, 4.61%; N, 11.00%; found, C, 63.32%; H, 4.52%; N, 11.08%.

RESULTS AND DISCUSSION

Earlier Ismail and Mohamed have reported the synthesis of ethyl 4-(1-ethyl-4-hydroxy-2-oxo-1,2-dihydroquinolin-3-yl)-2,4-dioxobutyrate (**1**), in good yield [15]. The chemical behavior of this diketoester **1** was studied towards a variety of 1,2- binucleophiles, such as cyanoacetohydrazide, nicotinohydrazide and 7-chloroquinolin-4-ylhydrazine (**2**). Thus, treatment of diketoester **1** with these hydrazine derivatives, in absolute ethanol containing few drops of acetic acid, gave the corresponding pyrazole derivatives **3**-**5**, in 37-54% yields (Scheme 1). Formation of pyrazole derivatives **3-5** may occur initially via condensation of NH_2 group at ($C=O_{α\text{-keto}}$) group to give hydrazone intermediates which in turn underwent an intramolecular cyclocondensation at ($C=O_{γ\text{-keto}}$) group. The FT-IR spectra of pyrazoles **3-5** displayed characteristic absorption bands attributed to $C=O_{ester}$ at 1756, 1706, and 1707 cm^{-1}, respectively.

The FT-IR spectrum of compound **3** showed characteristic absorption bands attributed to the C≡N and $C=O_{ketone}$ at 2263 and 1695 cm^{-1}, respectively. The ^1H NMR spectra of compounds **3-5** showed characteristic signals singlet attributed to $H\text{-}4_{pyrazole}$ at δ 7.20, 7.10 and 6.40 ppm, respectively. Furthermore, the mass spectra of compounds **3**, **4** and **5** showed their molecular ion peaks at m/z 394, 432 and 489 and assigned their formula weights, respectively.

Next, the diketoester **1** was allowed to react with some 1,3-N,N-binucleophiles. Condensation of diketoester **1** with 3-amino[1,2,4]triazole (**6**), in boiling ethanol containing few drops of acetic acid, led to [1,2,4]triazolo[4,3-a]pyrimidine derivative **7** bearing the quinoline moiety (Scheme 2). The FT-IR spectrum of compound **7** showed characteristic absorption vibrations at 3447 (O-H), 1751 ($C=O_{ester}$) and 1635 cm^{-1} ($C=O_{quinoline}$). Its ^1H NMR spectrum showed two characteristic singlets at δ 8.73 ($H\text{-}5_{pyrimidine}$) and 9.40 ppm ($H\text{-}3_{triazole}$). Further, the mass spectrum of compound **7** showed the molecular ion peak at m/z 379, which is coincident with its formula weight (379.39) and supports the identity of the structure.

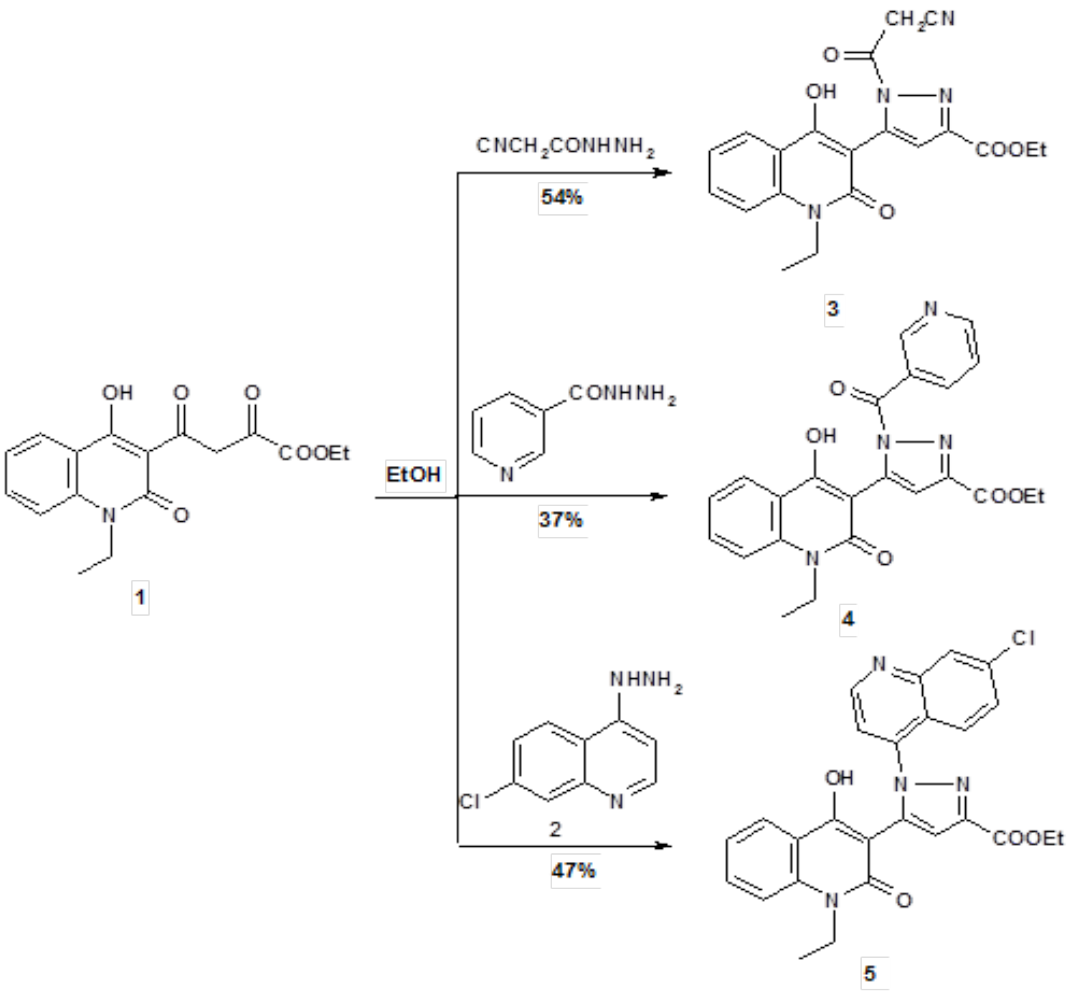

Scheme 1.

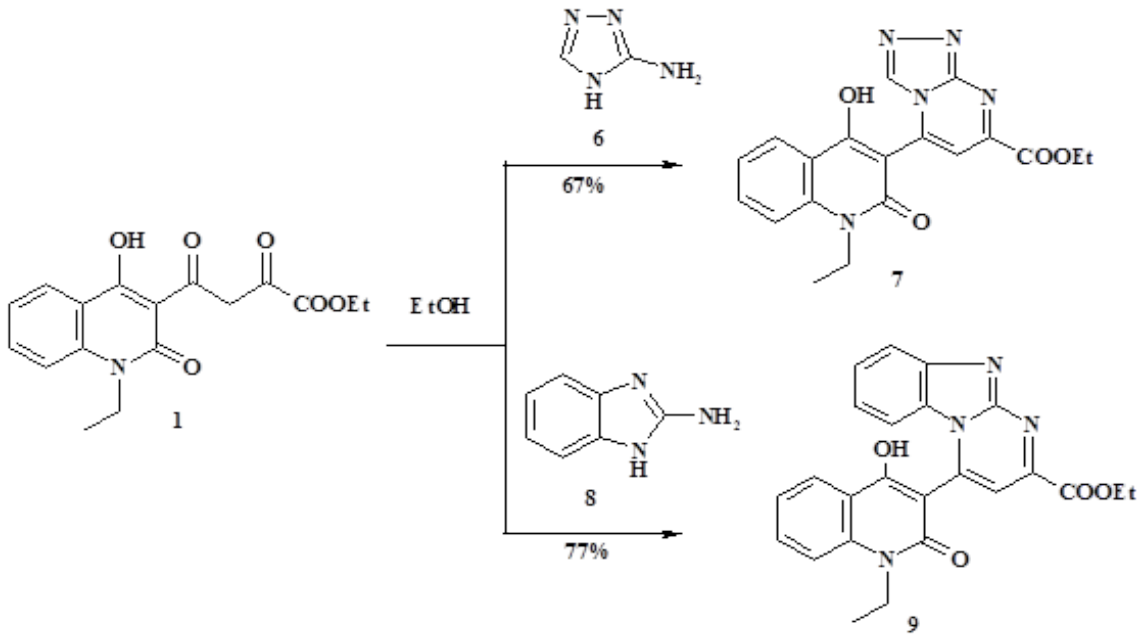

Scheme 2.

In the same manner, condensation of diketoester **1** with 2-aminobenzimidazole (**8**), in absolute ethanol containing few drops of acetic acid, produced pyrimido[1,2-*a*] benzimidazole derivative **9** linked to the quinolinone moiety (Scheme 2). The FT-IR spectrum indicated characteristic absorption vibrations at 3359 (O-H), 1707 ($C=O_{ester}$) and 1645 cm^{-1} ($C=O_{quinolone}$). The ^1H NMR spectrum of compound **9** showed characteristic singlet at δ 6.90 ($H\text{-}5_{pyrimidine}$). Further, its mass spectrum showed the molecular ion peak at m/z 370 and confirms the suggested structure.

Then, the chemical reactivity of diketoester **1** was studied towards a variety of 1,4-binucleophiles. Therefore, treatment of diketoester **1** with ethylene diamine, 1,2-phenylene diamine and 2-aminophenol, in boiling ethanol containing few drops of acetic acid, furnished the corresponding pyrazine, quinoxaline and benzoxazine derivatives **10-12**, respectively (Scheme 3).

The ^1H NMR spectra of compounds **10**, **11** and **12** showed a singlet distinguishable for the active methylene protons at δ 2.70 (in compound **10**) and 2.60 ppm (in compound **11** and **12**). In addition, the FT-IR spectra of compounds **10** and **11** demonstrated stretching vibrations attributed to ($C=O_{amide}$) at 1675 and 1685 cm^{-1}, respectively, while the FT-IR spectrum of compound **12** displayed characteristic absorption band assigned to ($C=O_{\alpha\text{-}pyrone}$) group at 1752 cm^{-1}.

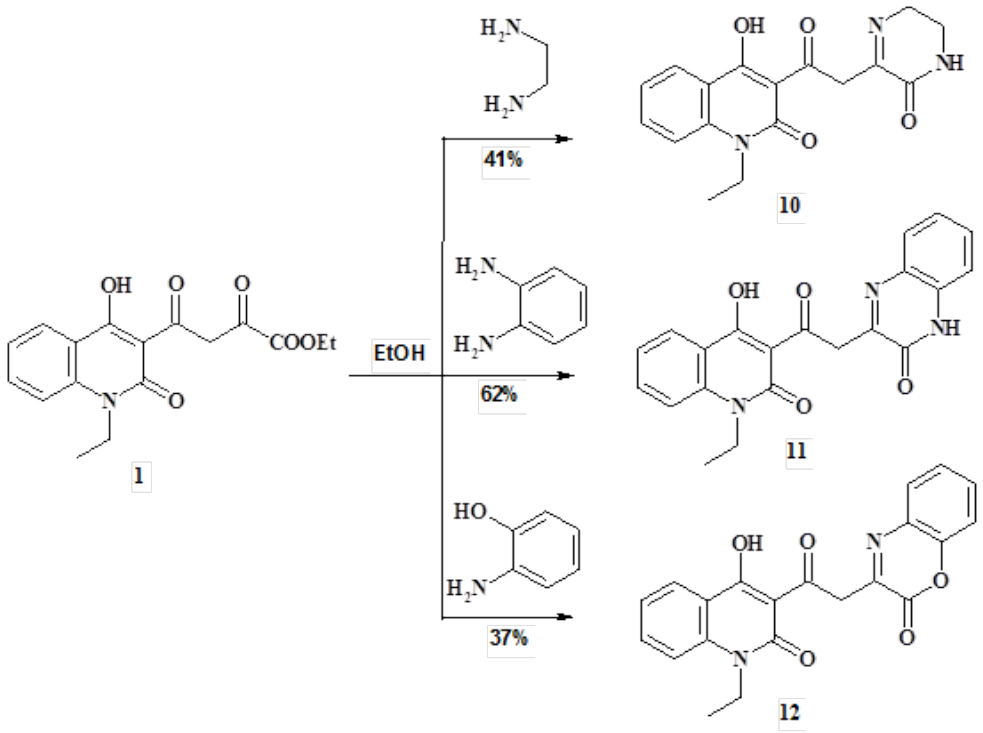

Scheme 3.

Condensation of compound **11** with hydrazine hydrate in boiling ethanol containing few drops of sulfuric acid produced pyrazolo[4,3-*c*]quinolinone **13** linked with a quinoxaline moiety in one molecular frame through an active methylene group (Scheme 4). The ^{1}H NMR spectrum of compound **13** showed a singlet distinguishable for the active methylene protons 2.60 and showed exchangeable signals at δ 12.09 and 13.68 assigned to two NH protons.

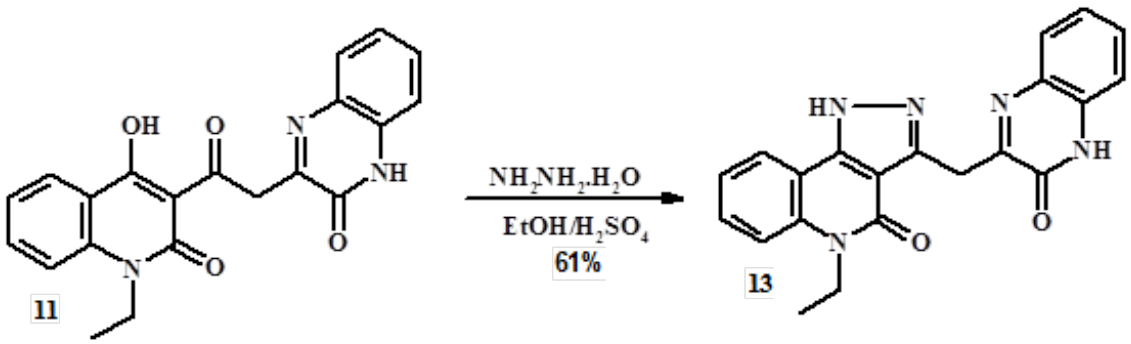

Scheme 4.

Next, the chemical reactivity of compound **11** was studied towards some electrophilic reagents. Chlorination, bromination and nitration of compound **11** afforded the chlorinated, brominated and nitrated products **14-16**, respectively (Scheme 5). The ^{1}H NMR spectra of compounds **14**, **15** and **16** showed characteristic singlets attributed to the $CH_{aliphatic}$ protons at 7.03, 7.05 and 7.07 ppm, respectively.

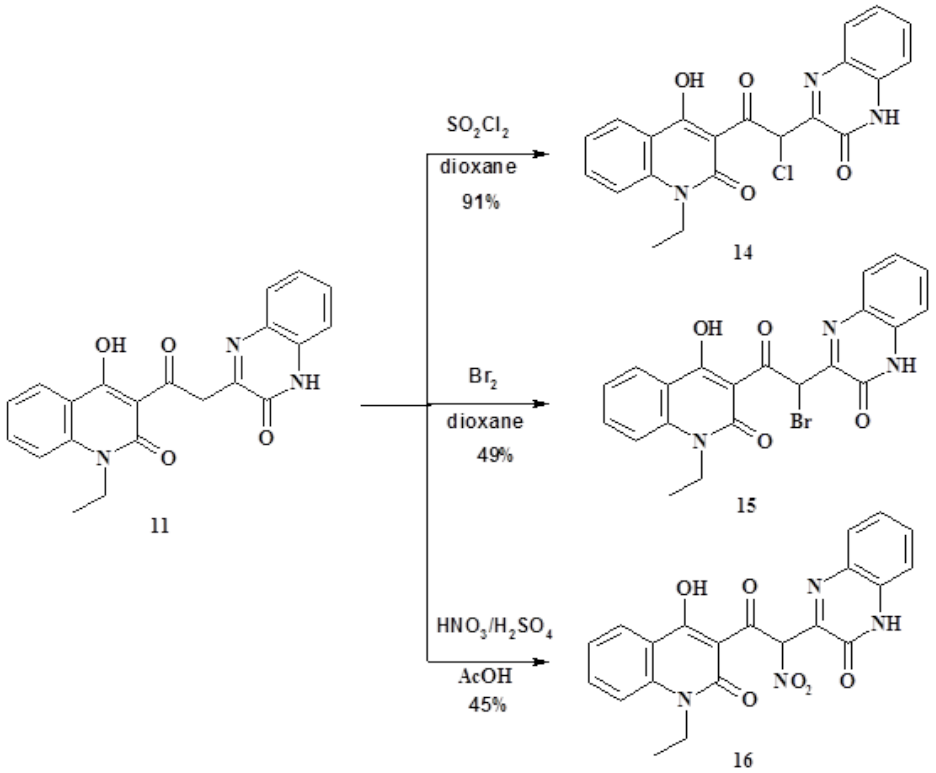

Scheme 5.

Treatment of diketoester **1** with thiocarbohydrazide, in absolute ethanol, containing few drops of acetic acid, furnished 1,2,4-triazine derivative **17** (Scheme 6). The FT-IR spectrum of compound **17** presented characteristic absorption bands at 3333, 3238 (NH, NH_2) and 1669 cm^{-1} ($C=O_{triazine}$). The ^{1}H-NMR spectrum of compound **17** showed a singlet assigned to CH_2 protons at δ 4.48, in addition to D_2O exchangeable signals at δ 6.54 and 12.70 assigned to NH_2 and NH protons, respectively.

Acetylation of compound **17** by using glacial acetic acid under reflux led to the acetylated product **18** (Scheme 6). A new absorption band appeared at 1739 cm^{-1} in the FT-IR spectrum of compound **18**, which might be assigned to ($C=O_{acetamide}$). The ^{1}H NMR spectrum of compound **18** showed exchangeable signals at δ 8.97 and 12.70 due to 2NH, respectively.

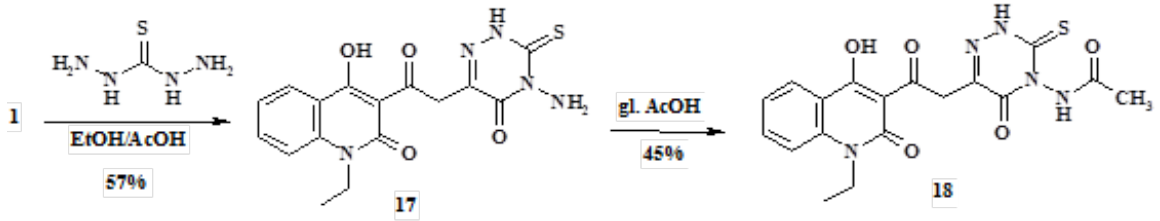

Scheme 6.

Moreover, the present work aimed to study the chemical reactivity of diketoester **1** towards malononitrile as carbon nucleophilic reagents. Thus, condensation of diketoester **1** with malononitrile, in boiling ethanol containing some drops of acetic acid, led to 3-cyano-6-(1-ethyl-1,2-dihydro-4-hydroxy-2-oxoquinolin-3-yl)-2-oxo- 2H-pyran-4-carboxylate (**19**) (Scheme 7). The FT-IR spectrum of compound **19** exhibited characteristic absorption bands at 2228 and 1726 cm^{-1} assigned to the (C≡N) and ($C=O_{ester}$), respectively. Its ^{1}H NMR spectrum indicated the presence of characteristic singlet at δ 8.20 ppm due to $H\text{-}5_{pyrane}$.

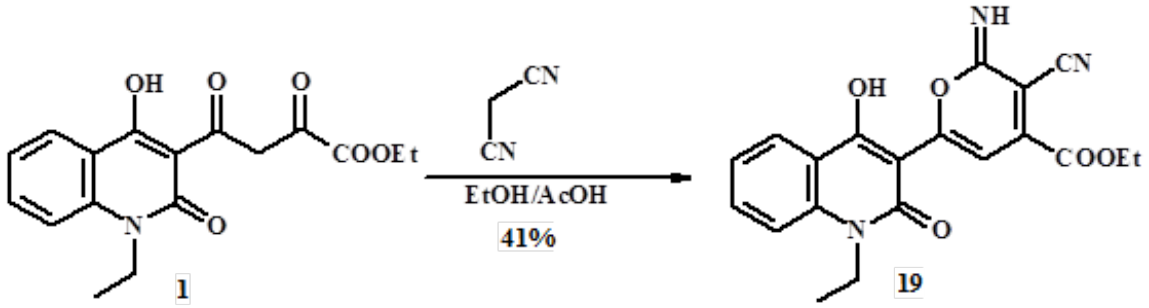

Scheme 7.

REFERENCES

[1] Ibrahim MA, Hassanin HM, Gabr YA, Alnamer YA. Studies on the chemical behavior of 3-(nitroacetyl)-1-ethyl-4-hydroxyquinolin-2(1H)-one towards some electrophilic and nucleophilic reagents. Journal of the Brazilian Chemical Society. 2012 May;23(5):905–12. DOI: 10.1590/S0103-50532012000500016.

[2] Moradi Rufchahi EO, Pouramir H, Yazdanbakhsh MR, Yousefi H, Bagheri M, Rassa M. Novel azo dyes derived from 8-methyl-4-hydroxyl-2-quinolone: Synthesis, UV–vis studies and biological activity. Chinese Chemical Letters. 2013 May;24(5):425–8. DOI: 10.1016/j.cclet.2013.03.002.

[3] De Melo EB. Multivariate SAR/QSAR of 3-aryl-4-hydroxyquinolin-2(1H)-one derivatives as type I fatty acid synthase (FAS) inhibitors. European Journal of Medicinal Chemistry. 2010 Dec;45(12):5817–26. DOI: 10.1016/j.ejmech.2010.09.044.

[4] Abass M, Mostafa BB. Synthesis and evaluation of molluscicidal and larvicidal activities of some novel enaminones derived from 4-hydroxyquinolinones: Part IX. Bioorganic & Medicinal Chemistry. 2005 Nov;13(22):6133–44. DOI: 10.1016/j.bmc.2005.06.038.

[5] Chen Y-L, Fang K-C, Sheu J-Y, Hsu S-L, Tzeng C-C. Synthesis and Antibacterial Evaluation of Certain Quinolone Derivatives. Journal of Medicinal Chemistry. 2001 Jul;44(14):2374–7. DOI: 10.1021/jm0100335.

[6] Detsi A, Bouloumbasi D, Prousis KC, Koufaki M, Athanasellis G, Melagraki G, et al. Design and Synthesis of Novel Quinolinone-3-aminoamides and Their α-Lipoic Acid Adducts as Antioxidant and Anti-inflammatory Agents. Journal of Medicinal Chemistry. 2007 May;50(10):2450–8. DOI: 10.1021/jm061173n.

[7] Kaur K, Jain M, Kaur T, Jain R. Antimalarials from nature. Bioorganic & Medicinal Chemistry. 2009 May;17(9):3229–56. DOI: 10.1016/j.bmc.2009.02.050.

[8] Behforouz M, Cai W, Mohammadi F, Stocksdale MG, Gu Z, Ahmadian M, et al. Synthesis and evaluation of antitumor activity of novel N-acyllavendamycin analogues and quinoline-5,8-diones. Bioorganic & Medicinal Chemistry. 2007 Jan 1;15(1):495–510. DOI: 10.1016/j.bmc.2006.09.039.

[9] Abas F, Lajis NH, Israf DA, Khozirah S, Umi Kalsom Y. Antioxidant and nitric oxide inhibition activities of selected Malay traditional vegetables. Food Chemistry. 2006 Apr;95(4):566–73. DOI: 10.1016/j.foodchem.2005.01.034.

[10] Rocha LG, Almeida JRGS, Macêdo RO, Barbosa-Filho JM. A review of natural products with antileishmanial activity. Phytomedicine. 2005 Jun;12(6-7):514–35. DOI: 10.1016/j.phymed.2003.10.006.

[11] Kuo R-Y, Chang F-R, Chen C-Y, Teng C-M, Yen H-F, Wu Y-C. Antiplatelet activity of N-methoxycarbonyl aporphines from Rollinia mucosa. Phytochemistry. 2001 Jun;57(3):421–5. DOI: 10.1016/S0031-9422(01)00076-0.

[12] Chen Y-L, Chen I-L, Tzeng C-C, Wang T-C. Synthesis and Cytotoxicity Evaluation of Certainα-Methylidene-γ-butyrolactones Bearing Coumarin, Flavone, Xanthone, Carbazole, and Dibenzofuran Moieties. Helvetica Chimica Acta. 2000 May 10;83(5):989–94. DOI: 10.1002/(SICI)1522-2675(20000510)83:5<989::AID-HLCA989>3.0.CO;2-E.

[13] Rivkin A, Kim YR, Goulet MT, Bays N, Hill AD, Kariv I, et al. 3-Aryl-4-hydroxyquinolin-2(1H)-one derivatives as type I fatty acid synthase inhibitors. Bioorganic & Medicinal Chemistry Letters. 2006 Sep;16(17):4620–3. DOI: 10.1016/j.bmcl.2006.06.014.

[14] Roussaki M, Hall B, Lima SC, da Silva AC, Wilkinson S, Detsi A. Synthesis and anti-parasitic activity of a novel quinolinone–chalcone series. Bioorganic & Medicinal Chemistry Letters. 2013 Dec;23(23):6436–41. DOI: 10.1016/j.bmcl.2013.09.047.

[15] Ismail M, Mohamed H. Synthesis and cyclization reactions with quinolinyl keto esters II. Synthesis of novel 3-diazolylquunolinones and their enzymic activity. Chemical Papers. 2005;59(2):127–38. URL: http://www.chempap.org/file_access.php?file=592a127.pdf.

4-(1-ETİL-1,2-DİHİDRO-4-HİDROKSİ-2-OKSOKİNOLİN-3-İL)2,4-DİOKSOBUTANOATIN BAZI NÜKLEOFİLİK REAKTİFLERE KARŞI KİMYASAL REAKTİVİTESİ

Kinolin-2-on ile bağlanmış yeni bir seri heterosiklik sistemler, etil 4-(1-etil-1,2-dihidro-4-hidroksi-2-oksokinolin-3-il)-2,4-dioksobutanoat (**1**) bileşiğinin bir seri azotlu ve/veya karbonlu nükleofillerle tepkimesinden etkili bir şekilde sentezlenmiştir. Kinolin grubu içeren pirazoller, pirimidinler, pirazinler, oksazinler ve triazinler gibi bir seri heterosiklik sistemler elde edilmiştir. Yeni sentezlenmiş ürünlerin yapıları analitik ve spektral veriler temelinde doğrulanmıştır.

Anahtar Kelimeler: Kinolin-2-on, diketoester, aktif metilen, nükleofil reaksiyon, heterohalkalaşma.

Gönderilme tarihi: 12 Aralık 2015. **Düzeltme tarihi:** 11 Ocak 2016. **Kabul tarihi:** 7 Şubat 2016.

JOTCSA, Volume 3, issue 2, (2016), pp. 89-102. **Research article**

Journal homepage: http://dergipark.ulakbim.gov.tr/jotcsa

e-ISSN: 2149-0120

A USEFUL METHOD FOR THE PREDICTION OF MOLECULAR ELECTROPHILICITY AND NUCLEOPHILICITY

Savaş Kaya[1]*, Cemal Kaya[1], Ilkay Uğurlu[1], and Nazmul Islam[2]

[1]Department of Chemistry, Faculty of Science, Cumhuriyet University, Sivas, 58140, Turkey.
[2]Theoretical and Computational Chemistry Research Laboratory, Department of Basic Science and Humanities/ Chemistry, Techno Global-Balurghat, Balurghat, D. Dinajpur –733103, India.

Abstract: In the present study, a new theoretical model for the calculation of molecular electrophilicity and molecular nucleophilicity based on group electronegativity and molecular hardness equations, derived by us in recent years, is presented. Furthermore, a validity test of the present model is performed with 33 molecules by comparing the computed electrophilicity and nucleophilicity data with the electrophilicity and nucleophilicity data computed using some well-known theoretical methods and their experimental counterparts. The comparative study reveals excellent correlation between theory and experiment. Thus the new theoretical model presented in this work for the calculation of molecular reactivity indices like electrophilicity and nucleophilicity is logical and reliable.

Keywords: Electronegativity, Hardness, Electrophilicity, Nucleophilicity, DFT.
Submitted: February 29, 2016. **Revised:** March 29, 2016. **Accepted:** April 12, 2016.

Cite this: Kaya S, Kaya C, Uğurlu İ, Islam N. A Useful Method for the Prediction of Molecular Electrophilicity and Nucleophilicity. Journal of the Turkish Chemical Society, Section A: Chemistry. 2016 Apr;3(2):89–101.
DOI: 10.18596/jotcsa.04933.
***Correspondence to:** Savaş Kaya. E-mail: savaskaya@cumhuriyet.edu.tr.

INTRODUCTION

It now becomes well established that the molecular reactivity descriptors such as chemical hardness, electronegativity, electrophilicity, and nucleophilicity have greatly taken advantage of the development of Density Functional Theory [1-3]. The DFT has proven to be an important tool in modern quantum chemistry because of its ability to provide the quantitative definitions for chemical concepts like chemical potential (μ) [4] chemical hardness (η) [5-8], and electronegativity (χ) [9,10]. The first and second derivatives of electronic energy (E) with respect to the number of electron (N) under the constant external potential, $\upsilon(r)$, are described as chemical potential and chemical hardness, respectively. Softness (σ) [11] is the inverse of chemical hardness. Qualitative expressions related to these chemical concepts are given as follows:

$$\mu = -\chi = (\partial E/\partial N)_{v(r)} \quad \textbf{(1)}$$

$$\eta = (\partial^2 E/\partial N^2)_{v(r)} \quad \textbf{(2)}$$

$$\sigma = 1/\eta \quad \textbf{(3)}$$

Parr and Pearson, with the help of finite differences method, put forwarded the approximate and operational definition of electronegativity and chemical hardness of chemical species as [12, 13]:

$$\chi = -\mu = \frac{I + A}{2} \quad \textbf{(4)}$$

$$\eta = I - A \quad \textbf{(5)}$$

where I is the first vertical ionization energy and A is the electron affinity values of the chemical species.

Ingold [14] introduced the terms of nucleophile and electrophile in the glossary of chemistry. The electrophilicity and nucleophilicity are two very useful theoretical constructs of conceptual chemistry originating from the fruition of the long effort of understanding the mechanism of organic reaction [15]. Electrophilicity is a property of atoms and molecules which signifies the energy lowering process on soaking electrons from donors. Hence, the electrophilicity measures the energy stabilization when the system acquires an additional electronic charge from the environment/donor [15]. The quantitative definition of electrophilicity was put forward by Parr and co-workers [16] following the work of Maynard et al. [17] as a quantitative intrinsic numerical value and suggested the term electrophilicity index, ω, a new global reactivity descriptor of atoms and molecules, as presented below:

$$\omega = \frac{\mu^2}{2\eta} = \frac{\chi^2}{2\eta} = \frac{(I+A)^2}{8(I-A)} \quad \textbf{(6)}$$

Nucleophilicity and electrophilicity are physically multiplicative inverse of each other ($N=1/\omega$) [18].

Based on the valence electron theory of Lewis, Ingold [14] proposed an electrophilicity scale to describe electron-deficient (electrophile) and electron-rich (nucleophile) species as follows:

$$k_\sigma = C\omega N \quad \textbf{(7)}$$

where C is the proportionality constant. k_σ is the hydrogen bond stretching force constant. Further, it is important to note that nucleophilicity (N) is proportional to (1/electrophilicity) as noted above.

One of the remarkable developments regarding electronegativity concept has been provided by Sanderson by introducing a new electronic structure principle famous as "Electronegativity equalization principle [19-21]." According to this principle "when two or more different atoms combine to form a molecule, their electronegativities change to a common intermediate value and become equalized." In recent times, we presented a new equation to calculate the electronegativities of molecules and functional groups from ionization energies and electron affinities of pre-bonded atoms considering Sanderson's electronegativity equalization principle and Iczkowski-Margrave's electronegativity study [22]. The equation [23] derived by us is presented below:

$$\chi_M = \frac{\sum_{i=1}^{N}\left(\frac{I_i + A_i}{I_i - A_i}\right) + 2q_M}{\sum_{i=1}^{N}\left(\frac{2}{I_i - A_i}\right)} \quad \textbf{(8)}$$

where, χ_M and q_M are electronegativity and charge of molecule or functional group, respectively. N is number of atoms in the molecule and I_i and A_i are the ionization energy and electron affinity of i-th atom.

Chemical hardness is a measure of the resistance of a chemical species towards the deformation of electric charge cloud under small perturbation and this quantity is an indicator of chemical reactivity [24, 25]. The concept introduced by Pearson has important applications in chemistry.

Hard and Soft Acid-Base (HSAB) [26, 27] Principle and Maximum Hardness Principle (MHP) [28] based on chemical hardness concept make the structure-reactivity relationship more understandable. Recently we presented a new equation shown below [29] to calculate the chemical hardnesses of molecules and functional groups:

$$\eta_M = \frac{\left(2\sum_{i=1}^{N}\frac{b_i}{a_i}\right)+q_M}{\sum_{i=1}^{N}\frac{1}{a_i}} \quad \textbf{(9)}$$

In this equation, η_M and q_M are chemical hardness and charge of molecule, respectively. N is the total number of atoms in the molecule. a_i and b_i parameters in Eq. 9 are defined as: $a_i=(I+A)/2$ and $b_i=(I-A)/2$. These parameters for some selected atoms are presented in Table 1.

The aim of this article is to calculate the nucleophilicity and electrophilicity data of molecules with the help of new theoretical model mentioned above.

RESULTS AND DISCUSSION

In the present study, we calculated the nucleophilicity and electrophilicity of some selected molecules considering Eq. 10 for charged molecules and Eq. 11 for neutral molecules. Then, we compared the results obtained by us with other theoretical methodologies and experimental data. Table 2 reports the electrophilicity and nucleophilicity values calculated via various methods for some selected molecules. Considering the calculated values, we can say that the obtained results using Eq.10 and Eq. 11 are exceptionally compatible with the results of geometric mean equation of Chattaraj. Chattaraj has proposed the geometric mean equation for calculations regarding the electrophilicity values of molecules assuming that electrophilicity gets equalized like chemical hardness and electronegativity during molecule formation process. The electrophilicity equalization principle of Chattaraj, Giri and Duley [30] has been criticized by Szentpaly [31]. Considering large molecules such as fullerene, Szentpaly suggested that there is not an acceptable evidence regarding equalization of electrophilicity. After the publication of Szentpaly, Chattaraj [32] tried to justify and to urge the electrophilicity equalization principle. Indeed, this situation is suggestive that the equalization of electrophilicity becomes difficult depending on number of atoms of the molecule. We believe that electrophilicity equalization principle of Chattaraj is useful for the calculating of electrophilicities of small molecules and this electronic structure principle cannot be ignored entirely. The agreement between the results of geometric mean of Chattaraj and the results of present study in Table 2 will provide as a support to Electrophilicity equalization principle because the electrophilicity and nucleophilicity values obtained by us is very close to Chattaraj's results.

Table 1. Experimental Parameters for Some Atoms (eV)

Atom	*I*	*A*	*a*	*b*
H	13.598	0.754	7.176	6.422
Li	5.392	0.618	3.005	2.387
Be	9.323	0.295	4.809	4.514
B	8.298	0.280	4.289	4.009
C	11.260	1.262	6.261	4.999
N	14.534	0.070	7.302	7.232
O	13.618	1.461	7.539	6.078
F	17.423	3.401	10.412	7.011
Na	5.139	0.548	2.843	2.295
Mg	7.646	0.541	4.093	3.552
Al	5.986	0.433	3.209	2.776
Si	8.152	1.390	4.771	3.381
P	10.487	0.747	5.617	4.870
S	10.360	2.077	6.218	4.141
Cl	12.968	3.613	8.290	4.677
K	4.341	0.501	2.421	1.920
Ca	6.113	0.024	3.068	3.044
Sc	6.561	0.188	3.374	3.186
Cr	6.767	0.666	3.716	3.050
Mn	7.434	-0.498	3.468	3.960
Fe	7.902	0.151	4.026	3.875
Ni	7.640	1.156	4.398	3.242
Cu	7.726	1.235	4.480	3.245
Zn	9.390	-0.490	4.450	4.940
As	9.789	0.814	5.301	4.487
Se	9.752	2.020	5.886	3.866
Cs	3.894	0.471	2.180	1.710
Br	11.814	3.363	7.588	4.225
I	10.451	3.059	6.755	3.696

Although geometric mean equation and Equation 13 presented by Islam and Ghosh does not contain any statement that gives the relation with the charge of nucleophilicity and electrophilicity, electrophilicity and nucleophilicity values of charged molecules can be determined with the help of Equation 10. In Table 3, the calculated chemical hardness, electronegativity, electrophilicity and nucleophilicity values for the some functional groups are provided. Electrophilicity is a measure of interest that exhibits to electrons of chemical species and it is anticipated that electrophilicity increases as positive charge increases. On the other hand, it is predicted that the nucleophilicity that is a measure of tendency of electron giving of chemical species decreases as the charge increases. In our past publications, we showed that the chemical hardness and electronegativity of any functional group increases as linear as its charge increases. However, it is understood from Figure 1 that denotes the change with the charge of nucleophilicities and electrophilicities of some functional groups, there is a parabolic correlation between charge with electrophilicity and nucleophilicity.

The electrophilicity of any functional groups increases as parabolic with the increasing of its charge. On the contrary, the nucleophilicity of any functional group decreases as parabolic with the decreasing of its charge.

Table 2. Comparison of nucleophilicity and electrophilicity values that was calculated via various methods.

	Electrophilicities (eV)			Nucleophilicities (eV)		
Molecule	**Parr**	**Chattaraj**	**Present work**	**Parr**	**Chattaraj**	**Present work**
I_2	2.60	3.088	3.104	0.385	0.323	0.322
BrI	2.629	3.245	3.240	0.381	0.308	0.308
S_2	1.98	2.334	2.336	0.505	0.428	0.428
Br_2	2.68	3.409	3.406	0.373	0.293	0.294
Cl_2	3.31	3.677	3.681	0.302	0.271	0.272
P_2	1.56	1.619	1.619	0.641	0.617	0.617
SO	1.78	2.336	2.315	0.562	0.428	0.432
CH	1.83	1.984	1.974	0.546	0.504	0.506
O_2	1.88	2.338	2.338	0.532	0.427	0.427
OH	2.481	2.165	2.172	0.403	0.462	0.460
NH	1.786	1.909	1.921	0.559	0.524	0.521
F_2	3.493	3.864	3.864	0.286	0.258	0.258
CS_2	1.64	2.203	2.195	0.609	0.454	0.456
COS	1.58	2.204	1.984	0.632	0.454	0.504
SO_2	2.01	2.337	2.278	0.497	0.428	0.439
O_3	2.419	2.338	2.338	0.413	0.428	0.428
NH_2	1.71	1.940	1.948	0.585	0.515	0.514
N_2O	1.70	1.977	2.003	0.588	0.505	0.499
$POCl_3$	2.048	2.851	2.910	0.488	0.350	0.344
SO_3	2.168	2.337	2.289	0.461	0.428	0.437
C_2H_2	1.62	1.984	1.961	0.617	0.504	0.509
CH_3	1.26	1.994	1.972	0.793	0.502	0.507
HNO_3	1.72	2.156	2.163	0.581	0.464	0.463
$C_6H_4O_2$	2.147	2.035	2.015	0.466	0.491	0.496
LiF	2.41	2.014	3.12	0.414	0.496	0.321
LiCl	2.08	1.905	2.75	0.480	0.525	0.364
LiBr	1.77	1.878	2.51	0.564	0.532	0.398
NaF	2.26	2.014	3.12	0.442	0.496	0.321
NaCl	2.78	1.905	2.75	0.359	0.525	0.360
NaBr	1.95	1.850	2.51	0.513	0.541	0.398
KF	2.06	1.850	3.19	0.485	0.541	0.314
KCl	2.28	1.769	2.82	0.438	0.565	0.355
KBr	2.00	1.714	2.58	0.500	0.584	0.386

Table 3. The nucleophilicity and electrophilicity (eV) values calculated for charged molecules.

Molecule	Charge	Chemical Hardness	Electronegativity	Electrophilicity	Nucleophilicity
CH_3	-1	10.33	3.91	0.740	1.352
	0	12.07	6.90	1.973	0.507
	+1	13.80	9.91	3.558	0.281
NH_2	-1	10.97	2.77	0.349	2.865
	0	13.38	7.21	1.942	0.515
	+1	15.78	11.66	4.307	0.232
NO_2	-1	10.45	3.19	0.486	2.057
	0	12.94	7.47	2.156	0.464
	+1	15.42	11.75	4.476	0.224
NO_3	-1	10.88	4.32	0.857	1.167
	0	12.75	7.49	2.200	0.455
	+1	14.62	10.65	3.879	0.258
OH	-1	8.84	1.12	0.071	14.08
	0	12.50	7.37	2.173	0.460
	+1	16.20	13.62	5.725	0.175
CN	-1	8.69	0.78	0.035	28.57
	0	12.06	6.69	1.856	0.538
	+1	15.43	12.61	5.153	0.194
SCN	-1	8.54	3.04	0.541	1.848
	0	10.73	6.49	1.963	0.509
	+1	12.91	9.94	3.827	0.262
COOH	-1	9.94	4.16	0.870	1.149
	0	11.71	7.08	2.140	0.467
	+1	13.48	10.00	3.709	0.269
SO_3H	-1	9.97	4.87	1.189	0.841
	0	11.40	7.12	2.223	0.449
	+1	12.84	9.36	3.411	0.293
SO_2Cl	-1	8.57	4.79	1.339	0.746
	0	10.39	7.33	2.586	0.387
	+1	12.23	9.89	3.999	0.250

Although geometric mean equation and Equation 13 presented by Islam and Ghosh does not contain any statement that gives the relation with the charge of nucleophilicity and electrophilicity, electrophilicity and nucleophilicity values of charged molecules can be determined with the help of Equation 10. In Table 3, the calculated chemical hardness, electronegativity, electrophilicity and nucleophilicity values for the some functional groups are provided. Electrophilicity is a measure of interest that exhibits to electrons of chemical species and it is anticipated that electrophilicity increases as positive charge increases.

On the other hand, it is predicted that the nucleophilicity that is a measure of tendency of electron giving of chemical species decreases as the charge increases. In our past publications, we showed that the chemical hardness and electronegativity of any functional group increases as linear as its charge increases. However, it is understood from Figure 1 that denotes the change with the charge of nucleophilicities and electrophilicities of some functional groups, there is a parabolic correlation between charge with electrophilicity and nucleophilicity. The electrophilicity of any functional groups increases as parabolic with the increasing of its charge. On the contrary, the nucleophilicity of any functional group decreases as parabolic with the decreasing of its charge.

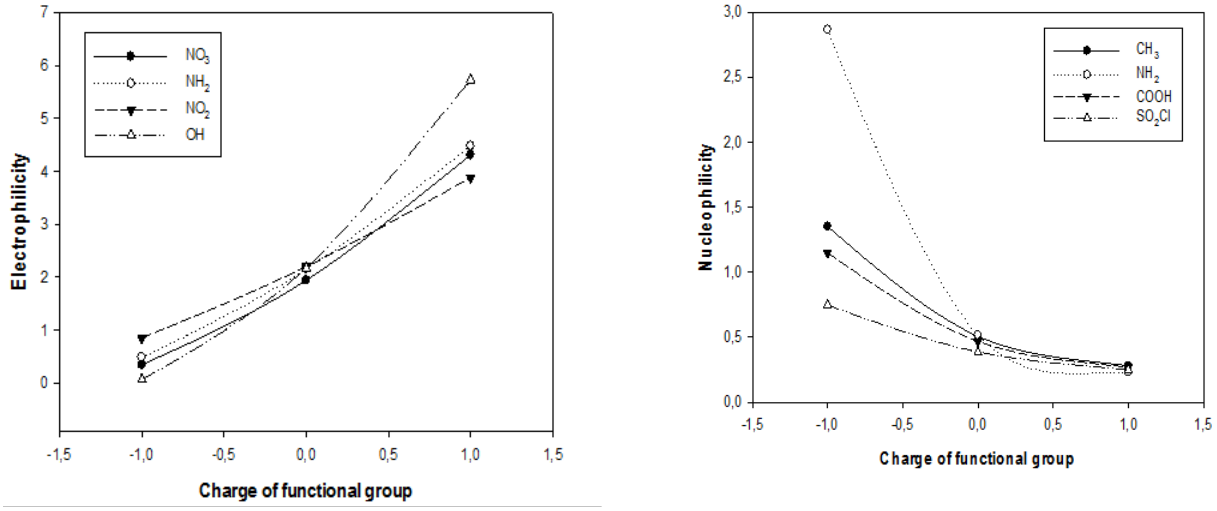

Figure 1. The change with the charge of electrophilicity and nucleophilicity for some selected functional groups.

Consequently, it can be said that nucleophilicity and electrophilicity values of both neutral molecules or functional groups and charged molecules or functional groups can be calculated considering the ionization energy and electron affinity values of constituent atoms. In addition to this, the results of present method are compatible with geometric mean method of Chattaraj. We proposed that Chattaraj's equalization principle and geometric mean equation related to electrophilicity concept are convenient for the studies regarding small molecules. Lastly, it is required to mention from the limitation of proposed methodology. It should be noted that the proposed new useful method is more reliable for small molecules such as in Table 2. In the calculation regarding big molecules, the method proposed can give incorrect results.

Theoretical Model

As mentioned above, the electrophilic power of a chemical species is associated with electronegativity and chemical hardness of that species. It is important to note that chemical hardness and electronegativity values for all molecules considered in this study have been calculated via Eq. 9 and Eq. 8, respectively. To determine the electrophilicity values of molecules and functional groups, Parr's formula (Equation 6) has been considered.

To calculate the electrophilicity of any molecule, with the help of Parr's electrophilicity index and equations derived by us, we proposed the following equation:

$$\omega_M = \frac{{\chi_M}^2}{2\eta_M} = \frac{\left[\sum_{i=1}^{N}\left(\frac{I_i + A_i}{I_i - A_i}\right) + 2q_M \Big/ \sum_{i=1}^{N}\left(\frac{2}{I_i - A_i}\right)\right]^2}{2\left[\left(2\sum_{i=1}^{N}\frac{I_i - A_i}{I_i + A_i}\right) + q_M \Big/ \sum_{i=1}^{N}\frac{1}{I_i - A_i}\right]} \quad \textbf{(10)}$$

It should be noted that the charge effect on electrophilicity and nucleophilicity can be analyzed through Eq. 10. As for neutral species q_M=0, the Equation 10 can be simplified for the calculation of electrophilicities of neutral molecules as the following:

$$\omega_M = \frac{1}{8}\frac{\sum_{i=1}^{N}(I_i + A_i)^2}{\sum_{i=1}^{N}(I_i - A_i)} \quad \textbf{(11)}$$

The Equation 11 above looks similar to Equation 6. But Eq. 6 provides the calculation of molecular electrophilicities from ionization energy and electron affinities of molecules. On the other hand, the Eq. 11 provides the computation of molecular electrophilicity using the ionization energy and electron affinities of constituent atoms forming the molecule. So the scope of application of Equation 11 is wider than equation 6. In addition, the inverse of Eq. 11 can be used to calculate the nucleophilicities of neutral molecules because electrophilicity and nucleophilicity are physically multiplicative inverse of each other.

In the literature, for calculation of electrophilicities of molecules, a few methods different from Parr's electrophilicity index are available. One of them was proposed by Chattaraj and co-workers. According to Chattaraj, the electrophilicity of a molecule may be expressed as geometric mean of electrophilicities of constituent atoms in the molecule and can be calculated via following equation [30]:

$$\omega_{\mathrm{M}} = \left(\prod_{i=1}^{\mathrm{N}}\omega_i\right)^{1/\mathrm{N}} \quad \textbf{(12)}$$

In the Equation 12, ω_i (i= 1, 2, 3… N) refers to isolated atom electrophilicity value and N is number of atoms in the molecule.

Another method for determination of electrophilicities of molecules was proposed by N. Islam and D. C. Ghosh [15]. According to their study, electrophilicity index (ωM) in electron volts unit of molecules can be calculated via following equation:

$$\omega_M = \frac{K.7{,}2(n+1)}{\sum_i r_i} \quad \textbf{(12)}$$

In this equation, n stands for number of atoms connected to central atom in molecule, ri is atomic radius in angstrom (Å) unit and standardized value of K is 0.382516 for diatomic molecules and is 0.712 for polyatomic molecules. In this stage, we want to state that all methods mentioned in the study can be used for the calculation for both electrophilicities and nucleophilicities of molecules.

CONCLUSION

In the present study, a new method based on molecular hardness and molecular electronegativity to calculate the nucleophilicities and electrophilicities of molecules is presented. The results obtained in the study support the electrophilicity equalization principle. Thus the new theoretical model presented in this work for the calculation of molecular reactivity indices like electrophilicity and nucleophilicity is logical and reliable.

REFERENCES

[1] Geerlings P, De Proft F, Langenaeker W. Conceptual Density Functional Theory. Chemical Reviews. 2003 May;103(5):1793–874. DOI: 10.1021/cr990029p.

[2] Chattaraj PK, editor. Chemical reactivity theory: a density functional view. Boca Raton: CRC Press/Taylor & Francis; 2009. 576 p. ISBN: 978-1-4200-6543-5

[3] Liu S. Conceptual density functional theory and some recent developments. Acta Phys Chim Sinica. 25:590–600. URL: http://www.ingentaconnect.com/content/apcs/apcs/2009/00000025/00000003/art00033#expand/collapse.

[4] Nataraj A, Balachandran V, Karthick T. Molecular orbital studies (hardness, chemical potential, electrophilicity, and first electron excitation), vibrational investigation and theoretical NBO analysis of 2-hydroxy-5-bromobenzaldehyde by density functional method. Journal of Molecular Structure. 2013 Jan;1031:221–33. DOI: 10.1016/j.molstruc.2012.09.047.

[5] Kaya S, Kaya C. Derivation of ionization energy and electron affinity equations using chemical hardness and absolute electronegativity in isoelectronic series. Journal of Physical & Theoretical Chemistry. 2015;11(4):155–63. URL: http://jptc.srbiau.ac.ir/pdf_6246_94c596367c3fea5c0d54f9671b940188.html.

[6] Malek A, Balawender R. Revisiting the chemical reactivity indices as the state function derivatives. The role of classical chemical hardness. The Journal of Chemical Physics. 2015 Feb 7;142(5):054104. URL: 10.1063/1.4906555.

[7] Beg H, De SP, Ash S, Das D, Misra A. Polarizability, chemical hardness and ionization potential as descriptors to understand the mechanism of double proton transfer in acetamide dimer. Computational and Theoretical Chemistry. 2013 Feb;1005:1–8. DOI: 10.1016/j.comptc.2012.10.023.

[8] Kaya S, Kaya C. A Simple Method for the Calculation of Lattice Energies of Inorganic Ionic Crystals Based on the Chemical Hardness. Inorganic Chemistry. 2015 Sep 8;54(17):8207–13. DOI: 10.1021/acs.inorgchem.5b00383.

[9] Chermette H. Chemical reactivity indexes in density functional theory. Journal of Computational Chemistry. 1999 Jan 15;20(1):129–54. DOI: 10.1002/(SICI)1096-987X(19990115)20:1<129::AID-JCC13>3.0.CO;2-A.

[10] Putz MV. Electronegativity: Quantum observable. International Journal of Quantum Chemistry. 2009 Mar 15;109(4):733–8. DOI: 10.1002/qua.21957.

[11] Putz MV, Chattaraj PK. Electrophilicity kernel and its hierarchy through softness in conceptual density functional theory. International Journal of Quantum Chemistry. 2013 Sep 15;113(18):2163–71. DOI: 10.1002/qua.24473.

[12] Ghosh DC, Islam N. Whether there is a hardness equalization principle analogous to the electronegativity equalization principle-A quest. International Journal of Quantum Chemistry. 2011 Aug 5;111(9):1961–9. DOI: 10.1002/qua.22499.

[13] Ghosh DC, Islam N. A quest for the algorithm for evaluating the molecular hardness. International Journal of Quantum Chemistry. 2011 Aug 5;111(9):1931–41. DOI: 10.1021/cr60051a003.

[14] Ingold CK. Principles of an Electronic Theory of Organic Reactions. Chemical Reviews. 1934 Oct;15(2):225–74. DOI: 10.1021/cr60051a003.

[15] Islam N, Ghosh DC. On the Electrophilic Character of Molecules Through Its Relation with Electronegativity and Chemical Hardness. International Journal of Molecular Sciences. 2012 Feb 17;13(12):2160–75. DOI: 10.3390/ijms13022160.

[16] Parr RG, Szentpály L v., Liu S. Electrophilicity Index. Journal of the American Chemical Society. 1999 Mar;121(9):1922–4. DOI: 10.1021/ja983494x.

[17] Maynard AT, Huang M, Rice WG, Covell DG. Reactivity of the HIV-1 nucleocapsid protein p7 zinc finger domains from the perspective of density-functional theory. Proceedings of the National Academy of Sciences. 1998 Sep 29;95(20):11578–83. DOI: 10.1073/pnas.95.20.11578.

[18] Chattaraj PK, Sarkar U, Roy DR. Electrophilicity Index. Chemical Reviews. 2006 Jun;106(6):2065–91. DOI: 10.1021/cr040109f.

[19] Verstraelen T, Bultinck P. Can the electronegativity equalization method predict spectroscopic properties? Spectrochimica Acta Part A: Molecular and Biomolecular Spectroscopy. 2015 Feb;136:76–80. DOI: 10.1016/j.saa.2013.10.124.

[20] Ionescu C-M, Geidl S, Svobodová Vařeková R, Koča J. Rapid Calculation of Accurate Atomic Charges for Proteins via the Electronegativity Equalization Method. Journal of Chemical Information and Modeling. 2013 Oct 28;53(10):2548–58. DOI: 10.1021/ci400448n.

[21] Ouyang Y, Ye F, Liang Y. A modified electronegativity equalization method for fast and accurate calculation of atomic charges in large biological molecules. Physical Chemistry Chemical Physics. 2009;11(29):6082. DOI: 10.1039/B821696G.

[22] Iczkowski RP, Margrave JL. Electronegativity. Journal of the American Chemical Society. 1961 Sep;83(17):3547–51. DOI: 10.1021/ja01478a001.

[23] Kaya S, Kaya C. A new equation based on ionization energies and electron affinities of atoms for calculating of group electronegativity. Computational and Theoretical Chemistry. 2015 Jan;1052:42–6. DOI: 10.1016/j.comptc.2014.11.017.

[24] Kaya C. İnorganik kimya. Ankara: Palme Yayıncılık; 2008. ISBN: 9789944341776.

[25] Pearson RG. Chemical hardness. Weinheim, Germany ; New York: Wiley-VCH; 1997. 198 p. ISBN: 3527294821.

[26] Chattaraj PK. Chemical Reactivity and Selectivity: Local HSAB Principle versus Frontier Orbital Theory. The Journal of Physical Chemistry A. 2001 Jan;105(2):511–3. DOI: 10.1021/jp003786w.

[27] Chattaraj PK, Maiti B. HSAB Principle Applied to the Time Evolution of Chemical Reactions †. Journal of the American Chemical Society. 2003 Mar;125(9):2705–10. DOI: 10.1021/ja0276063.

[28] Kaya S, Kaya C, Islam N. Maximum hardness and minimum polarizability principles through lattice energies of ionic compounds. Physica B: Condensed Matter. 2016 Mar;485:60–6. 10.1016/j.physb.2016.01.010.

[29] Kaya S, Kaya C. A new equation for calculation of chemical hardness of groups and molecules. Molecular Physics. 2015 Jun 3;113(11):1311–9. DOI: 10.1080/00268976.2014.991771.

[30] Chattaraj PK, Giri S, Duley S. Electrophilicity Equalization Principle. The Journal of Physical Chemistry Letters. 2010 Apr;1(7):1064–7. DOI: 10.1021/jz1001117.

[31] Von Szentpály L. Ruling Out Any Electrophilicity Equalization Principle. The Journal of Physical Chemistry A. 2011 Aug 4;115(30):8528–31. DOI: 10.1021/jp203319y.

[32] Chattaraj PK, Giri S, Duley S. Comment on "Ruling Out Any Electrophilicity Equalization Principle." The Journal of Physical Chemistry A. 2012 Jan 12;116(1):790–1. DOI: 10.1021/jp208541x.

MOLEKÜLER ELEKTROFİLLİK VE NÜKLEOFİLLİĞİN TAHMİN EDİLMESİ İÇİN FAYDALI BİR YÖNTEM

Öz: Bu çalışmada, tarafımızdan son yıllarda türetilen grup elektronegativite ve moleküler sertlik eşitliklerine dayalı moleküler elektrofillik ve moleküler nükleofillik değerlerinin hesaplanması için yeni bir teorik model sunulmuştur. Bunun dışında, mevcut modelin geçerlilik testi 33 molekül ile yapılmış, bazı iyi bilinen teorik yöntemler ve onların deneysel kısımları kullanılarak bulunan elektrofillik ve nükleofillik verileri bizim çalışmamızda üretilenlerle karşılaştırılmıştır. Karşılaştırmalı çalışma teori ve deney arasında mükemmel bir uyum göstermektedir. Bu sebeple, bu çalışmada gösterilen yeni teorik model, elektrofillik ve nükleofillik gibi moleküler reaktivite indislerinin hesaplanması için mantıksal ve güvenilir sonuçlar vermektedir.

Anahtar kelimeler: Elektronegatiflik, Sertlik, Elektrofillik, Nükleofillik, DFT.

Gönderilme tarihi: 29 Şubat 2016, **Düzenleme tarihi:** 29 Mart 2016, **Kabul tarihi:** 12 Nisan 2016.

JOTCSA, Volume 3, issue 2, (2016), pp. 103-116.

Research article

Journal homepage: http://dergipark.ulakbim.gov.tr/jotcsa

e-ISSN: 2149-0120

CONVENTIONAL AND MICROWAVE-ASSISTED SYNTHESIS AND CHARACTERIZATION of Ru(III)/Cu(II) COMPLEXES CONTAINING DICARBOXYLIC ACID GROUPS

Burak Ay[1], Emel Yıldız[1]

[1]Çukurova University, Department of Chemistry, Arts and Science Faculty, 01330, Adana, TURKEY. Fax: (90)(322)3386070; Tel: (90)(322)3386084-2481.

Abstract: In this study, microwave-assisted and conventional syntheses of Ru(III) and Cu(II) complexes with 2,4-pyridinedicarboxylic acid (L1), 3,5-pyridinedicarboxylic acid (L2), and 3,5-pyrazoledicarboxylic acid (L3) have been studied. A comparative study of microwave and conventional methods was performed to determine their differences in terms of reaction time, the amount of solvent, and reaction yield. The reaction time was reduced significantly from several hours to a few minutes, and high yields were obtained by microwave method while using considerably less amount of solvent. The synthesized complexes were characterized by FT-IR, UV-Vis, AAS, ^{1}H-NMR, elemental analyses, and magnetic susceptibility. These studies showed that copper and ruthenium complexes have square planar and octahedral geometries, respectively. The metal complexes of Cu(II) and Ru(III) were easily synthesized upon exposure to microwave irradiation.

Keywords: Microwave synthesis, Inorganic-organic hybrid, Ru(III)-Cu(II) complexes.

Submitted: February 22, 2016. **Accepted:** May 04, 2016.

Cite this: Ay B, Yıldız E. Conventional and Microwave-assisted Synthesis and Characterization of Ru(III)-/Cu(II) Complexes Containing Dicarboxylic Acid Groups. Journal of the Turkish Chemical Society, Section A: Chemistry. 2016;3(2):103–115. DOI: 10.18596/jotcsa.20088.

***Correspondence to:** Emel Yıldız. E-mail: eeyildiz@cu.edu.tr.

INTRODUCTION

Organic-inorganic hybrid materials attract considerable attention in recent years because of their interesting molecular topologies and crystal packing motifs along with potential applications in many areas, including gas storage, separation, catalysis, magnetism, optics, as well as electrical conductivity [1]. The functionality of such hybrid materials can be multiplied by the incorporation of organic and inorganic counterparts into one structural unit [2,3]. A microwave-assisted inorganic synthesis method is an important technique in green synthetic chemistry [4]. The technique offers several advantages over conventional synthesis, especially the synthesis of ruthenium complexes, which typically require many hours of refluxing in high-boiling solvents to affect a reaction. Similar reactions, when performed in a microwave reactor, can occur in a matter of minutes [5-7]. The main advantage of this reactor is the almost instantaneous 'in-core' heating of materials in a homogenous and selective manner [8]. Particularly, the reaction time and energy input are supposed to be mostly reduced in the reactions that are run for a long time at high temperatures under conventional conditions [9]. In this work, we present the syntheses of Cu(II) and Ru(III) having different stabilities as first and second row transition metal complexes with L1, L2 and L3 ligands (Scheme 1) because they have various side-bonding in their structures due to carboxylic moieties [10]. Both conventional and microwave methods were carried out and the obtained results were compared with each other. The complexes were characterized by analytical and spectroscopic methods.

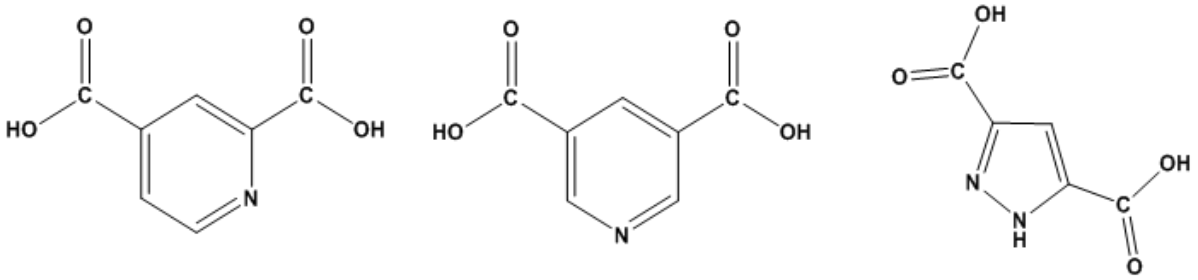

Scheme 1. The ligands used in this study (L1, L2, L3).

MATERIALS AND METHODS

Materials

$CuCl_2.2H_2O$, $RuCl_3.xH_2O$, 2,4-pyridinedicarboxylic acid, 3,5-pyridinedicarboxylic acid, and 3,5-pyrazinedicarboxylic acid were purchased from Sigma Aldrich and used without further purification. All other chemicals and solvents were commercially available (Merck, Fluka).

Physical measurements

FT-IR spectra were recorded on a Perkin-Elmer Spectrum RX I FT-IR spectrometer as KBr pellets in the 4000-400 cm^{-1} range. The UV-Vis spectra was determined in DMSO solvent with a concentration of 1.0×10^{-3} M for the free ligands and their complexes using a Perkin Elmer Lambda 25 Spectrophotometer with 1 cm quartz cell, in the range 200-800 nm. AAS analyses were recorded on a Perkin Elmer Analyst 400 spectrometer. The DC magnetic susceptibilities of powdered samples were measured by a Sherwood Scientific magnetic susceptibility meter.

Synthesis of [Cu(L1)$_2$] by the Conventional Method (CM)

Copper(II) chloride dihydrate (0.335 g, 2.50 mmol) in MeOH (10 mL) was slowly added to a solution of L1 acid (0.417 g, 2.50 mmol) in MeOH (40 mL) at room temperature. The mixture was left for 144 h. The light green solid product which precipitated was filtered off and washed with acetonitrile (Yield: 48%). M.P.:315-316°C. [Cu(L1)$_2$]: ^{1}H-NMR (300 MHz, DMSO, 25°C): δ (ppm) = 13.10 (s, 1H, OH), 8.26 (d, 1H, CH), 8.70 (s, H, CH), 7.58 (d, H, CH). UV-Vis (DMSO, λ_{max}(nm)): L1: 279, L1-Cu: 446. AAS. Calculated (1:2): 15.90%; Found: 15.18%.

Synthesis of [Cu(L1)$_2$] by the Microwave Method (MM)

The ligand (0.022 g, 0.13 mmol) and the metal salt (0.017 g, 0.130 mmol) were mixed thoroughly in a porcelain capsule. Methanol (5 mL) was added to this mixture and stirred. The mixture was irradiated for 3 minutes in the microwave oven at 850 W power. The product was washed with methanol to dissolve any unreacted material, if any, and filtered. The product was repeatedly washed with methanol and finally dried on air (Yield: 89%). M.P.:315-316°C. [Cu(L1)$_2$]: ^{1}H-NMR (300 MHz, DMSO, 25°C): δ (ppm) = 13.10 (s, 1H, OH), 8.26 (d, 1H, CH), 8.70 (s, H, CH), 7.58 (d, H, CH). UV-Vis (DMSO, λ_{max}(nm)): L1: 279, L1-Cu: 446. AAS. Calculated (1:2): 15.90%; Found: 15.18%.

Synthesis of [Cu(L2)Cl$_2$] by the Conventional Method

Copper(II)chloride dihydrate (0.202 g, 1.50 mmol) in MeOH (8 mL) was slowly added at room temperature to a solution of L2 (0.251 g, 1.50 mmol) in MeOH (90 mL). The mixture was left at room temperature for 144 h. The turquoise solid product was precipitated in and washed with acetonitrile (Yield: 41%). M.P.:259-260°C. [Cu(L2)Cl$_2$]: ^{1}H-NMR (300 MHz, DMSO, 25°C): δ (ppm) = 12.14 (s, 1H, OH), 3.09 (m, 2H, CH$_2$), 2.33 (m, 1H, CH), 2.09 (m, 2H, CH$_2$). UV-Vis (DMSO, λ_{max}(nm)): L2: 254, L2-Cu: 654. AAS. Calculated (1:1): 21.05%; Found: 21.00%.

Synthesis of [Cu(L2)Cl$_2$] by the Microwave Method

The synthesis was similar to that described for [Cu(L1)$_2$]. It used the L2 ligand (0.022 g, 0.13 mmol) and a turquoise solid was obtained (Yield: 82%). M.P.:259-260°C. [Cu(L2)Cl$_2$]: ^{1}H-NMR (300 MHz, DMSO, 25°C): δ (ppm) = 12.14 (s, 1H, OH), 3.09 (m, 2H, CH$_2$), 2.33 (m, 1H, CH), 2.09 (m, 2H, CH$_2$). UV-Vis (DMSO, λ_{max}(nm)): L2: 254, L2-Cu: 654. AAS. Calculated (1:1): 21.05%; Found: 21.00%.

Synthesis of [Cu(L3)$_2$] by the Conventional Method

Copper(II) chloride dihydrate (0.135 g, 1.0 mmol) in MeOH (10 mL) was slowly added, at room temperature, to a solution of L3 (0.175 g, 1.0 mmol) in MeOH (15 mL). The mixture was left at room temperature for 144 h. The green solid precipitate was filtered off and washed with acetonitrile (Yield: 60%). M.P.:>300°C. [Cu(L3)$_2$]: ^{1}H-NMR (300 MHz, DMSO, 25°C): δ (ppm) = 13.70 (s, 1H, NH), 12.20 (s, 1H, OH), 6.30 (s, 1H, CH) ppm. UV-Vis (DMSO, λ_{max}(nm)): L3: 257, L3-Cu: 648. AAS. Calculated (1:2): 15.40%; Found: 17.30%.

Synthesis of [Cu(L3)$_2$] by the Microwave Method

The synthesis was similar to that described for [Cu(L1)$_2$]. It used the L3 (0.023 g, 0.13 mmol) ligand and a green-colored solid were obtained (Yield: 86%). M.P.:>300°C. [Cu(L3)$_2$]: ^{1}H-NMR (300 MHz, DMSO, 25°C): δ (ppm) = 13.70 (s, 1H, NH), 12.20 (s, 1H, OH), 6.30 (s, 1H, CH). UV-Vis (DMSO, λ_{max}(nm)): L3: 257, L3-Cu: 648. AAS. Calculated (1:2): 15.40%; Found: 17.30%.

Synthesis of [Ru(L1)$_2$(H$_2$O)Cl] by the Conventional Method

RuCl$_3$.xH$_2$O (0.016 g, 0.08 mmol) in MeOH (12 mL) was slowly added at room temperature to a solution of L1 (0.013 g, 0.08 mmol) and NaOH (0.016 g, 0.04 mmol) in H$_2$O (10 mL). The mixture was left at room temperature for one month [11]. The green solid product which precipitated was filtered off and isolated from the methanolic solution (Yield: 62%). M.P.:310°C. [Ru(L1)$_2$(H$_2$O)Cl]: ^{1}H-NMR (300 MHz, DMSO, 25°C): δ (ppm) = 12.74 (s, 1H, OH), 9.24 (s, 1H, CH), 8.59 (s, 1H, CH). UV-Vis (DMSO, λ_{max}(nm)): L1: 279, L1-Ru: 447, AAS. Calculated (1:2): 20.74%; Found: 21.05%.

Synthesis of [Ru(L1)$_2$(H$_2$O)Cl] by the Microwave Method

RuCl$_3$.xH$_2$O (0.016 g, 0.08 mmol), L1 (0.013 g, 0.08 mmol) and ethylene glycol (2 mL) was mixed in a porcelain capsule, and they were dissolved in an ultrasonic mixer. The mixture was irradiated for 20 seconds in the microwave oven with a power of 850W. The capsule was cooled under tap water. Acetone (1.5 mL) was added into the solution and the mixture was stirred in 10 minutes. The solution was evaporated and the green product was recrystallized from ethanol (Yield: 76%). M.P.:310°C. [Ru(L1)$_2$(H$_2$O)Cl]: ^{1}H-NMR (300 MHz, DMSO, 25°C): δ (ppm) = 12.74 (s, 1H, OH), 9.24 (s, 1H, CH), 8.59 (s, 1H, CH). UV-Vis (DMSO, λ_{max}(nm)): L1: 279, L1-Ru: 447, AAS. Calculated (1:2): 20.74%; Found: 21.05%.

Synthesis of [Ru(L2)$_2$(H$_2$O)Cl] by the Conventional Method

RuCl$_3$.xH$_2$O (0.021 g, 0.10 mmol) in MeOH (15 mL) was slowly added, at room temperature, to a solution of L2 (0.017 g, 0.10 mmol) and NaOH (0.082 g, 2 mmol) in H$_2$O (10 mL). The mixture was left at room temperature for one month. The green solid product was filtered off and isolated from the methanolic solution (Yield: 65%). M.P.:>300°C. [Ru(L2)$_2$(H$_2$O)Cl]: ^{1}H-NMR (300 MHz, DMSO, 25°C): δ (ppm) = 12.74 (s, 1H, OH), 9.48 (d, 1H, CH), 8.93 (s, 1H, CH), 8.12 (d, 1, CH). UV-Vis (DMSO, λ_{max}(nm)): L2: 254, L2-Ru: 385, AAS. Calculated (1:2): 20.74%; Found: 19.82%.

Synthesis of [Ru(L2)$_2$(H$_2$O)Cl] by the Microwave Method

RuCl$_3$.xH$_2$O (0.021 g, 0.10 mmol), L2 (0.017 g, 0.10 mmol) and MeOH (15 mL) were added in a porcelain capsule, and they were dissolved in the ultrasonic mixer. The mixture was irradiated for 5 minutes in the microwave oven with a power of 850 W. The capsule was cooled under tap water. The solution was evaporated and the green product was washed with petroleum ether and recrystallized from acetone (Yield: 78%). M.P.:>300°C. [Ru(L2)$_2$(H$_2$O)Cl]: ^{1}H-NMR (300 MHz, DMSO, 25°C): δ (ppm) = 12.74 (s, 1H, OH), 9.48 (d, 1H, CH), 8.93 (s, 1H, CH), 8.12 (d, 1, CH). UV-Vis (DMSO, λ_{max}(nm)): L2: 254, L2-Ru: 385, AAS. Calculated (1:2): 20.74%; Found: 19.82%.

RESULTS AND DISCUSSION

The results of the elemental analyses and magnetic susceptibility values of the obtained compounds are given in Table 1. The complexes are air-stable, have higher melting points, and are insoluble in H_2O and most of the organic solvents except for DMSO and DMF. The elemental analysis and atomic absorption data of the complexes indicated a 1:2 metal: ligand ratio for all the complexes except for $[Cu(L2)Cl_2]$, (1:1). As shown in Table 1, elemental analyses and AAS results for both microwave and conventional methods are in agreement with theoretical data. Our proposed structural formulas are given in Schemes 2 and 3.

Fourier Transform Infrared Spectra

The main FT-IR data of the free ligands and their complexes are summarized in Table 2. All complexes containing H_2O or -OH groups exhibited characteristic absorption bands in the range 3390-3462 cm^{-1}. The FT-IR spectra of the ligands L1, L2, and L3 displayed absorption bands at 3092-3111 cm^{-1}, 1704-1721 cm^{-1}, and 1604-1702 cm^{-1} are assigned to υ(O-H), υ(C=O), and υ(C=N), respectively [12]. The spectra of the ligands exhibited broad medium intensity bands in the range 3092-3111 cm^{-1} which were assigned to the intramolecular H-bonding vibration (O-H…C). In the spectra of the complexes, these bands disappeared (Figs. 1 and 2), indicating the deprotonation of these groups on coordination with the metal atoms. In the ligands, the bands at 1704-1721 cm^{-1} and 1257-1277 cm^{-1} can be assigned to the υ(C=O) and υ(C-N) bond vibrations. In the metal complexes, these bands displaced variations in the frequencies because of coordination of oxygen and nitrogen to the metals.

In all the complexes, the bands at 682-693 cm^{-1}, 728-766 cm^{-1}, 408-475 cm^{-1} and 472-519 cm^{-1} can be attributed to the υ(Ru-O) and υ(Ru-N), υ(Cu-N) and υ(Cu-O) bonds respectively [13, 14]. In addition, the appearance of bands in the region of 395-486 cm^{-1} were due to υ(M-Cl) vibrations [15].

Magnetic Susceptibility Measurements

The magnetic susceptibility values of the ruthenium(III) and copper(II) complexes with L1, L2, and L3 ligands were measured at 298 K. Ruthenium(III) complexes were measured as antiferromagnetic while all other copper(II) complexes were paramagnetic for bearing unpaired electrons. The Ru(III) complexes displayed antiferromagnetic property, which involves σ interactions between the half-filled, e_g orbitals of Ru^{3+} ions [16,17]. The effective magnetic moments (μ_{eff}) derived from the Curie-law fit were 1.78, 1.83 and 1.96 B.M., respectively. These results agree well with the theoretical effective magnetic moment for Cu(II), 1.73 B.M. and they are comparable with the similar type of complexes in the literature [18,19].

Table 1. Analytical data and physical properties of Ru(III) and Cu(II) complexes.

Compounds	Analytical Data Found % (Calculated %)				
Conventional Method	**M**	**C**	**H**	**N**	**μ_{eff} (BM)**
$[Cu(L1)_2]$	15.18 (15.90)	37.17 (35.97)	2.93 (2.39)	5.91 (5.99)	1.78
$[Cu(L2)Cl_2]$	21.00 (21.05)	26.38 (27.50)	3.05 (2.96)	4.16 (4.65)	1.83
$[Cu(L3)_2]$	17.30 (15.40)	27.79 (26.84)	3.21 (2.79)	12.14 (12.53)	1.96
$[Ru(L1)_2(H_2O)Cl]$	21.05 (20.74)	24.11 (25.19)	2.99 (2.10)	4.23 (4.20)	N/A
$[Ru(L2)_2(H_2O)Cl]$	19.82 (20.74)	24.81 (25.19)	3.22 (2.10)	3.84 (4.20)	N/A
Microwave Method					
$[Cu(L1)_2]$	15.18 (15.90)	37.17 (35.97)	2.93 (2.39)	5.91 (5.99)	1.78
$[Cu(L2)Cl_2]$	21.00 (21.05)	26.38 (27.50)	3.05 (2.96)	4.16 (4.65)	1.83
$[Cu(L3)_2]$	17.30 (15.40)	27.79 (26.84)	3.21 (2.79)	12.14 (12.53)	1.96
$[Ru(L1)_2(H_2O)Cl]$	21.05 (20.74)	24.11 (25.19)	2.99 (2.10)	4.23 (4.20)	N/A
$[Ru(L2)_2(H_2O)Cl]$	19.82 (20.74)	24.81 (25.19)	3.22 (2.10)	3.84 (4.20)	N/A

UV-Visible Spectra

All the Ru(III) and Cu(II) complexes showed the characteristic $d_{п-п*}$ (L) MLCT bands in the region of 370-700 nm, in addition to the ligand п-п* (L) bands at 279 nm for L1, at 254 nm for L2 and at 257 nm for L3. The UV-Vis absorption spectra of Ru(III) complexes with L1, L2, and Cu(II) complexes with L1, L2 and L3 ligands were given in Figs. 3 and 4. All complexes showed the expected absorption bands at the main peaks appearing at λ_{max} = 446, 648 and 654 nm for Cu(II) [20,21], 379, 447 nm and 382, 385 nm for Ru(III), respectively [22]. These bands may be attributed for the metal to ligand charge transfer (MLCT) transitions.

Table 2. FT-IR spectral data of the ligands and their metal complexes (cm^{-1}).

Compounds	υ(OH)	υ(C=O)	υ(C=N)	υ(C-N)	υ(M-N)	υ(M-O)	υ(M-Cl)
L1	3105	1704	1611	1257	N/A	N/A	N/A
L2	3092	1721	1604	1267	N/A	N/A	N/A
L3	3111	1714	1702	1277	N/A	N/A	N/A
Microwave method							
$[Cu(L1)_2]$	3396	1725	1635	1257	422	472	N/A
$[Cu(L2)Cl_2]$	3390	1720	1640	1281	475	546	395
$[Cu(L3)_2]$	3462	1722	1648	1290	408	519	N/A
$[Ru(L1)_2(H_2O)Cl]$	3441	1729	1636	1248	766	690	473
$[Ru(L2)_2(H_2O)Cl]$	3429	1730	1652	1288	736	690	470
Conventional Method							
$[Cu(L2)Cl_2]$	3390	1725	1635	1257	422	472	N/A
$[Cu(L1)_2]$	3396	1720	1640	1281	475	546	395
$[Cu(L3)_2]$	3462	1722	1648	1290	408	519	N/A
$[Ru(L1)_2(H_2O)Cl]$	3441	1729	1636	1248	766	690	473
$[Ru(L2)_2(H_2O)Cl]$	3429	1730	1652	1288	736	690	470

Table 3. Comparison between conventional method (CM) and microwave method (MM).

Compounds	Yield (%)		Solvent (mL)		Time	
	CM	MM	CM	MM	CM (days)	MM (min)
$[Cu(L1)_2]$	48	89	50	5	6	3
$[Cu(L2)Cl_2]$	41	82	100	5	6	3
$[Cu(L3)_2]$	60	86	25	5	6	3
$[Ru(L1)_2(H_2O)Cl]$	62	76	25	2	30	1/3
$[Ru(L2)_2(H_2O)Cl]$	65	78	30	15	30	5

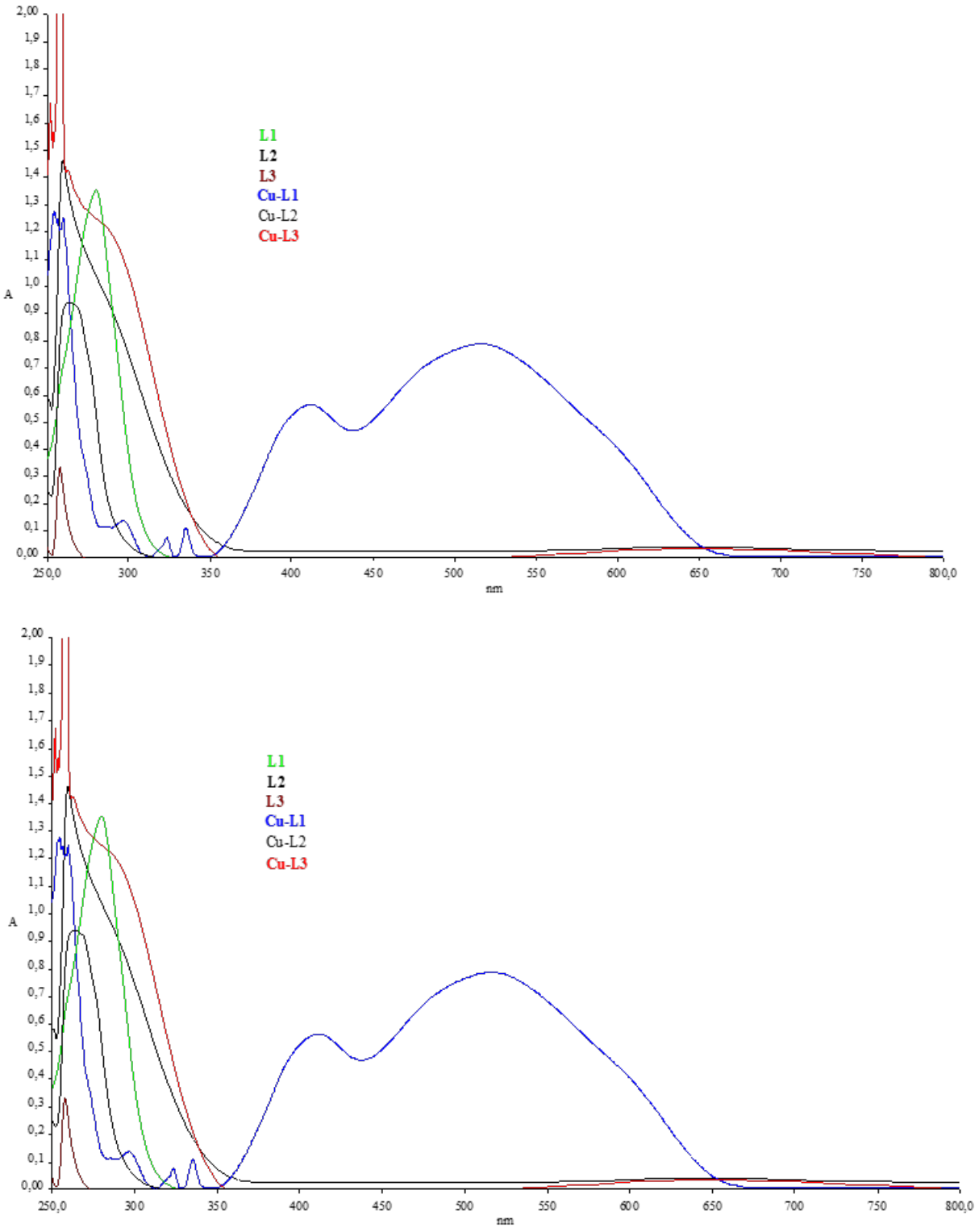

Figure 3. UV-Vis Spectra of compounds L1, L2, L3 and their Cu(II) complexes using microwave (top) and conventional methods (bottom).

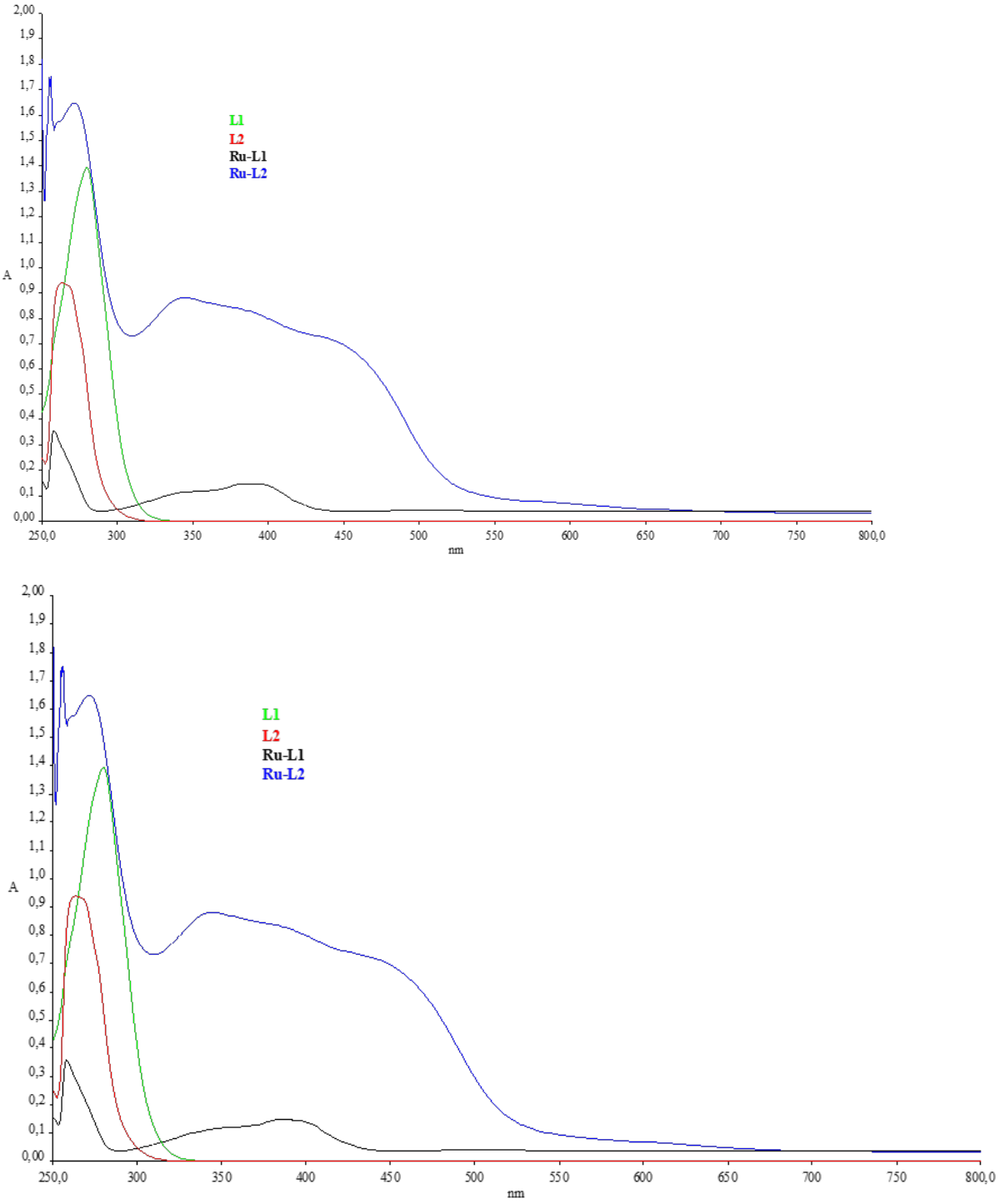

Figure 4. UV-Vis Spectra of compounds L1, L2, and their Ru(III) complexes using microwave (top) and conventional methods (bottom).

^{1}H-NMR and ^{13}C-NMR

^{1}H-NMR spectra were consistent with the proposed structures. The ^{1}H-NMR spectral data of the ligands and their corresponding Cu(II) and Ru(III) complexes were recorded in DMSO by employing TMS as an internal standard. The ^{1}H-NMR spectra of the ligands (L1, L2, and L3) exhibited aromatic signals at δ 8.13-9.30, δ 8.59-9.08 and δ 6.3 ppm, respectively. The protons of -OH groups of the ligands gave signals at δ 12.14-13.2 ppm. In the spectra of their metal complexes, these intension signals were reduced. The ^{1}H-NMR spectrum is shown in Fig. S1 (Supporting Information). These results showed that the chelation of the ligand moiety is via one of the carboxyl groups. In the spectra of the L3 ligand and its Cu(II) complex, the -NH proton signals appeared at δ 13.70 ppm, indicating the bonding of the other nitrogen atom [9]. ^{13}C-NMR spectral data for the complexes could not be obtained since they have paramagnetic character. Comparison of the microwave and conventional methods were given in Table 3. For the microwave assisted synthesis, 0-5 minutes were required for the reactions to complete. While using the conventional method, the reaction time was six days for the Cu(II) complexes and 30 days for Ru(III) complexes. The product yields were less in the conventional method as compared to that of the obtained complexes by the microwave synthesis. For the microwave synthesis, between 2-15 mL of solvent was consumed in the reactions, while this amount was 25-30 mL in the conventional method. Although [Cu(L1)$_2$] was synthesized in 48% yield by the conventional method, the reaction occurred in a few minutes by 89% yield by microwave method.

CONCLUSION

Herein, ruthenium(III) and copper(II) complexes were obtained by both microwave and conventional methods and were characterized by UV-Visible, FT-IR, ^{1}H-NMR, AAS, elemental analysis, and magnetic susceptibility techniques. Single crystals of the synthesized compounds could not be isolated from any solution; thus no definite structure may be described. Assuming the analytical data and spectral studies, the ligands coordinated to the copper(II) and ruthenium(III) metals in a bidentate manner as square planar and octahedral geometry, respectively. We compared these methods in terms of the reaction time, amount of solvent, and reaction yield. The salient features of microwave method include the simple reaction set-up, mild reaction conditions, and short reaction times. Because of these advantages, the method is more efficient and environmentally friendly for the synthesis of the related metal complexes.

ACKNOWLEDGEMENTS

This present work was supported by the Research Unit of Cukurova University (Grant No. FEF 2007 BAP17).

REFERENCES

[1] Lan A, Han L, Yuan D, Jiang F, Hong M. A blue luminescent inorganic–organic hybrid with infinite [Cd3(μ3-OH)2(μ2-Cl)2] connectivity. Inorganic Chemistry Communications. 2007 Sep;10(9):993–6. DOI: 10.1016/j.inoche.2007.05.009.

[2] Liu Y, Li Y-X, Zhang S-W, Ji H-M, Cao R-G, Liu S-X. Organic–inorganic hybrid based on the molybdenum tellurite. Journal of Molecular Structure. 2009 Mar;921(1-3):114–7. DOI: 10.1016/j.molstruc.2008.12.058.

[3] Wu L, Ma H, Han Z, Li C. Synthesis, structure and property of a new inorganic–organic hybrid compound [Cu(phen)2][Cu(phen)H2O]2[Mo5P2O23]·3.5H2O. Solid State Sciences. 2009 Jan;11(1):43–8. DOI: 10.1016/j.solidstatesciences.2008.05.016.

[4] Ellsworth JM, Smith MD, zur Loye H-C. Improved synthesis of 4,4′-bipyridine-2-carboxylic acid and its use in the construction of novel metal and mixed-metal coordination polymers. Solid State Sciences. 2008 Dec;10(12):1822–34. DOI: 10.1016/j.solidstatesciences.2008.03.014.

[5] Wang R, Lu X, Yu X, Shi L, Sun Y. Acid-catalyzed solvent-free synthesis of 2-arylbenzimidazoles under microwave irradiation. Journal of Molecular Catalysis A: Chemical. 2007 Apr;266(1-2):198–201. DOI: 10.1016/j.molcata.2006.04.071.

[6] Cortijo M, Delgado-Martínez P, González-Prieto R, Herrero S, Jiménez-Aparicio R, Perles J, et al. Microwave and solvothermal methods for the synthesis of nickel and ruthenium complexes with 9-anthracene carboxylate ligand. Inorganica Chimica Acta. 2015 Jan;424:176–85. DOI: 10.1016/j.ica.2014.07.063.

[7] Bui HTB, Ha QTK, Oh WK, Vo DD, Chau YNT, Tu CTK, et al. Microwave assisted synthesis and cytotoxic activity evaluations of new benzimidazole derivatives. Tetrahedron Letters. 2016 Feb;57(8):887–91. DOI: 10.1016/j.tetlet.2016.01.042.

[8] Anderson TJ, Scott JR, Millett F, Durham B. Decarboxylation of 2,2`-Bipyridinyl-4,4`-dicarboxylic Acid Diethyl Ester during Microwave Synthesis of the Corresponding Trichelated Ruthenium Complex. Inorganic Chemistry. 2006 May;45(10):3843–5. DOI: 10.1021/ic060008v.

[9] Singh RV, Chaudhary P, Chauhan S, Swami M. Microwave-assisted synthesis, characterization and biological activities of organotin (IV) complexes with some thio Schiff bases. Spectrochimica Acta Part A: Molecular and Biomolecular Spectroscopy. 2009 Mar;72(2):260–8. DOI: 10.1016/j.saa.2008.09.017.

[10] Shaabani A, Maleki-Moghaddam R, Maleki A, Rezayan AH. Microwave assisted synthesis of metal-free phthalocyanine and metallophthalocyanines. Dyes and Pigments. 2007 Jan;74(2):279–82. DOI: 10.1016/j.dyepig.2006.02.005.

[11] McDonald FC, Applefield RC, Halkides CJ, Reibenspies JH, Hancock RD. A thermodynamic and crystallographic study of complexes of the highly preorganized ligand 8-hydroxyquinoline-2-carboxylic acid. Inorganica Chimica Acta. 2008 May;361(7):1937–46. DOI: 10.1016/j.ica.2007.10.004.

[12] Sharma K, Singh R, Fahmi N, Singh RV. Microwave assisted synthesis, characterization and biological evaluation of palladium and platinum complexes with azomethines. Spectrochimica Acta Part A: Molecular and Biomolecular Spectroscopy. 2010 Jan;75(1):422–7. DOI: 10.1016/j.saa.2009.10.052.

[13] Refat MS, El-Korashy SA, Kumar DN, Ahmed AS. Syntheses and characterization of Ru(III) with chelating containing ONNO donor quadridentate Schiff bases. Spectrochimica Acta Part A: Molecular and Biomolecular Spectroscopy. 2008 Sep;70(4):898–906. DOI: 10.1016/j.saa.2007.10.005.

[14] Chandra S, Jain D, Sharma AK. EPR, mass, electronic, IR spectroscopic and thermal studies of bimetallic copper(II) complexes with tetradentate ligand, 1,4-diformyl piperazine bis(carbohydrazone). Spectrochimica Acta Part A: Molecular and Biomolecular Spectroscopy. 2009 Jan;71(5):1712–9. DOI: 10.1016/j.saa.2008.06.028.

[15] Mohanan K, Kumari BS, Rijulal G. Microwave assisted synthesis, spectroscopic, thermal, and antifungal studies of some lanthanide(III) complexes with a heterocyclic bishydrazone. Journal of Rare Earths. 2008 Feb;26(1):16–21. DOI: 10.1016/S1002-0721(08)60028-9.

[16] Jolly WL. Modern inorganic chemistry. New York: McGraw-Hill; 1984. 610 p. ISBN: 978-0-07-032760-3.

[17] Yıldız E, Bozkurt G. Synthesis of Ru(III) and Al(III) Complexes Containing Anthraquinone Moiety and Interactions of the UV Radiations. Asian Journal of Chemistry. 2009;5:4047–53. URL: http://search.proquest.com/openview/48f867dd7f5c02e0bb7ca95a21886989/1?pq-origsite=gscholar.

[18] Dong Y-B, Smith MD, zur Loye H-C. Synthesis and characterization of a novel copper(II)-silver(I) mixed-metal coordination polymer: Ag[Cu(2-pyrazinecarboxylate)2](H2O)(NO3). Solid State Sciences. 2000 May;2(3):335–41. DOI: 10.1016/S1293-2558(00)00139-4.

[19] Driessen WL, Chang L, Finazzo C, Gorter S, Rehorst D, Reedijk J, et al. Two pyrazolato-bridged, linear trinuclear Cu(II) complexes. Crystal structures and magnetic properties. Inorganica Chimica Acta. 2003 Jul;350:25–31. DOI: 10.1016/S0020-1693(02)01509-8.

[20] Serbest K, Değirmencioğlu İ, Ünver Y, Er M, Kantar C, Sancak K. Microwave-assisted synthesis and characterization and theoretical calculations of the first example of free and metallophthalocyanines from salen type Schiff base derivative bearing thiophen and triazole heterocyclic rings. Journal of Organometallic Chemistry. 2007 Dec;692(25):5646–54. DOI: 10.1016/j.jorganchem.2007.09.026.

[21] Kufelnicki A, Woźniczka M, Chęcińska L, Miernicka M, Budzisz E. Synthesis and structure of novel copper(II) complexes with pyrazole derived ligands and metal–ligand interaction in solution. Polyhedron. 2007 Jul;26(12):2589–96. DOI: 10.1016/j.poly.2006.12.043.

[22] Mizushima K, Nakaura M, Park S-B, Nishiyama H, Monjushiro H, Harada K, et al. Ruthenium(II) complexes with the tetradentate 6,6′-bis(oxazolinyl or benzimidazolyl)-2,2′-bipyridine ligand: synthesis, electrochemical properties, and catalytic reactivities. Inorganica Chimica Acta. 1997 Sep;261(2):175–80. DOI: 10.1016/S0020-1693(97)05479-0.

Research article

DİKARBOKSİLİK ASİT GRUPLARI İÇEREN Cu(II)/Ru(III) KOMPLEKSLERİNİN KONVANSİYONEL VE MİKRODALGA DESTEKLİ SENTEZ VE KARAKTERİZASYONLARI

Öz: Bu çalışmada, 2,4-piridindikarboksilik asit (L1), 3,5- piridindikarboksilik asit (L2) ve 3,5-pirazoldikarboksilik asit (L3) ligandları kullanılarak konvansiyonel ve mikrodalga yöntemleri ile Ru(III) ve Cu(II) metal kompleksleri sentezlenmiştir. Mikrodalga ve konvansiyonel yöntemlerinin kıyaslanması için yapılan bu çalışmada yöntemlerin birbirlerine göre farklılıkları, tepkime süresi, çözücü miktarı ve verim açısından değerlendirilmiştir. Tepkime süresi uzun saatlerden birkaç dakikaya kadar önemli derecede azaltılmıştır. Mikrodalga yöntemi ile çok daha az çözücü kullanılması sonucunda yüksek verimlerde kompleksler elde edilmiştir. Sentezlenen komplekslerin yapıları FT-IR, UV-Vis, AAS, 1H-NMR, elementel analiz ve manyetik duyarlılık teknikleri ile karakterize edilmiştir. Analiz sonuçları bakır ve rutenyum komplekslerinin sırasıyla kare düzlem ve düzgün sekizyüzlü geometrilere sahip olduğunu göstermiştir. Cu(II) ve Ru(III) metal kompleksleri mikrodalga ışınına maruz bırakılarak kolay bir şekilde sentezlenmiştir.

Anahtar Kelimeler: Mikrodalga sentez, İnorganik-organik hibrit, Rutenyum(III) ve Bakır(II) kompleksleri.

Gönderilme tarihi: 22 Şubat 2016, **Kabul tarihi:** 04 Mayıs 2016.

JOTCSA, Volume 3, issue 1, (2016), pp. 117-130.

Research article

Journal homepage: http://dergipark.ulakbim.gov.tr/jotcsa

e-ISSN: 2149-0120

EXTRACTION AND SPECTROTHERMAL STUDIES OF COPPER(II) DECANOATE COMPLEX

Hanene Rehali[1]* and Djamel Barkat[1]

[1]*Faculty of Sciences and Technology, Department of Industrial Chemistry, University of Biskra, BP 145, Algeria.*

Abstract: The extraction of copper (II) from 0.33 M Na_2SO_4 aqueous solutions with decanoic acid (HL) in chloroform at 25°C has been studied. The extracted species, when the decanoic acid compound was used alone, is $CuL_2.2(HL).2H_2O$. The complex of copper was synthesized and characterized by elemental analysis, infrared spectra, electronic spectra, X-ray diffraction (XRD), laser particle size analysis, and molar conductance measurements.

Keywords: Decanoic acid, metal carboxylate; extraction liquid; structural study.
Submitted: August 09, 2015. **Revised:** November 06, 2015. **Accepted:** April 17, 2016.

Cite this: Rehali H., Barkat D., EXTRACTION AND SPECTROTHERMAL STUDIES OF COPPER(II) DECANOATE COMPLEX. Journal of the Turkish Chemical Society, Section A: Chemistry. 2016;3(2):117–130.
DOI: 10.18596/jotcsa.30250.
Correspondence to: Hanene Rehali. E-mail: rahal.hanan@yahoo.fr.

INTRODUCTION

The separation of copper in an industrial environment mainly uses the technique of liquid-liquid extraction with complexing agents. This method is used in many chemical processes for the production of inorganic salts such as chlorides of copper or cobalt. There are a wide variety of complexing agents and separation conditions to effect the liquid-liquid extraction of copper. These extractants are mostly organic phosphoric acids which have the ability to complex with nickel, copper or cobalt. The separation is performed using two phases; an organic that has a high affinity for complexing agent and an aqueous phase. The organic phase is the most commonly used jet fuel. It is necessary to adjust with high accuracy the parameters such as pH, the concentration of complexing agents, and the addition of salts to optimize the separation.

Carboxylic acids are organic molecules. The carboxylate of the higher fatty acids with the metal ions have many applications in different industrial areas such as driers in paints, the components of lubricating greases, stabilizers of plastics, catalysts, additives to fuels, as well as corrosion preventive materials (promoters of rubber–steel cord adhesion) [4], *etc*. Therefore, metal carboxylates have promising applications depending upon the metal used to make the complex.

EXPERIMENTAL SECTION

Reagents

Decanoic acid (98%, Fluka) was used as purchased. Chloroform was pre-equilibrated with an aqueous solution which did not contain copper(II). The ionic strength of the aqueous medium was assumed to be unity ([Na_2SO_4]= 0.33 M). The initial concentration of copper was 100 ppm.

Materials and measurements

Conductivity measurements were performed at 25±1°C on a DDSJ-308A conductivity meter with an electrode. The cell constant was determined by use of KCl standard aqueous solution. The molar conductivity (ΛM) of the complexes was measured using a $2.0 \cdot 10^{-3}$ $mol.dm^{-3}$ solution in dimethyl formamide (DMF). X-ray diffraction was carried out on a Bruker SMART 1000 CCD area diffractometer. An electron microscopy (SEM) coupled energy dispersive spectrometer-based (EDX) microanalysis was performed in chemical composition. Electronic spectra of complexes in chloroform ($CHCl_3$) were obtained using a SHIMADZU UV VISIBLE1240 spectrophotometer in the range of 1200–300 nm. Infrared spectra of the ligands and their metal complexes were measured using KBr discs with a Fourier transform infrared spectrometer (SHIMADZU FTIR 8400) covering the range 4000–400 cm^{-1}. Thermogravimetry (TG 70/217) Thristor-Power supply linse thermal analyzer was used to record simultaneous DTG and DTA curves in a static air atmosphere, at a heating rate 10°C min^{-1} in the temperature range 0-500°C using a platinum crucible.

Extraction and analytical procedures

An aqueous copper solution (30 mL, 1.57×10^{-3} M) was placed in a thermostated vessel at 25 ± 0,05 °C. The solution contained an equal volume of chloroform solutions containing 1×10^{-3}– 4×10^{-2} M of decanoic acid.

The time was sufficient since the equilibrium was reached rapidly. After equilibrium, both phases were allowed to stand for more than 20 min for a complete phase separation. The pH of the solution was adjusted to between 4 and 8 by adding a few drops of 0.2 M NaOH. The metal ion concentrations were determined in aqueous phase photometrically at 810 nm using a Philips UV-VIS SP6-36. The metal ion concentrations in the organic phase were calculated from the difference between the metal ion concentrations in the aqueous phase before and after extraction.

RESULTS AND DISCUSSION

Extraction equilibrium of copper(II) with decanoic acid

Decanoic acid is known to exist as a dimer in the solvent of low polarity such as chloroform, hexane, toluene, and benzene [3]. The extraction of the metal, by a dimerized decanoic acid, $(HL)_2$, in chloroform can be represented by the general equation:

$$jM^{2+} + \frac{j(n+p)}{2}(HL)_{org} \overset{K_{ext}}{\longleftrightarrow} (ML_n p(HL))_{org} + jnH^+ \quad \textbf{(1)}$$

Where the subscript org corresponds to organic phases, and j is the degree of polymerization of the complex;
M : Metal
$(HL)_2$ extractant in dimeric form in the solvent of low polarity;
n: cationic charge;
org : organic phase
K_{ext} : constant of extraction
p : number of monomeric acid contained in the complex.
The extraction constant can be written as the following expression:

$$K_{ex1} = \frac{\left[(ML_n p(HL))_{org}\right][H^+]^{jn}}{[M^{+2}]^j \left[(HL)_{2org}\right]^{j(n+p)/2}} \quad \textbf{(2)}$$

The distribution coefficient D of the metal between the organic and aqueous phases may be expressed as follows:

$$D = \frac{C_{M,org}}{C_{M,aq}} = \sum_j \sum_a \frac{j[ML_n H_L p]_{org}}{[Cu^{2+}]\alpha_M} \quad \textbf{(3)}$$

$$= \sum_j \sum_p \left(jK_{ex(jah)} [M^{n+}]_{aq}{}^{(j-1)} \alpha_M{}^{-1} [(HL)_2]_{org}{}^{n+p/2} [H^+]^{-nj} \right) \quad \textbf{(4)}$$

Where M_{org} and M_{aq} are the total concentrations of the metal in the organic and aqueous phases, respectively, and the side reaction coefficient allowing for metal complex in the aqueous phase. If only $(ML_n(HL)_p)j$ is responsible for the extraction system, equation (5) is derived from equation (4).

$$logD = (j-1)log[M^{n+}]_{aq} + \frac{n+p}{2} log[(HL)_2]_{org} - njlog[H^+] - log\alpha_M + logj + logK_{ex} \quad \textbf{(5)}$$

Extraction of copper(II) with decanoic acid

The stoichiometry of the extracted species was determined by analyzing the experimental data. The conventional slope analysis method was used. The experimental results are arranged according to equation (5).

Figure 1 shows the results obtained for the extraction of copper(II) with solutions of various decanoic acid concentrations. The degree of extraction of copper(II) increases with increasing pH and decanoic acid concentration. The plots of logD versus pH for various concentration of decanoic acid are straight lines with slopes equal to two (n=2), This suggests full neutralization of copper(II) valence leading to release of two protons as given by equation (6). The data in Figure 1 also reveal no dependence of copper distribution upon the aqueous copper concentration, thereby confirming the monomeric nature of the extracted complex (j=1, α_{Cu}=1).

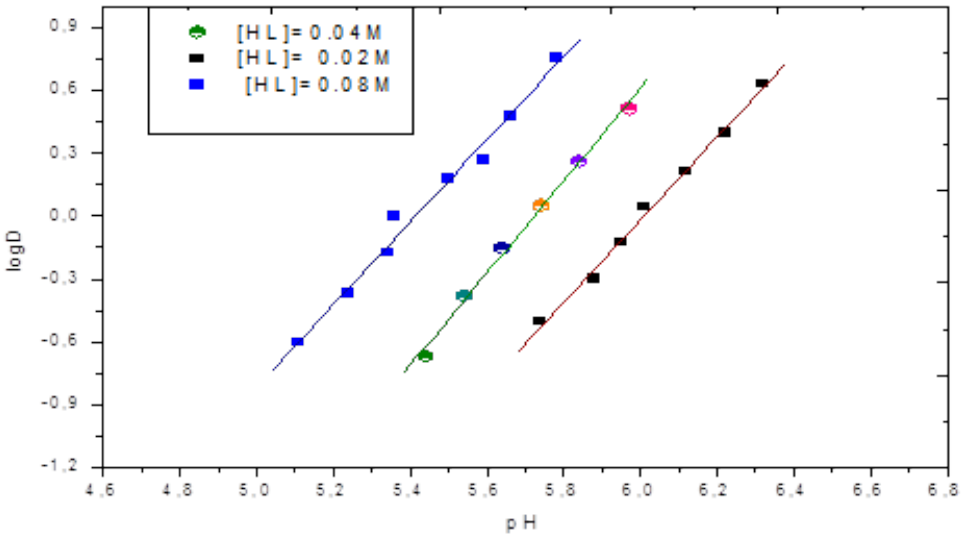

Figure 1. Extraction of copper (II) with decanoic acid.

$$Cu^{2+} + \frac{2+p}{2}(HL)_{2org} <=> CuL_2(HL)_{p\,org} + 2H^+ \quad \textbf{(6)}$$

Under the present experimental conditions, the concentration of metal in organic phase is negligible when compared to the concentration of extractant, therefore, concentration of the dimer was calculated as $[(HL)_2] = [HL] / 2$. According to equation (4), the number of capric acid molecules involved in the monomeric species can be determined from the slope of the plots of (log D) against $\log[(HL)_2]_{org}$ at constant pH. The plots of log D versus log $[(HL)_2]_{org}$ at constant pH values were also linear with a slope of (2+p) / 2 = 2, *i.e.*, p = 2, as shown in Figure 2. This suggests that two molecules of dimeric decanoic acid take part on the extraction of one ion of copper. This means that only the complex $CuL_2(HL)_2$ is extracted into chloroform [18].

The same type of extracted species was reported for the extraction of copper(II) with cyclopentylacetic acid [4] and α-bromostearic acid [5] in benzene. The complex formed has a structure of an adduct, in which particular places in the coordination sphere of copper ion is occupied in total by four molecules of the extractant.

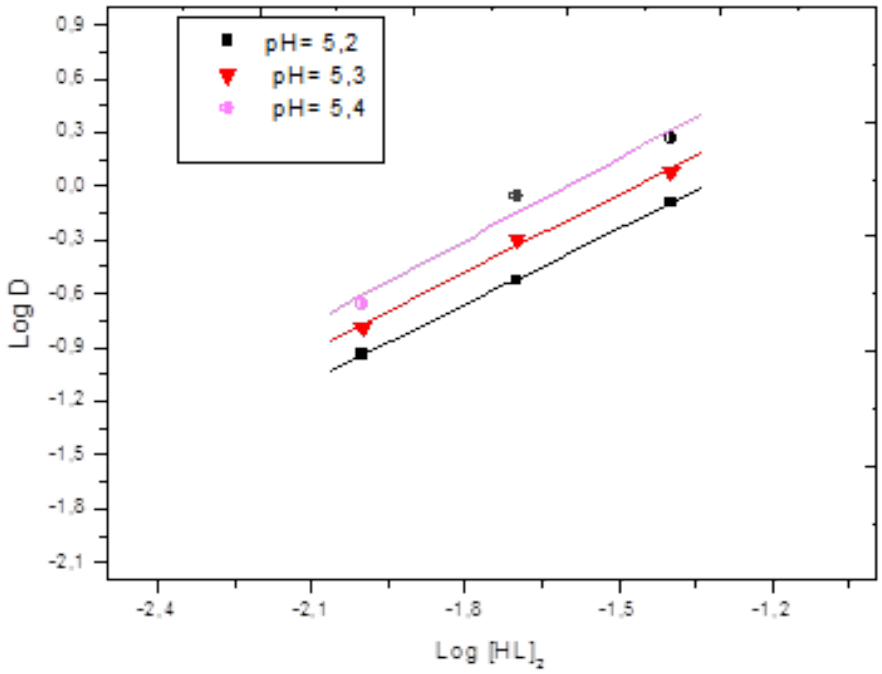

Figure 2. Effect of pH on the extraction of copper(II) with decanoic acid in chloroform.

The logarithmic value of K_{ex} of copper(II) can, therefore, be calculated for each experimental point ($\log K_{ex}$=-7.2).

Preparation of the complex

The organic solution of copper(II) carboxylate was prepared by solvent extraction from an aqueous $CuSO_4.5H_2O$ solution. During the extraction operation, the aqueous solution pH was adjusted at around pH 7 by the addition of dilute by a hydroxide solution. The initial concentration of copper(II) was 0.02 M. The initial concentration of free decanoic acid in the organic phase was 0.1 M. The single-metal carboxyl at solutions were washed with distilled water to remove residual anions and then passed through glass fiber paper and phase separating paper to remove physically entrained water. The precipitates were characterized by X-ray diffraction (XRD) analyses.

Microanalysis of complex copper(II) decanoate (EDX)

Electron microscopy (SEM) coupled with energy dispersive spectrometer microanalysis (EDX) is used in the chemical composition was also performed. Figure 3 is the composition of the different complex.

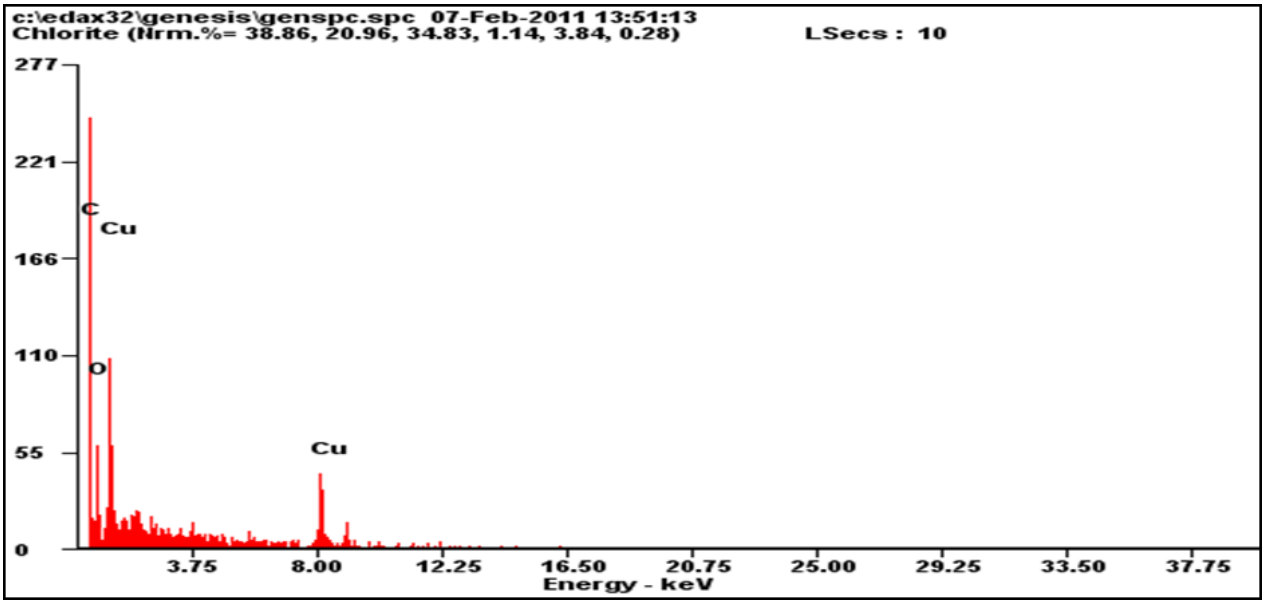

Figure 3. EDX pattern of copper (II) decanoate complex.

The contents of C, O, Cu(II) were determined by elemental analysis as shown in Table 1 [6].

Table 1. The analytical data of complex copper decanoate at 25 °C.

Element	Wt %	At %
L = $C_{10}H_{19}O$		
C K	4.70	20.46
O K	0.46	1.49
Cu K	94.84	78.04

X-Ray Diffraction

The measurement of lattice parameters of the powders was carried out using a Bruker D8 model type diffractometer with copper anticathode λ_{Cuak} = 1,54 Å. The recording condition and 0.04 ° / 5 s to 2θ taken between 10° and 90° is shown in Figure 4. The crystallographic data for the complex and oxide of copper are listed in Table 2.

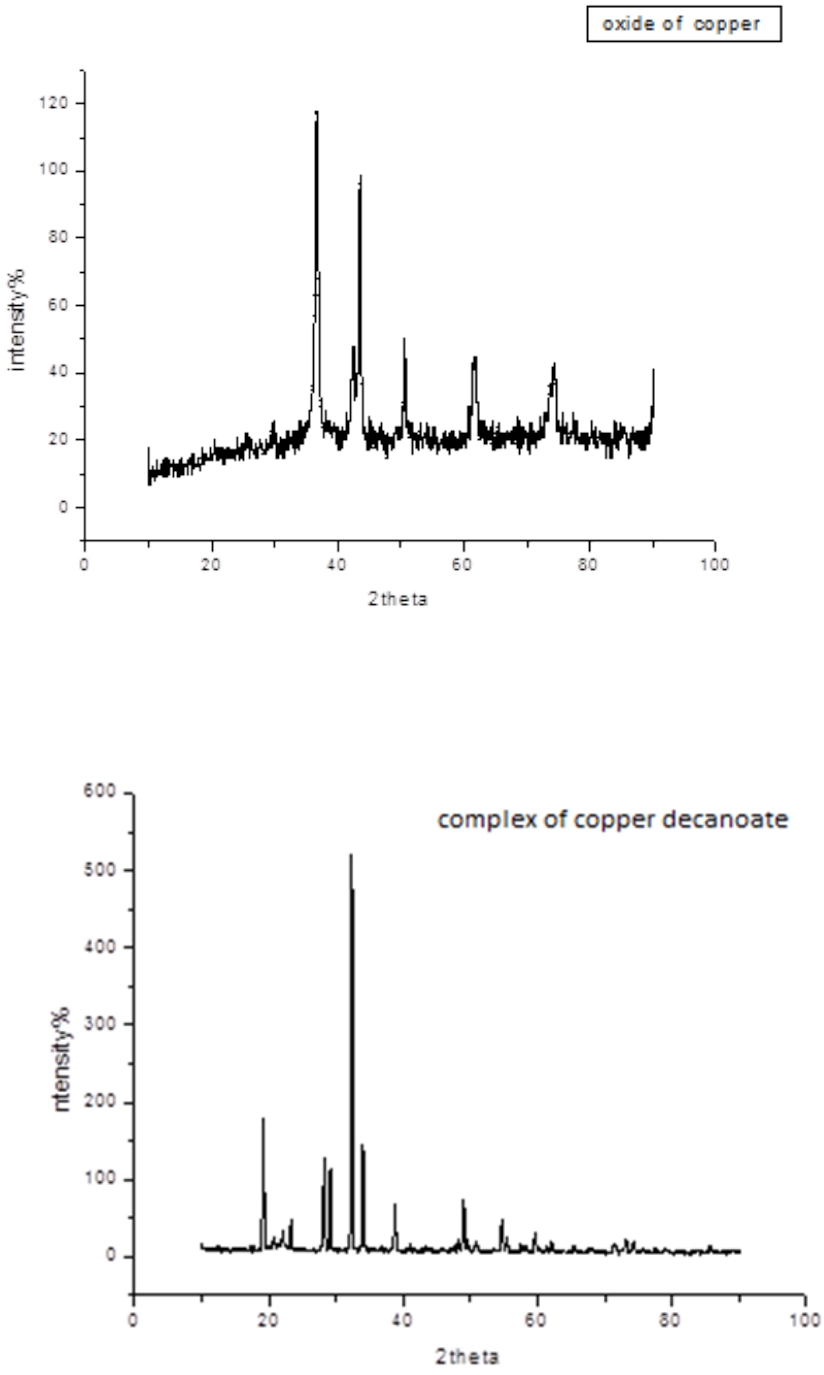

Figure 4. XRD patterns of complex copper(II) decanoate (top) and oxide of copper (bottom).

Table 2. Data of structure copper decanoate complex.

	Copper(II) decanoate complex	**Cu_2O**
Crystal system	monoclinic	Cubic
Space group	$P2_1/N$	PN3M
a (Å)	11.24	4.2494
b (Å)	4.68	4.2494
c (Å)	10.24	4.2494
α (°)	90	90
β (°)	92	90
γ (°)	90	90
V (A^3 °)	538	76.732
(h, k, l)	2≤h≤4 ,0≤K≤2 , 1≤h≤4	0≤h≤2 ,0≤K≤2 , 1≤h≤3

Molar conductivity measurements

Molar conductance value of the complex copper decanoate is found to be in the range 20.1-21.7 S. $cm^2.mol^{-1}$ in a dimethyl formamide (DMF) solution which proposes a non-electrolytic nature [7].

UV- Visible Spectra

The electronic absorption spectra of complexes were recorded in the range from 1200 to 400 nm at room temperature. The electronic absorption spectra are often very useful in the evaluation of results from other structural survey methods. Electronic spectral measurements were used to assign the stereochemistry of the metal ion in the complex based on the positions and the number of d-d transition peaks. Complexes' electronic absorption spectra were recorded in the range of 1100-400 nm, at room temperature. The electronic spectrum of the solid state of copper(II) has complex characteristics of Cu^{2+} ion octahedral environment of the strip is in the ranges from 690 to 680 [8, 9]. These transitions are characteristics of octahedral geometry of the metal atoms [10,11].

Infrared spectra

Fourier Transform Infrared spectra of the ligand and complex were recorded on Perkin Elmer Spectrometer Model -UMCAM FT.IR- 8400s using KBr pellets. The studied wavelength range from 4000 - 400 cm^{-1}, corresponds to the mid-infrared region. The infrared spectrum of the ligand shows a band at 3411 cm^{-1} can be attributed to the OH group. This band is absent in copper complex's spectrum and there is a strong C = O band at 1710 cm^{-1}, the bands were allocated to the asymmetric and symmetric vibrations of OCH_3 groups occurring at 2920 and 2849 cm^{-1}, respectively (Figure. 5). In the FTIR spectra of copper decanoate, the band at 1711 cm^{-1} disappears, which indicates that C=O group is not present in the analyzed complex [14].

Absorptions in the range of 1688-1678 and 1394-1352 cm^{-1} correspond to asymmetric and symmetric $v(COO^-)$ frequency bound to metal carboxylate. The great difference in frequency $\Delta v(COO^-)$ ($\Delta v > 200$ cm^{-1}) is indicative of monodentate coordination via both carboxylate groups [11, 12]. The copper complex shows strong bands in the region of 3420 and 3450 cm^{-1} range assignable to v(O-H) stretching vibrations of coordinated water molecules [7, 14]. The small bands of copper(II) to 478 cm^{-1} result from vibration v(M-O) expansion.

Analyses by thermogravimetric and differential A.T.G - A.T.D) precursor

In order to estimate beforehand calcination temperature for obtaining a well-crystallized oxide, the complex precursor was analyzed by thermogravimetric (T.G.A.) and differential temperature analysis (D.T.A.) respectively. On a Linseis 1600 type apparatus, a stream of air and in a temperature range of from ambient temperature to a temperature of 500 °C, using a heating rate of 10 °C / min was analyzed for our sample. The result for the composed precursor developed in ethanol as the solvent is represented in Figure 5. The thermal data of the complex are listed in Table 3. The composition of the intermediates and final products are those which best fit with the mass loss observed in the TG studies. Thermogravimetric results are in good agreement with the corresponding DTA data. The curves TG / DTA suggest the presence of $[CuL_2(HL)_2.2H_2O]$ complex. The weight loss observed between 20 and 200 °C, corresponding with an endothermic peak at 100 °C is due to dehydration with a loss of two molecules of water (3.3%). The thermal decomposition is produced in two stages between 200-500 °C and may be observed that three exotherms and endotherm to two (300, 340 and 420 °C), respectively. The final residue, found to be Cu_2O, had an observed mass of 89.9% [11, 19].

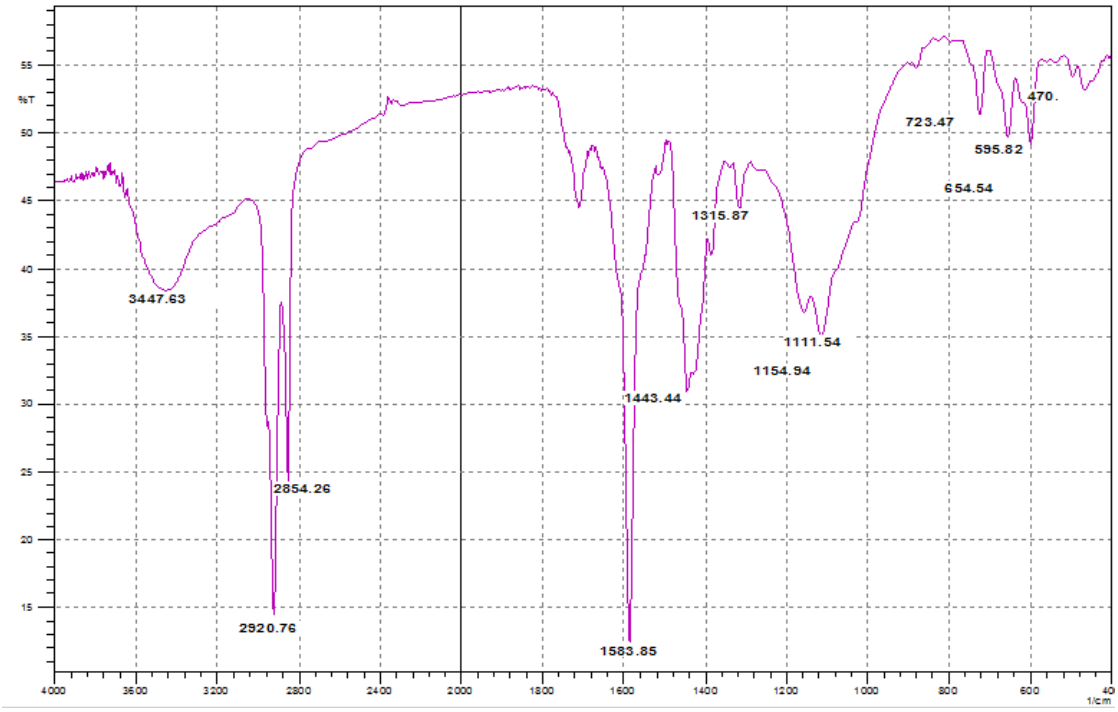

Figure 5. The infrared spectrum of copper decanoate complex.

Table 3. Thermal decomposition data of copper(II) complex with decanoic acid.

Complexes	T/°C	Mass loss / %	DTA / °C	intermediate product	color of the solid
$[Cu(L2)(HL)_2].2H_2O$	20-200	3.3	100	$Cu(L_2)HL_2$	blue
	200-500	89.9	exo / 420, 340, 300	Cu_2O	black

Particle size analysis

The particle size distribution depends on the diameter of the grains. They were chosen in order to show the influence of the complex on the particle size, made by laser granulometric method, showing the existence of two populations of medium sized complex copper decanoate, shown in Figure 6, representing a distribution of grain size in a range of sizes between 0.02 and 2000 µm (the first population of volume distribution of 2.83% and grain size 316.979 µm and second population is the volume of distribution of 3 to 84% and of size grains is 502.377178 µm. The main characteristics that can be extracted from analysis of the particle size complex are summarized in Table 4.

Table 4. Analysis of complex copper decanoate size distributions.

Average complex volume (µm)	d (0.1 µm)	d (0.5 µm)	d (0.9 µm)
$[Cu(HL)_2L_2].2H_2O$ 230.134	6.465	77.891	168.468

Conclusion

Thus on the basis of above mentioned studies, it is proposed that the ligand is decanoic acid. The geometry of copper decanoate complex is proposed to be octahedral on nature as given of structure present (see Scheme 1).

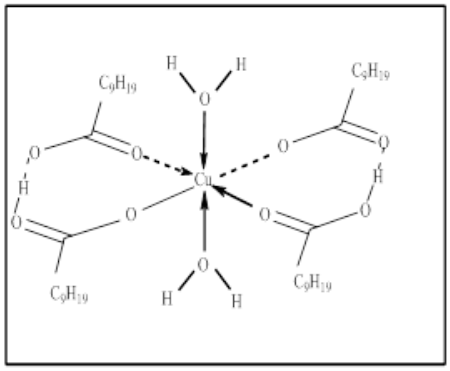

Scheme 1. Structure of the copper decanoate complex.

REFERENCES

[1] Ensafi A. Simultaneous determination of trace amounts of cadmium, nickel and cobalt in water samples by adsorptive voltammetry using ammonium 2-amino-cyclopentene dithiocarboxylate as a chelating agent. Talanta. 2000 Jun 30;52(3):435–40. DOI: 10.1016/S0039-9140(00)00334-9.

[2] W.Lauo, Y. Hos, J Anal Chem Acta. 280: 893,(1993).

[3] Yamada H, Tanaka M. Solvent effects on extraction of copper with capric acid. Journal of Inorganic and Nuclear Chemistry. 1976 Jan;38(8):1501–4. DOI: 10.1016/0022-1902(76)90016-6.

[4] Aidi A, Barkat D. Solvent extraction of copper(II) from sulfate medium with N -(2-hydroxybenzylidene)aniline. Journal of Coordination Chemistry. 2010 Dec 10;63(23):4136–44. DOI: 10.1080/00958972.2010.530662.

[5] Bold L, Bluescu A Rev Roum Chim 23: 1631 (1978).

[6] 1. Hou H, Wei Y, Song Y, Mi L, Tang M, Li L, et al. Metal Ions Play Different Roles in the Third-Order Nonlinear Optical Properties of d10 Metal-Organic Clusters. Angewandte Chemie International Edition. 2005 Sep 19;44(37):6067–74.

[7] Rigin V. Simultaneous atomic fluorescence spectrometric determination of traces of iron, cobalt and nickel after conversion to their carbonyls and gas-phase atomization by microwave-induced plasma. Analytica Chimica Acta. 1993 Nov;283(2):895–901. DOI: 10.1016/0003-2670(93)85303-2.

[8] Geary WJ. The use of conductivity measurements in organic solvents for the characterisation of coordination compounds. Coordination Chemistry Reviews. 1971 Oct;7(1):81–122. DOI: 10.1016/S0010-8545(00)80009-0.

[9] Kumar G, Kumar A, Shishodia N, Garg YP, Yadav BP. Synthesis, Spectral Characterization and Antimicrobial Evaluation of Schiff Base Cu(II), Ni(II) and Co(II) Novel Macrocyclic Complexes. E-Journal of Chemistry. 2011;8(4):1872–80. DOI: 10.1155/2011/497279.

[10] Kurdekar GS, Sathisha MP, Budagumpi S, Kulkarni NV, Revankar VK, Suresh DK. 4-Aminoantipyrine-based Schiff-base transition metal complexes as potent anticonvulsant agents. Medicinal Chemistry Research. 2012 Sep;21(9):2273–9. DOI: 10.1007/s00044-011-9749-3.

[11] Lever ABP. Inorganic electronic spectroscopy. 2nd ed. Amsterdam ; New York: Elsevier; 1984. 863 p. (Studies in physical and theoretical chemistry). ISBN: 978-0-444-42389-4.

[12] Olmez H, Arslan F, Icbudak H. Spectrothermal studies on Co(II), Ni(II), Cu(II) and Zn(II) salicylato (1,10-phenanthroline) complexes. Journal of Thermal Analysis and Calorimetry. 2004;76(3):793–800. DOI: 10.1023/B:JTAN.0000032264.74742.27.

[13] Konstantinović S, Radovanović B, Krkljes A. Thermal Behaviour of Co(II), Ni(II), Cu(II), Zn(II), Hg(II) and Pd(II) complexes with isatin-β-thiosemicarbazone. J Therm Anal Calorimet. 2007;90(2):525–31.

[14] Kumar G, Kumar A, Shishodia N, Garg YP, Yadav BP. Synthesis, Spectral Characterization and Antimicrobial Evaluation of Schiff Base Cu(II), Ni(II) and Co(II) Novel Macrocyclic Complexes. E-Journal of Chemistry. 2011;8(4):1872–80. DOI: 10.1155/2011/497279.

[15] Premkumar T, Govindarajan S. Divalent transition metal complexes of 3,5-pyrazoledicarboxylate. Journal of Thermal Analysis and Calorimetry. 2006 May;84(2):395–9. DOI: 10.1007/s10973-005-6932-0.

[16] Lever ABP. Inorganic Electronic Spectroscopy. Amsterdam: Elsevier; 1968. ISBN: 978-0-444-40675-0.

[17] Nakamoto K. Infrared and Raman spectra of inorganic and coordination compounds. 3d ed. New York: Wiley; 1978. 448 p. ISBN: 978-0-471-62979-5.

[18] Adjel F, Barkat D. Synergistic extraction of copper(II) from sulfate medium with capric acid and tri- n -octylphosphine oxide in chloroform. Journal of Coordination Chemistry. 2011 Feb 20;64(4):574–82. DOI: 10.1080/00958972.2010.551400.

[19] Rozyckia C. Chemical Analysis (Warsaw) 26: 37 (1981).

BAKIR(II) DEKANOAT KOMPLEKSİNİN EKSTRAKSİYONU VE SPEKTROTERMAL ÇALIŞMALARI

Öz: Bakır(II) iyonunun 0,33 M Na_2SO_4 sulu çözeltilerinden dekanoik asit (HL) ile kloroform içinde ve 25 °C'de ekstraksiyonu çalışılmıştır. Dekanoik asit tek başına kullanıldığı zaman ekstrakte olan tür $CuL_2.2(HL).2H_2O$'dur. Bakır kompleksi sentezlenmiş ve elementel analiz, kızılötesi spektrumları, elektronik spektrumlar, X-ışını saçılması (XRD), laser parçacık boyutu analizi ve molar iletkenlik ölçümleri ile karakterize edilmiştir.

Anahtar kelimeler: Dekanoik asit, metal karboksilat, ekstraksiyon sıvısı, yapısal çalışma.
Gönderilme 09 Ağustos 2015. **Düzenleme:** 06 Kasım 2015. **Kabul:** 17 Nisan 2016.

JOTCSA, Volume 3, issue 1, (2016), pp. 131-146.

Research article

Journal homepage: http://dergipark.ulakbim.gov.tr/jotcsa

e-ISSN: 2149-0120

Synthesis, Characterization, and Antioxidant Activity of Fe(III)-Valex Complex

Pelin Erdem[1], Sevcan Altaş[2], Sevil Emen Tanrıkut[2], Murat Kızıl[2], Mürüvvet Yurdakoc*[3]

[1]Dokuz Eylül University, Graduate School of Natural and Applied Sciences, Department of Chemistry, 35160 İzmir-Turkey.
[2]Dicle University, Faculty of Sciences, Department of Chemistry, 21280 Diyarbakır-Turkey.
[3]Dokuz Eylül University, Faculty of Sciences, Department of Chemistry, 35160 İzmir-Turkey.

Abstract: Valonia oak (*Quercus ithaburensis sp. macrolepis*), a fruit of Valonia, which is naturally and widely grown in the western Anatolian region in Turkey, is rich in tannin. They include hydrolyzable tannins used in many areas called Valex. Iron(III) complex with Valex was synthesized and characterized using various techniques. Stoichiometry of the complex was determined to be M_2L at pH 4.4 with the stability constant (K) of 1.5 x 10^8 L^2mol^{-2}. The antioxidant, antimicrobial, and antifungal activity of the Fe(III)-Valex complex was studied. The anti-oxidant activity of Fe(III)-Valex complex was determined based on the 2,2-diphenyl-1-picrylhydrazyl (DPPH) radical scavenging activity and butylated hydroxyanisole (BHA) and butylated hydroxytoluene (BHT). The antimicrobial activity of the complex was also determined by the disc diffusion test for five different bacterial cultures and one fungus. The Fe(III)-Valex complex was found to have antioxidant activity but did not show any antimicrobial and antifungal activity against the tested microorganisms.

Keywords: Valex, tannin; iron complex; antioxidant activity.
Submitted: March 16, 2016. **Revised:** April 04, 2016. **Accepted:** May 25, 2016.

Cite this: Erdem P, Altaş S, Emen Tanrıkut S, Kızıl M, Yurdakoç M. Synthesis, Characterization, and Antioxidant Activity of Fe(III)-Valex Complex. Journal of the Turkish Chemical Society, Section A: Chemistry. 2016 May;3(2):131–146.

DOI: http://dx.doi.org/10.18596/jotcsa.77778.
Correspondence to: Mürüvvet Yurdakoç. E-mail: m.yurdakoc@deu.edu.tr. **Tel:** +90 232 3018697; **fax:** +90 232 4534188.

INTRODUCTION

In our diets, tannins are other mixtures of biodegradable polyphenolic compounds. Tannins are a large part of the plant kingdom, containing the natural products. Tannins are complex mixtures of polyphenolic compounds and extracted from plants like chestnut, valonia oak, *etc*. They constitute a much diversified group of plant secondary metabolites in terms of structural, physicochemical, and biological properties. Tannins have also been described as oligomeric compounds with multiple structure units with free phenolic groups. Generally, tannins are classified into two broad groups; the hydrolyzable and condensed tannins [1]. Tannins are cyclic structures and have hydroxyl groups (-OH); this allows complex formation with metals such as thorium (IV) [2], uranium [3], hexavalent chromium [4], cadmium, mercury [5], copper [6-8], gold [9, 10], silver, palladium [11], lead [12, 13], vanadium(III) [14] and iron [15-18]. Also many biological activities, antioxidant and antimicrobial activities have been reported for plant tannins [19, 20], and current articles about tannins are still being published. Antioxidant properties of tannins are due to their free radical scavenging activity [21-23], but their ability to chelate transition metal ions also plays an important role. DPPH radical scavenging activity is a rapid, simple, and inexpensive method for determining antioxidant activity in an indirect manner. Antimicrobial activity of plant phenolics had been studied and the controlling invasion and growth of plant pathogens, their activity against human pathogens has been investigated to characterize and develop new healthy food ingredients, medical compounds and pharmaceuticals [19, 24].

Valonia oak fruit of Valonia (Quercus ithaburensis sp. macrolepis), being naturally and widely grown in the western Anatolian region of Turkey, is rich in tannin. They include hydrolyzable tannins used in many areas (in leather trade, pharmacy, painting and electrostatic spray painting *etc*.) known as Valex.

In this work, the Fe(III)-Valex complex was synthesized and its structure has been characterized by magnetic susceptibility, FT-IR, TGA, XRD, ESR and XPS analysis methods. The stoichiometry and stability constant (K) of the complex were determined. Its antioxidant antimicrobial and antifungal properties were examined with Valex.

EXPERIMENTAL

Materials

Valex was obtained from the Balaban Company from Salihli/Manisa-Turkey. The content of Valex was determined by the Filder method and it was found to contain the following: tannins, 68-70%; non-tannins, 25%; undissolved materials, 1.10-1.15%; moisture: 4.05-5.50% [25]. Both iron(III) chloride hexahydrate (Merck 103943) and Valex were prepared in acetic acid (Merck 100063) / sodium acetate trihydrate (Merck 106265) buffer solution for the Fe(III)-Valex complex. All the other chemicals used in this study were of analytical grade. Working solutions were freshly prepared from the stock solutions.

Synthesis of Fe(III)-Valex Complex (Stoichiometry and Stability Constant)

The calculated concentrations of Valex and Fe(III) solutions were mixed to form the complex. Valex powder (2.4 mg) corresponding to tannin powder (1,7 mg or $1x10^{-6}$ mol of tannin) and Fe(III) (10^{-3} M) solutions were prepared with acetate buffer (0.2 M acetic acid / 0.2 M sodium acetate) of pH 3.6, 4.4, 5.0 and 5.6. The pH range from 3.6 to 5.6 was selected, because at a lower pH, iron is in the Fe(II) form and at higher pH the precipitation of $Fe(OH)_3$ occurs. A mixture of equal amounts of these solutions has enabled the formation of the complex. The mixture was stirred mechanically at room temperature for one day. The formed precipitate was separated from the supernatant phase. The precipitate was washed with distilled water, dried under vacuum, and recrystallized from acetone before characterization. The melting point of Fe(III)-Valex complex was determined as 261 °C by using a melting point apparatus. After selecting the optimum pH value (pH=4.4) for the complexation, Valex and Fe(III)-Valex absorption spectra were recorded between 200-800 nm to determine the λ_{max}. The stoichiometry of the Fe(III)-Valex complex was determined by Slope Ratio method. Two series of experiments were prepared for the application of this method. In the first experiment, the Valex concentration was kept constant (2×10^{-3} mol dm^{-3}) while the Fe(III) concentration was increased over (0.6-3.0) $\times 10^{-4}$ mol dm^{-3} range in a regular way. In the second experiment, the Fe(III) concentration was kept constant (2×10^{-3} mol dm^{-3}) while the Valex concentration was increased over (0.6-3.0) $\times 10^{-4}$ mol dm^{-3} range in a regular way. The absorbances of the solutions were plotted against the concentration of the metal or ligand component. The obtained lines have different slope values. The first and second experiment slope values were equal to molar absorptivity constants of metal (ε_M) and ligand (ε_L), respectively. The ratio of the Fe(III) to Valex (Metal/Ligand) was calculated from the ratio of the molar absorptivity constants ($\varepsilon_M/\varepsilon_L$).

The stability constant of the complex was calculated according to the Equation 1 [18]:

$$2M + L \dashrightarrow M_2L,\ K_2 = [M_2L] / [M]^2 [L] \quad \textbf{(1)}$$

The characterization of complex was performed after the determination of the stoichiometry and stability constants of Fe(III)-Valex Complex.

Characterization Techniques

All spectrophotometric measurements were performed with a Shimadzu 1601 UV-Vis spectrophotometer. The pH was measured with a Denver 215 model pH meter and a Heidolph MR standard magnetic stirrer was used during the experiments.

FT-IR analyses of Valex and Fe(III)-Valex complex were performed with Perkin–Elmer Spectrum BX-II Model FT-IR spectrophotometer. FT-IR spectra of the samples as KBr pellets were recorded in the range of 4000 and 400 cm^{-1}, at a resolution of 4 cm^{-1} and an average of 50 scans.

Thermogravimetric analyses (TGA) of the samples were carried out with a Perkin Elmer Diamond TG/DTA Analyzer. The analyses were made in platinum pans under a dynamic nitrogen atmosphere in temperature range of 50-1000 °C at a heating rate of 10 °C min^{-1}.

The X-ray diffraction patterns (XRD) of the samples were recorded with oriented mounts, in a Philips X'Pert Pro X-Ray diffractometer using Cu Kα radiation at 45 kV and 40 mA in the 2θ range of 2-60°.

The Electron Spin Resonance (ESR) spectra was measured using a Bruker ELEXSYS E580 model spectrometer for the Fe(III)-Valex complex under the conditions of microwave frequency, 9.86 GHz; field amplitude, 100 mT; modulation frequency of 100 kHz, microwave power 5 mW, and the time constant, 0.01 s.

Magnetic Susceptibility measurement was carried out with Balance Sherwood Scientific. The complex magnetic susceptibility measurements were carried out at 293K and it was calculated by the following Eq. (2). In Equation 2, μ is the magnetic moment, X_M is the molecular weight of complex and T is the temperature (K).

$$\mu = 2.84 (X_M T)^{1/2} \quad \textbf{(2)}$$

X-ray photoelectron spectroscopy (XPS) analysis methods were performed by using non-monochromated Thermo Scientific K-ALPHA radiation and they were acquired with analyzer pass energy of 150 eV.

The melting point of Fe(III)-Valex complex was measured by using a digital melting point apparatus BI 9100 Barnstead/Electrothermal.

In vitro antioxidant activity of the Valex and Fe(III)-Valex complex

The antioxidant property of the Fe(III)-Valex complex was compared with Valex. The free radical scavenging activities of Valex and Fe(III)-Valex complex were determined by using DPPH (Aldrich D9132) method [26]. BHA (Sigma B1253) and BHT (Sigma B1378) were used as controls. All samples were reacted directly and quenched with DPPH radicals to different degrees with increased activities in a concentration-dependent manner. In the DPPH assay, 50 μL samples (5-50 μg/mL) were mixed with 50 μL of 500 μM DPPH in ethanol (Sigma-Aldrich 32221) and kept in the dark for 40 minutes. The absorbances of the mixtures were measured at 492 nm. The DPPH radical scavenging activity was determined based on percentage inhibition of absorbance, which was calculated using the following Eq. (3):

$$\text{DPPH radical scavenging activity (\%)} = [(A_0-A_1) / A_0) \times 100] \quad \textbf{(3)}$$

In Equation 3, A_0 is the absorbance of the control reaction and A_1 is the absorbance in the presence of the samples.

Antimicrobial and Antifungal Activities of the Valex and Fe(III)-Valex complex

Antimicrobial activity of samples was assayed by the disc diffusion susceptibility test according to the recommendation of the NCCLS methods [27]. Mueller Hinton Agar was used in the antimicrobial susceptibility testing by the Disc diffusion test. *Escherichia coli* [ATCC 25922], *Staphylococcus aureus* [ATCC 25923], *Streptococcus pyogenes* [ATCC 19615], *Pseudomonas aeruginosa* [ATCC 27853], *Bacillus subtilis* [ATCC 11774] were used as the bacteria and *Candida albicans* [ATCC 10231] was used as a fungus. Standard discs of amoxicillin / clavulanic acid (30 µg/disc), ofloxacin (5 µg/disc), netilmycin (30 µg/disc), erythromycin (15 µg/disc) and amphotericin B (30 µg/disc) were individually used as positive controls.

RESULTS AND DISCUSSION

Characterization of Fe(III)-Valex Complex UV analysis (Stoichiometry and Stability Constant)

The experiments were carried out in the range of acetate buffers of pH 3.6, 4.4, 5.0, and 5.6. The UV-Vis spectra were presented in Figure 1. As can be seen from Figure 1, the pH=4.4 was selected as the optimum pH for the complexation. All other experiments were performed with this buffer. UV-Vis spectra of 10^{-4} mol dm^{-3} Valex and 10^{-3} mol dm^{-3} Fe(III)-10^{-4} mol dm^{-3} Valex dark violet complex at pH=4.4 were shown in Figure 2. The peak at 221 nm and a shoulder at 252 nm were observed in the absorption spectra of Valex. These peaks assigned for π-π* transitions which was due to aromatic units and C=O groups in UV region (200-400 nm) [28]. In the absorption spectra of Fe(III)-Valex complex, two absorbance peaks were observed at 221 and 575 nm. The shoulder of Valex at 252 nm shifted to 273 nm due to the formation of Fe(III)-Valex complex. New absorbance peak observed at 575 nm was assigned to the complex peak in the visible range [29]. This may be assigned to the ligand-to-metal charge transfers energy (LMCT) between Fe(III) and Valex [30].

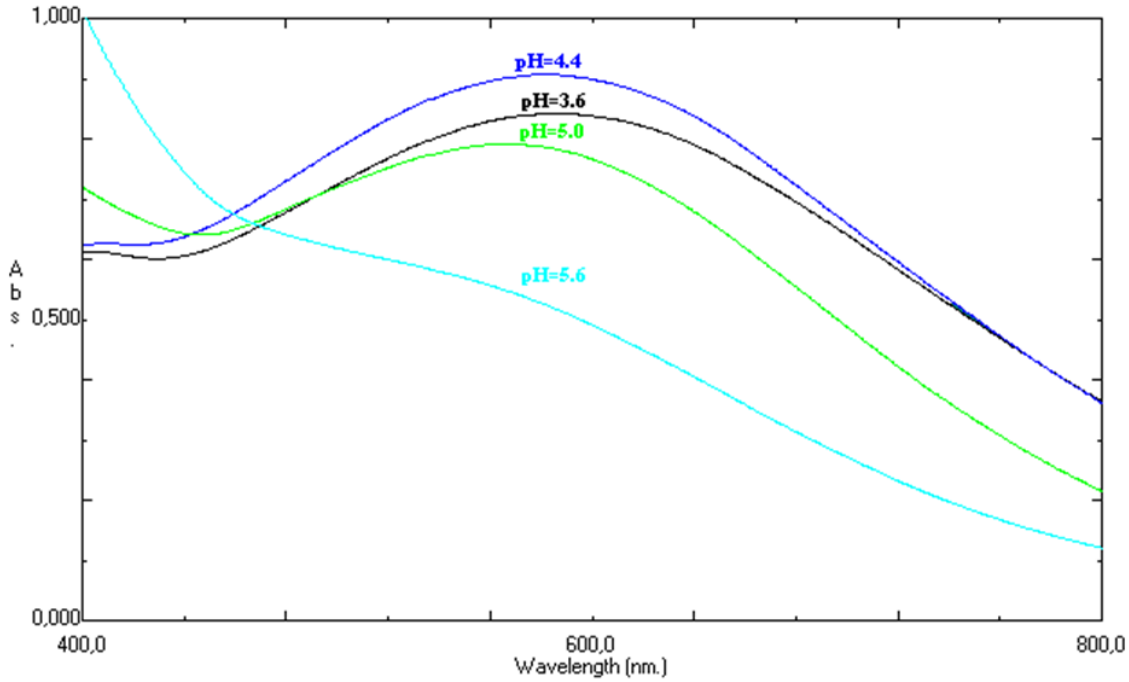

Figure 1: UV-Vis. spectra of Fe(III)-Valex at different pH of acetate buffer.

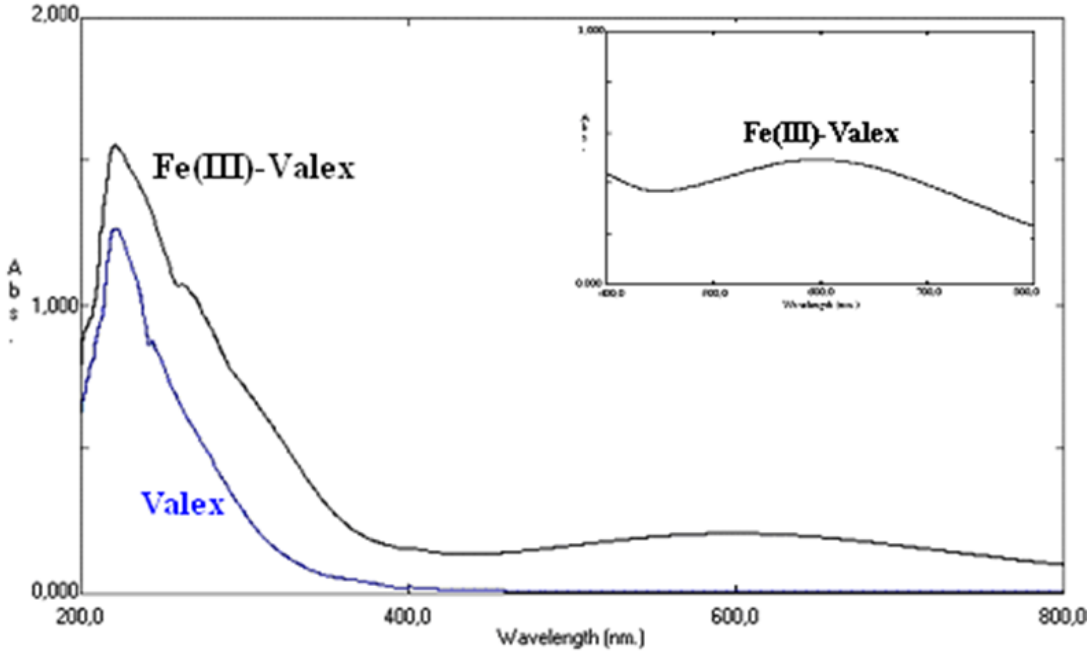

Figure 2: UV-Visible spectra of Fe(III)-Valex at optimum pH=4.4.

For the stoichiometry of Fe(III)-Valex complex, the slope ratio method was used at pH=4.4 and molar absorptivity constants of Fe(III) (ε_M=2110) and Valex (ε_L=1170) were obtained from the two series of experiments at λ_{max}= 575 nm. The ratio of the molar absorptivity constants of the Fe(III) and Valex was calculated as εM/εL=1.8 (≈2). The results obtained using slope ratio method indicates that the stoichiometry of Fe(III)-Valex complex is 2:1 ratio. An interaction between Valex and Fe(III) is important to understand the metal-ligand behavior. The M/L ratio or pH could be changed significantly the coordinated species in the solution [31-33].

Stability constant (K) of Fe(III)-Valex complex was calculated as 1.5 x 10^8 L^2 mol^{-2} at pH=4.4 (λ_{max}= 575 nm). This high stability constant reflected that Valex had very high affinity to the Fe(III), so they form a highly stable complex.

FTIR analysis

The FTIR spectra of Valex and Fe(III)-Valex were shown in Figure 3. In all spectra, the wide bands in the region of 3600–3000 cm^{-1} were due to the -OH stretchings. The characteristic phenolic -OH groups were intensively presented within the nature of Valex. A weak band was observed at the 2929 cm^{-1} due to aliphatic C-H stretching vibrations of Valex [34]. The band at 1736 cm^{-1} in the spectrum of Valex was related to carboxyl–carbonyl groups. The absorption band at 1607 cm^{-1} was due to aromatic -C=C- bonds and the band at 1448 cm^{-1} was due to C-C deformation vibrations in the phenolic groups. The bands at 1332 cm^{-1} and 1043 cm^{-1} in the spectrum of Valex were attributed to phenol groups. The aromatic C-H deformation bands were observed at 1186 cm^{-1}. The deformation vibrations of the C-H bonds in the benzene rings also gave weak absorption bands between the ranges of 900–550 cm^{-1}.

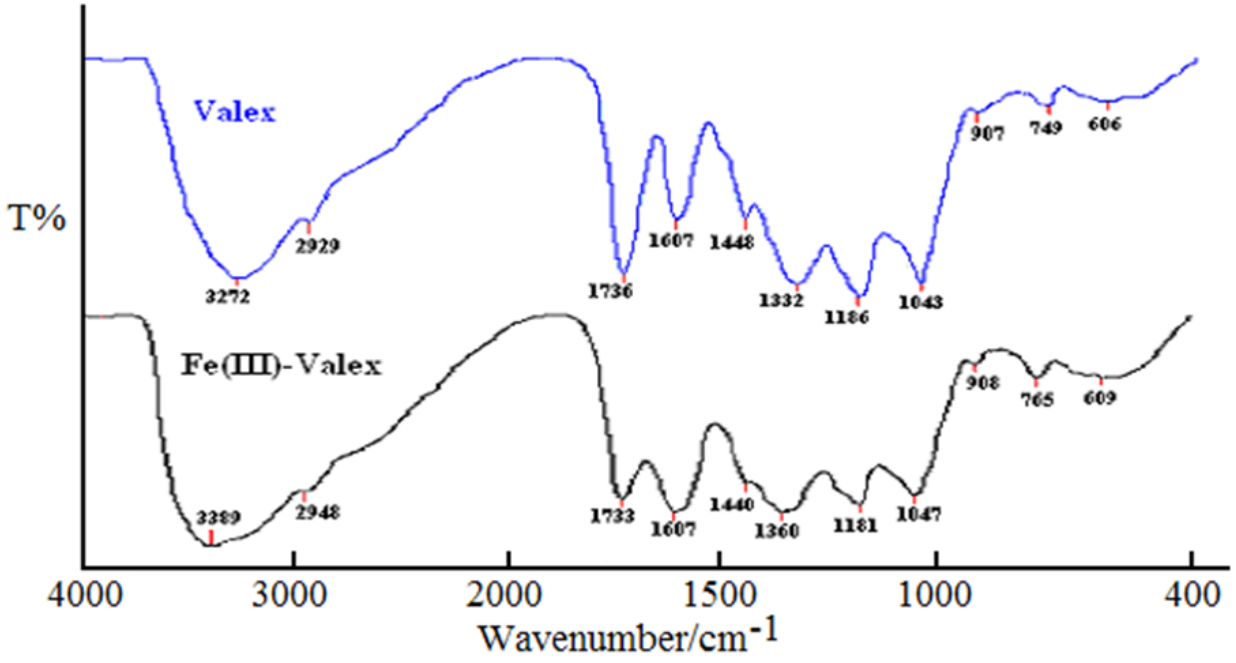

Figure 3: FTIR spectra of Valex and Fe(III)-Valex.

When the spectrum of Valex was compared with the spectrum of the Fe(III)-Valex complex, similar but some distinctive features were observed by the formation of the complex. Several bands were not only shifted slightly, but also reduced in intensity because of complex formation between metal ions and phenolic groups of Valex [35]. The broad band at 3272 cm^{-1} in Valex spectrum was shifted to 3389 cm^{-1} and the shape of this wide band was changed in the Fe(III)-Valex complex spectrum. The weak band at 2929 cm^{-1} was shifted to higher frequencies. The relative intensities of the bands of Fe(III)-Valex complex between 1750 and 1000 cm^{-1} region were shifted and remarkable changes were observed in the shapes of these bands. The intensities of the bands at 1736 cm^{-1} and 1607 cm^{-1} which were related to carboxylic acid group (-C=O) and -C=C- vibrations were reduced and the band at 1736 cm^{-1} was shifted to 1733 cm^{-1}. The -OH bending band at 1448 cm^{-1} became imperceptible in the Fe(III)-Valex complex spectrum. This can be a consequence of the formation of the Fe(III)-Valex complex involving the chelation with the hydroxyl groups. The bands at 1332, 1186, 1043 cm^{-1} were respectively shifted to 1360, 1181 and 1047 cm^{-1} and the intensities of these bands were reduced as compared within the Fe(III)-Valex complex spectrum. The Fe-O stretching vibrations were located in the region of 700-400 cm^{-1} [36, 37]. In the spectrum of Fe(III)-Valex, a very broad band at 609 cm^{-1} and the band at 765 cm^{-1} may be attributed for Fe-O stretching vibrations. However, significant changes in the band intensities were observed in the range of 1750 and 1000 cm^{-1} region on Fe(III)-Valex complex spectrum by the complexation of Fe(III) with the Valex.

TGA analysis

The TGA thermograms of Valex and Fe(III)-Valex complex were presented in Table 1. The TGA profiles of Valex and Fe(III)-Valex complex showed three steps, and four steps were shown for thermal decomposition, respectively. The first step of mass losses could be attributed to evaporation of adsorbed water and the other steps were due to thermal decompositions of the samples. Evaporation of adsorbed water was carried out approximately at 83°C with 5% and 4% for Valex and Fe(III)-Valex complex, respectively. The second step of Valex and Fe(III)-Valex complex occurred at approximately 270°C with a mass loss of 31% for Valex and 35% for Fe(III)-Valex complex. This corresponded to decarboxylation or may be attributed to partial decomposition of Valex and Fe(III)-Valex complex [38]. In the decomposition temperature range of 400-800°C, Valex and Fe(III)-Valex complex decomposed with 23% and 12% mass losses, respectively. This was probably corresponding to the further loss of hydroxyl groups of both sample or oxidation of high carbon residue (CO_2, H_2O and CO) [38, 39]. The fourth step of decomposition of the complex was carried out at an extremely high temperature (897 °C) with 34% mass loss. At 897 °C, the remaining group residues could be metal or metal oxides. On the other hand, this situation may be caused by the complexation of Fe(III)-Valex that inhibits the thermal stability of the Valex against degradation and it was provided the fourth step of decomposition. As a result, total mass losses of Valex and Fe(III)-Valex complex were obtained to be 59% and 85%, respectively.

Table 1: Thermogravimetric (TG and DTG) data of Valex and Fe(III)-Valex.

Sample	1st step DTG maxima (°C)	% mass loss	2nd step DTG maxima (°C)	% mass loss	3rd step DTG maxima (°C)	% mass loss	4th step DTG maxima (°C)	% mass loss
Valex	82	5	278	31	799	23	N/A	N/A
Fe(III)-Valex	83	4	262	32	435	12	897	34

XRD analysis

The X-ray diffraction patterns of Valex and Fe(III)-Valex complex were shown in Figure 4. A very broad and unresolved peak in the 2θ region of 20-30° was observed in the diffraction patterns. This may be due to their amorphous structures [40, 41]. In the XRD patterns, 2θ value of Valex shift to 23.7° to 26.2° at the Fe(III)-Valex complex.

The actual structure of the complex is not shown in this article due to the fact that single crystal form of the complex was not obtained.

ESR Analysis

Chemical environment of unpaired electrons that localize to the molecule affects the spectroscopic splitting factor (the g factor) showing the magnetic features. According to study of Abdallah and Chasteen [42], the ESR spectrum of Fe(III) ions are given ESR spectrum at about g=4.3. As shown in Figure 5, we also reported similar ESR spectrum and observed for the high spin Fe(III)-Valex complex.

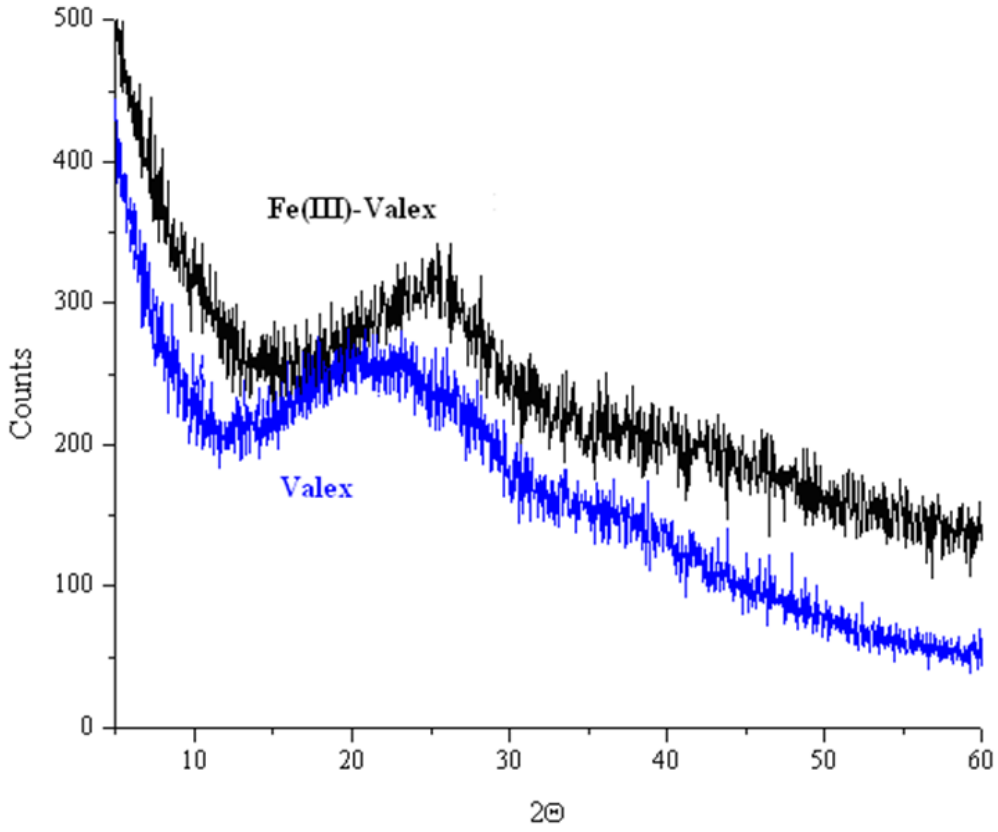

Figure 4: XRD patterns of Valex and Fe(III)-Valex.

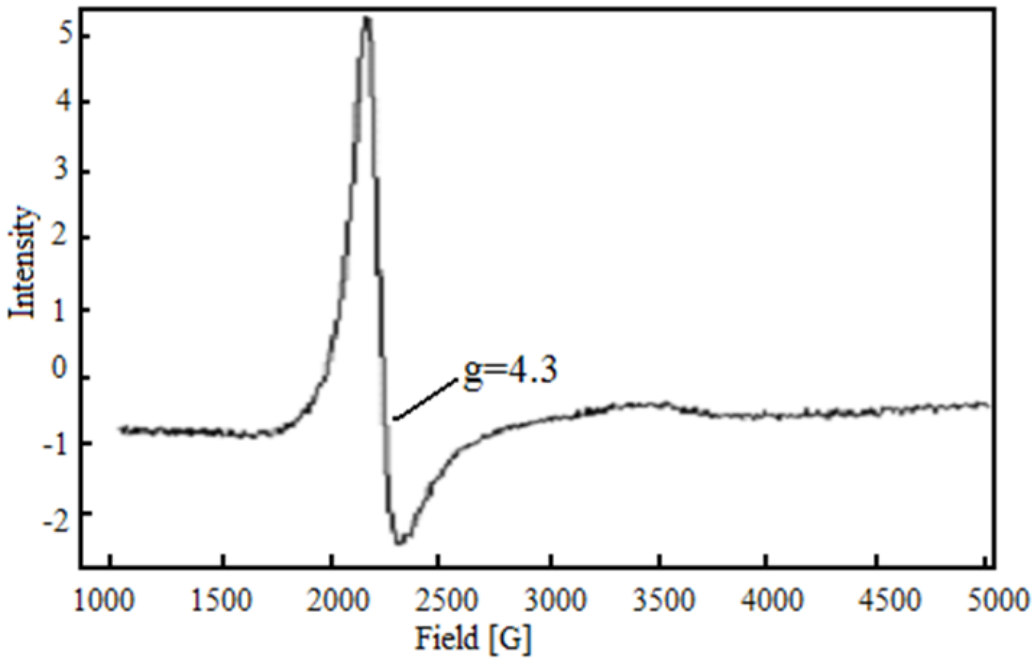

Figure 5: ESR spectra of Fe(III)-Valex at room temperature.

Magnetic Susceptibility Analysis

Magnetic susceptibility values of the Fe(III)-Valex complex were measured at 293 K and evaluated in terms of the number of unpaired electrons and hybrid species. The experimental magnetic susceptibility value was calculated as μ= 6.52 BM (Bohr Magneton). This result was consistent with the presence of Fe^{3+} and it indicated that the Fe(III)-Valex complex corresponds to five electrons and has paramagnetic properties.

X-Ray Photoelectron Spectroscopy (XPS) Analysis

XPS spectra of Fe(III)-Valex complex was shown in Figure 6. From the spectrum, the binding energies of 710 and 724 eV was obtained for $2p_{3/2}$ and $2p_{1/2}$ of Fe^{3+} ion, respectively. This confirmed the existence of Fe^{3+} ions. The similar results were also obtained for Fe^{3+} ions in the works of Mekki *et al.* and Panigrahy *et al.* [43, 44].

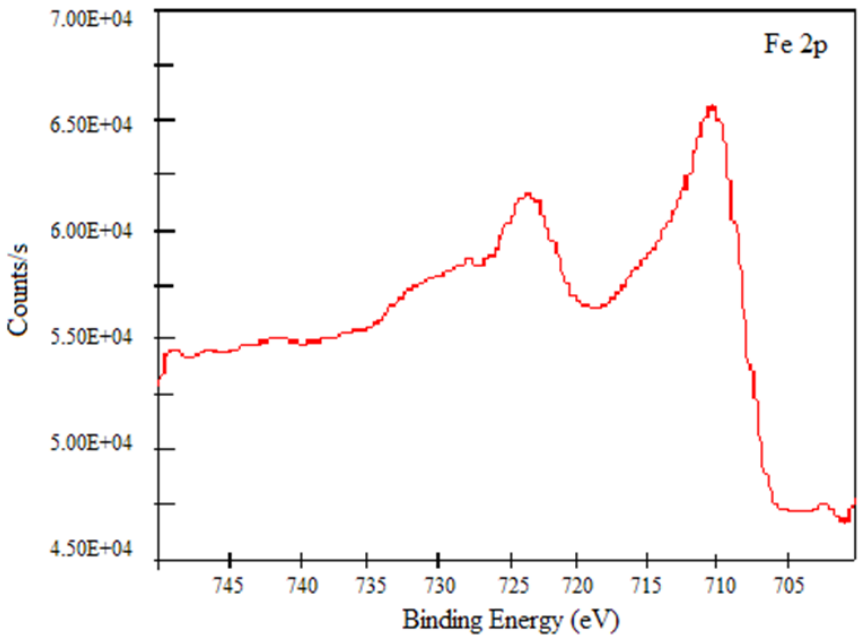

Figure 6: XPS spectra of Fe(III)-Valex.

Antioxidant Activity

At 50 μg/mL, DPPH radical scavenging activities of Valex, the Fe(III)-Valex complex, BHA, and BHT were compared with each other. As shown in Figure 7, Valex showed the stronger scavenging activity at 50 μg/mL with 84.22% on DPPH radicals. In addition, Fe(III)-Valex complex and BHA showed the slightly lower radical scavenging activities than Valex as 70.18%, 69.94%, respectively. The lowest activity was observed with BHT (46.92%) at 50 μg/mL. Statistically significant ($p<0.05$) correlation was found among the studied molecules and the controls. On the other hand, the antimicrobial and antifungal activities of Fe(III)-Valex complex were investigated but it has neither antimicrobial nor antifungal activity as a result of disk diffusion experiments.

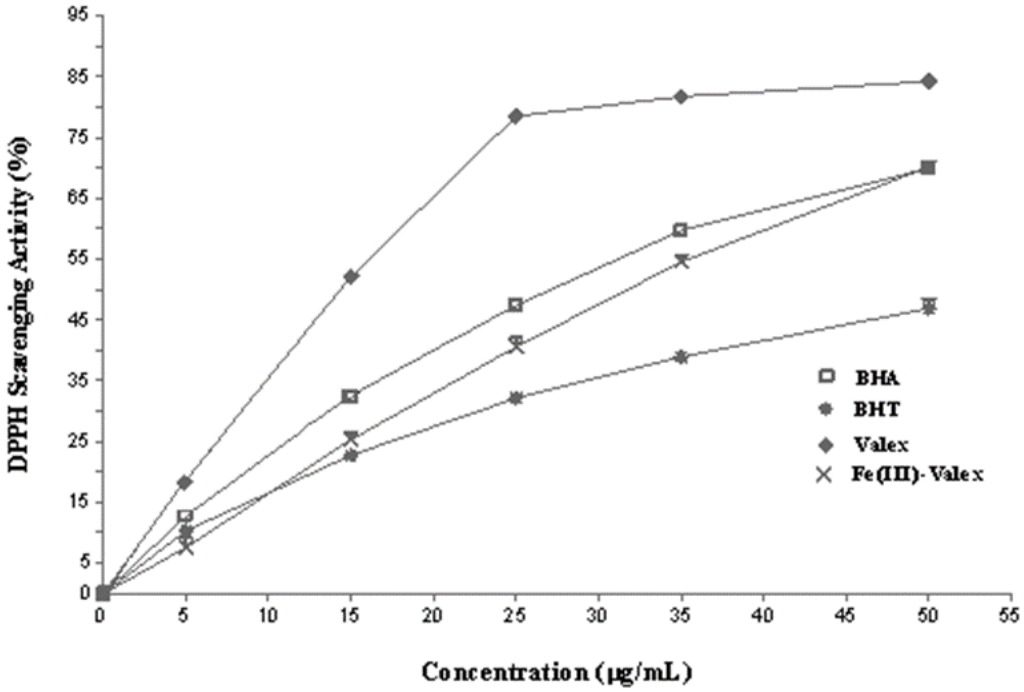

Figure 7: Antioxidant activity (%) of BHA, BHT, Valex and Fe(III)-Valex. Each value means ± SD of three different experiments.

CONCLUSIONS

This study presents the chelation of Fe(III) with valonia extract which is named Valex and its antioxidant activities. The OH groups of Valex were capable of forming a dark violet-colored complex and displaying high reactivity with Fe(III). When Fe(III) and Valex solutions were mixed in pH 4.4, the Fe(III)-Valex complex was formed with an absorbance maximum of 575 nm (pH=4.4). The stoichiometry of Fe(III)-Valex complex was determined as 2:1 by the slope ratio method and stability constant was calculated as 1.5×10^8 L^2mol^{-2}. In FT-IR spectrum of Valex, the intensities of band series between 1700 and 1000 cm^{-1} region were changed in the spectrum of complex due to the complex formation between Fe(III) and the phenolic groups of Valex. Thermal decomposition of Valex and Fe(III)-Valex complex were investigated under nitrogen atmosphere and total mass losses of Valex and Fe(III)-Valex complex were obtained as 59%, 85%, respectively. XRD patterns of Valex and Fe(III)-Valex complex showed that they are amorphous, that is, there was only 2.5° difference in 2θ values between Valex and its Fe(III) complex. In the ESR spectra, the g factor was determined as 4.3 which indicated that this complex was the Fe^{3+} complex. According to the magnetic susceptibility analysis, the magnetic susceptibility of complex was found to be µ=6.52 BM. XPS spectra of the Fe(III)-Valex complex proved the existence of Fe^{3+}. The antioxidant activity of Fe(III)-Valex complex was determined and DPPH radical scavenging activity was found to be concentration dependent. The scavenging effect of samples and controls on the DPPH radical decreased in the order of Valex > Fe(III)-Valex complex ≈ BHA > BHT, which were 84.22%, 70.18% and 69.94%, 46.92% at the concentration of 50 µg/mL, respectively.

On the other hand, regarding the disk diffusion experiments, the Fe(III)-Valex complex has neither antimicrobial nor antifungal activity. In conclusion, it can be stated that Valex has a high antioxidant activity (84.22%). This study clearly indicates that Valex has protective effects because of its high anti-oxidant radical scavenging properties.

ACKNOWLEDGMENTS

The authors are grateful to the Research Foundation of Dokuz Eylul University (Project 2008.KB.FEN.005) for the financial support. The authors would like to thank Dr. Hüseyin Al for his valuable comments and also to Balaban Company from Salihli/Manisa for the Valex sample.

REFERENCES

[1] Rahim A, Kassim J. Recent Development of Vegetal Tannins in Corrosion Protection of Iron and Steel. Recent Patents on Materials Sciencee. 2008 Nov 1;1(3):223–31. DOI: 10.2174/1874464810801030223.

[2] Liao X, Li L, Shi B. Adsorption recovery of thorium(IV) by Myrica rubra tannin and larch tannin immobilized onto collagen fibres. Journal of Radioanalytical and Nuclear Chemistry. 2004;260(3):619–25. DOI: 10.1023/B:JRNC.0000028222.85988.40.

[3] Liao X, Ma H, Wang R, Shi B. Adsorption of UO22+ on tannins immobilized collagen fiber membrane. Journal of Membrane Science. 2004 Nov;243(1-2):235–41. DOI: 10.1016/j.memsci.2004.06.025

[4] Nakano Y, Takeshita K, Tsutsumi T. Adsorption mechanism of hexavalent chromium by redox within condensed-tannin gel. Water Research. 2001 Feb;35(2):496–500. DOI: 10.1016/S0043-1354(00)00279-7.

[5] Vázquez G, González-Álvarez J, Freire S, López-Lorenzo M, Antorrena G. Removal of cadmium and mercury ions from aqueous solution by sorption on treated Pinus pinaster bark: kinetics and isotherms. Bioresource Technology. 2002 May;82(3):247–51. DOI: 10.1016/S0960-8524(01)00186-9.

[6] Liao X, Lu Z, Zhang M, Liu X, Shi B. Adsorption of Cu(II) from aqueous solutions by tannins immobilized on collagen. Journal of Chemical Technology & Biotechnology. 2004 Apr;79(4):335–42. DOI: 10.1002/jctb.974.

[7] Şengil İA, Özacar M, Türkmenler H. Kinetic and isotherm studies of Cu(II) biosorption onto valonia tannin resin. Journal of Hazardous Materials. 2009 Mar;162(2-3):1046–52. DOI: 10.1016/j.jhazmat.2008.05.160.

[8] Karamać M. Chelation of Cu(II), Zn(II), and Fe(II) by Tannin Constituents of Selected Edible Nuts. International Journal of Molecular Sciences. 2009 Dec 22;10(12):5485–97. DOI: 10.3390/ijms10125485.

[9] Parajuli D, Kawakita H, Inoue K, Ohto K, Kajiyama K. Persimmon peel gel for the selective recovery of gold. Hydrometallurgy. 2007 Jul;87(3-4):133–9. DOI: 10.1016/j.hydromet.2007.02.006.

[10] Liao X, Zhang M, Shi B. Collagen-Fiber-Immobilized Tannins and Their Adsorption of Au(III). Industrial & Engineering Chemistry Research. 2004 Apr;43(9):2222–7. DOI: 10.1021/ie0340894.

[11] Ho Kim Y, Nakano Y. Adsorption mechanism of palladium by redox within condensed-tannin gel. Water Research. 2005 Apr;39(7):1324–30. DOI: 10.1016/j.watres.2004.12.036.

[12] Zhan X-M, Zhao X. Mechanism of lead adsorption from aqueous solutions using an adsorbent synthesized from natural condensed tannin. Water Research. 2003 Sep;37(16):3905–12. DOI: 10.1016/S0043-1354(03)00312-9.

[13] Özacar M, Şengil İA, Türkmenler H. Equilibrium and kinetic data, and adsorption mechanism for adsorption of lead onto valonia tannin resin. Chemical Engineering Journal. 2008 Sep;143(1-3):32–42. DOI: 10.1016/j.cej.2007.12.005.

[14] Fatima N, Maqsood Z. Study of Formation Constants of Vanadium (III)-Catecholate Complexes. Journal of Saudi Chemical Society. 2005;9(3):519–28. URL: https://inis.iaea.org/search/searchsinglerecord.aspx?recordsFor=SingleRecord&RN=38108006.

[15] Jaén JA, Navarro C. Mössbauer and infrared spectroscopy as a diagnostic tool for the characterization of ferric tannates. Hyperfine Interactions. 2009 Jul;192(1-3):61–7. DOI: 10.1007/s10751-009-9947-2.

[16] Jaén JA, González L, Vargas A, Olave G. Gallic Acid, Ellagic Acid and Pyrogallol Reaction with Metallic Iron. Hyperfine Interactions. 2003;148/149(1-4):227–35. DOI: 10.1023/B:HYPE.0000003784.88539.d4.

[17] Fazary AE, Taha M, Ju Y-H. Iron Complexation Studies of Gallic Acid. Journal of Chemical & Engineering Data. 2009 Jan 8;54(1):35–42. DOI: 10.1021/je800441u.

[18] Sungur Ş, Uzar A. Investigation of complexes tannic acid and myricetin with Fe(III). Spectrochimica Acta Part A: Molecular and Biomolecular Spectroscopy. 2008 Jan;69(1):225–9. DOI: 10.1016/j.saa.2007.03.038.

[19] Nohynek LJ, Alakomi H-L, Kähkönen MP, Heinonen M, Helander IM, Oksman-Caldentey K-M, et al. Berry Phenolics: Antimicrobial Properties and Mechanisms of Action Against Severe Human Pathogens. Nutrition and Cancer. 2006 Jan;54(1):18–32. DOI: 10.1207/s15327914nc5401_4.

[20] Igbinoosa O, Igbinoosa E, Aiyegoro O. Antimicrobial activity and phytochemical screening of stem bark extracts from Jatropha curcas (Linn). African Journal of Pharmacy and Pharmacology. 2009;3(2):58–62. URL: https://www.researchgate.net/profile/Etinosa_Igbinosa2/publication/253974565_Antimicrobial_activity_and_phytochemical_screening_of_stem_bark_extracts_from_Jatropha_curcas_Linn/links/54f661b40cf27d8ed71d9dac.pdf.

[21]. Hagerman AE, Riedl KM, Jones GA, Sovik KN, Ritchard NT, Hartzfeld PW, et al. High Molecular Weight Plant Polyphenolics (Tannins) as Biological Antioxidants. Journal of Agricultural and Food Chemistry. 1998 May;46(5):1887–92. DOI: 10.1021/jf970975b.

[22] Saint-Cricq de Gaulejac N, Provost C, Vivas N. Comparative Study of Polyphenol Scavenging Activities Assessed by Different Methods. Journal of Agricultural and Food Chemistry. 1999 Feb;47(2):425–31. DOI: 10.1021/jf980700b.

[23] Karamać M. In-vitro study on the efficacy of tannin fractions of edible nuts as antioxidants. European Journal of Lipid Science and Technology. 2009 Nov;111(11):1063–71. DOI: 10.1002/ejlt.200900067.

[24] Rauha J-P, Remes S, Heinonen M, Hopia A, Kähkönen M, Kujala T, et al. Antimicrobial effects of Finnish plant extracts containing flavonoids and other phenolic compounds. International Journal of Food Microbiology. 2000 May;56(1):3–12. DOI: 10.1016/S0168-1605(00)00218-X.

[25] Dığrak M, İlçim A, Alma M, Şen S. Antimicrobial Activities of the Extracts of Various Plants (valex, mimosa bark, gallnut powders, Salvia sp. and Phlomis sp.). Turkish Journal of Biology. 1999;23:241–8. URL: http://journals.tubitak.gov.tr/biology/issues/biy-99-23-2/biy-23-2-12-98020.pdf.

[26] Chu W-L, Lim Y-W, Radhakrishnan A, Lim P-E. Protective effect of aqueous extract from Spirulina platensis against cell death induced by free radicals. BMS Complementary and Alternative Medicine. 2010;10(53):1–8. URL: http://bmccomplementalternmed.biomedcentral.com/articles/10.1186/1472-6882-10-53.

[27] Clark C, Jakobs M, Appelbaum P. Antipneumococcal Activities of Levofloxacin and Clarithromycin as Determined by Agar Dilution, Microdilution, E-Test, and Disk Diffusion Methodologies. Journal of Clinical Microbiology. 1998;36(12):3579–84. URL: http://jcm.asm.org/content/36/12/3579.short.

[28] Balaban A, Banciu M, Pogany I. Applications of Physical Methods to Organic Chemistry. Bucharest; 1983. 31 p. (Editura Stiintifica si Enciclopedica).

[29] Brune M, Hallberg L, Skånberg A-B. Determination of Iron-Binding Phenolic Groups in Foods. Journal of Food Science. 1991 Jan;56(1):128–31. DOI: 10.1111/j.1365-2621.1991.tb07992.x.

[30] Yang Z, Lu J, Wang L. Synthesis and Fluorescent Properties of Zn(II) Complex with Functionalized Polystyrene Containing Salicylaldehyde End Group. Polymer Bulletin. 2005 Feb;53(4):249–57. DOI: 10.1007/s00289-005-0335-z.

[31] Binbuga N, Chambers K, Henry WP, Schultz TP. Metal chelation studies relevant to wood preservation.1. Complexation of propyl gallate with Fe2+. Holzforschung [Internet]. 2005 Jan 1 [cited 2016 May 27];59(2). DOI: 10.1515/HF.2005.032.

[32] Perron NR, Hodges JN, Jenkins M, Brumaghim JL. Predicting How Polyphenol Antioxidants Prevent DNA Damage by Binding to Iron. Inorganic Chemistry. 2008 Jul;47(14):6153–61. DOI: 10.1021/ic7022727.

[33] Perron NR, Brumaghim JL. A Review of the Antioxidant Mechanisms of Polyphenol Compounds Related to Iron Binding. Cell Biochemistry and Biophysics. 2009 Mar;53(2):75–100. DOI: 10.1007/s12013-009-9043-x.

[34] Kim S, Kim H-J. Curing behavior and viscoelastic properties of pine and wattle tannin-based adhesives studied by dynamic mechanical thermal analysis and FT-IR-ATR spectroscopy. Journal of Adhesion Science and Technology. 2003 Jan;17(10):1369–83. DOI: 10.1163/156856103769172797.

[35] Özacar M, Soykan C, Şengül İA. Studies on synthesis, characterization, and metal adsorption of mimosa and valonia tannin resins. Journal of Applied Polymer Science. 2006 Oct 5;102(1):786–97. DOI: 10.1002/app.23944.

[36] Ardelean I, Toderas M, Paşcuţa P. Structural Study of the Fe 2 O 3 –B 2 O 3 –BaO Glass System by FTIR Spectroscopy. Modern Physics Letters B. 2003 Sep 20;17(22):1175–9. DOI: 10.1142/S0217984903006098.

[37] Predoi D. A study on iron oxide nanoparticles coated with dextrin obtained by coprecipitation. Digest Journal of Nanomaterials and Biostructures. 2007;2(1):169–73. URL: http://www.chalcogen.ro/Predoi-DJNB2.pdf.

[38] Garro Galvez JM, Riedl B, Conner AH. Analytical Studies on Tara Tannins. Holzforschung. 1997 Jan;51(3):235–43. DOI: 10.1515/hfsg.1997.51.3.235

[39] Aelenei N, Popa MI, Novac O, Lisa G, Balaita L. Tannic acid incorporation in chitosan-based microparticles and in vitro controlled release. Journal of Materials Science: Materials in Medicine. 2009 May;20(5):1095–102. DOI: 10.1007/s10856-008-3675-z.

[40] Beltrán JJ, Novegil FJ, García KE, Barrero CA. On the reaction of iron oxides and oxyhydroxides with tannic and phosphoric acid and their mixtures. Hyperfine Interactions. 2010 Jan;195(1-3):133–40. DOI: 10.1007/s10751-009-0110-x.

[41] Iglesias J, García de Saldaña E, Jaen J. On the tannic acid interaction with metallic iron. Hyperfine Interactions. 2001;134(1):109–14. URL: http://link.springer.com/article/10.1023/A:1013838600599.

[42] Bou-Abdallah F, Chasteen ND. Spin concentration measurements of high-spin (g′ = 4.3) rhombic iron(III) ions in biological samples: theory and application. JBIC Journal of Biological Inorganic Chemistry. 2007 Nov 29;13(1):15–24. DOI: 10.1007/s00775-007-0304-0.

[43] Mekki A, Holland D, McConville CF, Salim M. An XPS study of iron sodium silicate glass surfaces. Journal of Non-Crystalline Solids. 1996 Dec;208(3):267–76. DOI: 10.1016/S0022-3093(96)00523-6.

[44] Panigrahy B, Aslam M, Bahadur D. Effect of Fe doping concentration on optical and magnetic properties of ZnO nanorods. Nanotechnology. 2012 Mar 23;23(11):115601. DOI: 10.1088/0957-4484/23/11/115601.

Fe(III)-VALEX KOMPLEKSİNİN SENTEZİ, KARAKTERİZASYONU VE ANTİOKSİDAN AKTİVİTESİ

Öz: Palamut meşesi (*Quercus ithaburensis sp. macrolepis*), palamut ağacının meyvesi olup Türkiye'nin Batı Anadolu bölgesinde geniş ölçüde yetişir ve tanen açısından zengindir. Bu meyvelerde pek çok alanda kullanılan ve Valex adı verilen hidrolizlenebilir tanenler bulunmaktadır. Valex'in demir(III) kompleksi sentezlenmiş ve çeşitli teknikler kullanılarak karakterize edilmiştir. Kompleksin stokiyometrisinin pH 4,4'de M_2L olduğu ve kararlılık sabiti (K)'nin 1,5 x 10^8 L^2mol^{-2} olduğu bulunmuştur. Fe(III)-Valex kompleksinin antioksidan, antimikrobiyal ve antifungal aktivitesi çalışılmıştır. Fe(III)-Valex kompleksinin antioksidan aktivitesi 2,2-difenil-1-pikrilhidrazil (DPPH) radikal süpürme aktivitesi ile ve butillenmiş hidroksianisol (BHA) ile butillenmiş hidroksitoluen (BHT) karşısındaki aktivitesi ile bulunmuştur. Kompleksin antimikrobiyal aktivitesi beş farklı bakteriyel kültür ve bir mantar kültürü kullanılarak disk diffüzyon testi ile belirlenmiştir. Fe(III)-Valex kompleksinin antioksidan aktiviteye sahip olduğu, ancak denenen mikroorganizmalara karşı herhangi bir antimikrobiyal ve antifungal aktivite göstermediği bulunmuştur.

Anahtar kelimeler: Valex, tanen, demir kompleksi, antioksidan aktivitesi.
Gönderilme: 16 Mart 2016. **Düzeltme:** 4 Nisan 2016**. Kabul:** 25 Mayıs 2016.

JOTCSA, Volume 3, issue 1, (2016), pp. 147-158.

Research article

Journal homepage: http://dergipark.ulakbim.gov.tr/jotcsa

e-ISSN: 2149-0120

In Silico Modelling of Cytotoxic Behaviour of Anti-Leukemic Compounds on HL-60 Cell Line

David Ebuka Arthur*[1], Adamu Uzairu[1], Paul Mamza[1], Stephen Eyije Abechi[1], and Gideon Shallangwa[1]

[1]Department of Chemistry, Ahmadu Bello University (ABU) Zaria, Kaduna State, Nigeria.

Abstract: This research employs multiple linear regression technique in the modelling of some potent anti-leukemic compounds using paDEL molecular descriptor software calculator, to identify the best relationship between the chemical structure and toxicities of the anticancer datasets against some leukemic cell lines (HL-60). Statistical parameters such as Q^2 and R^2_{pred} (test set) were computed to validate the strength of the model, while Williams plot was used to assess its applicability domain. The mean effects of the molecular descriptors in the models were calculated to illuminate the principal properties of the molecules responsible for their cytotoxicity.

Keywords: HL-60 cell lines, leukemia, QSTR, applicability domain, y-randomization.
Submitted: April 01, 2016. **Revised:** April 30, 2016. **Accepted:** May 25, 2016.

Cite this: Arthur D, Uzairu A, Mamza P, Abechi S, Shallangwa G. IN SILICO MODELLING OF CYTOTOXIC BEHAVIOUR OF ANTI-LEUKEMIA COMPOUNDS ON HL-60 CELL LINE. Journal of the Turkish Chemical Society, Section A: Chemistry. 2016;3(2):147–158.
DOI: 10.18596/jotcsa.40785.
Correspondence to: David Ebuka Arthur. E-mail: hanslibs@myway.com. **Tel:** +2348138325431.

INTRODUCTION

Leukaemia is normally referred to as the cancer of the blood cells and these cancers do not form solid tumours, instead they form large numbers of abnormal white blood cells which builds up in the blood and bone marrow, crowding out normal blood cells. The low level of normal blood cells thereby makes it harder for the body to get oxygen to its tissues and fight infections. Cancer is a major disease; this can be seen from the WHO statistical report which shows that, at the present time, around one in five of all deaths are because of this disease. Presently the best way for treating metastasised cancer, is chemotherapy but their toxic nature often offers significant limitations.

Quantitative structure-activity relationship (QSAR) and quantitative structure-toxicity relationship (QSTR) make it conceivable to anticipate the activity/toxicity of a given compound as a function of its molecular descriptors. Despite the fact that there is impressive enthusiasm for the use of QSARs to predict toxicity, there seems to be some accompanying limitations. QSTR can be used to predict the toxicity of unknown chemicals in many ways. In industries, these models can be applied to screen new compounds and help with the procedure for designing less toxic but potent drugs.

MATERIALS AND METHODS

Experimental Dataset

In the present study, we used a dataset of 112 compounds whose anticancer activity against human acute lymphoblastic leukaemia (HL-60) leukaemia tumour cell line has been previously reported. The dataset along with their NSC number were taken from the drug discovery and development arm of the National Cancer Institute (NCI). Eligible compounds were determined by reviewing and curating the raw data collected from the literature (NCI database). The data encompasses aminopterin and camptothecin derivatives, and colchicine analogues. The anticancer toxicity results are expressed as pLC50, which is the lethal concentration for 50% of maximal inhibition of cell proliferation.

Geometric optimisation and molecular descriptors calculation

The 2D structures of the compounds were drawn using Chemdraw software and the spatial conformations of the compounds were determined using the Spartan 14 V1.1.4 wavefunction software package, the molecular structures were first minimised by Molecular Mechanics Force Field (MMFF) calculation to remove strain energy before subjecting it to DFT (density functional theory) method for complete geometric optimisation of the structures. Afterwards, we calculated 1875 descriptors (1444 1D, 2D descriptors and 431 3D descriptors) molecular descriptors using the paDEL program such as, atom-type electrotopological state descriptors, McGowan volume, RDF descriptors, *etc*.

Data Normalisation

The calculated molecular descriptors were normalised via a method preserving the range (maximum and minimum) and introducing the dispersion of the descriptors (standard deviation / variance) before they are converted into a N(0,1) distribution, making the comparison between descriptors (probabilities calculation) much easier.

Variable Selection

In this study, genetic algorithm technique was employed as a selection tool to select the most relevant descriptors with respect to an objective function. Genetic algorithm method as a selection tool was written in Matlab 6.5 program and used here. The genetic algorithm (GA) starts with the creation of a population of randomly generated parameter sets. The parameters set used for the GA includes mutation 0.1, crossover 0.9, population 10000, number of generations 1000, R^2 floor limit 50%, and objective function R2/N_par. Equations were developed between the observed toxicity and the descriptors. The best equation was taken based on statistical parameters such as squared regression coefficient (R^2) and leave-one-out cross-validated regression coefficient (Q^2_{cv}).

Data Division

In order to obtain validated QSAR models the dataset was divided into training and test sets. Ideally, this division should be performed such that points representing both training (80% of compounds) and test sets (20% percent of compounds) are distributed within the whole descriptor space occupied by the entire dataset, and each point of the test set is close to at least one point of the training set. This partitioning ensures that a similar principle can be employed for the toxicity prediction of the test set. Kennard-Stone Algorithm will be applied for dividing Dataset into a Training and Test set.

Model development

MLR is a method used for modelling linear relationship between a dependent variable Y (pLC50) and independent variable X (molecular descriptors). MLR is based on least squares: the model is fit such that sum-of-squares of differences of observed and a predicted value is minimized. MLR estimates values of regression coefficients (R^2) by applying least squares curve fitting method.

Evaluation of the QSAR Models

The Developed QSAR models are evaluated using the following statistical measures: n (Number of compounds in regression); K (Number of descriptors); R^2 (the squared correlation coefficient); F test (Fischer's Value) for statistical significance; Q^2 (cross-validated correlation coefficient); pred R^2 (R^2 for external test set). The regression coefficient R^2 is a relative measure of fit by the regression equation. It represents the part of the variation in the observed data is explained by the regression. However, a QSAR model is considered to be predictive, if the following conditions are satisfied: $R^2>0.6$, $q^2>0.6$ and pred $R^2>0.5$. The low standard error of pred R^2se, Q^2se and R^2se shows absolute quality of the fitness of the model.

Validation of the QSAR model

The predictive capability of the QSAR equation was determined using the leave-one-out cross-validation method. The cross-validation regression coefficient (Q^2_{cv}) was calculated by the following equation:

$$q^2_{CV} = 1 - PRESS/_{TOTAL} = 1 - \frac{\sum_{i=1}^{n}(y_{exp} - y_{pred})^2}{\sum_{i=1}^{n}(y_{exp} - \bar{y})^2} \quad \textbf{(1)}$$

Where y_{pred}, y_{exp}, and $\tilde{y}$ are the predicted, experimental, and mean values of experimental activity, respectively. Also, the accuracy of the prediction of the QSAR equation was validated by F_{value}, R^2, and R^2_{adj}. A large F indicates that the model fit is not a chance occurrence. It has been shown that a high value of statistical characteristics is not necessary for the proof of a highly predictive model. Hence, to evaluate the predictive ability of our QSAR model, we used the method described by Roy *et al.* The coefficient of determination in the test set, R^2_{test}, was calculated using the following equation:

$$R^2_{Test} = 1 - \frac{\sum\left(Y_{pred_{test}} - Y_{Test}\right)^2}{\sum\left(Y_{pred_{test}} - \bar{Y}_{Training}\right)^2} \quad \textbf{(2)}$$

where $Y_{predtest}$ and Y_{Test} are the predicted value based on the QSAR equation (model response) and experimental activity values, respectively, of the external test set compounds. $\tilde{Y}_{Training}$ is the mean activity value of the training set compounds. Further evaluation of the predictive ability of the QSAR model for the external test set compounds was done by determining the value of r_m^2 by the following equation:

$$rm^2 = r^2_{test}\left(1 - \left|\sqrt{r^2_{test} - r^2_{test_o}}\right|\right) \quad \textbf{(3)}$$

where is the square correlation coefficient between experimental and predicted values and is the squared correlation coefficient between experimental and predicted values without intercept for the external test set compounds.

See Table 1 in Supplementary Files.

Evaluation of the applicability domain of the model

Evaluation of the applicability domain of the QSAR model is considered an important step to establish that the model is reliable to make predictions within the chemical space for which it was developed. There are several methods for defining the applicability domain of a QSAR model, but we used the most commonly used leverage approach in this study. Leverage of a given chemical compound h_i is defined as: $h_i = x_i(X^TX)^{-1} x_i^T$, where x_i is the descriptor row-vector of the query compound i, and x is the n x k descriptor matrix of the training set compounds used to develop the model. As a prediction tool, the warning leverage (h*) which is the limit of normal values for X outliers, its defined as: $h^* = 3(p + 1) / n$, where n is the number of training compounds, and k is the number of descriptors in the model. The test compounds with leverages are considered to be reliably predicted by the model. The Williams plot, a plot of standardized residuals vs. leverage values, is used to interpret the applicability domain of the model.

RESULTS AND DISCUSSION

A QSAR analysis was performed to explore the structure–activity relationship of different 112 compounds with different organic moiety acting as anticancer. In a QSAR study, generally, the quality of a model is expressed by its fitting and prediction ability (see Table 2 in Supplementary Files).

QSAR on HL-60 cell line dataset

HL-60 cell line

$$pLC_{50} = 4.097(\boldsymbol{Secondary\ butyl}) + 0.861(\boldsymbol{nAcid}) + 1.268(\boldsymbol{nS}) + 2.298(\boldsymbol{AATSC5i}) + 3.315(\boldsymbol{SHBint6}) + 4.039(\boldsymbol{SaaaC}) - 1.584(\boldsymbol{minHBint7}) - 2.476(\boldsymbol{minHBint8}) - 1.112\ (\boldsymbol{minaaN}) + 2.386\ (\boldsymbol{minddssS}) + 2.938(\boldsymbol{WPSA-1}) - 1.684(\boldsymbol{RDF140s}) - 1.070$$

$$N_{train} = 90, R^2_{train} = 0.873, R^2_{adjusted} = 0.852, F_{train} = 46.92, Q^2_{LOO} = 0.826, Outliers > 3.0 = 1, N_{test} = 22$$

N is the number of compounds, R^2 is the squared correlation coefficient, Q^2_{LOO}, is the squared cross-validation coefficients for leave one out, F is the Fisher F statistic, and RMSE is the root mean square error. The built model was used to predict the test set data, and the prediction results are given in Table 1 (See Supplementary Files). The predicted values for pLC_{50} for the compounds in the training and test sets for HL-60 leukaemia cell line were plotted against the experimental pLC50 values in Figure 1, while the plot of the residual for the predicted values of pLC50 for both the training and test sets against the experimental pLC50 values of HL-60 cell line is shown in Figure 2. As can be seen the model did not show any proportional and systematic error, because the propagation of the residuals on both sides of zero is random.

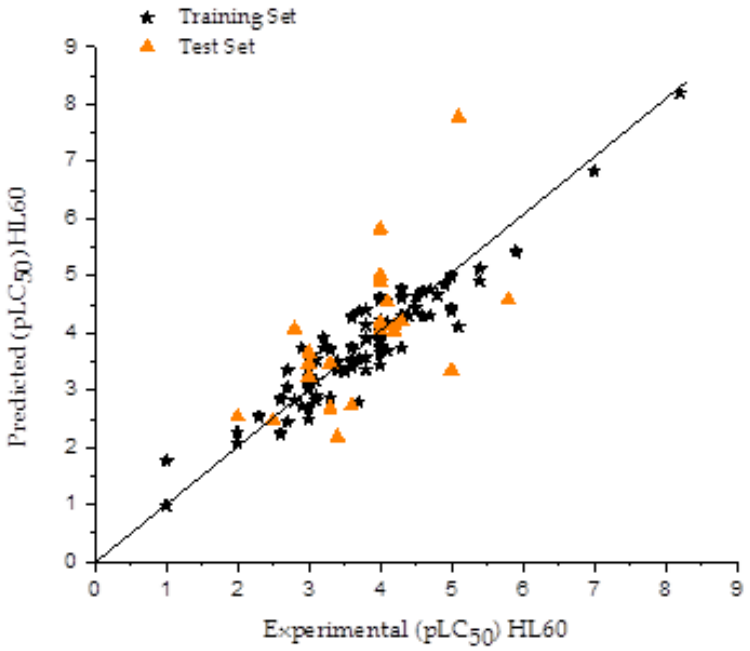

Figure 1. The predicted toxicity values (pLC50) against the experimental values for the training and test sets of the compounds on HL60 leukaemia cell line.

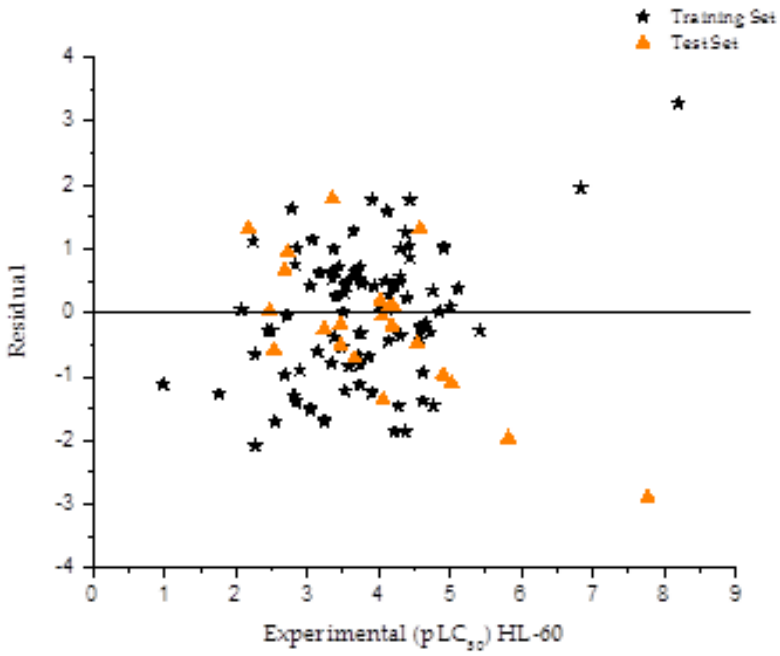

Figure 2. The Residuals against the Predicted pLC50 values for the training and test sets of HL-60 leukaemia cell line.

QSAR model validation

The real usefulness of QSAR models is not just their ability to reproduce known data, verified by their fitting power (R^2), but mainly is their potential for predictive application. For this reason, the internal consistency of the training set was confirmed by using leave-one-out (LOO) cross-validation method to ensure the robustness of the model. The high calculated Q^2_{LOO} value for HL-60 given as 0.826 suggests a good internal validation, other statistical information is presented in Table 2 (See Supplementary Files).

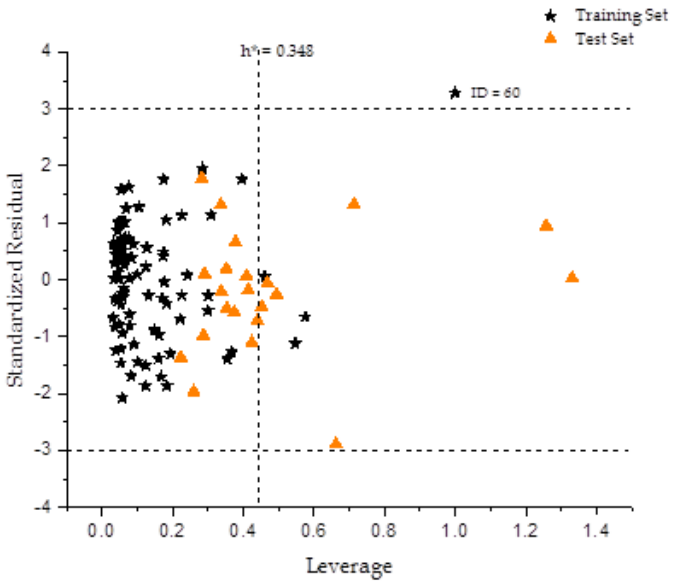

Figure 3. The Williams plot, the plot of the standardised residuals versus the Toxicity (pLC50) leverage value for HL-60 dataset.

The leverage values can be calculated for every compound and plotted vs. standardised residuals, and it allows a graphical detection of both the outliers and the influential chemicals in a model. Figure 3, which shows the Williams plot of HL-60 dataset, the applicability domain is established inside a squared area within ±3 bound for residuals and a leverage threshold h* (h* = 3p° / n), where p° is the number of model parameters and n is the number of compounds). It identifies that all the compounds of the training set and test set for HL-60 dataset are inside of this square area, with an exception of one compounds with ID number (60), which was found to be an outlier related to experimental errors of the data set, nine other compounds were not within the applicability domain or the model, though this was found to be as a result of strong differences in their structures with the rest of the dataset. From Figure 3, it could be seen that only one outlier compound with standard residuals >3d of the data set. Furthermore, most of the chemicals had a leverage lower than the warning h* value of 0.433. The descriptors in the models were subjected to variance inflation factor test (VIF), the test confirms that there is no intercollinerity of descriptors within the model (Table 3; see Supplementary Files), thus each descriptor relays unique information that cannot be correlated with that of other descriptors in the model.

In order to assess the robustness of the model, the Y-randomisation test was applied in this study. Y-randomisation test confirms whether the model is obtained by chance correlation, and is a true structure–activity relationship to validate the adequacy of the training set molecules.

If the activity prediction of the random model is comparable to that of the original equation, the set of observations is not sufficient to support the model. The new QSAR models (after several repetitions) would be expected to have low R^2 and Q^2_{LOO} values for HL-60 cytotoxicity (Table 4). If the opposite happens, then an acceptable QSAR model cannot be obtained for the specific modelling method and data. The results of Table 3 indicate that an acceptable model is obtained by GA–MLR method, and the model developed is statistically significant and robust.

To examine the relative importance, and the contribution of each descriptor in the model, for each descriptor the value of the mean effect (MF) was calculated. This calculation was performed with the equation below:

$$MF_j = \frac{\beta_j \sum_{i=1}^{i=n} d_{ij}}{\sum_j^m \beta_j \sum_i^n d_{ij}} \quad \textbf{(4)}$$

MF_j represents the mean effect for the considered descriptor *j*, β_j is the coefficient of the descriptor *j*, d_{ij} stands for the value of the target descriptors for each molecule, and m is the descriptor's number in the model. The MF value indicates the relative importance of a descriptor, compared with the other descriptors in the model. Its sign shows the direction of variation in the toxicity values as a result of the increase (or reduction) of the descriptor values. The mean effect values are presented in Table 3 for HL-60, The descriptors AATSC5i, SHBint6 and WPSA-1 molecular descriptors were found to contribute negatively to the toxicity of the anticancer compounds used in developing the model, and their mean effects were reported as 0.473, 0.403 and 0.254 respectively (See Supplementary Files for the table).

Elucidation of Descriptors in HL-60 models

By interpreting the descriptors contained in the QSAR model it is possible to gain some insights into factors, which are related to the anti-leukaemic activity. For this reason, an acceptable interpretation of the selected descriptors is given below. The brief presentations of the descriptors in the model are shown in Table 3 (See Supplementary Files for the table). In order to quantitatively determine the relative importance of each descriptor in the model, the value of the mean effect (MF) was calculated for each descriptor. The MF value gives an account of the contribution of each descriptor to the model independent of the rest. Its sign indicates the difference in the direction of the activities as a result increase or decrease of the descriptor values. The mean effect values are presented in Table 3 (See Supplementary Files for the table).

n-Secondary butyl is a 2D descriptor representing the total number of secondary butyl group found in the data set, while n-acid is the total number of acidic groups, which is defined as a two dimensional acid group count descriptor. Their mean effects were recorded to as 0.013 accordingly, though the value is small and even insignificant when compared to some other descriptors in the model. n-S known as number of sulphur atoms was also found to contribute a little more than the previous descriptors and having an overall mean effect of 0.035 on the model. A positive mean effect for these descriptor illustrates that the toxicity increases with decreasing the values of the descriptors, which means that a large number of sulphur atoms, secondary butyl and acid groups will benefit the activity and reduce its toxicity. AATSC5i (Average centered Broto-Moreau autocorrelation - lag 5/weighted by first ionisation potential) belongs to the 2D autocorrelation descriptors. The 2D autocorrelation descriptors have been successfully employed by Fernandez *et al.* (2005). The physico-chemical property for AATSC5i is the ionisation potential of the molecule. Hence increasing the ionisation potential of a molecule increases its AATSC5i value. Mean effect of AATSCi has the positive sign, which indicates that an increase in the ionisation potential of a molecule leads to a decrease in its toxicity.

SHBint6 is defined as the Sum of E-State descriptors of strength for potential hydrogen bonds of path length 6, it a 2D atom type electrotopological state descriptor developed by Hall. The mean effect was reported in Table 3 as 0.403 and increasing its value leads to a decrease in the toxicity (pLC50; see Supplementary Files for the table).

MinHBint7 and minHBint8 are Minimum E-State descriptors of strength for potential Hydrogen Bonds of path length 7 and path length 8. These are atom-type electrotopological state molecular descriptors with mean effect of 0.133 and – 0.182, respectively. The mean effect of minHBint8 is higher than that of minHBint7 and its negative sign indicates that an increase in the hydrogen bonds potential for path length 8 will increase the cytotoxicity (pLC50). WPSA-1 (PPSA-1 * total molecular surface area / 1000) is a 3D CPSA Descriptor which utilises the total molecular surface area of the molecule to predict the direction of the activity when compared to the descriptor. The value of the mean effect is given as 0.254, this descriptor displays a positive sign, which indicates that toxicity is inversely related to this descriptor. This shows that by decreasing the value of this descriptor will increase toxicities of the compounds.

The final descriptor of the GA-MLR model was the (RDF140s) Radial distribution function - 140 / weighted by relative I-state, which is one of the 3D RDF Descriptors. The descriptor is related to the I-state weight of the molecules, and its toxicity is inversely related to the descriptor since the mean effect is reported in Table 3 as 0.200.

CONCLUSION

In the present study, a genetic algorithm was used to construct a quantitative relationship between the leukemia HL-60 cell lines cytotoxicity (pLC50) of 112 anti-leukemic compounds and their calculated descriptors. The GA-MLR method resulted in a training set with good statistical significance and acceptable external predictions. Also the AATSC5i, SHBint6 and WPSA-1 molecular descriptors were found to have the highest contribution in the model, their mean effects were reported as 0.473, 0.403 and 0.254, respectively.

Additionally, the proposed model identified and provided some insight into what structural features are related to the toxicity of compounds, as well as how these effects could be used to alter the toxicity of the compounds.

REFERENCES

[1] Kwon H-C, Kim S-H, Kim J-S, Han H, Sook Roh M, Han J-Y, et al. Establishment and characterization of an STI571-resistant human myelogenous leukemia cell line, SR-1. Cancer Genetics and Cytogenetics. 2004 Oct;154(1):52–6. DOI: 10.1016/j.cancergencyto.2004.01.009.

[2] Monga M, Sausville E. Developmental Therapeutics Program at the NCI: molecular target and drug discovery process. Leukemia. 2002;16:520–6. URL: https://www.researchgate.net/profile/Manish_Monga2/publication/11407712_Developmental_therapeutics_program_at_the_NCI_molecular_target_and_drug_discovery_process/links/546f54740cf2d67fc0310d3b.pdf.

[3] Bhat KS, Poojary B, Prasad DJ, Naik P, Holla BS. Synthesis and antitumor activity studies of some new fused 1,2,4-triazole derivatives carrying 2,4-dichloro-5-fluorophenyl moiety. European Journal of Medicinal Chemistry. 2009 Dec;44(12):5066–70. DOI: http://dx.doi.org/10.1016/j.ejmech.2009.09.010.

[4] Jemal A, Bray F, Center MM, Ferlay J, Ward E, Forman D. Global cancer statistics. CA: A Cancer Journal for Clinicians. 2011 Mar;61(2):69–90. DOI: 10.3322/caac.20107.

[5] Yap CW. PaDEL-descriptor: An open source software to calculate molecular descriptors and fingerprints. Journal of Computational Chemistry. 2011 May;32(7):1466–74. DOI: 10.1002/jcc.21707.

[6] Anonymous. 2013 ESC Guidelines on cardiac pacing and cardiac resynchronization therapy: The Task Force on cardiac pacing and resynchronization therapy of the European Society of Cardiology (ESC). Developed in collaboration with the European Heart Rhythm Association (EHRA). European Heart Journal. 2013 Aug 1;34(29):2281–329.

[7] Waller CL, Bradley MP. Development and Validation of a Novel Variable Selection Technique with Application to Multidimensional Quantitative Structure−Activity Relationship Studies. Journal of Chemical Information and Computer Sciences. 1999 Mar;39(2):345–55. DOI: 10.1021/ci980405r.

[8] Gomes AR, Santos Sanches I, Aires de Sousa M, Castañeda E, de Lencastre H. Molecular Epidemiology of Methicillin-Resistant Staphylococcus aureus in Colombian Hospitals: Dominance of a Single Unique Multidrug-Resistant Clone. Microbial Drug Resistance. 2001 Mar;7(1):23–32. DOI: 10.1089/107662901750152729.

[9] Ahmad S, Gromiha MM. Design and training of a neural network for predicting the solvent accessibility of proteins. Journal of Computational Chemistry. 2003 Aug;24(11):1313–20. DOI: 10.1002/jcc.10298.

[10] Caballero J, Fernandez M. Artificial Neural Networks from MATLAB® in Medicinal Chemistry. Bayesian-Regularized Genetic Neural Networks (BRGNN): Application to the Prediction of the Antagonistic Activity Against Human Platelet Thrombin Receptor (PAR-1). Current Topics in Medicinal Chemistry. 2008 Dec 1;8(18):1580–605. DOI: 10.2174/156802608786786570.

[11] Galvao R, Araujo M, Jose G, Pontes M, Silva E, Saldanha T. A method for calibration and validation subset partitioning. Talanta. 2005 Oct 15;67(4):736–40. DOI: 10.1016/j.talanta.2005.03.025.

[12] Kennard RW, Stone LA. Computer Aided Design of Experiments. Technometrics. 1969 Feb;11(1):137–48. DOI: 10.1080/00401706.1969.10490666.

[13] Golbraikh A, Tropsha A. Beware of q2! Journal of Molecular Graphics and Modelling. 2002 Jan;20(4):269–76. DOI: 10.1016/S1093-3263(01)00123-1.

[14] Roy K, Kar S, Das RN. Background of QSAR and Historical Developments. In: Understanding the Basics of QSAR for Applications in Pharmaceutical Sciences and Risk Assessment [Internet]. Elsevier; 2015 [cited 2016 Jun 1]. p. 1–46. Available from: http://linkinghub.elsevier.com/retrieve/pii/B9780128015056000016.

[15] Eriksson L, Jaworska J, Worth A, Cronin M, McDowell R, Gramatica P. Methods for reliability and uncertainty assessment and for applicability evaluations of classification- and regression-based QSARs. Environ Health Perspect. 2003 Aug;111(10):1361–75. URL: http://www.ncbi.nlm.nih.gov/pmc/articles/PMC1241620/pdf/ehp0111-001361.pdf.

[16] Ojha PK, Mitra I, Das RN, Roy K. Further exploring rm2 metrics for validation of QSPR models. Chemometrics and Intelligent Laboratory Systems. 2011 May;107(1):194–205. DOI: 10.1016/j.chemolab.2011.03.011.

[17] Golbraikh A, Shen M, Xiao Z, Xiao Y-D, Lee K-H, Tropsha A. Rational selection of training and test sets for the development of validated QSAR models. Journal of Computer-Aided Molecular Design. 2003 Feb;17(2):241–53.

[18] Gramatica P, Giani E, Papa E. Statistical external validation and consensus modeling: A QSPR case study for Koc prediction. Journal of Molecular Graphics and Modelling. 2007 Mar;25(6):755–66. DOI: 10.1016/j.jmgm.2006.06.005.

[19] Schultz TW, Netzeva TI, Roberts DW, Cronin MTD. Structure−Toxicity Relationships for the Effects to Tetrahymena pyriformis of Aliphatic, Carbonyl-Containing, α,β-Unsaturated Chemicals. Chemical Research in Toxicology. 2005 Feb;18(2):330–41. DOI: 10.1021/tx049833j.

[20] OECD. Guidance document on the validation of (quantitative) structure-activity relationships [(Q) SAR] models. OECD Series on Testing and Assessment No 69 ENV/JM/MONO (2007) 2. 2007;154.

[21] Riahi S, Pourbasheer E, Ganjali MR, Norouzi P. Investigation of different linear and nonlinear chemometric methods for modeling of retention index of essential oil components: Concerns to support vector machine. Journal of Hazardous Materials. 2009 Jul 30;166(2–3):853–9. DOI: 10.1016/j.jhazmat.2008.11.097.

[22] Zhu X, Kruhlak NL. Construction and analysis of a human hepatotoxicity database suitable for QSAR modeling using post-market safety data. Toxicology. 2014 Jul;321:62–72. DOI: 10.1016/j.tox.2014.03.009.

[23] Todeschini R, Consonni V. Molecular descriptors for chemoinformatics. Weinheim: Wiley-VCH; 2009. (Methods and principles in medicinal chemistry). ISBN: 978-3-527-31852-0.

Research article

HL-60 Hücre Dizisi Üzerinde Anti-Lösemi Bileşiklerinin Sitotoksik Davranışının İn Siliko Modellenmesi

David Ebuka Arthur, Adamu Uzairu, Paul Mamza, Stephen Eyije Abechi, Gideon Shallangwa

Öz: Bu çalışma çoklu lineer regresyon tekniğini bazı kuvvetli anti-lösemik bileşiklerin modellenmesinde kullanarak paDEL moleküler tarif edici yazılım hesap makinesi ile bazı lösemik hücre sıralarına (HL-60) karşı antikanser veri setlerinin kimyasal yapısı ve zehirlilikleri arasındaki en iyi ilişkiyi tanımlamayı amaçlamaktadır. Q^2 ve R^2_{pred} (test seti) gibi istatistik parametreler modelin kuvvetini doğrulamak için hesaplanmıştır, Williams eğrisi de bunların uygulanma alanlarını değerlendirmek için kullanılmıştır. Modellerdeki moleküler tanımlayıcıların ortalama etkisi, bunların zehirliliklerinden sorumlu olan moleküllerin birincil özelliklerine ışık tutmak için hesaplanmıştır.

Anahtar kelimeler: HL-60 hücre sırası, lösemi, QSTR, uygulama alanı, y-rasgeleleştirme.
Gönderilme: 1 Nisan 2016, **Düzeltme**: 30 Nisan 2016, **Kabul**: 25 Mayıs 2016.

JOTCSA, Volume 3, issue 1, (2016), pp. 159-166.

Research article

Journal homepage: http://dergipark.ulakbim.gov.tr/jotcsa

e-ISSN: 2149-0120

Base Catalyzed Dimerization of ω-Formyl-2-Hydroxyacetophenones

Magdy Ahmed Ibrahim*[1] and Salah Sayed Ibrahim[1]

Department of Chemistry, Faculty of Education, Ain Shams University, Roxy 11711, Cairo, Egypt

Abstract: Refluxing ω-formyl-2-hydroxyacetophenones **1** in ethanol containing triethylamine as a basic catalyst produced the dimerized product identified as 2-(2-hydroxyaryl)-4H,5H-pyrano[2,3-*b*]chromen-5-ones **2**. Meanwhile, heating ω-formyl-2-hydroxyacetophenones **1** in 2 M aqueous sodium hydroxide solution afforded another type of dimeric product identified as 3-[2-(2-hydroxy-5-substituted benzoyl)vinyl]-6-substituted-4H-chromen-4-ones **3**. The proposed mechanisms were discussed. The mode of dimerization of ω-formyl-2-hydroxyacetophenones **1** depends on the type of catalyst used and the reaction conditions. Structures of the synthesized compounds were deduced on the basis of their analytical and spectral data.

Keywords: ω-formyl-2-hydroxyacetophenones, dimerization, chromone, spectral data, α, β-unsaturated ketones.

Submitted: May 05, 2016. **Revised:** June 10, 2016. **Accepted:** June 16, 2016.

Cite this: Ibrahim M, Ibrahim S. BASE CATALYZED DIMERIZATION OF ω-FORMYL-2-HYDROXYACETOPHENONES. Journal of the Turkish Chemical Society, Section A: Chemistry. 2016;3(2):159–166.

DOI: 10.18596/jotcsa.10789.

Correspondence to: Magdy Ahmed Ibrahim, E-mail: magdy_ahmed1977@yahoo.com. **Tel:** +2 01007887204; fax: +2 022581243.

INTRODUCTION

A large number of nitrogen heterocyclic rings of a broad spectrum of pharmaceutical activity were synthesized using 1,3-dicarbonyl compounds as precursors [1-6]. Typically, these nitrogen heterocyclic systems are synthesized through condensation of 1,3-dicarbonyl compounds with bifunctional nucleophiles under mild reaction conditions [7-9]. The research on the synthesis and reactions of β-keto-aldehydes is rare [10]. ω-Formyl-2-hydroxyacetophenones **1** represent one of the simplest β-keto-aldehyde and only few publications described its chemical reactivity under basic reaction conditions [10, 11]. In 1966, Kostka [12] reported that heating ω-formyl-2-hydroxyacetophenone (**1a**) with triethylamine (Et_3N) to 60 °C led to an unidentified product with a high melting point. In the present work, we aimed to try to explain and identify this unidentified product, via the elemental microanalysis and different spectroscopic techniques.

EXPERIMENTAL

General

Melting points of the synthesized compounds were measured on a digital Stuart SMP3 apparatus. Fourier Transform Infrared spectra were measured on Perkin-Elmer 293 spectrometer (cm^{-1}), using KBr disks. Mass spectrometry were obtained using GC-2010 Shimadzu Gas chromatograph-mass spectrometer (70 eV). ^1H NMR (300 MHz) and ^{13}C NMR (75 MHz) spectra were measured on Mercury-300BB, using DMSO-d6 as a solvent and TMS (δ) as the internal standard. Elemental microanalyses were performed on a Perkin–Elmer CHN-2400 analyzer. ω-Formyl-2-hydroxyacetophenones **1** were prepared according to the published method [13].

Dimerization of ω-formyl-2-hydroxyacetophenones 1a-c using Et_3N

General procedure: ω-Formyl-2-hydroxyacetophenones **1a-c** (5 mmol) in absolute ethanol (10 mL) containing few drops of triethylamine (Et_3N) was heated under reflux for 15 min. The white crystals obtained during heating were filtered and recrystallized to give compounds **2a-c**.

2-(2-Hydroxyphenyl)-4H,5H-pyrano[2,3-b]chromen-6-one (2a)

Crystallized from DMF/EtOH as white crystals, mp > 300 °C (lit. mp > 300 °C) [14], yield (41%). FTIR (KBr, cm^{-1}): 3423 (br, OH), 3071 ($CH_{arom.}$), 2911 ($CH_{aliph.}$), 1632 ($C{=}O_{\gamma\text{-pyrone}}$), 1600 (C=C). ^1H-NMR (DMSO-d_6, δ): 3.90 (d, 2H, J = 7.2 Hz, CH2), 4.79 (t, 1H, J = 7.2 Hz, H–3), 6.95 (t, 1H, J = 8.1 Hz, Ar–H) 7.47–7.63 (m, 2H, Ar–H), 7.61 (t, 1H, Ar–H), 7.78 (t, 1H, Ar–H), 7.97–8.17 (m, 2H, Ar–H), 8.41 (d, 1H, H–6), 11.60 (brs, 1H, OH exchangeable with D_2O). MS (m/z, %): 293 (M+1, 6 %), 292 (M+, 20), 275 (8), 258 (19), 205 (14), 156 (12), 129 (17), 91 (24), 77 (100), 65 (32). Anal. Calcd for $C_{18}H_{12}O_4$ (292.29): C, 73.97; H, 4.14. Found: C, 73.72; H, 4.05.

2-(2-Hydroxy-5-methylphenyl)-7-methyl-4H,5H-pyrano[2,3-b]chromen-5-one (2b)

Crystallized from DMF as white crystals, mp > 300 °C, yield (40%), FTIR (KBr, cm^{-1}): 3419 (br, OH), 3052 ($CH_{arom.}$), 2940, 2884 ($CH_{aliph.}$), 1637 ($C=O_{\gamma\text{-pyrone}}$), 1602 (C=C). ^{1}H-NMR (DMSO-d_6, δ): 2.31 (s, 3H, CH_3), 2.40 (s, 3H, CH_3), 3.80 (d, 2H, CH_2), 4.20 (t, 1H, H–3), 7.53-7.85 (m, 5H, Ar–H), 7.95 (s, 1H, H-6), 11.56 (brs, 1H, OH exchangeable with D_2O). MS (m/z, %): 321 (M+1, 30 %), 320 (M+, 100), 292 (85), 276 (27), 260 (34), 134 (70), 108 (25), 92 (65), 77 (19), 65 (55). Anal. Calcd for $C_{20}H_{16}O_4$ (320.34): C, 74.99; H, 5.03. Found: C, 74.60; H, 5.00.

7-Bromo-2-(5-bromo-2-hydroxyphenyl)-4H,5H-pyrano[2,3-b]chromen-5-one (2c)

Crystallized from DMF as white crystals, mp > 300 °C, yield (39%), FTIR (KBr, cm^{-1}): 3420 (br, OH), 3039 ($CH_{arom.}$), 2916 ($CH_{aliph.}$), 1635 ($C=O_{\gamma\text{-pyrone}}$), 1599 (C=C). ^{1}H-NMR (DMSO-d_6, δ): 3.86 (d, 2H, CH_2), 4.30 (t, 1H, H–3), 7.51-7.78 (m, 5H, Ar–H), 7.91 (s, 1H, H-6), 11.96 (brs, 1H, OH exchangeable with D_2O). MS (m/z, %): 452 (M+4, 35 %), 450 (M+2, 72 %), 448 (M+, 34 %), 424 (49 %), 422 (100 %), 420 (47 %), 412 (12 %), 410 (25), 408 (11), 201 (14), 199 (14), 185 (35), 183 (34), 173 (50), 171 (49), 158 (11), 156 (11), 77 (31), 65 (19). Anal. Calcd for $C_{18}H_{10}Br_2O_4$ (450.08): C, 48.03; H, 2.24. Found: C, 47.90; H, 2.20.

Dimerization of ω-formyl-2-hydroxyacetophenones 1b,c using 2 M aqueous NaOH solution

General procedure: ω-Formyl-2-hydroxyacetophenones **1b,c** (5 mmol) in 2 M aqueous sodium hydroxide solution (10 mL) was stirred at 60 °C for 2h. After cooling, the reaction mixture was neutralized with conc. HCl. The solid so formed was filtered and recrystallized to give compounds **3a,b.**

3-[2-(2-Hydroxy-5-methylbenzoyl)vinyl]-6-methyl-4H-chromen-4-one (3a)

Crystallized from AcOH as yellow crystals, mp, 196 °C, yield (42%). FTIR (KBr, cm^{-1}): 3390 (br, OH), 3071 ($CH_{aromatic}$), 2930, 2892 ($CH_{aliph.}$), 1645 ($C=O_{\gamma\text{-pyrone}}$), 1630 ($C=O_{ketones}$), 1604 (C=C). ^{1}H-NMR (DMSO-d_6, δ): 2.30 (s, 3H, CH_3), 2.44 (s, 3H, CH_3), 6.91 (d, 1H, J = 8.1 Hz, H-3`), 7.32 (d, 1H, J = 8.1 Hz, H-4`), 7.43 (d, 1H, J = 8.4 Hz, H-8), 7.56 (d, 1H, J = 8.4 Hz, H-7), 7.60 (d, 1H, J = 15.3, α-$H_{olefinic}$), 7.80 (s, 1H, H-6`), 7.92 (s, 1H, H-8), 8.12 (d, 1H, J = 15.3, β-$H_{olefinic}$), 8.50 (s, 1H, H-2), 12.40 (br, 1H, OH exchangeable with D_2O). ^{13}C-NMR (DMSO-d_6, δ): 20.2, 22.6, 116.3, 117.2, 119.5, 122.0, 123.4, 129.1, 130.7, 131.5, 134.8, 135.1, 136.3, 143.3, 148.2, 151.2, 157.5, 176.0, 188.4. MS (m/z, %): 320 (M+, 18), 292 (61), 276 (53), 214 (30), 185 (45), 160 (14), 135 (100), 108 (33), 92 (65), 77 (40), 65 (23). Anal. Calcd for $C_{20}H_{16}O_4$ (320.34): C, 74.99; H, 5.03. Found: C, 74.70; H, 4.80.

3-[2-(2-Hydroxy-5-bromobenzoyl)vinyl]-6-bromo-4H-chromen-4-one (3b)
Crystallized from DMF/MeOH as dark yellow crystals, mp, 290-291 °C, yield (45%), FTIR (KBr, cm^{-1}): 3402 (br, OH), 3040 ($CH_{aromatic}$), 2932, 2879 ($CH_{aliph.}$), 1649 ($C=O_{\gamma\text{-pyrone}}$), 1633 ($C=O_{ketones}$), 1601 (C=C). ^{1}H-NMR (DMSO-d_6, δ): 7.02 (d, 1H, J = 6.7 Hz, H-3`), 7.40 (d, 1H, J = 6.7 Hz, H-4`), 7.62 (d, 1H, J = 8.1 Hz, H-8), 7.70 (d, 1H, J = 8.1 Hz, H-7), 7.79 (d, 1H, J = 14.4, α-$H_{olefinic}$), 7.87 (s, 1H, H-6`), 7.99 (s, 1H, H-8), 8.18 (d, 1H, J = 14.4, β-$H_{olefinic}$), 8.56 (s, 1H, H-2), 12.55 (br, 1H, OH exchangeable with D_2O). Anal. Calcd for $C_{18}H_{10}Br_2O_4$ (450.08): C, 48.03; H, 2.24. Found: C, 47.75; H, 2.12.

RESULTS AND DISCUSSION

The present work aimed to study the chemical reactivity of a variety of substituted ω-formyl-2-hydroxyacetophenone upon refluxing in absolute ethanol containing few drops of triethylamine (Et_3N) as a basic catalyst. Previously Kostka [12] found that, heating ω-formyl-2-hydroxyacetophenone (**1a**) with triethylamine (Et_3N) to 60 °C led to an unidentified product having a high melting point, but he was not able to identify the isolated product. Herein, we repeat this reaction under the same conditions and we succeeded to identify the isolated product using the different spectroscopic techniques.

The basic condition of the previous reaction may involve dimerization process and the reaction may proceed via deprotonation of the active methylene group, by Et_3N, followed by condensation with the formyl group of another molecule leading to intermediate A (self-condensation) which tautomerized to the enolic form (intermediate B) followed by cycloaddition of the hydroxyl group onto the carbonyl function (intermediate C) with concomitant intramolecular dehydration producing intermediate D. The latter intermediate underwent proton transfer to afford the final dimeric product, 2-(2-hydroxyphenyl)-4H,5H-pyrano[2,3-b]chromen-5-one (**2a**) (Scheme 1). The mass spectrum of compound **2a** showed the molecular ion peak at m/z 292 which is consistent with its molecular formula and supports the proposed structure. Its ^{1}H NMR spectrum revealed distinctive doublet and triplet signals at δ 3.90 and 4.79 attributable to CH_2 and H-3 protons, respectively, while the phenolic OH proton appeared at δ 11.60 as a broad D_2O-exchangeable signal. Also, the ^{13}C NMR spectrum exhibited three characteristic signals at δ 28.9, 94.0 and 175.8 assignable to CH_2, C-3 and C=O, respectively.

In the same manner, boiling ω-formyl-2-hydroxy-5-methylacetophenone (1b) and ω-formyl-5-bromo-2-hydroxyacetophenone (**1c**) in ethanol containing few drops of Et_3N yielded pyrano[2,3-b]chromene derivatives **2b** and **2c**, respectively, via the suggested mechanism depicted in Scheme 1. The ^{1}H NMR spectra of compounds **2b** and **2c** showed distinctive doublet and triplet signals attributed to CH_2 and H-3 protons, respectively. In addition, their mass spectrum revealed their molecular ion peaks which agree well with the proposed structures.

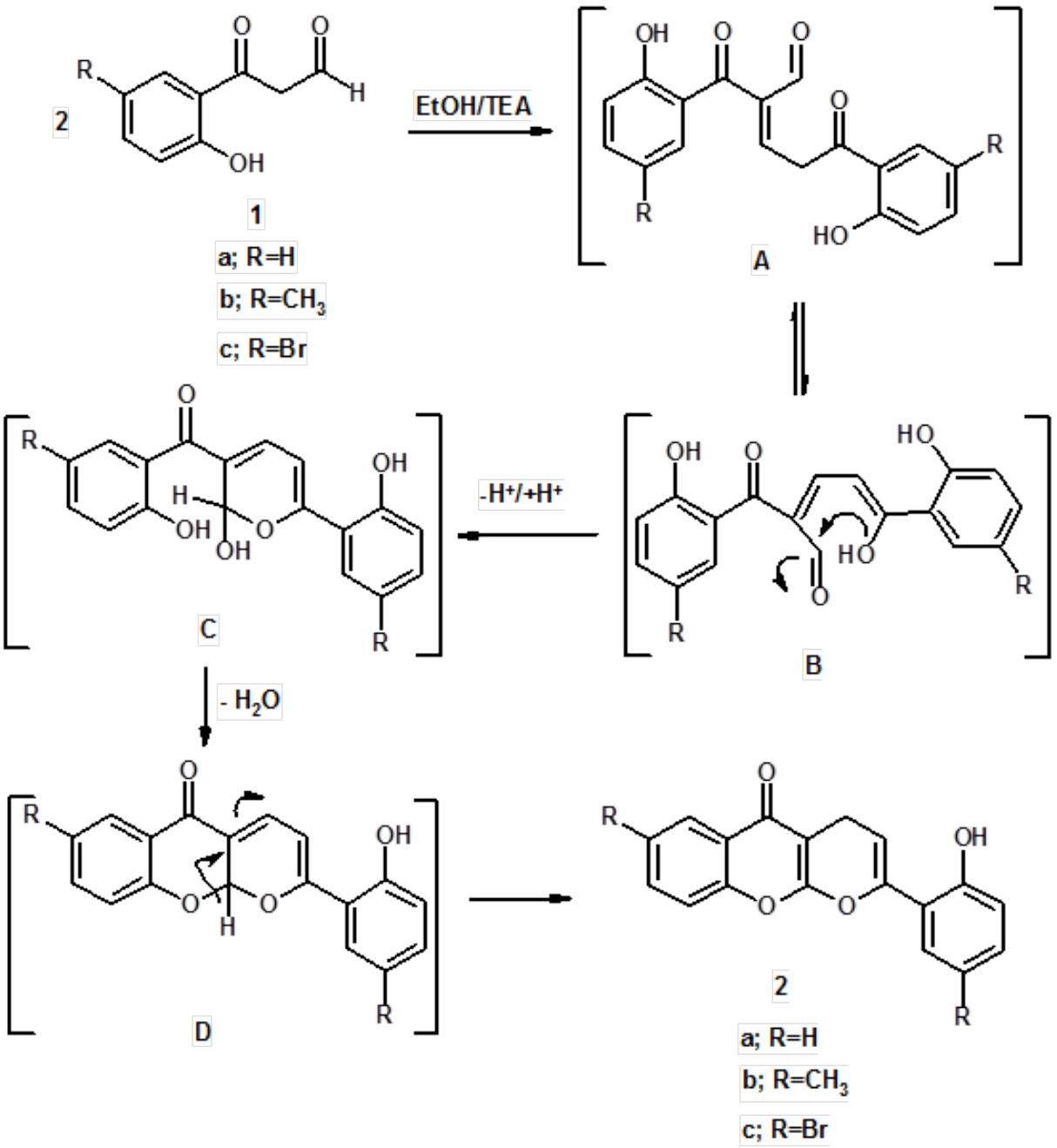

Scheme 1. The suggested mechanism for the dimerization of ω-formyl-2-hydroxyacetophenones **1a-c**, in the presence of TEA.

On the other hand, treatment of compounds **1b,c** with 2 M aqueous NaOH solution under stirring at 60 °C gave another type of dimeric products; 3-[2-(2-hydroxy-5-methylbenzoyl)vinyl]-6-methyl-4H-chromen-4-one (**3a**) and 3-[2-(5-bromo-2-hydroxybenzoyl)vinyl]-6-bromo-4H-chromen-4-one (**3b**), respectively (Scheme 2). The ^{1}H NMR spectra of compounds **3a,b** showed characteristic two doublets (at δ 7.60 and 8.12 for compound **3a** and δ 7.79 and 8.18 for compound **3b**) with high coupling constant indicating the presence of two hydrogen atoms in E-configuration around the olefinic bond. In addition, the spectra also revealed characteristic downfield singlet attributed to H-2$_{chromone}$ at δ 8.50 and 8.56 for compounds **3a,b**, respectively.

Formation of chromone derivatives **3a,b** may occur via self-condensation of ω-formyl-2-hydroxyacetophenones **1b,c** leading to intermediate A which underwent cyclization reaction producing intermediate E followed by dehydration to yield the final products (Scheme 2).

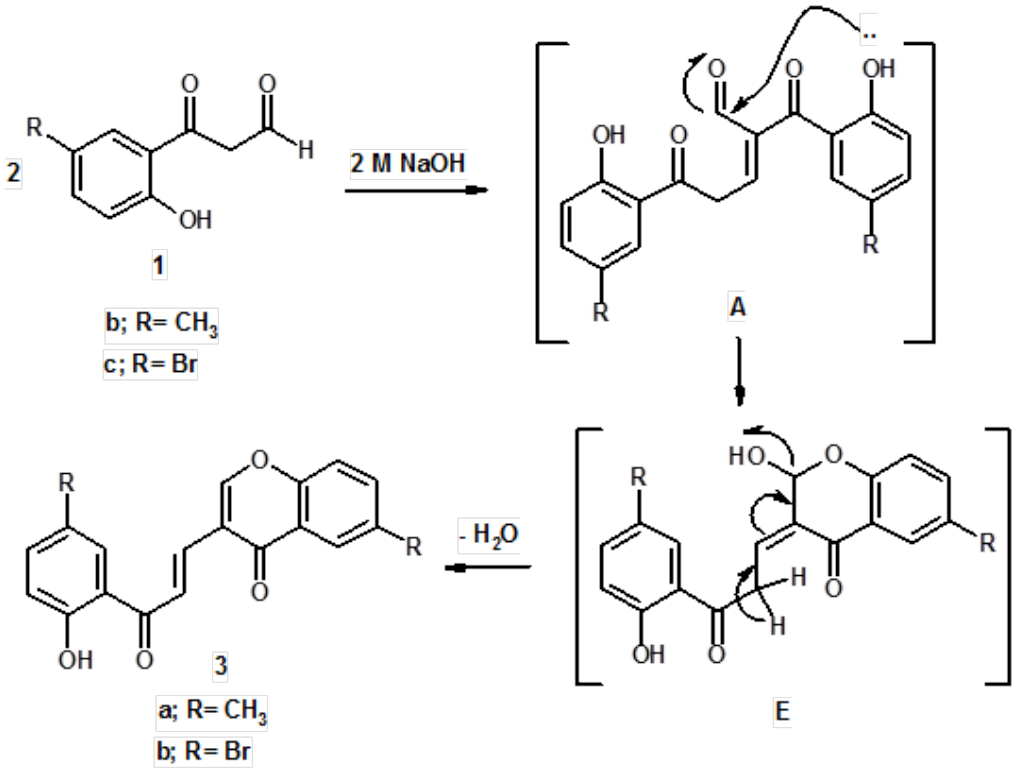

Scheme 2. The suggested mechanism for the dimerization of ω-formyl-2-hydroxyacetophenones **1b,c** in the presence of 2 M NaOH.

The proposed mechanisms depicted in Schemes 1 and 2 indicate that, the mode of dimerization of ω-formyl-2-hydroxyacetophenones **1** depend on the type of catalyst used and the reaction conditions.

CONCLUSION

In conclusion, the present work studied the effect of triethylamine and sodium hydroxide on the active substrate ω-formyl-2-hydroxyacetophenones **1**. The dimerization process of ω-formyl-2-hydroxyacetophenones **1** depends on the basic catalyst used and the reaction conditions. Et_3N mediated self-dimerization of ω-formyl-2-hydroxyacetophenones **1** producing 2-(2-aryl)-4H,5H-pyrano[2,3-b]chromen-5-ones **2**, while NaOH mediated self-dimerization of ω-formyl-2-hydroxyacetophenones **1** affording 3-[2-(2-hydroxy-5-substituted benzoyl)vinyl]-6-substituted-4H-chromen-4-ones **3**.

ACKNOWLEDGMENT

MAI would like to acknowledge the financial support provided by Ain-Shams University.

REFERENCES

1. Nikolaev VA, Ivanov AV, Shakhmin AA, Sieler J, Rodina LL. The first examples of cycloadditions of 2-diazo-1,3-dicarbonyl compounds to aromatic thioketones. Tetrahedron Letters. 2012 Jun;53(24):3095–9. DOI: 10.1016/j.tetlet.2012.04.036.

2. Ohtsuka Y, Uraguchi D, Yamamoto K, Tokuhisa K, Yamakawa T. Syntheses of 2-(trifluoromethyl)-1,3-dicarbonyl compounds through direct trifluoromethylation with CF3I and their application to fluorinated pyrazoles syntheses. Tetrahedron. 2012 Mar;68(12):2636–49. DOI: 10.1016/j.tet.2012.01.075.

3. Ng EPJ, Wang Y-F, Hui BW-Q, Lapointe G, Chiba S. Orthogonal synthesis of pyrroles and 1,2,3-triazoles from vinyl azides and 1,3-dicarbonyl compounds. Tetrahedron. 2011 Oct;67(40):7728–37. DOI: 10.1016/j.tet.2011.08.006.

4. Wang J-L, Liu B-K, Yin C, Wu Q, Lin X-F. Candida antarctica lipase B-catalyzed the unprecedented three-component Hantzsch-type reaction of aldehyde with acetamide and 1,3-dicarbonyl compounds in non-aqueous solvent. Tetrahedron. 2011 Apr;67(14):2689–92. DOI: 10.1016/j.tet.2011.01.045.

5. Arcadi A, Alfonsi M, Chiarini M, Marinelli F. Sequential gold-catalyzed reactions of 1-phenylprop-2-yn-1-ol with 1,3-dicarbonyl compounds. Journal of Organometallic Chemistry. 2009 Feb;694(4):576–82. DOI: 10.1016/j.jorganchem.2008.12.013.

6. Wang Y, Dong D, Yang Y, Huang J, Ouyang Y, Liu Q. A facile and convenient one-pot synthesis of polysubstituted thiophenes from 1,3-dicarbonyl compounds in water. Tetrahedron. 2007 Mar;63(12):2724–8. DOI: 10.1016/j.tet.2006.12.090.

7. Hassanin H, Ibrahim M, Alnamer Y. Synthesis and antimicrobial activity of some novel 4-hydroxyquinolin-2(1H)-ones and pyrano[3,2-c]quinolinones from 3-(1-ethy1-4-hydroxy-2-oxo-1,2-dihydroquinolin-3-yl)-3-oxopropanoic acid. Turkish Journal of Chemistry. 2012;36:682–99. DOI: 10.3906/kim-1111-14. An author's name is missing.

8. Ismail M, Othman E, Mohamed H. Synthesis and Cyclization Reactions with Quinolinyl Keto Esters I. Chemical Reactivity of Quinolinyl beta-Keto Ester and Quinolinyl alpha,beta-Unsaturated Ketones. Chemical Papers. 2005;59(2):117–26. URL: http://www.chempap.org/file_access.php?file=592a117.pdf.

9. Ibrahim SS. Uses of o -Hydroxybenzoylacetone in the Synthesis of Some Substituted 2-Methylchromones, Chelating Agents, and Related Materials. Industrial & Engineering Chemistry Research. 2001 Jan;40(1):37–9. DOI: 10.1021/ie9906767.

10. Széll T, Sohár P, Horváth G. On the chemistry of α-formyl-2-hydroxyacetophenone. Liebigs Annalen. 1995 Nov;1995(11):2043–4. DOI: 10.1002/jlac.1995199511286.

11. Ibrahim M. Ring transformation of chromone-3-carboxylic acid under nucleophilic conditions. ARKIVOC. 2008;xvii:192–204. URL: http://www.arkat-usa.org/get-file/27587/.

12. Kostka K. Chromones. IV. Cyclization of ω-formyl-o-hydroxyacetophenone and o-hydroxyphenyl-1,3-diketones. Roczniki Chemii. 1966;40:1861. Please look at the Chemical Abstracts page for more information (ending page, etc.)

13. Schönberg A, Sina A. On Visnagin and Khellin and Related Compounds. A Simple Synthesis of Chromone. Journal of the American Chemical Society. 1950 Aug;72(8):3396–9. DOI: 10.1021/ja01164a022.

14. Ibrahim M, Ali T. Ring opening and ring closure reactions of chromone-3-carboxylic acid: unexpected routes to synthesize functionalized benzoxocinones and heteroannulated pyranochromenes. Turkish Journal of Chemistry. 2015;39:412–25. DOI: 10.3906/kim-1410-41.

Research article

ω-FORMİL-2-HİDROKSİASETOFENONLARIN BAZ KATALİZLİ DİMERLEŞMESİ

Magdy Ahmed Ibrahim and Salah Sayed Ibrahim

Öz: ω-formil-2-hidroksiasetofenon bileşikleri (**1**) bazik katalizör olarak trietilamin içerecek şekilde etanolde reflüks edildiğinde 2-(2-hidroksiaril)-4H-5H-pirano[2,3-*b*]kromen-5-on bileşiklerini (**2**) vermektedir. Bu arada, ω-formil-2-hidroksiasetofenon bileşiklerini (**1**) 2 M sulu sodyum hidroksit çözeltisinde ısıtmakla 3-[2-(2-hidroksi-5-sübstitüe benzoil)vinil]6-sübstitüe-4H-kromen-4-on bileşikleri (**3**) ele geçmektedir. Önerilen mekanizmalar tartışılmıştır. ω-formil-2-hidroksiasetofenon (**1**) bileşiklerinin dimerleşme biçimi kullanılan katalizöre ve tepkime koşullarına bağlıdır. Sentezlenmiş bileşiklerin yapıları analitik ve spektral verilere dayanarak sonuca bağlanmıştır.

Anahtar kelimeler: ω-Formil-2-hidroksiasetofenonlar, dimerileşme, kromon, spektral veriler, α, β-doymamış ketonlar.

Gönderme: 5 Mayıs 2016. **Düzeltme:** 10 Haziran 2016. **Kabul:** 16 Haziran 2016.

JOTCSA, Volume 3, issue 2, (2016), pp. 167-182. **Research article**

Journal homepage: http://dergipark.ulakbim.gov.tr/jotcsa

e-ISSN: 2149-0120

Synthesis and Characterization of Novel Inorganic and Organic Hybrid Poly[cyclotriphosphazene-co-(4,4'-diaminophenylmethane)] Microspheres via One-Pot Self-Assembly Polycondensation Approach

Yasemin Süzen*[1], Simge Metinoğlu[1]

[1]Anadolu University, Yunusemre Campus, Faculty of Science, Department of Chemistry, 26470, Eskişehir, Turkey.

Abstract: Cross-linked cyclomatrix polyphosphazene microspheres have been successfully synthesized via self-assembly polycondensation reaction between hexachlorocyclotriphosphazene (HCCP) and 4,4'-diaminodiphenylmethane (DADPM) in acetonitrile. The absence of any stabilizing agent or surfactant and usage of only an ultrasonic bath have been the advantages for this reaction. HCCP and DADPM ratios have been attempted to obtain the best morphology by SEM-EDX. The size of microspheres were ranging from 4.46 to 4.74 μm. The inorganic-organic hybrid microspheres were characterized by FTIR, TGA, UV, Fluorescence and XRD.

Keywords: Cyclomatrix microspheres, polyphosphazene, self-assembly, precipitation polymerization.

Submitted: May 11, 2016. **Revised:** May 31, 2016. **Accepted:** June 21, 2016.

Cite this: Süzen Y, Metinoğlu S. SYNTHESIS AND CHARACTERIZATION OF NOVEL INORGANIC AND ORGANIC HYBRID POLY[CYCLOTRIPHOSPHAZENE-co-(4,4'-DIAMINODIPHENYLMETHANE)] MICROSPHERES via ONE-POT SELF-ASSEMBLY POLYCONDENSATION APPROACH. Journal of the Turkish Chemical Society, Section A: Chemistry. 2016; 3(1):167-182.

DOI: 10.18596/jotcsa.36886.

Correspondence to: Yasemin Süzen, e-mail: ysuzen@anadolu.edu.tr.

INTRODUCTION

Recently, research for synthesizing micro or nano-sized particles have paid notable attention with the development of science and technology [1-2]. Among these particles, phosphazene-based polymers have attracted great interest due to their chemical stability, excellent thermal/flame-retardant properties [3-7] and also their applications in biomedical delivery systems [8] and tissue engineering [9]. Apart from the most known linear poly(dichloro)phosphazene containing polymers, cyclomatrix type polyphosphazenes comprise of highly crosslinked framework and can be synthesized by the reaction of hexachlorocyclotriphosphazene (HCCP), which is one of the important inorganic rings and a building block for development of new polymers because of high tunability of its backbone and structural diversity [10-12] with various difunctional alcohols, phenols and diamines [11,13-15].

Fully crosslinked nano/microspheres are generally synthesized via precipitation polymerization approach which has some advantages like avoiding the use of any surfactant or stabilizer [16]. Besides, particle size and morphologies of microspheres can controlled by changing some experimental conditions such ratio of HCCP or reagents, temperature, reaction time and ultrasonic power [17]. In this article, we have synthesized novel inorganic-organic hybrid polyphosphazene microspheres by the reaction of HCCP (hexachlorocyclotriphosphazene) and DADPM (4,4'-diaminodiphenylmethane) in acetonitrile using an ultasonic bath. Otherwise, the effect on formation of microspheres were investigated by storing in darkness and light. Then, characterizations of the microspheres were elucidated by FTIR, SEM-EDX, TGA, ZETA, UV, Fluorescence and XRD.

MATERIALS AND METHODS

HCCP (Aldrich) was recrystallized from dry hexane followed by double sublimation before use. The melting point of the purified HCCP was 113-114°C. 4,4'-diaminodiphenylmethane (DADPM), triethylamine (TEA), acetonitrile and tetrahydrofuran (THF) were purchased from Sigma-Aldrich Company and were used as received. Also, distilled water was used in all experiments.

Characterization of DADPM-MS Microspheres

Scanning electron microscopy (SEM-EDX) measurements were performed on an ZEISS Ultra Plus (ZEISS ULTRA 55, APOLLO XP3) electron microscope. The samples were coated with gold before SEM analyses. Fourier Transform Infrared spectroscopy (FT-IR, Perkin Elmer Spectrum 100 spectrometer) and Thermogravimetric analysis (SETARAM LABSYS, N_2 atmosphere and a heating rate of 20 °C/min) were used to explain the structure and thermal features of the microspheres. Ultraviolet-visible (UV-Vis) absorbance spectra were measured on a Shimadzu UV-3150 spectrometer. The fluorescent spectra measurements were performed on a Varian Cary Eclipse Fluorescence spectrophotometer. Particle size measurements were performed with a Malvern ZEN 3600 instrument. X-ray diffraction (XRD) patterns were recorded by using a Bruker AXS, S8 TIGER Advance instrument equipped with Cu Kα radiation performed at 40 kV and 40 mA.

Synthesis of the DADPM-MS Microspheres

The microspheres were synthesized using precipitation polymerization technique (Tables 1 and 2) [16,18-20]. HCCP and TEA were used as a crosslinker and an acid acceptor, respectively. In a typical synthetic procedure, 3.5 mL of TEA was added to a solution of HCCP and DADPM in acetonitrile (50 mL), in a flask (100 mL). The reaction mixture was stirred at 40°C in an ultrasonic bath (100 W, 53 kHz) for 5 hours. Then, it was stored in darkness for 72 h (Scheme 1). The precipitated polyphosphazene microspheres were isolated by centrifugation (5000 rpm, 30 min), then washed first with THF and afterwards with distilled water three times. Finally, the product was dried under vacuum at 40 °C. The same procedure was used for other molar ratios of HCCP and DADPM.

Table 1. Compositions of microspheres at constant HCCP concentration.

Molar ratio (HCCP:DADPM)	HCCP (g)	DADPM (g)	TEA (mL)
1:1	0.175	0.1	3.5
1:2	0.175	0.2	3.5
1:3	0.175	0.3	3.5
1:4	0.175	0.4	3.5

Table 2. Compositions of microspheres at constant DADPM concentration.

Molar ratio (HCCP:DADPM)	HCCP (g)	DADPM (g)	TEA (mL)
1:1	0.175	0.1	3.5
1:2	0.35	0.1	7.0
1:3	0.52	0.1	10.5
1:4	0.70	0.1	14.0

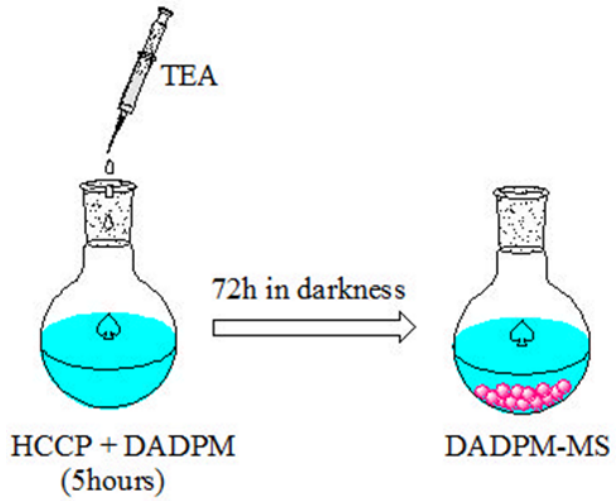

Scheme 1. Preparation of DADPM-MS polyphosphazene microspheres.

RESULTS

The formation of DADPM-MS microspheres was achieved via self-assembly polycondensation reaction of HCCP and DADPM. The optimization of DADPM-MS was made by changing concentrations of HCCP and DADPM in order to obtain the best morphology. Besides, some experiments were performed to determine light and darkness effects on formation of microspheres. Finally, characterization of microspheres was investigated by FTIR, SEM-EDX, TGA, ZETA, UV, Fluorescence and XRD.

Preparation of the DADPM-MS microspheres

Synthetic route and formation mechanism of the DADPM-MS polyphosphazene microspheres are shown in Schemes 2 and 3. HCCP and DADPM were reacted with excessive amount of TEA as an acid acceptor, using acetonitrile as solvent, under ultrasonic conditions via precipitation polymerization without using any stabilizing agent or surfactant [11,17,21]. During the polycondensation, hydrochloric acid (HCl) formed from the nucleophilic substitution reaction between P-Cl bonds and terminal amino groups and was absorbed by TEA to afford TEA.HCl. The generation of TEA.HCl spontaneously accelerated the nucleophilic replacement. HCCP shows function as a cross linker molecule to obtain fully cross-linked polyphosphazene microspheres [24].

In previous studies, formation mechanism of cross-linked polyphosphazene microspheres had been explained as follows [18,22]. At the first stage of the precipitation polymerization, oligomers are formed by reaction between monomer and crosslinker. Then, oligomers aggregate together to form primary nucleus particles. Afterwards, primary stable microspheres are generated through the aggregation of the primary nucleus particles with each other by hydrogen bonds. As soon as the stable particles are generated, the particles grow in size by absorbing oligomeric species instead of primary particles. Hence, microspheres which were acquired at the end of the polymerization, do not have pores inside (see Scheme 3).

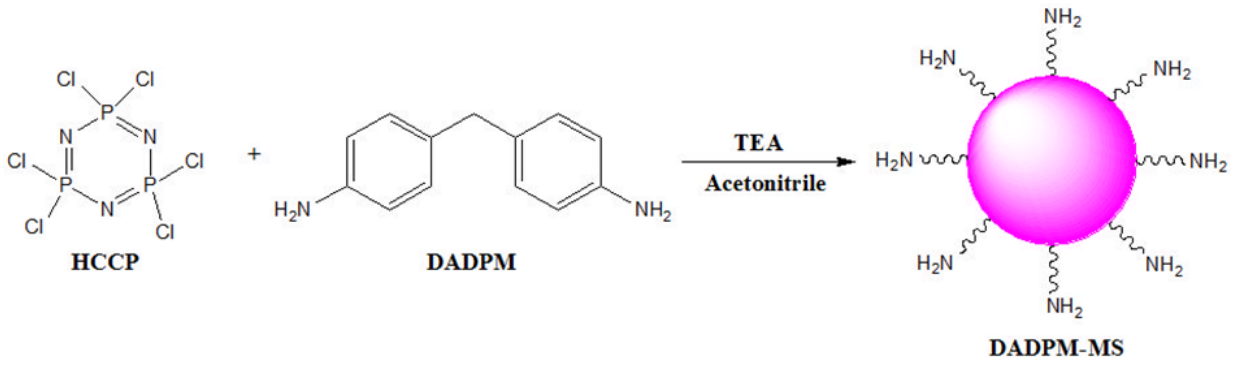

Scheme 2. Synthesis of DADPM-MS polyphosphazene microspheres.

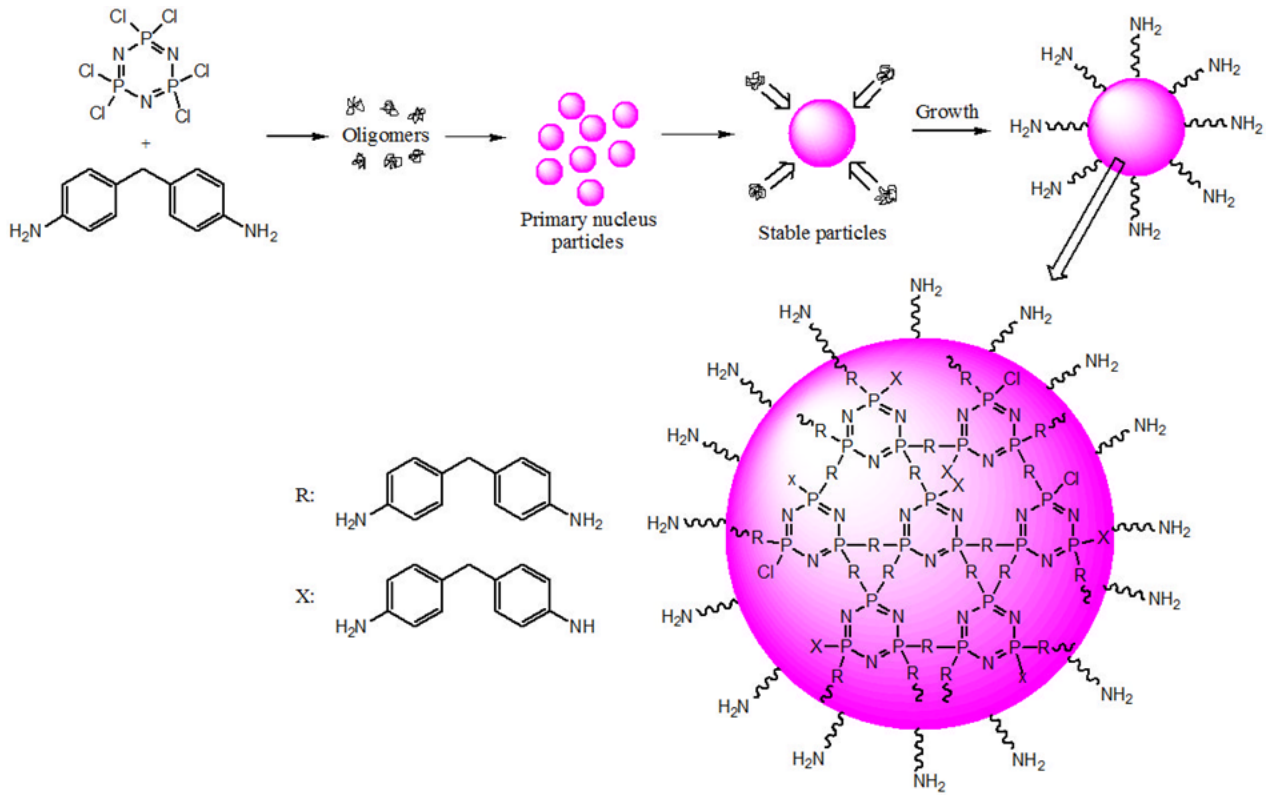

Scheme 3. Schematic illustration of the formation mechanism of the DADPM-MS microspheres.

On the purpose of obtaining the best morphology of microspheres, experiments were performed using different concentrations of HCCP and DADPM. It was observed that in the trials, when DADPM concentration was increased, morphologically better microspheres were obtained (Figure 1). Because DADPM has two functional groups whereas HCCP has six functional groups. So, when DADPM concentration was increased, crosslinking between DADPM and HCCP was better. Besides, it was thought that sizes of obtained primary nucleus particles were approximate. So, the growth of primary nucleus particles are same rate and obtained microspheres were smooth. The Dn value ranged from 4.510 to 4.737 μm and the particle size of the microspheres did not change remarkably with increasing molar ratios of DADPM. The particle-size distribution of as-synthesized microspheres have narrow size distribution as shown in Figure 2. However, it was determined that when HCCP concentration was increased, the crosslinker in polymerization reaction, the formation of microspheres was not smooth and sphericity was broken down (Figure 3). DADPM ratio was the determining factor to form oligomers. When DADPM were run out of in polycondensation reaction, oligomers and primary nucleus particles will not be obtained. Because of oligomers were not form sufficiently, particles could not grow and were not smooth. Besides, multiplet particles were observed increased with molar ratios crosslinker HCCP. Because primary particles can come into collision with each other [16]. SEM images revealed that the best molar ratio was 1:4/HCCP:DADPM (Figures 1 and 3). Thus, all characterization studies were performed using microspheres with obtained from 1:4 molar ratio of HCCP:DADPM.

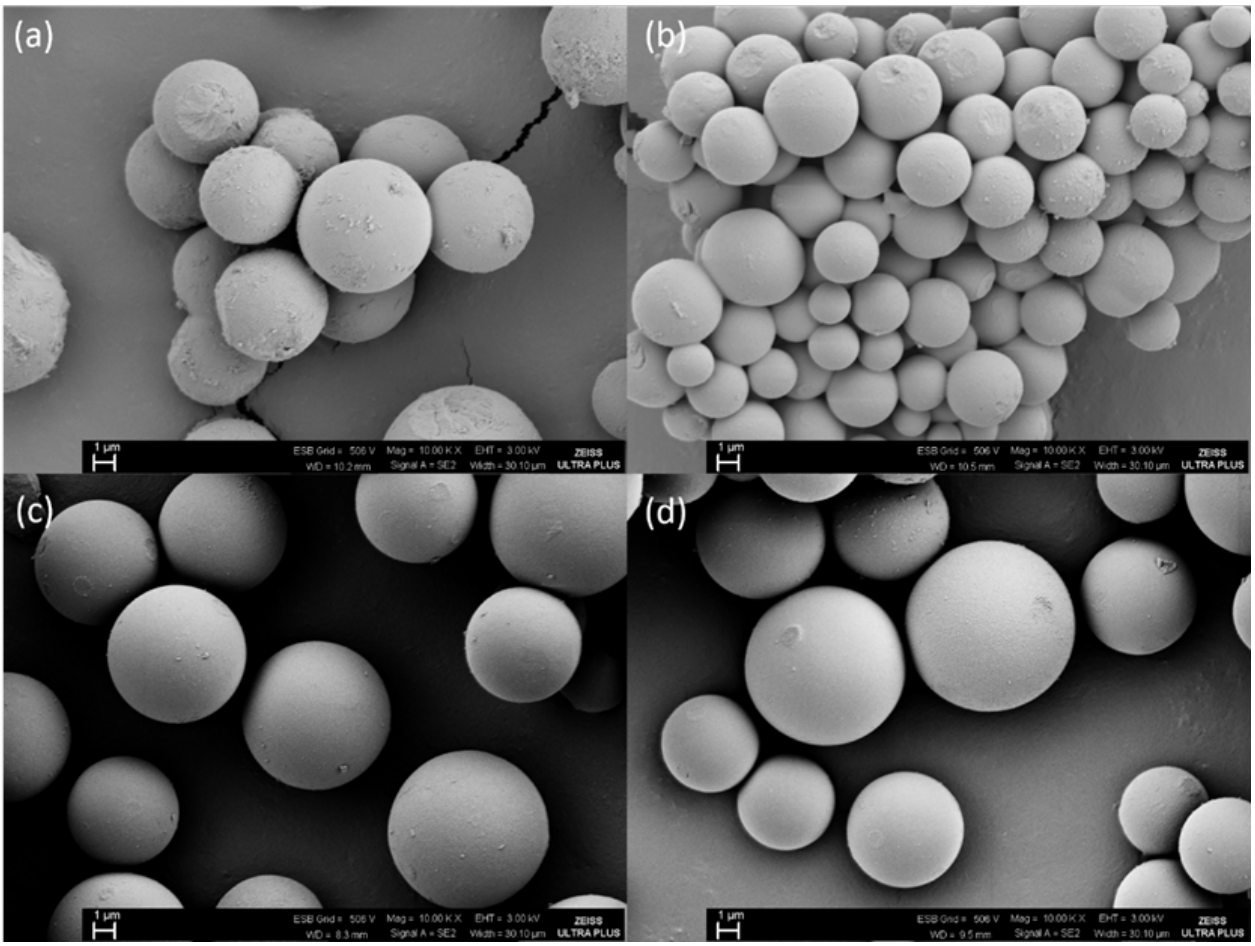

Figure 1. SEM images of (a) 1:1, (b) 1:2, (c) 1:3 and (d) 1:4 (molar ratios) HCCP:DADPM microspheres.

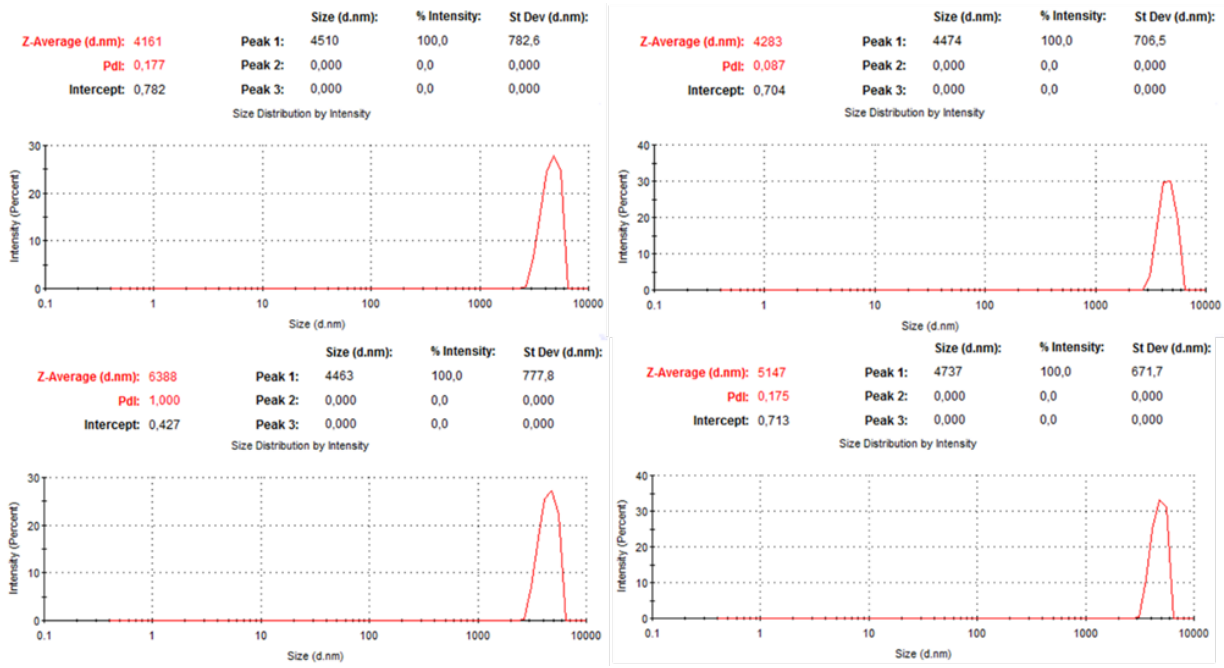

Figure 2. Particle size distributions of microspheres by precipitation polymerization. (a) 1:1, (b)1:2, (c)1:3, (d)1:4 HCCP:DADPM molar ratios.

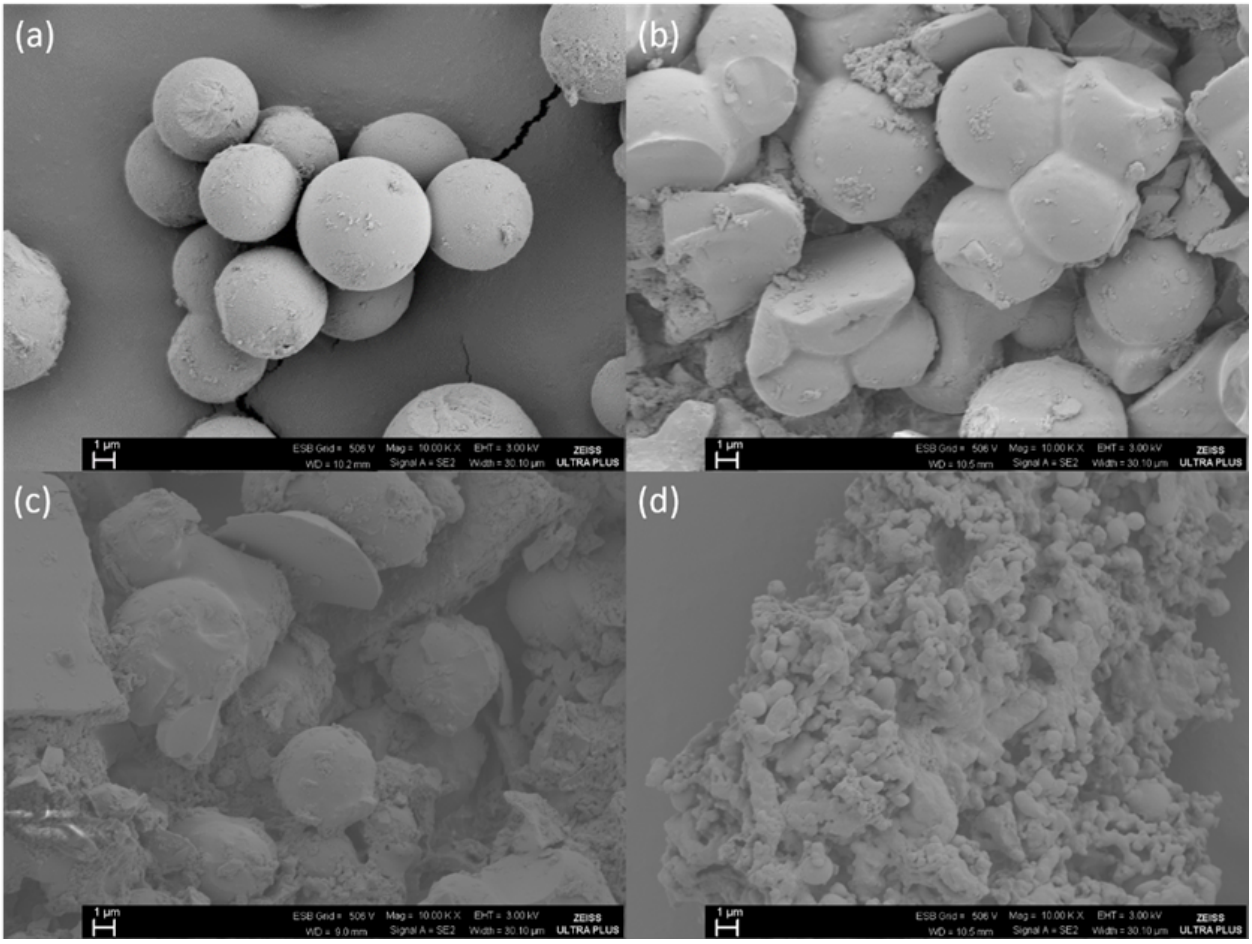

Figure 3. SEM images of (a) 1:1, (b) 2:1, (c) 3:1 and (d) 4:1 (mol. ratios) HCCP:DADPM microspheres.

Besides, it was thought that during the 5-hour reaction, only the oligomers obtained by polycondensation reaction of HCCP and 4,4'-DADPM and primary nucleus particles did not precipitate by aggregation of oligomers in 5 hours. Therefore, the reaction medium was stored in darkness and precipitation began to form in the flask. After storing for 18 hours in the dark, the precipitated product was analyzed by SEM and it was observed that formation of the microspheres were started but was not totally completed yet. On the other hand, after 72 hours in the dark, when the precipitated product was analyzed by SEM, it was seen that the formation of microspheres were completed and were morphologically good spheres (Figure 4). Also, when compared the EDX results of microspheres which were stored in the darkness for both 18 and 72 hours, it was determined that in EDX spectrum of microspheres which were stored 72 hours in the darkness, P (13.46%) and N (13.69%) ratios were similar and chloride ratio (3.99%) was lower (Figure 5a). However, the EDX spectrum of microspheres, which were stored 18 hours in the darkness, indicated the following values: P (08.56%), N (14.39%) and Cl (04.29%) (Figure 5b). When the reaction medium was stored in light for 72 hours, instead of darkness, it was seen that sphericity did not totally complete and formed a different morphology except sphericity (Figure 6a). Moreover, the yield of microspheres which were obtained in light was lower (59%) than that in the darkness (76%).

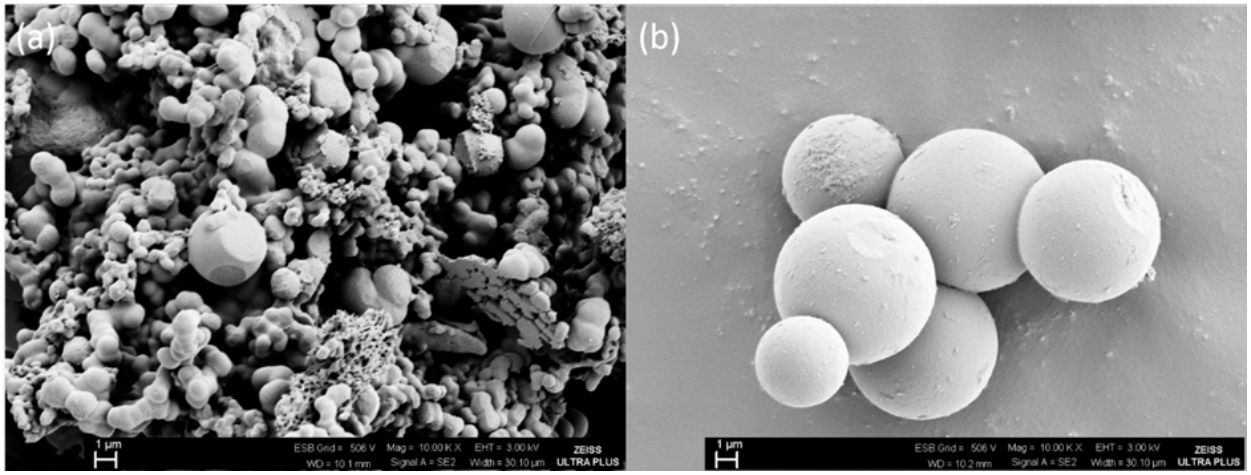

Figure 4. SEM images of DADPM-MS (1:1) which were stored in darkness (a) 18 hours (b) 72 hours.

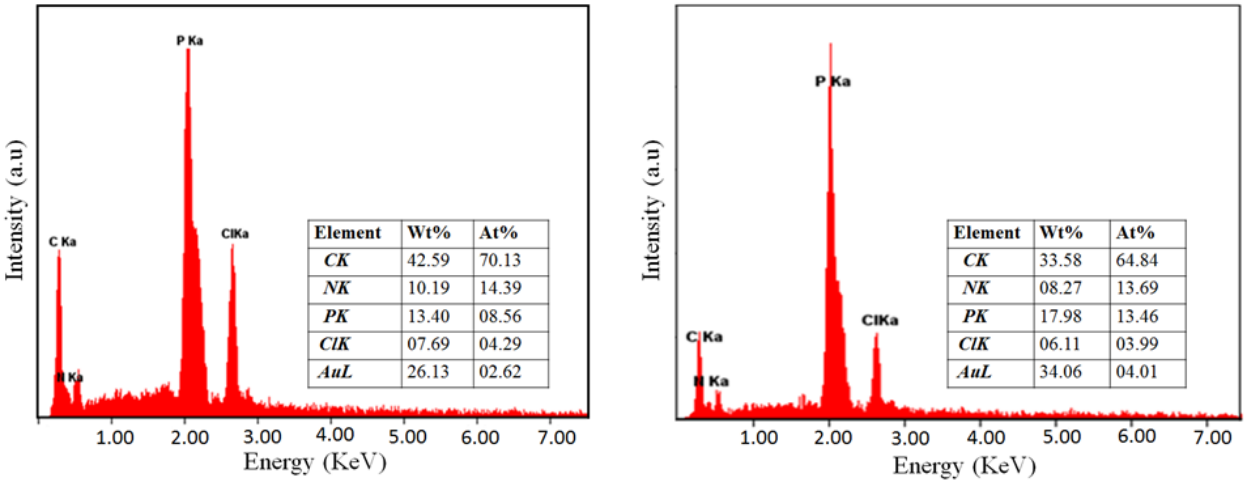

Figure 5. EDX spectra of DADPM-MS (1:1) which were stored in darkness for (a) 18 hours (b) 72 hours.

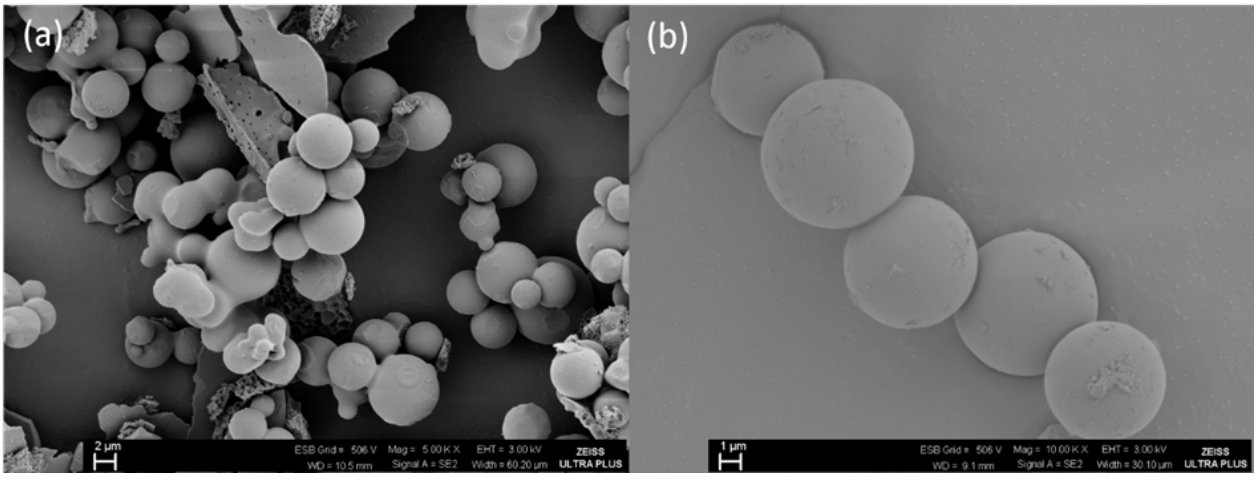

Figure 6. SEM images of DADPM-MS (1:1) which were stored in light (a) and darkness (b) 72 hours.

FTIR spectral analysis

The chemical structure of the microspheres (1:4 HCCP:DADPM) was characterized by FT-IR. As shown in Figure 7, N-H stretching and bending bands indicating the existence of primary amine groups on the microspheres were observed at 3336–3182 (1, 2) and 1613 cm^{-1} (6), respectively. The absorption at 3027 cm^{-1} (3) was assigned to the aromatic C–H stretching vibration of aromatic rings. Aliphatic C-H stretching vibrations can be seen at 2905 and 2841 cm^{-1} (4, 5). Aromatic C-C stretching bands correspond to 1509, 1452 and 1378 cm^{-1} (7, 8, 9). C-N stretching band was observed at 1288 cm^{-1} (10). Furthermore, the characteristic P=N and P-N absorption bands of HCCP were observed at 1253, 1166 and 934 cm^{-1} (11, 12, 13), respectively. The weak P-Cl bands at 568 and 504 cm^{-1} (14, 15) showed that microspheres still contain chloride atoms in small quantities [16, 19]. Obviously, the FTIR spectrum of DADPM-MS contain characteristic bands which are expected from the polymeric structure synthesized from HCCP and DADPM molecules. Thus, the polycondensation reaction between HCCP and DADPM has been successfully achieved.

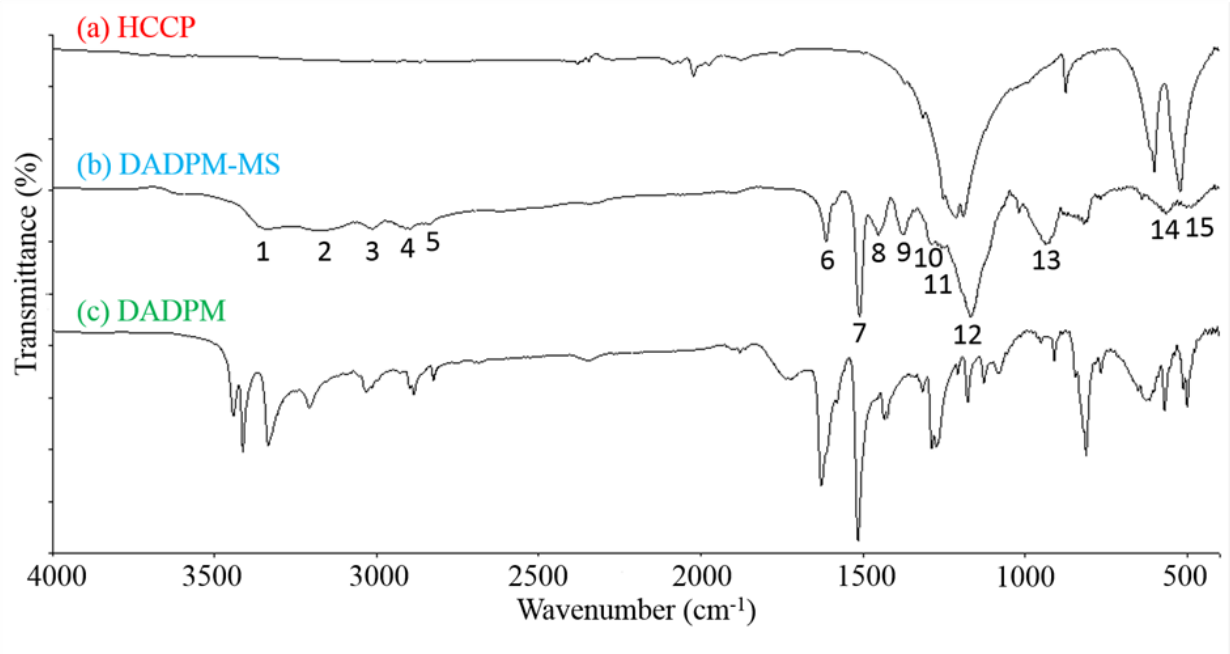

Figure 7. FT-IR spectra of HCCP, DADPM-MS, and DADPM.

Thermal properties

The thermal properties of the DADPM-MS obtained from the precipitation polymerization were also characterized with thermogravimetric analyses (Figure 8). A mass loss of 5% below 100 °C was observed due to the desorption of adsorbed water. Remarkably, under nitrogen atmosphere, it was indicated that the material was thermally stable up to a temperature of 415 °C and a sharp mass loss was observed from 415 to 784 °C that is likely to be associated with carbonization of the organic groups and the depolymerization of the P–N framework in the fully crosslinked structures [23,27].

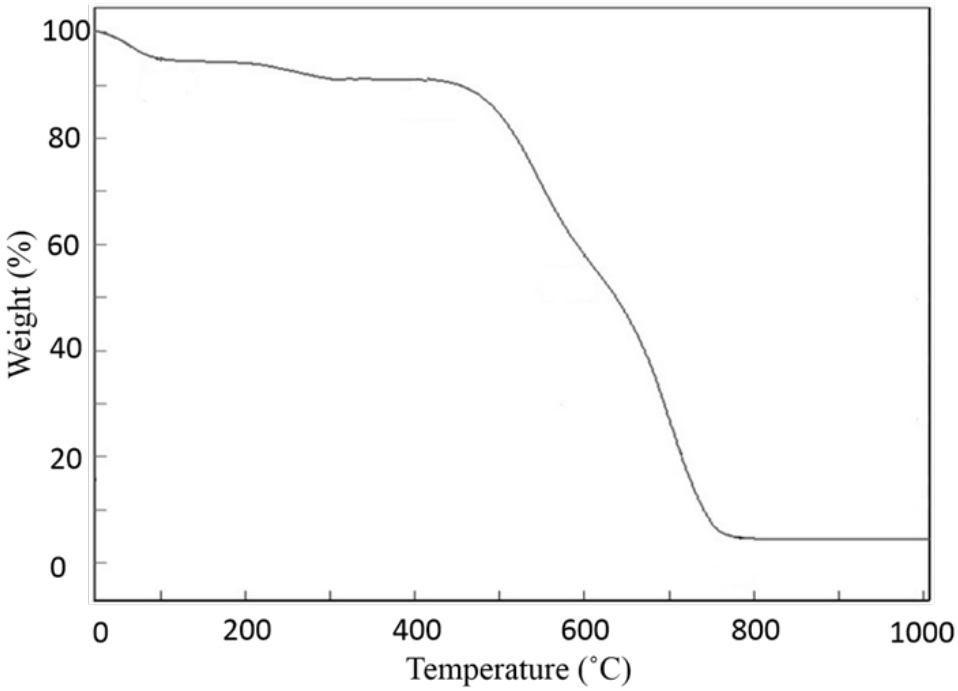

Figure 8. TGA curve of DADPM-MS (1:4).

Optical and crystallographic properties

Microspheres (DADPM-MS) were dispersed in methanol under ultrasonic conditions and the UV and fluorescence properties were investigated. DADPM and DADPM-MS displayed absorption peaks at 290 and 245 nm in methanol, respectively (Figure 9). It was understood that DADPM-MS does not absolutely have an absorption of light in the visible range. The fluorescence emission spectra of DADPM and DADPM-MS of which were dispersed in methanol are shown in Figure 10. DADPM revealed a fluorescent emission peak at 349 nm when excited with 280 nm light. Similarly, DADPM-MS displayed a fluorescence emission peak at 347 nm when excited with 240 nm light because of π-conjugation in the polymeric structure.

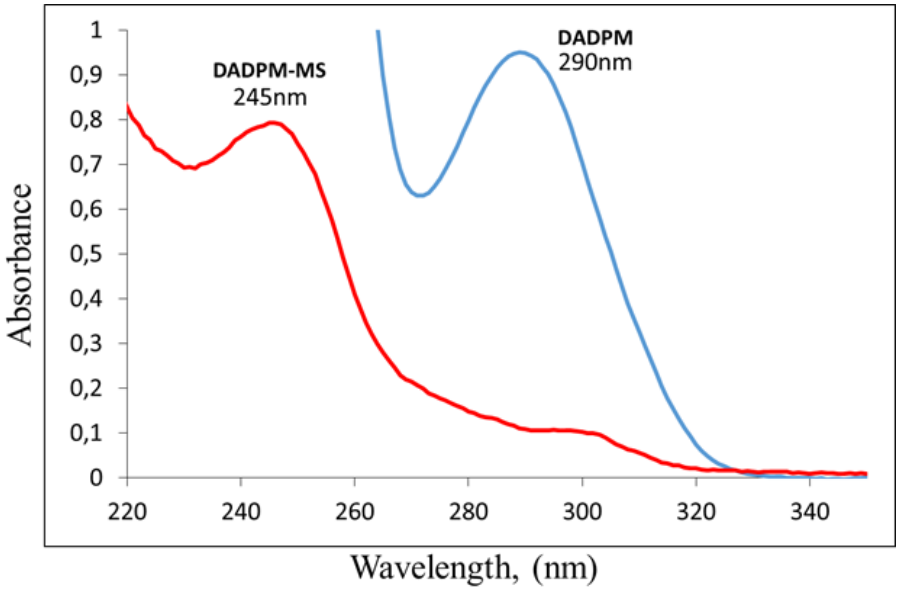

Figure 9. UV absorption spectra of DADPM-MS (a) and DADPM (b) in methanol.

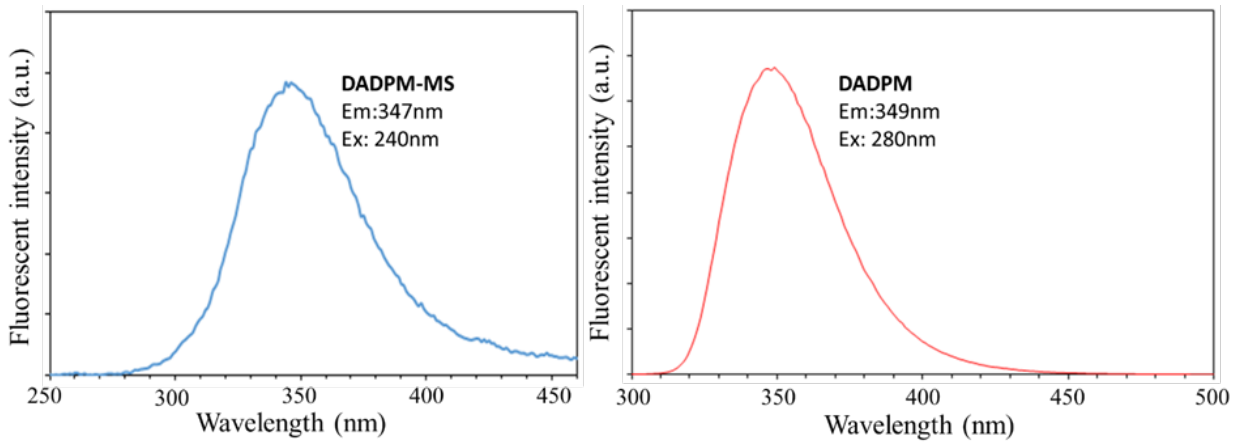

Figure 10. Fluorescent emission spectra of DADPM-MS (left) and DADPM (right) in methanol.

The XRD patterns of the powder DADPM-MS microspheres indicated a broad diffraction peak corresponding typical amorphous structure (see Figure 11) [17, 25, 26].

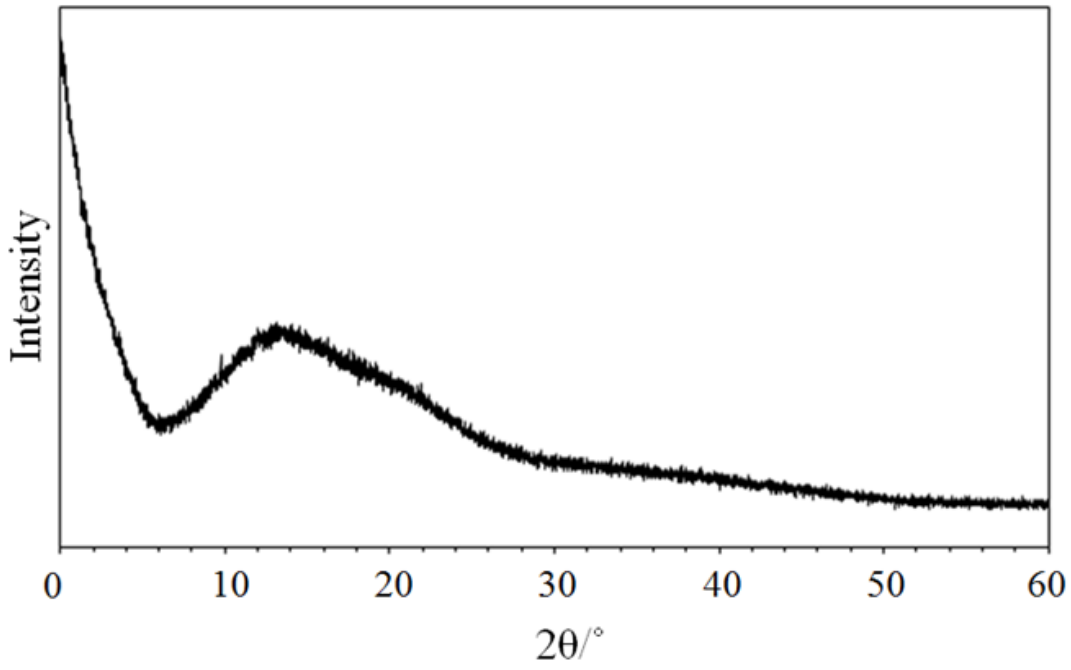

Figure 11. XRD spectrum of DADPM-MS.

CONCLUSION

In conclusion, inorganic-organic hybrid cross-linked polyphosphazene microspheres, DADPM-MS, were synthesized by polycondensation reaction between HCCP and DADPM. Variable HCCP and DADPM mol ratios were studied and morphologically the best ratio was determined as (1:4) HCCP:DADPM. The size range of obtained microspheres were 4.510 to 4.737 μm. The storage time in darkness was determined 72 hours to complete the formation of microspheres by SEM-EDX. It was seen that storing in darkness is more effective than light to obtain morphologically good spheres by SEM. FTIR spectra demonstrated that the formation of the microspheres were achieved succesfully when compared with the FTIR spectra of HCCP and DADPM molecules. On the other hand, the TGA measurement showed that the obtained microspheres have perfect thermal stability and the thermal degradation temperature was determined as 415 ºC. DADPM-MS indicated UV and fluorescent property because of π-conjugation of aromatic rings in the polymeric structure. Also, it was understood, from the XRD spectrum, that microspheres have characteristic amorphous structure.

ACKNOWLEDGMENTS

The authors acknowledge to the "Anadolu University, Scientific Researches Unit'' Grant No. 1505F309 for their financial support.

REFERENCES

[1] Pan T, Huang X, Wei H, Tang X. Controlled Fabrication of Uniform Hollow Bowl-Shaped Microspheres Based on Polyphosphazene Material. Macromolecular Chemistry and Physics. 2012 Dec 21;213(24):2606–10. DOI: 10.1002/macp.201200441.

[2] Zhu Y, Huang X, Fu J, Wang G, Tang X. Morphology control between microspheres and nanofibers by solvent-induced approach based on crosslinked phosphazene-containing materials. Materials Science and Engineering: B. 2008 Sep;153(1-3):62–5. DOI: 10.1016/j.mseb.2008.10.027.

[3] Mathew D, Nair CR, Ninan K. Phosphazene-triazine cyclomatrix network polymers: some aspects of synthesis, thermal- and flame-retardant characteristics. Polymer International. 2000 Jan;49(1):48–56. DOI: 10.1002/(SICI)1097-0126(200001)49:1<48::AID-PI309>3.0.CO;2-M.

[4] Zhang T, Cai Q, Wu D-Z, Jin R-G. Phosphazene cyclomatrix network polymers: Some aspects of the synthesis, characterization, and flame-retardant mechanisms of polymer. Journal of Applied Polymer Science. 2005 Feb 15;95(4):880–9. DOI: 10.1002/app.21295.

[5] Gleria M, De Jaeger R. Polyphosphazenes: A Review. In: New Aspects in Phosphorus Chemistry V [Internet]. Springer; p. 165–251. (Topics in Current Chemistry; vol. 250). ISBN: 978-3-540-22498-3.

[6] Stone DA, Allcock HR. A New Polymeric Intermediate for the Synthesis of Hybrid Inorganic−Organic Polymers. Macromolecules. 2006 Jul;39(15):4935–7. DOI: 10.1021/ma061079g.

[7] Zhou Y, Huang X, Kang X, Fu J, Zhu Y, Tang X. Synthesis and Characterization of Novel Polyurethane Composites Based on Hybrid Inorganic/Organic Phosphazene-Containing Microspheres. Macromolecular Materials and Engineering. 2009 Sep 14;294(9):605–10. DOI: 10.1002/mame.200900161.

[8] Shim D-H, Ko H-J, Volker G, Potter AA, Mutwiri G, Babiuk LA, et al. Efficacy of poly[di(sodium carboxylatophenoxy)phosphazene] (PCPP) as mucosal adjuvant to induce protective immunity against respiratory pathogens. Vaccine. 2010 Mar;28(11):2311–7. DOI: 10.1016/j.vaccine.2009.12.069.

[9] Nichol JL, Morozowich NL, Allcock HR. Biodegradable alanine and phenylalanine alkyl ester polyphosphazenes as potential ligament and tendon tissue scaffolds. Polym Chem. 2013;4(3):600–6. DOI: 10.1039/C2PY20631E.

[10] Allcock HR. THE CRUCIAL ROLE OF INORGANIC RING CHEMISTRY IN THE DEVELOPMENT OF NEW POLYMERS. Phosphorus, Sulfur, and Silicon and the Related Elements. 2004 Apr;179(4-5):661–71. DOI: 10.1080/10426500490426386.

[11] Zhu Y, Fu J, Zhu L, Tang X, Huang X. Preparation of novel hybrid inorganic-organic hollow microspheres via a self-template approach. Polymer International. 2008 Mar;57(3):449–53. DOI: 10.1002/pi.2366.

[12] Singh A, Krogman NR, Sethuraman S, Nair LS, Sturgeon JL, Brown PW, et al. Effect of Side Group Chemistry on the Properties of Biodegradable L -Alanine Cosubstituted Polyphosphazenes. Biomacromolecules. 2006 Mar;7(3):914–8. DOI: 10.1021/bm050752r.

[13] Zhu L, Zhu Y, Pan Y, Huang Y, Huang X, Tang X. Fully Crosslinked Poly[cyclotriphosphazene-co-(4,4′-sulfonyldiphenol)] Microspheres via Precipitation Polymerization and Their Superior Thermal Properties. Macromolecular Reaction Engineering. 2007 Jan 9;1(1):45–52. DOI: 10.1002/mren.200600005.

[14] Fu J, Huang Y, Pan Y, Zhu Y, Huang X, Tang X. An attempt to prepare carbon nanotubes by carbonizing polyphosphazene nanotubes with high carbon content. Materials Letters. 2008 Sep;62(25):4130–3.

[15] Zhang P, Huang X, Fu J, Huang Y, Tang X. Fabrication of Amino-Terminated Multiwalled Carbon Nanotubes via Layer-by-Layer Self-Assembly Approach. Macromolecular Materials and Engineering. 2010 Mar 2;4130 – 4133. DOI: 10.1016/j.matlet.2008.06.020. DOI: 10.1002/mame.200900306.

[16] Zhang P, Huang X, Fu J, Huang Y, Zhu Y, Tang X. A One-Pot Approach to Novel Cross-Linked Polyphosphazene Microspheres with Active Amino Groups. Macromolecular Chemistry and Physics. 2009 May 6;210(9):792–8. DOI: 10.1002/macp.200800597.

[17] Wang Y, Mu J, Li L, Shi L, Zhang W, Jiang Z. Preparation and properties of novel fluorinated cross-linked polyphosphazene micro-nano spheres. High Performance Polymers. 2012 May 1;24(3):229–36. DOI: 10.1177/0954008311436221.

[18] Pan T, Huang X, Wei H, Wei W, Tang X. Intrinsically Fluorescent Microspheres with Superior Thermal Stability and Broad Ultraviolet-Visible Absorption Based on Hybrid Polyphosphazene Material. Macromolecular Chemistry and Physics. 2012 Aug 14;213(15):1590–5. DOI: 10.1002/macp.201200099.

[19] Wei W, Huang X, Chen K, Tao Y, Tang X. Fluorescent organic–inorganic hybrid polyphosphazene microspheres for the trace detection of nitroaromatic explosives. RSC Advances. 2012;2(9):3765. DOI: 10.1039/c2ra20263h.

[20] Köhler J, Kühl S, Keul H, Möller M, Pich A. Synthesis and characterization of polyamine-based cyclophosphazene hybrid microspheres. Journal of Polymer Science Part A: Polymer Chemistry. 2014 Feb 15;52(4):527–36. DOI: 10.1002/pola.27028.

[21] Wang M, Fu J, Chen Z, Wang X, Xu Q. In situ growth of gold nanoparticles onto polyphosphazene microspheres with amino-groups for alcohol oxidation in aqueous solutions. Materials Letters. 2015 Mar;143:201–4. DOI: 10.1016/j.matlet.2014.12.114.

[22] Zhao Z, Ji J. Synthesis and Tribological Behaviors of Epoxy/Phosphazene-Microspheres Coatings under Dry Sliding Condition: Synthesis and Behaviors of Epoxy/Phosphazene-Microspheres Coatings. Advanced Engineering Materials. 2014 Aug;16(8):988–95. DOI: 10.1002/adem.201300491.

[23] Mohanty P, Landskron K. Simple systematic synthesis of size-tunable covalent organophosphonitridic framework nano- and microspheres. New Journal of Chemistry. 2010;34(2):215. DOI: 10.1039/b9nj00446g.

[24] Xu R, Pang W, Huo Q, editors. Modern inorganic synthetic chemistry. Amsterdam: Elsevier; 2011. 590 p. ISBN: 9780444535993.

[25] Hu Y, Meng L, Niu L, Lu Q. Highly Cross-Linked and Biocompatible Polyphosphazene-Coated Superparamagnetic Fe 3 O 4 Nanoparticles for Magnetic Resonance Imaging. Langmuir. 2013 Jul 23;29(29):9156–63. DOI: 10.1021/la402119s.

[26] Tarassoli A, Sedaghat T, Ansari-Asl Z. Surface functionalization of phosphazenenanosphere derivatives by Schiff-base-assisted metal complexes through a Si-spacer. Journal of Industrial and Engineering Chemistry. 2014 Jul;20(4):2287–91. DOI: 10.1016/j.jiec.2013.10.003.

[27] Wang X, Fu J, Chen Z, Li Q, Wu X, Xu Q. Hollow polyphosphazene microspheres with cross-linked chemical structure: synthesis, formation mechanism and applications. RSC Adv. 2015;5(43):33720–8. DOI: 10.1039/C5RA00560D.

Research article

YENİ ANORGANİK VE ORGANİK HİBRİD POLİ[SİKLOTRİFOSFAZEN-co-(4,4'-DİAMİNODİFENİLMETAN)] MİKROKÜRELERİNİN TEK ORTAM İÇERİSİNDE KENDİLİĞİNDEN DÜZENLENMELİ POLİKONDENZASYON YAKLAŞIMI İLE SENTEZİ VE KARAKTERİZASYONU

Öz: Çapraz bağlı siklomatriks polifosfazen mikroküreler, hekzaklorosiklotrifosfazen (HCCP) ile 4,4'-diaminodifenilmetanın (DADPM) asetonitril ortamında kendiliğinden düzenlenmeli polikondenzasyon tepkimesi sonucu, başarı ile sentezlenmiştir. Herhangi bir stabilize edici ajan veya surfaktant gerektirmemesi ve sadece ultrasonik banyo kullanımı bu reaksiyonun avantajlarıdır. SEM-EDX ile en iyi morfolojiyi elde etmek için, HCCP ve DADPM oranları değişimi denenmiştir. Mikrokürelerin boyutları 4,46 ile 4,74 μm arasında değişmektedir. Anorganik-organik hibrid mikroküreler FTIR, TGA, UV, Fluoresans ve XRD ile karakterize edilmiştir.

Anahtar kelimeler: Siklomatriks mikroküreler, polifosfazen, kendiliğinden düzenlenme, çöktürme polimerizasyonu.

Sunulma: 11 Mayıs 2016. **Düzenleme:** 31 Mayıs 2016. **Kabul:** 21 Haziran 2016.

JOTCSA, Volume 3, issue 2, (2016), pp. 183-206. **Research article**

Journal homepage: http://dergipark.ulakbim.gov.tr/jotcsa

e-ISSN: 2149-0120

Structural Characterization and Gas Permeation Properties of Polyetherimide (PEI)/Zeolitic imidazolate (ZIF-11) Mixed Matrix Membranes

Mehtap ŞAFAK BOROĞLU[1]*

[1]Department of Chemical Engineering, Faculty of Engineering, Istanbul University, Istanbul, Turkey.

Abstract: In this study, the preparation of polyetherimide (PEI-Ultem1000)/ZIF-11 mixed matrix membranes was studied in various ZIF-11 particle loadings (0, 10, 15, 20, and 30 wt.%). The newly synthesized ZIF-11 submicron particles with an average particle size of ~280 nm were integrated in PEI membranes as novel mixed matrix membranes (MMMs). The effect of ZIF-11 loading was scrutinized for H_2, CO_2, and CH_4 gas separation performances at 35 °C and 4 bar. The incorporation of ZIF-11 submicron particles improved the gas permeation properties of the MMMs with an increase in ZIF-11 loading. As the ZIF-11 loading increased up to 20 wt.%, the permeability of H_2 and CO_2 increased to four times higher than that of the pure polymer. Moderate increase of CH_4 permeability was also recorded. At higher loadings above 20 wt.%, the permeability decreased for all gases and the CO_2/CH_4, and H_2/CH_4 selectivities increased consistent with the ZIF-11 loading.

Keywords: Metal organic frameworks, zeolite imidazolate frameworks, polyetherimide, gas separation.

Submitted: May 28, 2016. **Revised:** June 24, 2016. **Accepted:** June 28, 2016.

Cite this: ŞAFAK BOROĞLU M. STRUCTURAL CHARACTERIZATION AND GAS PERMEATION PROPERTIES OF POLYETHERIMIDE (PEI)/ZEOLITIC IMIDAZOLATE (ZIF-11) MIXED MATRIX MEMBRANES. Journal of the Turkish Chemical Society, Section A: Chemistry. 2016;3(2):183–206.

DOI: 10.18596/jotcsa.36886.

Correspondence to: Mehtap ŞAFAK BOROĞLU, e-mail: mehtap@istanbul.edu.tr.

INTRODUCTION

The gas separation by membranes is an active and rapidly growing research area. In membrane-based gas separation processes, components are separated from their mixtures by differential permeation through membranes. Some technologies (*e.g.* distillation and absorption processes) prescribe a phase change in the mixture. The change of this phase adds a significant energetic disadvantage. On the other hand, gas separation by the membrane does not necessitate a phase change (1). The gas separation membrane market has grown significantly and continued progression is expected to escalate in the coming years as technology improves and applications are multiplied (2). Membrane technology for gas separation has been carried out in a variety of applications, such as, oxygen, nitrogen enrichment, hydrogen recovery, and natural gas dehydration (3). However, the development of polymeric membrane separation technology has been necessitated by a so-called performance upper bound in the trade-off curve between the gas permeability and selectivity (4). Permeability and selectivity trade-off for gas pairs were well illustrated in the so-called Robeson Plots (5). There is tremendous research effort to surpass Robeson trade-off limit curve by adding creative additives into appropriate polymeric material (6). Addition of synthetic nanoparticles compatible with polymers, known as mixed matrix membranes (MMMs), was the one of the approaches to advance membrane separation processes (7,8). MMMs combine the potential advantages of both inorganic particles and organic polymer membranes, such as, superior permeability and selectivity of the inorganic particles with good processability and mechanical properties of the polymer membranes (9). MMMs which were prepared from different inorganic and organic materials produced superior separation performance due to the incorporation of synthetic molecular sieves and Metal Organic Frameworks (MOFs) are a relatively new class of microporous materials, and consist of transition metals and transition metal oxides connected by organic linkages to create one-, two- and three-dimensional microporous structures (10). The recent development in the synthesis of MOFs led to the promising applications as drug delivery carriers, storage media, adsorbents for separations, and catalysts (11–13). They have large surface area, affinity towards certain gases and controlled porosity (14). The main advantage of MOFs over well-known nanoporous materials was the ability to arrange their chemical and physical properties during synthesis process by changing the combination of metals and organic linkers (15). Zeolitic imidazolate frameworks (ZIFs) have received world-wide attention to enhance MMMs' compatibility and permeability (16). Several ZIFs have been synthesized in the literature and considered as potential candidates for gas separations due to the diversity in their pore sizes, higher thermal and chemical stability compared to zeolites and other MOFs (17). Yaghi and co-workers have developed various zeolitic topologies, such as rhombic dodecahedron (RHO) and sodalite (SOD) topologies (18). Particularly, several ZIFs have been successfully prepared to be incorporated into mixed matrix membranes. ZIF-8 type metal organic framework was the most widely used one and reported due to the enhanced membrane performances (19). Selfert and co-workers showed that ZIF-11 has exceptional thermal and chemical properties and ZIF-11 has bigger H2 adsorption energies than that on ZIF-8 (20). Keskin *et al.* reported that ZIF-11 was settled above the upper bound because of higher CO_2 selectivity (>100) and permeability (104−105 Barrer). Molecular simulation results showed that this high CO_2 selectivity resulted from the large differences in diffusion rates of CO_2 and CH_4 gases in the ZIFs' pores (17).

ZIF-11 has been obtained through solvothermal synthesis by using diethylformamide (DEF) as solvent (21). RHO type zeolite structure ZIF-11 has larger cavities of 14.6 Å connected with the pore apertures of 3.0 Å. These preferable properties make it suitable for H_2 separation (Figure 1) (22). Difficulties in removing DEF from the pores of ZIF-11, Wang *et al.* studied a new synthetic method at room temperature by using methanol as solvent and toluene as the structure template (23).

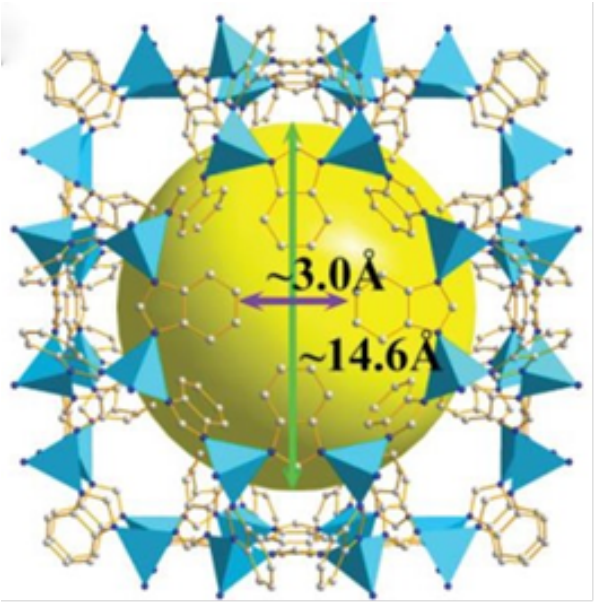

Figure 1. Crystalline structure of ZIF 11 (RHO) particle (23).

Commercial polyetherimide (PEI-Ultem1000) has several important advantages as an organic membrane material. As one of them, PEI has high diffusivity selectivity provided by their rigid backbones and fused ring structures. These properties render them attractive in polymeric membrane developed for gas separations. PEI's glass transition temperature was 216 °C and high T_g temperature allowed the usage of higher pressures and temperatures in applications without plastic deformation. The studies on gas permeation of the PEI dense films revealed that PEI exhibited high selectivity for many important gas pairs especially He and H_2 separation from other gases (24).

In this work, ZIF-11 particles were synthesized and used as filler, and PEI (Ultem 1000) as the continuous phase were utilized to prepare MOF-based mixed matrix membranes for CO_2/CH_4, H_2/CH_4, H_2/CO_2 separation. The separation performance of these MMMS as a function of ZIF-11 loading in the PEI matrix was systematically investigated. The thermal, morphological, and gas separation properties of the synthesized membranes have been investigated using XRD, FTIR, SEM, TGA, DSC, and single gas permeation setup.

MATERIALS AND METHODS

Materials

Polyetherimide (Ultem® 1000) was purchased from Sigma Aldrich, Germany. Typical chemical structure of PEI and some properties were shown in Figure 2 and Table 1. Zinc acetate dihydrate ($C_4H_6O_4Zn.2H_2O$, ≥98%, Sigma-Aldrich, USA) was used as a source of zinc. Benzimidazole ($C_7H_6N_2$, BIm, > 98%, Sigma-Aldrich, Germany) was the primary ligand used. Ammonium hydroxide (NH_3, min. 25% aqueous solution) was purchased from Lachema, Czech Republic and all chemicals were used without further purification. N-Methyl-2-pyrrolidone (NMP, >99.5%), methanol (for analysis) and toluene (>99.9%) were purchased from Merck. Single gases used in the permeation experiments were carbon dioxide (CO_2), methane (CH_4) and hydrogen (H_2) of gas chromatographic grades (purities >99.8 %) from Linde Gas Company (Linde Gaz, Turkey). The properties of gases are given in Table 2.

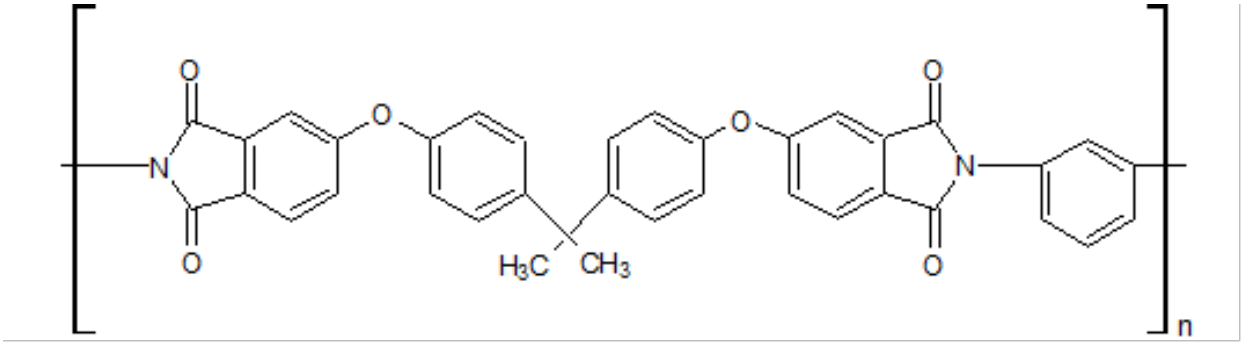

Figure 2. The chemical structure of PEI (Ultem 1000).

Table 1. Physical properties of unmodified PEI (Ultem 1000).

Properties	Symbol	Value
Molecular weight (kg/kmol)	M_w	55,000
Glass Transition Temperature (°C)	T_g	216
Density (kg/m^3)	d	1270
Melting Point (°C)	T_m	219

Table 2. Properties of H_2, CH_4 and CO_2.

Gases	Critical temperature (K)	Critical Volume (cm^3/mol)	Kinetic diameters (nm)
H_2	33.20	64.9	0.289
CH_4	190.6	98.6	0.380
CO_2	304.2	91.9	0.330

EXPERIMENTAL PROCEDURE

Preparation of ZIF-11 particles

The recipe for the synthesis of ZIF-11 powder was a modified version of the method developed by the Wang and Yaghi group (23,25). In the synthesis of ZIF-11 submicron particles, 4.8 g of BIm (4 mmol) was dissolved in 16.61 g of methanol, followed by the addition of 20.88 g of toluene (226.6 mmol). 0.14 g of NH_3 (aq) (4.014 mmol) was added into the solution at room temperature. 4.4 g of zinc acetate dihydrate (20 mmol) was added and stirred for 2 h at room temperature to complete the crystallization step. The final solution had a Zn: BIm : NH_3 : C_2H_5OH : toluene molar composition of 1 : 2 : 2 : 300 : 100. After 2 hours, the as-synthesized submicron particles were collected by centrifugation and then washed with anhydrous methanol. After 2nd centrifugation, the particles were re-suspended in methanol prior to use. By doing this, the particle agglomeration occurring in the drying process can be avoided, as suggested in a report (26). The yield of ZIF-11 was about 90% on the basis of the amount of zinc element.

Membrane preparation

Fabrication of PEI Solution: Prior to use, PEI powder were dried overnight at 120 °C under vacuum and the desired polymer solution (15 wt.%) was prepared by dissolving a certain amount of PEI in NMP by stirring it for 24 h at room temperature until a clear uniform viscous solution was obtained.

Membrane Formation: Dense MMMs were prepared using the solution casting method. ZIF-11 particles were slurried into NMP solvent and sonicated 2 hours to obtain a homogenous dispersion. Ultrasonication Water Bath, VWR, was operated at 120 W and 40 Hz. After sonication, ZIF-11 particles stirred 1 day to fully disperse the fine powder. ZIF-11 crystals were first "primed" by adding a small amount, approximately 10 wt.% of the total PEI solution to the ZIF-11 mixture, after which the mixture was further stirred 2 hours and sonicated for another 30 min. Next, another 10 wt.% of PEI polymer was added into the solution. The suspension was stirred for 30 min and then bath sonicated for 30 min. After five additional iterations of stirring and sonication, the mixture was stirred overnight. Then, a final 30-min sonication period was completed before casting to remove any trapped air bubbles. After degassing the polymer solution, uniform films were cast on a glass plate by a film applicator. Mixed-matrix membranes were formed using 0-10-20-30 wt.% suspensions of ZIF-11 loadings in the polymer solution. The particle loadings of ZIF-11 particles in the MMMs were calculated based on the following equations (Eq. 1).

$$Particle\ \ loading\ \ wt.\% = \frac{Weight\ \ of\ \ particle}{(weight\ \ of\ \ particle + weight\ \ of\ \ polymer)} \times 100 \quad \textbf{(Eq. 1)}$$

Thermal annealing procedures: Membranes were cast on a glass plate using 400 µm film applicator. Thermal annealing of PEI MMMs membranes was conducted with a vacuum oven equipped with a temperature controller. Membranes were placed in the oven and heated to the required temperatures. After casting, the membranes were dried in the vacuum oven at 70 °C at 0.3 atm vacuum for at least 4 days to remove the solvent. Then, the dense films were formed and peeled off from the plate and placed into the vacuum oven to be further vacuum dried at 100 °C for 24 h and 120 °C for 24 h to remove any residual solvents. The membrane thickness was determined using RVS Micrometer. The resultant membranes had a thickness of 50±10 µm. The PEI and PEI-ZIF-11 mixed matrix membranes with a loading of 0-10-15-20-30 wt.% ZIF-11 was transparent with good flexibility as shown in Figure 3.

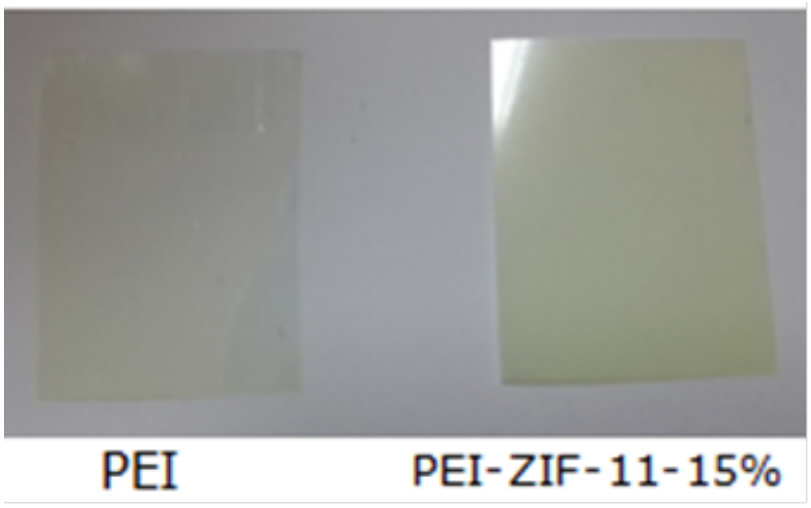

Figure 3. Image of PEI and PEI-ZIF-11-15% membranes.

Apparatus

The crystallographic structure of samples was analyzed using a Rigaku D/max-2200 Ultima X-ray diffractometer with CuKα radiation at a scan rate of 2θ = 0.01°/s from 2° to 40°. The accelerating voltage and applied current were 40 kV and 30 mA, respectively. Powder diffraction files (PDFs) from the International Centre of Diffraction Data (ICDD) in the Rigaku software (Rigaku, Japan) were used for qualitative phase analysis.

The number average mean size and size distributions of ZIF-11 particles were analyzed by a particle size analyzer (BI-90 Plus, Brookhaven Instruments Co.). The ZIF-11 particles were dispersed in methanol by means of an ultrasonic bath at room temperature and then quickly analyzed. In the dispersion process, no surfactants were used hence only submicrometer particles were suspended long enough to let particle size distribution be gathered.

The morphologies of ZIF-11 particles and PEI-ZIF-11 MMMs were analyzed by scanning electron microscopy. The SEM analyses were performed with a field-emission SEM (FEI-QUANTA FEG 450) attached with a METEK Energy Dispersive X-ray analyzer of silicon drift detector type.

FTIR spectra of the membranes was acquired on a Bruker Alpha-P ATR between 400 and 4000 cm^{-1}. The thermal stability of the ZIF-11 particles and PEI-ZIF-11 mixed matrix membranes were analyzed by thermogravimetric analysis (Perkin Elmer Pyris1 TGA) under flowing air from 25 °C to 1000 °C at a constant heating rate of 10 °C/min.

The glass transition temperatures (T_g) of the synthesized products were investigated by a Linseis DSC PT10 differential scanning calorimeter (DSC). A pre-conditioning procedure of heating up to 400 °C with 5 °C/min and natural cooling down to 30 °C was applied to all samples. Then in the second run, preconditioned samples (~10 mg) were heated up to 400 °C with a heating rate of 20 °C/min under N_2 atmosphere and the glass transition temperatures of the films were recorded.

The pure gas permeabilities were determined by constant volume and variable pressure method. Three gases (purity of 99.999%) having various kinetic diameters were used during this study; H_2 (2.89 Å), CO_2 (3.30 Å) and CH_4 (3.80 Å). All gases were used without further purification. 316 stainless steel gas permeation cell was custom designed and constructed for this study. The cell consisted of two parts, a permeate half and a feed half. The pressure built up was followed by means of vacuum pressure gauge, Leybold CTR 100 Ceravac 10 Torr. The values of change in the permeate pressure were collected on a local PC. The steady state slope of the downstream pressure vs. time was used to calculate permeability using the solution-diffusion model. Each test was started after the cell was pumped overnight. This enabled the evacuation of adsorbed water, gases and solvent. Each membrane was tested three times for each gas to determine reproducibility and the averages of three trials were reported along with one standard deviation. In each experiment, 2 cm^2 of membranes were cut and the ends were covered by aluminum tape to limit the gas permeation outside the reserved open area. Both sides of the cell were evacuated until a constant value of vacuum, approximately 10^{-3} atm was achieved. The retentate and permeate side pressures were equalized before switching to high pressure on the former side. Then, the feed pressure at retentate side was 4 bar and the testing temperature was 35 °C for all trials. The gas permeabilities were determined from the rate of downstream-pressure increase (dp/dt) obtained when permeation reached steady state according to the following equation (Eq. 2):

$$P = \frac{273.15\times10^{10}VL}{760AT((p_2\times76)/14.7)}\left(\frac{dp}{dt}\right) \qquad \textbf{(Eq. 2)}$$

where P is the permeability of the membrane to a gas and its unit is in Barrer (1 Barrer=1×10^{-10} cm3 (STP)-cm/cm^2s cmHg), V is the volume of the downstream chamber (cm^3) and L is the film thickness (cm). T is the experimental temperature (K), A assigns to the effective area of the membrane (cm^2) and the pressure of the feed gas in the upstream chamber is given by p_2 (psia).

The ideal separation factor of a membrane for gas A to gas B was evaluated as follows (Eq. 3):

$$\alpha_{A/B} = \frac{P_A}{P_B} \qquad \textbf{(Eq. 3)}$$

RESULTS AND DISCUSSION

Characterizations of ZIF-11 particles

Metal organic framework ZIF-11 was characterized via different methods. Figure 4a shows X-ray diffraction (XRD) pattern of ZIF-11 crystals by comparing with reported data (inset in Figure 4a) (27). The ZIF-11 crystals exhibited characteristic peaks (4.40°, 6.21°, 7.60°) well matched to the simulated ZIF-11 XRD pattern. ZIF-11 crystals with ideal inner structures had been successfully synthesized and Figure 4b showed the particle size analysis of ZIF-11 crystals. It was clear that size of the prepared ZIF-11 particles was mostly between 265 and 330 nm (an average of 280 nm) and ZIF-11 crystals had a narrow distribution of particle size based on DLS measurements. Figure 4c showed the typical FT-IR spectrum of ZIF-11 crystals (23). The ZIF-11 crystals showed characteristic absorption bands at 3088, 3057, 3032 cm^{-1} (=C–H stretching of aromatics), and 1611, 1465 cm^{-1} (C–C stretching in the aromatic ring). The bands occurring around 530–400 cm^{-1} were characteristic of ZnO molecules and were observed clearly in the ZIF-11 spectra (23). The band at 421 cm^{-1} corresponded to Zn–N stretching. Thereby, the above results confirmed the successful reaction of Zn^{2+} and benzimidazole in ZIF-11 crystals (28).

The thermal stability of the as-prepared ZIF-11 particles was investigated using TGA as shown in Figure 4d. The TGA curve of ZIF-11 yielded the first weight-loss of 2.8 wt.% between 130 and 200 °C corresponding to the loss of toluene (b.p.~110 °C) withheld in the particle cages. ZIF-11 particles were thermally stable up to 465 °C and then decomposed to form zinc oxide with a sharp weight loss at approximately 70% within the range of 465–830 °C. The residue at the end of the analysis (24.86 wt.%) was due to the oxidation of bound Zn metal to ZnO. Figure 4e showed the SEM image of ZIF-11 particles with a rhombic dodecahedron structure, which was consistent with the predicted one in the reported literatures (27,29). The average crystal size of ZIF-11 was about 280 nm with a size range of 0.2–1.5 μm (Figure 2e) as determined from SEM pictures. As seen in the SEM pictures in Figure 4e, it was observed that few large crystals as well as numerous smaller particles (~250-350 nm) exist together. In the DLS measurements, the number of average values were measured and it was highly likely that the larger ones than the reported particles were probably settled before the measurements were counted and recorded.

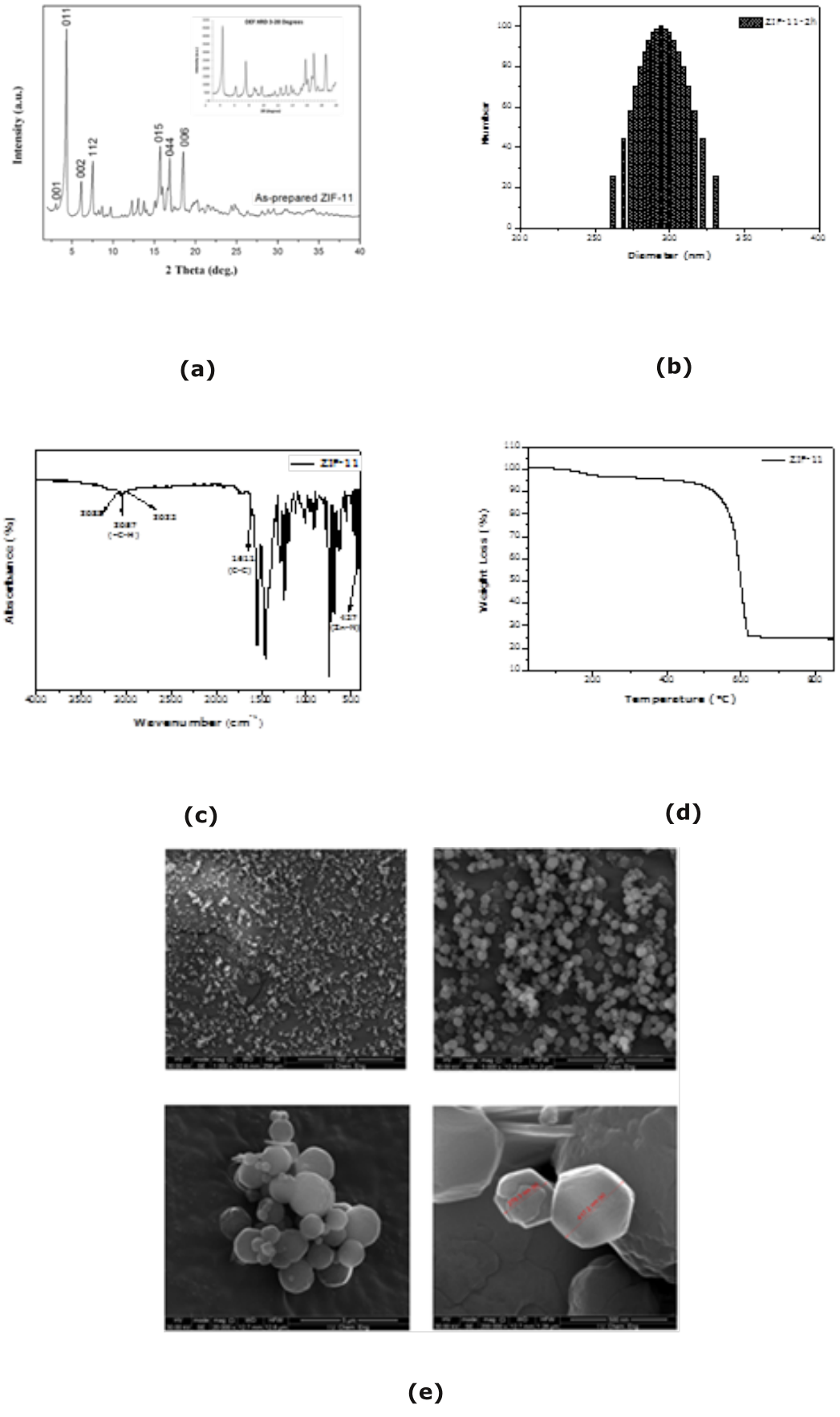

Figure 4. X-Ray diffraction pattern (a), the particle size distribution, (b), FT-IR spectrum (c), TG curve (d), and SEM image (e) of ZIF-11 crystals.

Characterizations of PEI-ZIF-11 mixed matrix membranes

Structural and thermal properties

Figure 5 showed the XRD patterns of pure PEI and PEI–ZIF-11 MMMs between 2° and 40° in order to determine their crystalline structures. The XRD pattern of pure PEI showed a broad amorphous peak of all the polyimides (30). From the XRD patterns of the MMMs (Figure 5) we can clearly observe a combination of the crystalline peaks of ZIF-11 and waved curve of pure PEI membrane. Thus, it was concluded that after the incorporation of MOF into PEI, ZIF-11 maintained its original structure integrity in the PEI-ZIF-11 MMMs. Pure ZIF-11 showed several sharp peaks (Figure 4a) while the main peak with highest intensity was around 2θ = 4.40°. Matching extremely well with pure ZIF-11 and PEI patterns (31). Furthermore, the intensity of characteristic peaks of ZIF-11 increased with accumulative ZIF-11 loading in MMMs. This finding showed that ZIF-11 crystalline structure remained unaffected after being embedded into the PEI matrix.

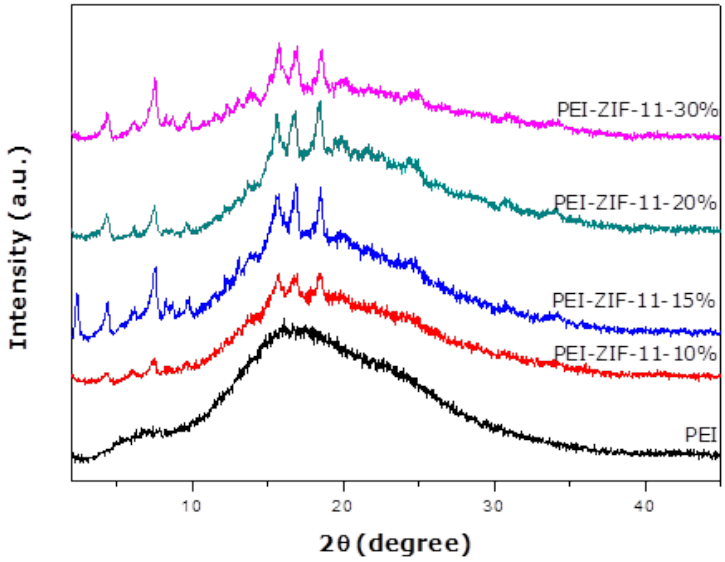

Figure 5. XRD patterns of PEI MMMs with different ZIF-11 loadings.

The FTIR spectra of pure PEI and PEI-ZIF-11 MMMs were shown in Figure 6. The FTIR spectra for the pure PEI membrane exhibited that characteristic absorption bands at 1779 cm^{-1}, 1718 cm^{-1} (asymmetric and symmetric C=O stretching vibration), 1240 cm^{-1} (Ar-O-Ar aromatic etheric stretching) and also vibrations at 1232, 777 cm^{-1} are characteristic adsorption peaks of polyetherimide structure (3,32). The ATR-FTIR spectra of PEI-ZIF-11 MMMs exhibited the features that was present in both ZIF-11 particles and a PEI film. Partial overlapping of the bands of the ZIF-11 crystals and PEI was also observed due to analogous chemical bonds (the presence of benzene rings in PEI and ZIF-11). The band occurring at 419 cm^{-1} was characteristic of Zn-N stretching and becoming more visible at 10, 15, 20, 30 wt.% loadings was a supplementary proof for the existence of ZIF-11 particles in the polymer matrix.

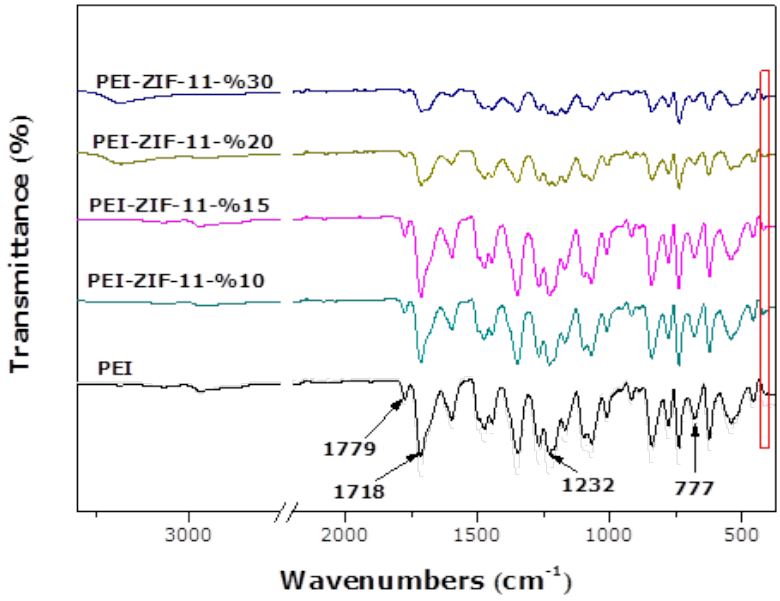

Figure 6. FTIR spectra of PEI-ZIF-11 (0-10-15-20-30 %) mixed matrix membranes.

SEM analysis was performed to investigate the structural morphology of the PEI-ZIF-11 mixed matrix membranes and the adhesion between ZIF-11 and PEI. Figure 7 showed the cross-section of pure PEI membrane (Figure 7a) and cross-sections of PEI-ZIF-11 MMMs containing 20 wt.% of ZIF-11 particles (Figure 7b-c-d), respectively. The pure PEI membrane showed a dense morphology without any visible deformation. Mixed matrix membrane morphology of dispersed phase strongly influenced the gas transport properties. Cross-sectional SEM images of the PEI-ZIF-11 MMMs were acquired to probe the dispersion of particles in the polymer matrix. The SEM images of MMMs showed good dispersion of the ZIF-11 particles throughout the polymer matrix. Any defect or agglomerates of ZIF-11 particles were not observed in the cross-sectional surfaces of the PEI-ZIF-11 MMM. On the other hand, the concentric cavities in the MMMs (Figure 7b, c and d) indicated a strong interfacial interaction between the PEI polymer and the ZIF-11 particles (14). The ZIF-11 crystals were completely enfolded by a polymer film as seen in Figure 7. Comparing MMMs with pure PEI membrane, a flat and homogenous structure was transformed into a crater-like structure in homogeneous pattern upon addition of ZIF-11 in the matrix (29). Formation of the crater-like morphology was due to de-bonding of added particles to polymeric matrix during freeze fracturing.

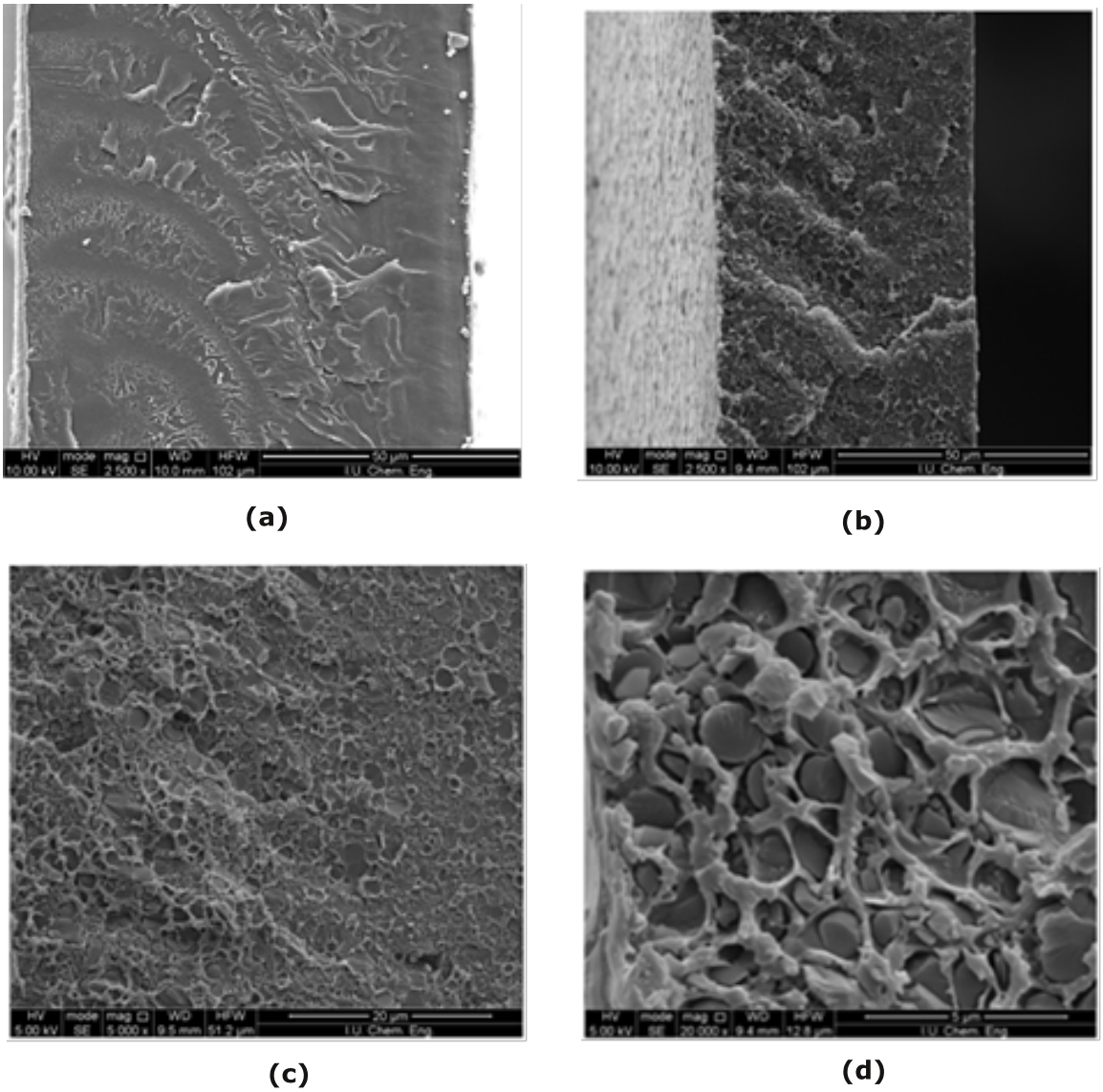

Figure 7. Cross-sectional SEM images of (a) PEI, (b-c-d) PEI-ZIF-11-20 wt.%.

TGA analysis was also carried out to determine the thermal degradation of all MMMs as a function of temperature and to study the effect of ZIF-11 on thermal stability of the membranes. The TGA curves for PEI-ZIF-11 MMMs were shown in Figure 8. The PEI membrane exhibited a two-step degradation pattern whereas the PEI-ZIF-11 MMMs exhibited a three-step degradation pattern. In the curve of the PEI membrane, first weight loss occurred between 150 and 300 °C, corresponding to the weight loss of the NMP solvent on the PEI matrix. The major weight loss observed at 567.25 °C was attributed to the complete decomposition of the polymer.

For PEI-ZIF-11 MMMs, three peaks associated with three weight loss stages were illustrated in Figure 8. The first weight loss rate for neat PEI, PEI-ZIF-11 (10 wt.%), PEI-ZIF-11 (15 wt.%), PEI-ZIF-11 (20 wt.%) and PEI-ZIF-11 (30 wt.%) up to 300 °C is 3.28, 6.12, 6.15, 7.32 and 7.27%, respectively (Table 3). Similar to the PEI membrane, the peaks between 152 and 307 °C correspond to some residual solvent in ZIF-11 and the polymer matrix. The weight loss corresponding to the second peak was attributed to the decomposition of organic groups into the MMMs matrix. The final weight loss is associated with the structural decomposition of the ZIF-11 groups to give residual ZnO and carbonaceous species. The thermal degradation of the ZIF-11 alone started around 465 °C (Figure 4d). The addition of the ZIF-11 into the polymer matrix slightly decreased the stability of the pure PEI membranes, possibly due to the fact that the ZIF-11 might have catalyzed the polymer degradation. The thermal stability of these composites was still preserved mostly up to 460 °C. This high thermal stability was acceptable for PEI-based materials in many applications.

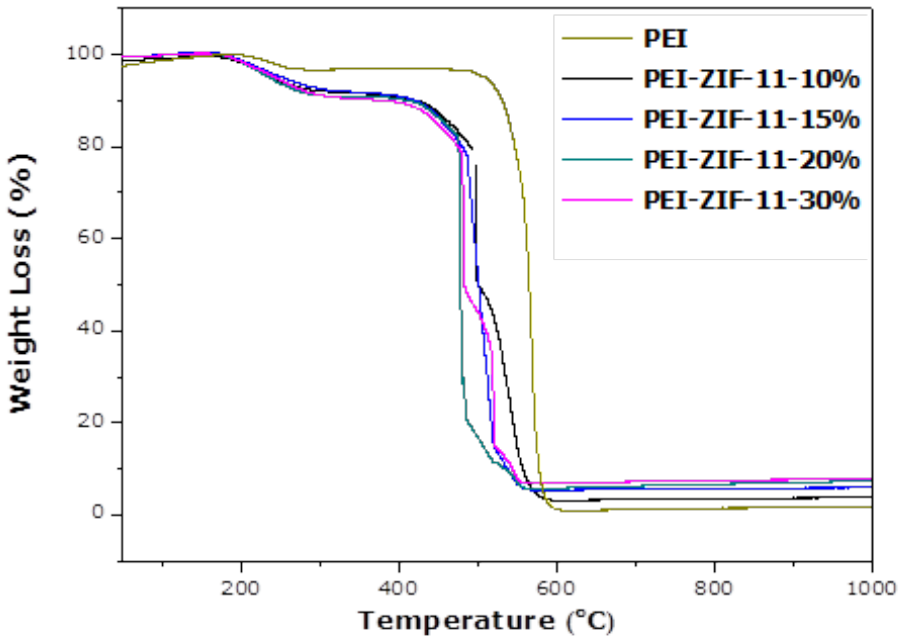

Figure 8. TGA analysis of PEI-ZIF-11 mixed matrix membranes in air atmosphere.

Table 3. TGA and DSC results of PEI-ZIF-11 MMMs.

Membrane	Weight loss (%) 200 - 300°C	Residue (%) 900°C	T_g (°C)
PEI	3.28	1.60	210.5
PEI-ZIF-11-10%	6.12	3.66	217.0
PEI-ZIF-11-15%	6.53	5.83	218.5
PEI-ZIF-11-20%	7.32	7.04	219.0
PEI-ZIF-11-30%	7.27	7.99	217.5

The influence of the addition of ZIF-11 particles on the glass transition temperature (T_g) of PEI-ZIF-11 MMMs, was illustrated in Table 3. There were some changes in the T_g of the MMMs relative to the pure polymer. The DSC result of neat PEI film indicated its T_g value as 210.5 °C. T_g values of MMMs showed that by increasing ZIF-11 loading in the MMMs, their T_g values increased and shifted from 210.5 °C to 219.0 °C once ZIF-11 loading reached 20 wt.%. By adding more ZIF-11, free volume of the polymer chain reduced due to the progressively increasing association of polymer chains to the ZIF-11 surface and/or their entrance into the ZIF-11 pores. These interactions between polymer chains and incorporated ZIF-11 restricted the movement of the polymer chains and this restriction in movement resulted in higher T_g values of MMMs (33). Clearly, this increased T_g values were an indication of interactions between ZIF-11 and PEI at a molecular level.

Gas Separation properties

Gas separation properties of pure PEI membrane and PEI-ZIF-11 MMMs with various ZIF-11 loadings were tested to investigate the influences of ZIF-11 on the MMMs. Permeability measurements for H_2, CO_2 and CH_4 at various ZIF-11 loadings (0-10-15-20-30 wt.%) into PEI membrane films were carried out and listed in Table 4. Also, CO_2/CH_4, H_2/CO_2 and H_2/CH_4 ideal selectivities were calculated from the single gas permeability results. The permeance measurements were performed at 35 °C and to assess reproducibility, at each percentage of loading experiments was repeated at least three times. The error of the measurements was calculated as the standard deviation percentage [(standard deviation / average) x 100].

Figure 9 showed the gas separation performance of PEI and PEI-ZIF-11 MMMs incorporating ZIF-11 particles. The gas separation performance of the pure PEI membrane achieved in this study was found to be consistent with the values reported in the literature (34). In the pure PEI membrane, the gas permeation fluxes for H_2, CO_2, and CH_4 pure gases were found to be 6.30, 1.36, and 0.187 Barrer, respectively. The CO_2/CH_4, H_2/CO_2, and H_2/CH_4 ideal gas pair selectivities were found to be 7.27, 4.63, and 33.69, respectively.

The incorporation of ZIF-11 particles evidently increased the gas permeation of H_2, CO_2, and CH_4 pure gases and CO_2/CH_4, and H_2/CH_4 ideal gas selectivity of the membranes. It can be seen from Table 4 that the PEI-ZIF-11 MMMs exhibited higher selectivity and permeability than the pure PEI membranes. For example, incorporation of 20 wt.% of ZIF-11 to PEI resulted in ~330% increase in H_2 permeability, while permeabilities of CH_4 and CO_2 were increased by ~71% and 80%, respectively. The reason for the permeability enhancement on MMMs was thought to be due to that ZIF-11 particles provided well-aligned channels within polymer to facilitate the permeation. On the other hand, as stated in the previous sections, the average pore size of ZIF-11 was approximately 3.0 Å which permitted the transport of gas molecules with smaller kinetic diameter (such as, H2, 2.89 Å) and partially block the large molecules (such as CH_4, 3.8 Å). ZIF-11 had naturally the most promising pore dimensions with window cut-offs ranging between 3.08 and 3.10 Å, which were ideal for hydrogen sieving applications. However, sharp size selectivity for gases with a bigger diameter than the pore size of ZIF-11 was not observed owing to the flexibility of the ZIF-11 framework (19). Thus, flexibility significantly affected the diffusion of large gas molecules in the narrow pored materials. CO_2 and CH_4 were also able to get adsorbed in ZIF-11 because of aperture flexibility of ZIF-11. On the other hand, the increase in permeability may be due to both intermitted chain packing in polymer matrix by the dispersed phase in polymer-phase and also the presence of the porous ZIF-11 (35).

From Figure 9, at the 30 wt.% ZIF-11 loading, the permeability of all gases was also decreased significantly relative to the 20 wt.% loading, However, the permeability was still higher than the pristine PEI membrane. The decrease in permeability at the higher loading values can be interpreted due to high ratio of ZIF-11 which played as barrier across the gas diffusion path on polymer. A reduction in permeability with the introduction of inorganic particles to polymer membranes has also been observed by other researchers. Ordonez et al. reported that the higher percentage of ZIF particles in the MMM reduced the amount of polymer available area for gas transport. Also, higher ZIF loading was increased the diffusion path length for the gases as they were constrained to take a more tortuous path around the ZIF particles, and likely increased the density of the remaining polymer chains thereby reducing free volume in the membrane (36). Moore et al. also explained this phenomenon well as Case I or Case V (37). These membranes exhibited some increases in selectivity while similar decreases in permeability observed, compared to the neat polymer.

Moreover, the above observations may also be attributed to the interaction between ZIF-11 particles and the PEI polymer, which was due to the affinity of the organic linkers in ZIF-11 to the PEI chains and also the coordination of some unsaturated metal ions in MOFs to carbonyl groups in the PEI chains.

In conclusion, the results were interpreted as no voids or large channels were present in the polymer and ZIF-11 interface, because such voids and channels would have resulted in a continuing increase in the permeabilities of H_2, CO_2 and CH_4 as the ZIF-11 loading increased to higher values. The results for MMMs also validated by the SEM images that showed no significant voids at the polymer/filler interface. This change in the trend also put forward as an indirect evidence that the mixed matrix membranes were defect free and the interaction between the ZIF-11 particles and the polymer played a role in gas permeation mechanism.

The experimental results were shown in Robeson's trade-off plot in Figure 10 and Figure 11. Adding ZIF-11 particles to the polymer matrix resulted in the performances closer to the Robeson upper bound due to enhancement of H_2 permeability and selectivity. The pure gas permeation results of the pristine PEI membrane were just placed below the upper bound, whereas the gas permeation results of MMMs gathered near the upper bound, particularly for PEI-ZIF11–30% and PEI-ZIF11–20% MMMs. These results indicated that ZIF-11 had the vast potential of separating H_2/CH_4 and CO_2/CH_4 mixture due to high H_2 selectivity of ZIF-11 particles.

Table 4. Gas permeability values (Barrer) of the pure PEI and PEI-ZIF-11 MMMs at 35°C and 4 bar.

Membrane	**Permeability (Barrer)**			**Ideal Selectivity**		
	$P(H_2)$	**$P(CH_4)$**	**$P(CO_2)$**	**$\alpha_{(CO2/CH4)}$**	**$\alpha_{(H2/CO2)}$**	**$\alpha_{(H2/CH4)}$**
PEI	6.30 ± 0.070	0.187 ± 0.050	1.36 ± 0.080	7.27	4.63	33.69
PEI-ZIF-11-10%	7.38 ± 0.290	0.19 ± 0.008	1.54 ± 0.120	8.10	4.79	38.84
PEI-ZIF-11-15%	20.73 ±0.600	0.25 ± 0.002	4.63 ± 0.300	18.52	4.47	82.92
PEI-ZIF-11-20%	27.10 ±1.200	0.32 ± 0.007	6.95 ± 0.770	21.18	3.89	84.68
PEI-ZIF-11-30%	8.70 ± 0.330	0.048 ± 0.017	2.73 ± 0.107	56.87	3.18	181.25

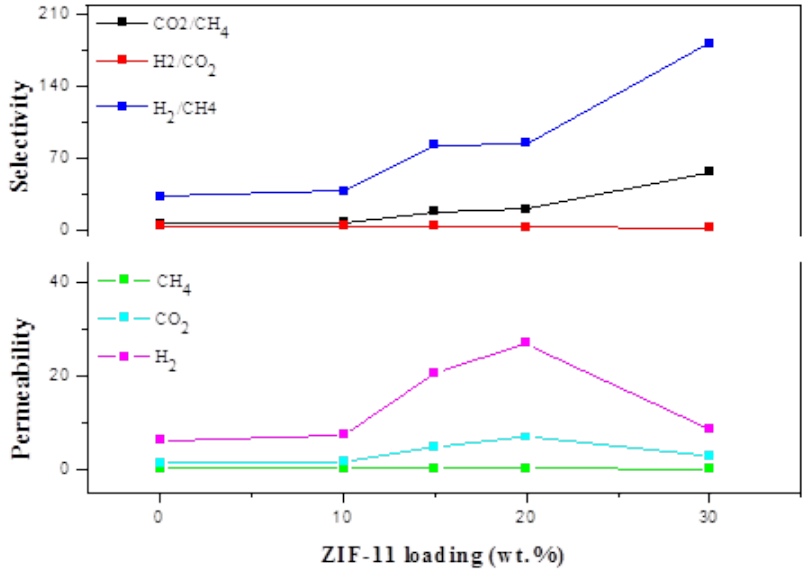

Figure 9. Enhancement of gas transport properties for H_2, CH_4, and, CO_2 as a function of ZIF-11 loading in PEI-ZIF-11 MMMs.

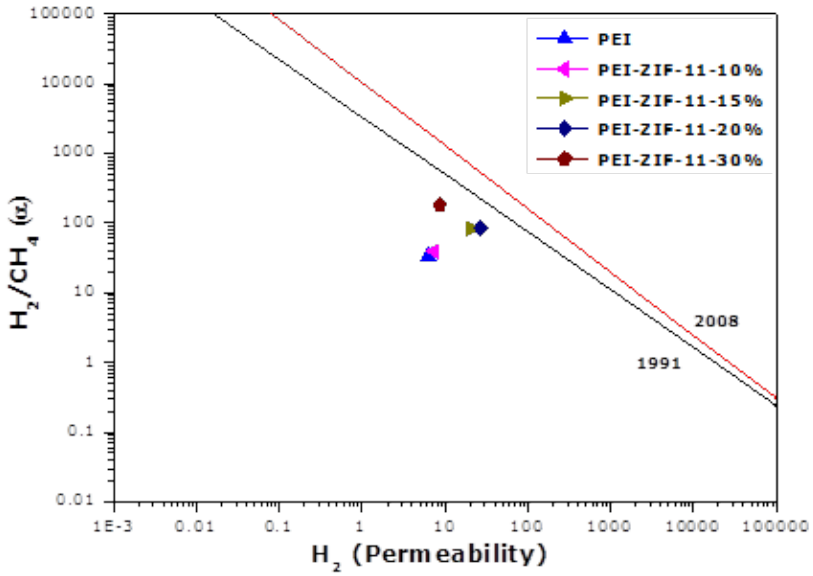

Figure 10. Comparison of pure and mixed H_2/CH_4 separation performance of PEI-ZIF-11 MMMs with the upper bound.

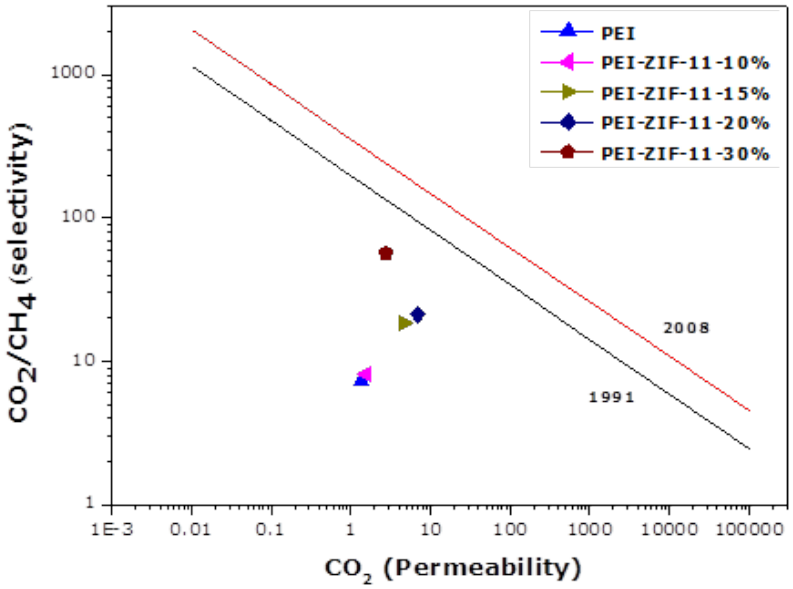

Figure 11. Comparison of pure and mixed CO_2/CH_4 separation performance of PEI-ZIF-11 MMMs with the upper bound.

The influence of MOF particles in MMMs for H_2, CO_2, and CH_4 gases separations was studied by preparing dense and asymmetric PEI membrane filled with various ZIF-11 loading. A zeolitic imidazolate framework, ZIF-11, was successfully synthesized, characterized, and evaluated as a potential adsorbent for H_2/CH_4 and CO_2/CH_4 separation. The priming protocol to prepare the MMMs resulted in a good distribution of fillers in the polymer matrix even under high loading. The XRD pattern of the MMMs showed that ZIF-11 maintained its crystallinity through and after the heating processes in the membrane preparation procedure. FTIR and TGA analysis showed interaction of ZIF-11 samples with PEI polymer. Both the selectivity and permeability for H_2/CH_4 and CO_2/CH_4 were increased by inclusion of ZIF-11 particles (up to 20 wt.% loading). At high loading of the ZIF-11 particles, the selectivity was further increased but the permeability was reduced. The increase in selectivity interpreted as the absence of voids at the PEI–ZIF-11 interface. This was confirmed by the SEM image of the membrane cross-section. The incorporation of ZIF-11 particles in the PEI matrix, can lead to an overall improvement in performance of permeability and selectivity. In the literature, Lunxi *et al.* studied ZIF-11/PBI composite membranes and tested gas separation performances of membranes for H_2 and CO_2 gases at room temperature. They obtained H_2/CO_2 ideal selectivity of 5.6 for 16.1 wt. % ZIF-11/PBI composite membrane (38). Coronas *et al.* synthesized nano-sized ZIF-11/Matrimid MMMs and investigated selectivity and permeability of H_2/CO_2 in MMMs. They showed that 25 wt.% ZIF-11 MMM showed improvement in H_2/CO_2, with a H_2/CO_2 separation selectivity of 4.4 at 35 °C (22). On the other hand, Lunxi and Coronas did not test the gas separation performance of membranes for CH_4 gas. Finally, the selectivity of H_2/CH_4 was achieved equal to 181.25. The results confirmed that PEI was a suitable candidate for hydrogen separation membranes.

ACKNOWLEDGMENTS

This work was supported in part by the Scientific and Technological Research Council of Turkey (TUBITAK) through [Grant no. 113M278].

REFERENCES

1. Zornoza B, Tellez C, Coronas J, Gascon J, Kapteijn F. Metal organic framework based mixed matrix membranes: An increasingly important field of research with a large application potential. Microporous Mesoporous Mater. 2013;166:67–78. DOI: 10.1016/j.micromeso.2012.03.012.

2. Sanders DF, Smith ZP, Guo R, Robeson LM, McGrath JE, Paul DR, et al. Energy-efficient polymeric gas separation membranes for a sustainable future: A review. Vol. 54, Polymer (United Kingdom). 2013. p. 4729–61. DOI: 10.1016/j.polymer.2013.05.075.

3. Arjmandi M, Pakizeh M. Mixed matrix membranes incorporated with cubic-MOF-5 for improved polyetherimide gas separation membranes: Theory and experiment. J Ind Eng Chem. 2014;20(5):3857–68. DOI: 10.1016/j.jiec.2013.12.091.

4. Bastani D, Esmaeili N, Asadollahi M. Polymeric mixed matrix membranes containing zeolites as a filler for gas separation applications: A review. Vol. 19, Journal of Industrial and Engineering Chemistry. 2013. p. 375–93. DOI: 10.1016/j.jiec.2012.09.019.

5. Robeson LM. The upper bound revisited. J Memb Sci. 2008;320(1-2):390–400. DOI: 10.1016/j.memsci.2008.04.030.

6. Keser Demir N, Topuz B, Yilmaz L, Kalipcilar H. Synthesis of ZIF-8 from recycled mother liquors. Microporous Mesoporous Mater. 2014;198:291–300. DOI: 10.1016/j.micromeso.2014.07.052.

7. Dorosti F, Omidkhah M, Abedini R. Fabrication and characterization of Matrimid/MIL-53 mixed matrix membrane for CO2/CH4 separation. Chem Eng Res Des. 2014;92(11):2439–48. DOI: 10.1016/j.cherd.2014.02.018.

8. Hu T, Dong G, Li H, Chen V. Effect of PEG and PEO-PDMS copolymer additives on the structure and performance of Matrimid hollow fibers for CO2 separation. J Memb Sci. 2014;468:107–17. DOI: 10.1016/j.memsci.2014.05.024.

9. Chen XY, Vinh-Thang H, Rodrigue D, Kaliaguine S. Amine-Functionalized MIL-53 Metal-Organic Framework in Polyimide Mixed Matrix Membranes for CO2/CH4 Separation. Ind Eng Chem Res. 2012;51(19):6895–906. DOI: 10.1021/Ie3004336.

10. Dai Y, Johnson JR, Karvan O, Sholl DS, Koros WJ. Ultem ??/ZIF-8 mixed matrix hollow fiber membranes for CO 2/N 2 separations. J Memb Sci. 2012;401-402:76–82. DOI: 10.1016/j.memsci.2012.01.044.

11. Nevruzoglu V, Demir S, Karaca G, Tomakin M, Bilgin N, Yilmaz F. Improving the stability of solar cells using metal–organic frameworks. J Mater Chem A. 2016;4:7930–5. DOI: 10.1039/C6TA02609E.

12. Demir S, Çepni HM, Topcu Y, Holynska M, Keskin S. A phytochemical-containing metal–organic framework: Synthesis, characterization and molecular simulations for hydrogen adsorption. Inorganica Chem Acata. 2015;427:138–43. DOI: 10.1016/j.ica.2014.12.010.

13. Günay G, Yeşilel OZ, Erer H, Keskin S, Tabak A. A zinc(II) metal organic framework based on flexible o-phenylenediacetate and rigid 4,4′-azobis(pyridine) ligands: Synthesis, crystal structure and hydrogen gas adsorption property. Polyhedron. 2015;100:108–13. DOI: 10.1016/j.poly.2015.07.017.

14. Basu S, Cano-Odena A, Vankelecom IFJ. MOF-containing mixed-matrix membranes for CO2/CH4 and CO2/N2 binary gas mixture separations. Sep Purif Technol. 2011;81(1):31–40. DOI: 10.1016/j.seppur.2011.06.037.

15. Erucar I, Keskin S. Computational screening of metal organic frameworks for mixed matrix membrane applications. J Memb Sci. 2012;407-408:221–30. DOI: 10.1016/j.memsci.2012.03.050.

16. Askari M, Chung T-S. Natural gas purification and olefin/paraffin separation using thermal cross-linkable co-polyimide/ZIF-8 mixed matrix membranes. J Memb Sci. 2013;444:173–83. DOI: 10.1016/j.memsci.2013.05.016.

17. Yilmaz G, Keskin S. Predicting the Performance of Zeolite Imidazolate Framework/Polymer Mixed Matrix Membranes for CO2 , CH4 , and H2 Separations Using Molecular Simulations. Ind Eng Chem Res. 2012;51(43):14218–28. DOI: 10.1021/ie302290a.

18. Morris W, He N, Ray KG, Klonowski P, Furukawa H, Daniels IN, et al. A combined experimental-computational study on the effect of topology on carbon dioxide adsorption in zeolitic imidazolate frameworks. J Phys Chem C. 2012;116(45):24084–90. DOI: 10.1021/jp307170a.

19. Wijenayake SN, Panapitiya NP, Versteeg SH, Nguyen CN, Goel S, Balkus KJ, et al. Surface cross-linking of ZIF-8/polyimide mixed matrix membranes (MMMs) for gas separation. Ind Eng Chem Res. 2013;52(21):6991–7001. DOI: 10.1021/ie400149e.

20. Assfour B, Leoni S, Seifert G. Hydrogen adsorption sites in zeolite imidazolate frameworks ZIF-8 and ZIF-11. J Phys Chem C. 2010;114(31):13381–4. DOI: 10.1021/jp101958p.

21. Banerjee R, Phan A, Wang B, Knobler C, Furukawa H, O'Keeffe M, et al. High-throughput synthesis of zeolitic imidazolate frameworks and application to CO2 capture. Science. 2008;319(5865):939–43. DOI: 10.1126/science.1152516.

22. Sanchez-Lainez J, Zornoza B, Mayoral A, Berenguer-Murcia Á, Cazorla-Amorós D, Tellez C, et al. Beyond the H2/CO2 upper bound: one-step crystallization and separation of nano-sized ZIF-11 by centrifugation and its application in mixed matrix membranes. J Mater Chem A. 2015;7:6549–56. DOI: 10.1039/C4TA06820C.

23. He M, Yao J, Liu Q, Zhong Z, Wang H. Toluene-assisted synthesis of RHO-type zeolitic imidazolate frameworks: synthesis and formation mechanism of ZIF-11 and ZIF-12. Dalton Trans. 2013;42(47):16608–13. DOI: 10.1039/c3dt52103f.

24. Shamsabadi AA, Kargari A, Babaheidari MB, Laki S, Ajami H. Role of critical concentration of PEI in NMP solutions on gas permeation characteristics of PEI gas separation membranes. J Ind Eng Chem. 2013;19(2):677–85. DOI: 10.1016/j.jiec.2012.10.006.

25. Park KS, Ni Z, Cote AP, Choi JY, Huang R, Uribe-Romo FJ, et al. Exceptional chemical and thermal stability of zeolitic imidazolate frameworks. Proc Natl Acad Sci U S A. 2006;103(27):10186–91. DOI: 10.1073/pnas.0602439103.

26. Cravillon J, Monzer S, Lohmeier SJ, Feldhoff A, Huber K, Wiebcke M. Rapid room-temperature synthesis and characterization of nanocrystals of a prototypical zeolitic imidazolate framework. Chem Mater. 2009;21(8):1410–2. DOI: 10.1021/cm900166h.

27. Thorkelson J. A Study of the Synthesis of the Zeolitic Imidazolate Framework Membrane Zif-11. Texas A&M University; 2011. Available from: http://oaktrust.library.tamu.edu/bitstream/handle/1969.1/148789/Thorkelson1.pdf?sequence=1.

28. Hu H, Liu S, Chen C, Wang J, Zou Y, Lin L, et al. Two novel zeolitic imidazolate frameworks (ZIFs) as sorbents for solid-phase extraction (SPE) of polycyclic aromatic hydrocarbons (PAHs) in environmental water samples. Analyst. 2014;139(22):5818–26. DOI: 10.1039/C4AN01410C .

29. Ahmad J, Hägg MB. Development of matrimid/zeolite 4A mixed matrix membranes using low boiling point solvent. Sep Purif Technol. 2013;115:190–7. DOI: 10.1016/j.seppur.2013.04.049.

30. Koley T, Bandyopadhyay P, Mohanty AK, Banerjee S. Synthesis and characterization of new aromatic poly(ether imide)s and their gas transport properties. Eur Polym J. 2013;49(12):4212–23. DOI: 10.1016/j.eurpolymj.2013.10.001.

31. Perez E V., Balkus KJ, Ferraris JP, Musselman IH. Metal-organic polyhedra 18 mixed-matrix membranes for gas separation. J Memb Sci. 2014;463:82–93. DOI: 10.1016/j.memsci.2014.03.045.

32. Namvar-Mahboub M, Pakizeh M. Development of a novel thin film composite membrane by interfacial polymerization on polyetherimide/modified SiO2 support for organic solvent nanofiltration. Sep Purif Technol. 2013;119:35–45. DOI: 10.1016/j.seppur.2013.09.003.

33. Khosravi T, Mosleh S, Bakhtiari O, Mohammadi T. Mixed matrix membranes of Matrimid 5218 loaded with zeolite 4A for pervaporation separation of water-isopropanol mixtures. Chem Eng Res Des. 2012;90(12):2353–63. DOI: 10.1016/j.cherd.2012.06.005.

34. Takahashi S, Paul DR. Gas permeation in poly(ether imide) nanocomposite membranes based on surface-treated silica. Part 1: Without chemical coupling to matrix. Polymer (Guildf). 2006;47(21):7519–34. DOI: 10.1016/j.polymer.2006.08.029.

35. Nafisi V, Hägg MB. Development of dual layer of ZIF-8/PEBAX-2533 mixed matrix membrane for CO2 capture. J Memb Sci. 2014;459:244–55. DOI: 10.1016/j.seppur.2014.03.006.

36. Ordonez MJC, Balkus KJ, Ferraris JP, Musselman IH. Molecular sieving realized with ZIF-8/Matrimid?? mixed-matrix membranes. J Memb Sci. 2010;361(1-2):28–37. DOI: 10.1016/j.memsci.2010.06.017.

37. Moore TT, Koros WJ. Non-ideal effects in organic-inorganic materials for gas separation membranes. J Mol Struct. 2005;739(1-3):87–98. DOI: 10.1016/j.molstruc.2004.05.043.

38. Li L, Yao J, Wang X, Cheng YB, Wang H. ZIF-11/Polybenzimidazole composite membrane with improved hydrogen separation performance. J Appl Polym Sci. 2014;131(22):41056. DOI: 10.1002/app.41056.

Research article

Türkçe öz ve anahtar kelimeler

POLİETERİMİD (PEI)/ZEOLİTİK İMİDAZOLAT (ZIF-11) KARIŞIMI MATRİS MEMBRANLARIN YAPISAL KARAKTERİZASYONU VE GAZ GEÇİRME ÖZELLİKLERİ

Bu çalışmada, polieterimid (PEI-Ultem1000)/ZIF-11 karışık matris membranlarının hazırlanması ve farklı oranlarda ZIF-11 partikülleri (ağırlıkça % 0, 10, 15, 20, ve 30) yüklenmesinin etkisi incelenmiştir. Ortalama partikül boyutu ~280 nm olarak sentezlenen ZIF-11 partikülleri PEI membranına katkısı ile karışık matris membranlar (KMM) hazırlanmıştır. ZIF-11 yüklemesinin gaz ayırma performansına etkisi H_2, CO_2 ve CH_4 gazları için 35 °C ve 4 bar basınçta incelenmiştir. ZIF-11 yüklemesindeki artış ile KMM'lerin gaz geçirgenlik özellikleri artmıştır. %20 ZIF-11 yüklemesinde H_2 ve CO_2 gazlarının geçirgenlik katkısız polimere göre dört kat artmıştır. CH_4 geçirgenliğinde ise bir miktar artış gözlenmiştir. Ağırlıkça %20'nin üzerinde ZIF-11 yüklemesinde, bütün gazlar için geçirgenlik değerleri düşerken CO_2/CH_4 ve H_2/CH_4 seçicilikleri ZIF-11 yüklemesine bağlı olarak artmıştır.

Anahtar Kelimeler: Karışık matris membranlar, zeolit imidazolat kafesler, polieterimid, gaz ayırma.
Gonderme: 28 Mayıs 2016, **Düzeltme:** 24 Haziran 2016, **Kabul:** 28 Haziran 2016.

JOTCSA, Volume 3, issue 2, (2016), pp. 207-218. **Research article**

Journal homepage: http://dergipark.ulakbim.gov.tr/jotcsa

e-ISSN: 2149-0120

Phytochemical Profile and Insecticidal Activity of Essential Oil from Fresh and Dried Leaves of Nigerian Grown *Citrus meyerii*

Usman Lamidi Ajao[1]*, Olanipekun Bolatito Eunice[2], Ogundele Victor Ayorinde[2] and Musa AbdulRasak Kannike[3]

1. Department of Chemistry, University of Ilorin, P.M.B 1515, Ilorin, Nigeria.
2. Department of Chemical, Geological and Physical Science, Kwara State University, P.M.B 1530, Malete, Nigeria.
3. Department of Crop Protection, University of Ilorin, P.M.B 1515, Ilorin, Nigeria.

Abstract: Leaves of *Citrus meyerii* harvested fresh and dried for four consecutive days were separately hydro-distilled and yielded 0.11 – 0.24 %(w/w) of essential oils. Characterisation of the oils using Gas chromatography - mass spectrometry (GC-MS) revealed the predominance of hydrocarbon monoterpenoids 51.1 – 68.3%. Oxygenated monoterpenoids, hydrocarbon sesquiterpenoids, and oxygenated sesquiterpenoids constituted (17.4 - 24.9%), (12.2 - 19.8%) and (0.0 – 2.5%) of the oils respectively. Principal constituents of the oils were; 3-carene (10.1 - 30.7%), α-pinene (1.0% - 18.7%), d-limonene (5.2 - 6.4%), cis-β-ocimene (5.8 - 14.2%), citronellal (5.4 - 6.8%), and β-elemene (3.0 - 5.8%). The oils were of 3-carene and α-pinene chemotypes. Oils that were of 3-carene chemotype were those from fresh and the leaves dried for one and four days while the oils from leaves dried for two and three days were of α-pinene chemotype. Insecticidal activities of the oils were determined using contact toxicity test on *Callosobruchus maculatus*. Regardless of whether the leaves were fresh or dried, the oils were active against the insect. Interestingly, there was no significant difference in the activities of the oils against the insect.

Keywords: *Citrus meyerii*, Chemotype, 3-carene synthase, β-elemene synthase, insecticidal activities.

Submitted: May 30, 2016. **Revised:** June 30, 2016. **Accepted:** July 11, 2016.

Cite this: Lamidi Ajao *et al.* Phytochemical Profile and Incesticidal Activity of Essential Oil From Fresh and Dried Leaves of Nigerian Grown *Citrus meyerii*. Journal of the Turkish Chemical Society, Section A: Chemistry. 2016;3(2):207–218.

DOI: 10.18596/jotcsa.09331.

Correspondence to: Lamidi Ajao Usman. usmanlamidi@unilorin.edu.ng. Tel: +2348035032378.

INTRODUCTION

Citrus meyerii is a hybrid of *Citrus sinensis* and *Citrus limonium* gotten via budding of the parent plants. Just like the parent plants, the plant is odorous, hence, bearing essential oils. Several chemotypes of oil from the parent plants have been reported in various part of the world. For instance, limonene, α-fenchene, α-terpinolene, 3-carene, and β-pinene chemotypes of leaf essential oil of *Citrus sinensis* grown in Turkey, Pakistan, and Nigeria have been identified [1-3]. Similarly, limonene and α-pinene chemotypes of the leaf essential oil of *Citrus limonium* grown in Crete, Syria, and Iran have been discovered [4-6]. Occurrence of various chemotypes of the oils signified that the formations of its constituents were catalysed by different terpene synthase [7]. The activities of the synthases depend on biotic and abiotic factors which may affect phytochemical profiles and biological activity of the oils.

Usman *et al.*, 2016 investigated the effect of drying on the phytochemical profile and insecticidal activity of leaf essential oil of *C. sinensis* grown in Nigeria. In their investigation, α-fenchene, 3-carene, α-terpinolene and β-pinene chemotypes of the oil were detected. Despite the fact that the oils were of different chemotypes, they were active against *Callosobruchus maculatus* without any significant difference.

Phellandrene chemotype of leaf essential oils of *C. sinensis* from two different harvests (7:00 am and 4:00 pm) were characterised by Omoniwa *et al.,* 2014. The oils significantly ameliorated the impaired hepatic and renal functions. This implies that the time of harvest of leaves did not affect the oil's chemotype and its biochemical activity despite the fact that the quantity of most abundant compound differs appreciably [8]. Vekaria *et al.,* 2002 reported that seasonal variation did not affect the chemotype of leaf essential oil of *Citrus limonium* as they were of limonene chemotype. However, the quantities of the predominant compounds varied significantly [4].

Earlier works on the leaf essential oil of *C. meyerii* revealed the existence of oil of thymol and limonene chemotypes of the plants grown in Florida and Cameroon [9, 10]. The antioxidant assay of the oil from Cameroonian grown *C. meyerii* showed that, the oil demonstrated higher antioxidant property than the synthetic antioxidant (Butylhydroxyltoluene (BHT)). The oil also has higher inflammatory activity than the reference drug nordihydroguaieretic acid (NDGA). Higher biochemical activity of the oil may be due to synergistic actions of the constituents of the oil.

To the best of our knowledge, there are no reports on the effect of dryness of *C. meyerii* leaves on the chemical composition and insecticidal activity of its essential oil. It is on the basis of this that this work aims at monitoring the effect of drying on the chemical composition and insecticidal property of essential oil from the leaf of the plant.

MATERIALS AND METHODS

Sample Collection

Leaves of *Citrus meyerii* were harvested from Park and garden, University of Ilorin, Ilorin, Kwara state. The leaves were air-dried at ambient temperature for four consecutive days and subsequently pulverised.

Oil Isolation

500 g of each of the pulverised leaves of *C. meyerii* was hydro-distilled for 3 hours in a Clevenger-type apparatus, according to the British Pharmacopoeia specification [11]. The resulting oil from each sample was collected, preserved in a sealed sample tube, and stored under refrigeration until analysis.

GC-MS Analysis

An Agilent 19091S gas chromatograph coupled with a quadruple focusing mass spectrometer 433HP-5 mass detector was used. Helium was used as the carrier gas at a flow rate of 1.5 mL/min; all analyses were performed at constant flow. The GC was fitted with a 30 m x 0.25 mm fused silica capillary column coated with phenyl methyl siloxane at a split ratio of 1:50. The film thickness was 0.25 µm. Oven temperature was initially kept at 100 °C for 5 min then 150 °C at a rate of 4 °C for 8 min and to 250 °C at a rate of 20 °C /min. Mass detector conditions were as follows: Transfer line temperature at 300 °C, ionisation mode electron impact at 70 eV. The percentage composition of the oils was computed in each case from GC peak areas. The identification of the components was done based on comparison of retention indices (determined relative to the retention times of series of n-alkanes) and mass spectra with those of authentic samples and with data from literature [12-14].

Insecticidal Activity

Insect Culture

Cowpea beetles (*Callosobruchus maculatus*) were obtained from heavily infested cowpea. They were reared on clean beans and maintained under ambient environmental condition (28 ± 2 °C). The rearing jars were covered with muslin fabric to allow aeration and prevent escape of the insects. The jars were placed inside a wire-netted shelf in the laboratory.

Mortality Determination

10 g of clean, uninfected sweet cowpea grains were separately put into sixteen plastic containers (4 cm diameter) including the one meant for control. 0.1 mL of essential oil from fresh and the leaves dried for four consecutive days were separately added to the beans in the containers except the one meant for the control in triplicate. Apart from the control, the samples were agitated thoroughly for uniform distribution of the oil. Ten active adult *Callosobruchus maculatus* insects were introduced into each container. The control consisted of ten active adult *Callosobruchus maculatus* insects kept in a plastic container containing 10 g of clean, uninfected beans without any portion of the oil in it. The percentage mortality was reported at 6 hours interval for 42 hours.

Data Analysis

The adult toxicity experiments were carried out in a Completely Randomised Design by which the percentage mortality data from the experiment was subjected to one way Analysis of Variance (ANOVA) and where there was a significant difference, the mean separation was done using Duncan Multiple Range Test at 1% level of significance (0.01 probabilities). This statistical analysis was performed using SPSS software, version 21.

RESULTS AND DISCUSSION

Fresh and dried leaves of *Citrus meyerii* afforded oils in the range of 0.11-0.24% (w/w). The yield increased with increase in day of drying (Fig 1). The highest yield was obtained in the leaves dried for four days (0.37%) while fresh leaves afforded the lowest yield (0.11%). The increase in oil yield could be attributed to the decrease in moisture content as the day of drying increases. The oil yields from the fresh and dried leaves were lower than the yield from Cameroonian grown *C. meyerii* [10]. This could be attributed to the variation in agro-climatic conditions of the two countries.

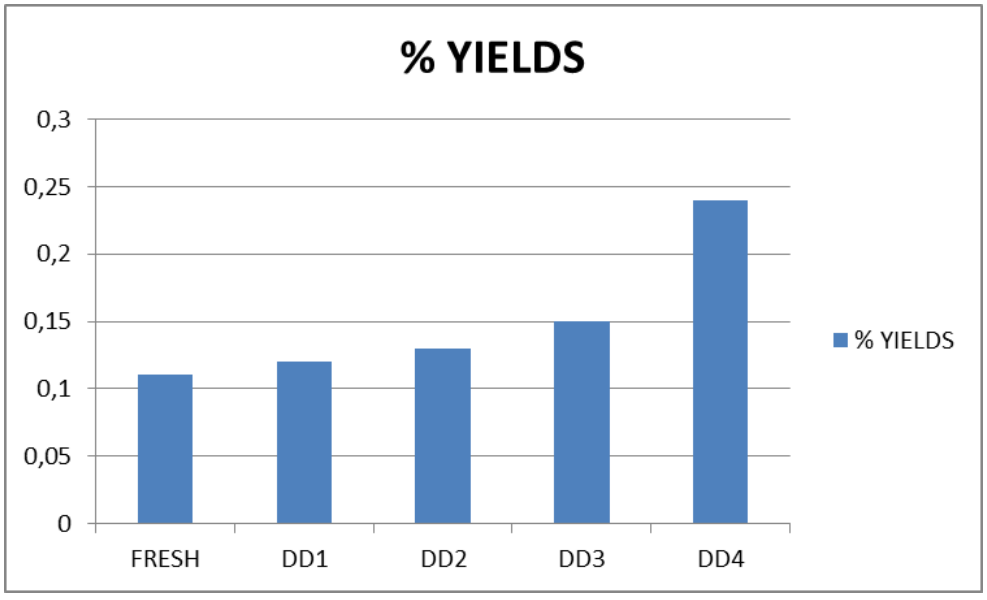

Figure 1. Yield of *Citrus meyerii* oils.

KEY TO FIGURE 1

FRESH: Fresh leaves
DD1: Leaves dried for one day
DD2: Leaves dried for two days
DD3: Leaves dried for three days
DD4: Leaves dried for four days

Table 1 (see Supplementary File) shows the identities, kovats indices and percentage composition of the constituents of essential oils obtained from fresh and dried leaves of *Citrus meyerii*. In the Table, 25-35 compounds that represented 92.0 - 99.9% of the oils were identified. Hydrocarbon monoterpenoids constituted 51.1 - 68.3% of the oils while the percentage composition of oxygenated monoterpenoids ranged from 17.4 - 24.9%. Meanwhile, 9.4 - 19.8% of the oils were hydrocarbon sesquiterpenoids. 0.5 - 2.5% of the oil, were oxygenated sesquiterpenoids which were not detected in the oil obtained from fresh and leaves dried for three days.

The principal constituents of the oils were; α-pinene (1.0 – 18.9%), 3-carene (10.1 – 30.7%), D-limonene (5.2 – 6.4%), Cis-β-ocimene (5.8 – 14.9%), 2-carene (0 – 4.4%), terpinolene (0 – 5.4%), Citronellal (0 – 6.8%), geraniol (0.9 – 5.4%), neral (0.3 – 9.1%), terpinen-4-ol (3.1 – 4.5%), β-elemene (3.0 – 5.5%), γ-elemene (0.0 – 4.8%), cis-β-farnesene (0.6 – 4.4%) and eremophilene (0 – 4.0%). α-Thujene (0 – 1.4%), β-pinene (2.2 – 3.6%), α-phellandrene (1.0 – 1.5%), o-cymene (0.2 – 1.8%), γ-terpinene (0 – 2.7%), 1,3,8-p-menthatriene (0.0 – 1.8%), citronellol (0.0 – 3.7%), geranial (0.0 – 3.5%), humulene 1.0 – 1.6%), β-caryophyllene (2.3 – 3.6%), and phytol acetate (0.5 – 1.4%) were also detected in appreciable quantities. However, some of the compounds that existed in significant quantities in the oils occurred as minor constituents in oil of leaves dried for one and four days. For instance, isopulegol (0.4% and 0.3%) was detected as minor constituent of the oils. α-Terpinene (0.3%), decanal (0.4%), β-copaene (0.4%), aromadendrene (0.2%), spathulenol (0.2%) and caryophyllene oxide (0.3%) were also identified as minor constituents in the oil of leaves dried for one day. Furthermore, geranial (0.4%), methyl geranate (0.3%), β-copaene (0.4%) and γ-muurolene (0.3%) were found in minor quantities in the oil of leaves dried for four days. Their existence as minor constituents signifies that their formations were prematurely terminated by synthase that mediates the transformations of their respective precursors to the compounds.

Comparison of the oils revealed that the composition patterns of the oils differ significantly. Qualitatively, geranyl butyrate, γ-elemene, guaia-9,11-diene that existed in the oil from fresh leaves were not found in the oils from the dried leaves. α-Terpinene, isoterpinolene, decanal, α-copaene, aromadendrene, spathulenol and caryophyllene oxide were identified in the oil from the leaves dried for one day but were not detected in other oils. However, δ-cadinene and eremophilene existed in the oil of leaves dried for three days and did not exist in other oils. γ-muurolene, geranyl acetate, and geranyl linalool were detected in the oils from leaves dried for four days but were not detected in other oils.

Limonene and ortho-cymene were identified in the oil of fresh leaves but not detected in the oils from dried leaves. Furthermore, β-pinene, citronellyl acetate, and methyl geranate were found in the oil of leaves dried for two days but not found in other oils. Similarly, Cis-β-ocimene and phytol were identified in the oils except the oil from leaves dried for three days. α-Thujene and eremophilene were detected in the oils but were not found in the oil of the leaves dried for five days. Absence of some compounds in the oils of the leaves may be due to the fact that the physiological conditions of the plant did not favour their biosynthesis.

Quantitatively, α-pinene, α-phellandrene, 3-carene, o-cymene, d-limonene, cis-β-ocimene, trans-β-ocimene, α-terpineol, neral, geraniol, β-elemene, humulene, β-caryophyllene and cis-β-farnesene were detected in the oils but at varying quantities. α-Terpineol, geraniol, humulene and β-caryophyllene were detected in appreciable quantities in the oil of fresh leaves than other oils. Neral predominates the oil of the leaves dried for one day than other oils. α-Pinene and d-limonene were of greater abundance in the oil of the leaves dried for two days than other oils. Furthermore, terpinen-4-ol and cis-β-ocimene occurred in higher amounts in the oil of the leaves dried for three days than other oils. Similarly, β-elemene, trans-β-ocimene, and 3-carene occur in appreciable quantities in the oil of the leaves dried for four days than other oils. The variations in the quantities of the constituents of the oil are attributable to difference in activity of synthases that mediate the formation of the compounds from their respective precursors [15].

Oils of the fresh leaf of Nigerian and Cameroonian grown *C. meyerii* were of 3-carene and d-limonene chemotypes respectively. Interestingly, 3-carene was not detected in the oil of Cameroonian grown *C. meyerii* which implies that the physiological conditions of the plant did not favour its biosynthesis. The conditions depend on the agro-climatic conditions which determine the activity of the enzyme that aid the formation of the terpenoids. Meanwhile, the biosynthesis of terpenoids is usually catalysed by the most active enzyme that forms the most abundant mono- and sesqui-terpenoids. [7, 15].

The predominance of α-pinene in the oils obtained from the leaves dried for two and three days implied that its synthase mediates the transformation of its precursor to all monoterpenoids. However, the most abundant monoterpenoids in the oils obtained from fresh and the leaves dried for one and four days was 3-carene, its synthase catalysed the formation of all monoterpenoids in the oils. Differences in monoterpenoid synthases that aided the formation of the compounds implied that the period of drying affects the activity of the synthase which depend on the physiological condition of the leaves. Despite the fact that β-elemene was the most abundant sesquiterpenoid in the oils from the fresh and dried leaves and its quantity varied significantly, its synthase catalysed the formation of all sesquiterpenoids in the oils. Quantitative difference in β-elemene content is attributable to variation in physiological condition of the leaves that determine the activities of the enzyme. This variation connotes that the period of drying of the leaves affect the activity of the enzyme. The enzymes catalysed the transformation of mono- and sesquiterpenoid precursor to the respective terpenoids via cationic mechanisms (Schemes 1 and 2).

Reaction mechanisms

In Reaction Scheme 1, 3-carene and α-pinene synthases aided the transformation of neryl **(1)** and geranyl pyrophosphate **(2)** to their respective cationic intermediates (neryl **(3)**, linalyl **(4)** and geranyl **(5)** cations). Hydration of geranyl cation with subsequent hydrogenation at C2 and C3 gives citronellol **(6)** which further undergoes oxidation to give citronellal **(7)**. Neryl cation **(3)** undergoes hydration to give nerol **(8)** which subsequently oxidises to neral **(9)**. Nucleophillic attack of carbonyl carbon of the compound **(9)**, by C6-C7 double bond form isopulegyl cation. Deprotonation of the ion at C7 follow by protonation of alkoxide intermediate with hydrogenation at C2-C3 produce isopulegol **(10)**. Linalyl cation **(4)** deprotonate at C1 to form trans-β-ocimene **(11)**. The ion **(3)** undergoes electrophilic attack on C6-C7 double bond to give α-terpinyl cation **(12)**. C8 deprotonation of the ion **(12)** gives limonene **(13)**. 6,7-hydride shift of the ion **(12)** gives terpinyl-4-yl cation **(14)**. Subsequent deprotonation of the latter **(14)** at C1 and C7 gives α-terpinene **(15)** and α-terpinolene **(16)** accordingly. Deprotonation of ion **(12)** at C5 followed by electrophilic attack on C7 forms car-3-ene **(17)**. Folding of the ion (12) towards C2-C3 double bond followed by electrophilic attack of the ion via C2 gives pinyl cation **(18)**. Deprotonation of the ion at C4 and C10 give α-pinene **(19)** and β-pinene **(20)** respectively.

The abundance of β-elemene in the oils implied that its synthase mediated the biosynthesis of all the sesquiterpenoids (Reaction Scheme 2). In the scheme, β-elemene synthase catalysed the ionisation of farnesyl pyrophosphate **(21)** to nerolidyl **(22)** and farnesyl **(23)** cations. Loss of proton at C15 by the ion **(22)** forms β-farnesene **(24)**. Electrophilic attack of the ion on C10-C11 double bond give humulyl cation **(25)** which further under goes deprotonation at C9 to form humulene **(26)**. Electrophyllic attack of the ion **(25)** on C2-C3 double bond form caryophyllyl cation **(27)**. Deprotonation of the ion **(24)** at C15 form β-caryophyllene **(28)**. Epoxidation of the compound **(28)** at C5-C7 double bond produces caryophyllene epoxide **(29)**. Electrophyllic attack of ion **(23)** on C10-C11 double bond gives germacrenyl cation **(30)**. Ion **(30)** undergoes 2, 7-ring closure to form β-selinyl cation **(31)**. Subsequent hydride shift from C11-C10, C10-C1 and deprotonation at C6 followed by electrophilic attack of the ion **(31)** on C6 forms α-copaene **(32)**. Hydride shift from C11-C10, C10-C1 followed by deprotonation of the ion **(30)** at C6 gives δ-cadinene **(33)**. This ion **(30)** undergoes 2, 11- hydride shift and 2,7-cyclisation to give eudesmanyl cation **(34)** which undergoes 4,5-cleavage and deprotonation at C15 to form β-elemene **(35)**.

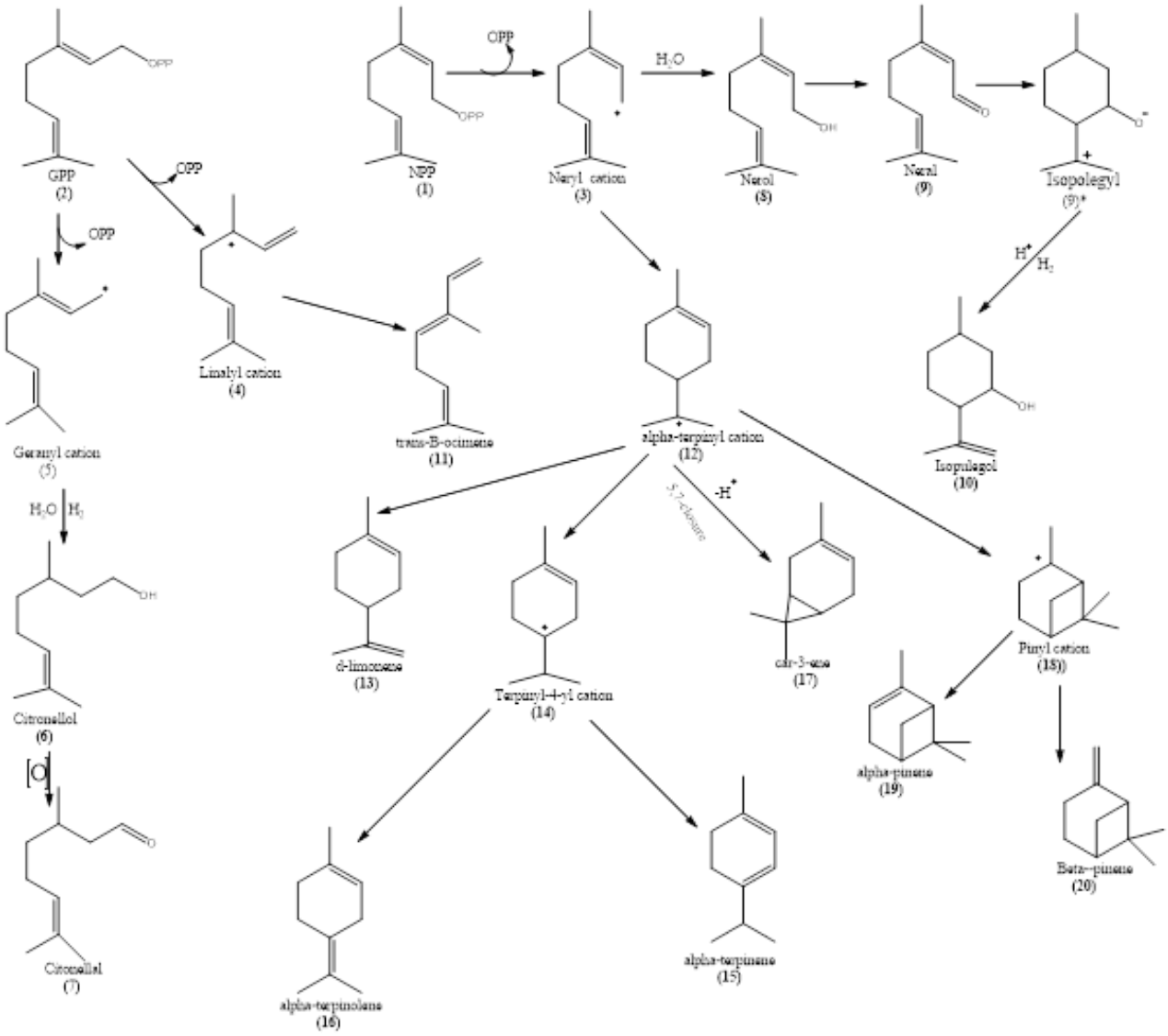

Reaction Scheme 1. Biosynthesis of monoterpenoids catalysed by 3-carene and α-pinene synthases.

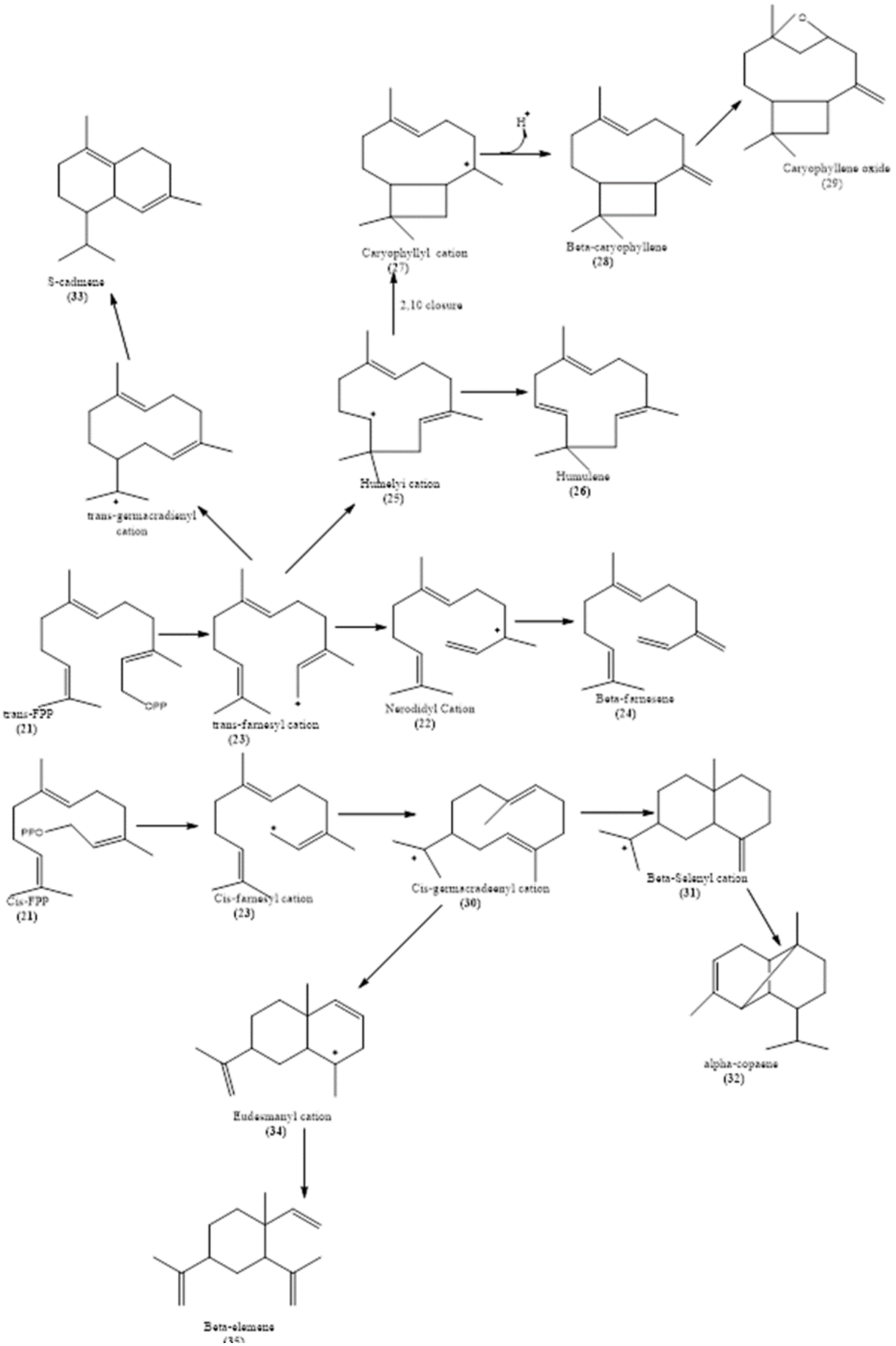

Reaction Scheme 2. Biosynthesis of Sesquiterpenoids catalysed by β-elemene synthase.

Insecticidal Activity

Contact toxicity data of the oils of fresh and dried leaves of *C. meyerii* against adult *Callosobruchus maculatus* are shown in Table 2 (see Supplementary File). The table revealed that at the end of 42 hours of exposure, oils from the fresh leaves and leaves dried for a day caused 85% mortality of *C. maculatus*. Meanwhile, the oils from the leaves dried for two, three, and four days caused 95% mortality of *C. maculatus*. However, irrespective of the days of drying, the oils were highly active, that is, caused very high percentage adult mortality with no significant difference between them at 0.01 probabilities. Rajendra *et al.,* 2007 linked the toxicity of essential oils to stored insect pests with the individual and synergistic actions of the compounds present in the oils [16]. Such compounds include; α-pinene, β-pinene, phellandrene, limonene, γ-terpinene, citronellal, and geraniol. The presence of these compounds in substantial amounts in the oil may be responsible for their activity against *C. maculatus*. However, the contact toxicity activity of the oil compared favourably with activities of the leaf oils of other Citrus species.

CONCLUSION

Oil yields from the leaves varied significantly. It increases with increase in period of drying. This can be attributed to the loss of moisture by drying from the leaves samples which subsequently increase the yields. Phytochemical profile of the oil was also affected by drying as it affects the chemical composition of the leaf oil of *Citrus sinensis* [3]. This could justify the presence of both plants in citrus family. However, the drying did not affect their insecticidal activity against *C. maculatus*. Since the oils have significant activities against the insect. Hence, they can be use as alternative to synthetic insecticide for *C. maculatus*. Meanwhile, it is preferable to extract the oils from dried samples as they afforded more oils than fresh leaf sample.

REFERENCES

1. Kırbaşlar F, Tavman A, Dülger B, Türker G. Antimicrobial activity of Turkish citrus peel oils. Pakistan Journal of Botany. 2009;41(6):3207–12. URL: www.pakbs.org/pjbot/PDFs/41(6)/PJB41(6)3207.pdf.

2. Kamal G, Anwar F, Hussain A, Sarri N, Ashraf M. Yield and chemical composition of Citrus essential oils as affected by drying pretreatment of peels. Int Food Res J. 2011;18(4):1275–82.

3. Usman LA, Watti OI, Ismaeel RO, Ojumoola AO. Effect of Drying on Yield, Chemical Composition and Insecticidal Activity of Leaf Essential Oils of Sweet Orange (*Citrus sinensis*). Journal of the Turkish Chemical Society, Section A: Chemistry. 2015 Dec 14;3(1):1. DOI: 10.18596/jotcsa.98689.

4. Vekiari SA, Protopapadakis EE, Papadopoulou P, Papanicolaou D, Panou C, Vamvakias M. Composition and Seasonal Variation of the Essential Oil from Leaves and Peel of a Cretan Lemon Variety. Journal of Agricultural and Food Chemistry. 2002 Jan;50(1):147–53. DOI: 10.1021/jf001369a.

5. Odeh F, Rahmo A, Alnori A, Chaty M. The Cytotoxic Effect of Essential Oils *Citrus Aurantium* Peels on Human Colorectal Carcinoma Cell Line (LIM1863). The Journal of Microbiology, Biotechnology and Food Sciences. 2012;1(6):1476–87.

6. Oshaghi M, Ghalandari R, Vatandoost H, Shayeghi M, Kamali-Nejad M, Tourabi-Khaledi H, et al. Repellent effect of extracts and essential oils of Citrus limon (Rutaceae) and Melissa officinalis (Labiatae) against main malaria vector, Anopheles stephensi (Diptera: Culicidae). Iranian Journal of Public Health. 2003;32(4):47–52. URL: http://ijph.tums.ac.ir/index.php/ijph/article/download/1940/1921.

7. Wise ML, Savage TJ, Katahira E, Croteau R. Monoterpene Synthases from Common Sage (*Salvia officinalis*): cDNA Isolation, Characterization, AND Functional Expression of (+)-Sabinene Synthase, 1,8-Cineole Synthase, and (+)-Bornyl Diphosphate Synthase. Journal of Biological Chemistry. 1998 Jun 12;273(24):14891–9. DOI: 10.1074/jbc.273.24.14891.

8. Soji-Omoniwa O, Muhammad N, Usman L, Omoniwa B. Effect of leaf essential oil of Citrus sinensis at different harvest time on some liver and kidney function indices of diabetic rats. Int J Biol Vet Agric Food Eng. 2014;8:484–488. URL: http://www.waset.org/publications/9998274.

9. Moshonas MG, Shaw PE, Veldhuis MK. Analysis of volatile constituents from Meyer lemon oil. Journal of Agricultural and Food Chemistry. 1972 Jul;20(4):751–2. DOI: 10.1021/jf60182a018.

10. Dongmo PMJ, Tchoumbougnang F, Boyom FF, Sonwa ET, Zollo PHA, Menut C, et al. Antiradical, antioxidant activities and anti-inflammatory potential of the essential oils of the varieties of Citrus limon and Citrus aurantifolia growing in Cameroon. Journal of Asian Scientific Research. 2013;3(10):1046–1057. URL: http://www.aessweb.com/pdf-files/jasr%203(10),%201046-1057.pdf.

11. Pharmacopoeia B. Vol. 11, London: HM Stationary Office. PA; 1980.

12. Adams RP. Identification of essential oil components by gas chromatography/mass spectrometry. 4th ed. Carol Stream, Ill: Allured Pub. Corp; 2007. 804 p. ISBN: 978-1-932633-21-4.

13. Joulain D, König WA. The atlas of spectral data of sesquiterpene hydrocarbons. EB-Verlag; 1998.

14. Jennings W, Shibamoto T. Qualitative analysis of flavor and fragrance volatiles by glass capillary gas chromatography. San Francisco: Academic Press; 1980. 472 p. ISBN: 978-0-12-384250-3.

15. Degenhardt J, Köllner TG, Gershenzon J. Monoterpene and sesquiterpene synthases and the origin of terpene skeletal diversity in plants. Phytochemistry. 2009 Oct;70(15–16):1621–37. DOI: 10.1016/j.phytochem.2009.07.030.

16. Rajendran S, Sriranjini V. Plant products as fumigants for stored-product insect control. Journal of Stored Products Research. 2008 Jan;44(2):126–35. DOI: 10.1016/j.jspr.2007.08.003.

Research article

Türkçe Öz ve Anahtar Kelimeler

Nijerya Bölgesinde Yetişen *Citrus meyerii*'nin Taze ve Kurutulmuş Yapraklarından Elde Edilen Esansiyel Yağın Fitokimyasal Profili ve İnsektisit Aktivitesi

Usman Lamidi Ajao, Olanipekun Bolatito Eunice, Ogundele Victor Ayorinde ve Musa AbdulRasak Kannike

Öz: *Citrus meyerii* yaprakları taze olarak ve dört ardışık gün kurutularak ayrı ayrı hidrodistilasyona uğratılmış ve ağırlıkça %0,11-0,24 esansiyel yağ vermiştir. Yağların Gaz kromatografisi - kütle spektrometrisi (GC-MS) ile karakterizasyonu %51,1 - 68,3 oranında baskın bir hidrokarbon monoterpenoidlerini göstermiştir. Oksijenli monoterpenoidler, hidrokarbon seskiterpenoidler ve oksijenli seskiterpenoidler yağların sırası ile (%17,4 - 24,9), (%12,2 - 19,8) ve (%0,0 - 2,5) kısmını oluşturmuştur. Yağların baskın bileşenleri 3-karen (%10,1 - 30,7), α-pinen (%1,0 - 18,7), d-limonen (%5,2 - 6,4), cis-β-osimen (%5,8 - 14,2), sitronellal (%5,4 - 6,8) ve β-elemen (%3,0 - 5,8) olarak tespit edilmiştir. Yağlar 3-karen ve α-pinen kemotiplerinden oluşmaktadır. 3-Karen kemotipi olan yağlar taze ve bir ve dört gün kurutulan yapraklardaki esansiyel yağdan oluşmaktadır, buna karşılık iki ve üç gün kurutulan yapraklardaki yağlar α-pinen kemotipi ağırlıklıdır. Yağların insektisit aktiviteleri *Callosobruchus maculatus* üzerindeki temas toksisite testleri ile belirlenmiştir. Yaprakların taze veya kurutulmuş olmasından bağımsız olarak, yağlar böceklere karşı aktivite göstermiştir. İlginç bir şekilde, yağların böceğe karşı aktivitesinde belirgin bir farklılık tespit edilmemiştir.

Anahtar kelimeler: *Citrus meyerii*, Kemotip, kar-3-ene sentaz, β-elemen sentaz, insektisit aktivitesi.

Sunulma: 30 Mayıs 2016. **Gözden geçirme:** 30 Haziran 2016. **Kabul:** 11 Temmuz 2016.